Processing-Structure-Property Relationship in Fused Filament Fabrication of Nylon-12



Benjamin de Jager

Trinity College

University of Oxford

A thesis submitted for the degree of

Doctor of Philosophy

Michaelmas Term 2021

Acknowledgements

My first and foremost thanks must of course go to my supervisor Professor Alexander Korsunsky. AMK first exposed me to serious experimental science nearly a decade ago, when I had the chance to see the team hard at work on the B16 beamline at DLS. If you had told me at the time that 5 years later I would be experimenting there myself, with the same team on the same project, I might have called you insane...

AMK gave me the opportunity to experience academic research and a chance to apply what I had learnt from my undergraduate dissertation. Having worked on an SLM project for Moog and Renishaw, I came as a research assistant to the AMK group and realised that academic research was something I genuinely enjoyed. If not for that opportunity, and all the many many insights into my project he has given me, I would never have made it here. Thanks must also go to his wife Tanya, my piano teacher of years gone by, through whom I first met Alexander! I would also like to thank the other members of the AMK group for helping train me on equipment, carry me through beamtime sessions at DLS and look through my terrible MATLAB code. Particular thanks must go to Hongjia Zhang, Enrico Salvati, Leon Romano Brandt, Joris Everaerts and Tom Moxham who have kept me sane during this DPhil.

I am grateful to Dr Song Xu from SIMTech A*STAR in Singapore, and Professor Alexei Salimon and Eugene Statnik from Skoltech in Moscow for collaborating with me and providing samples. From the Department, Kalin Dragnevski and Marzena Tkaczyk from LIMA, Nick Hawkins from the Thermomechanical Lab and Peter Walters from the 3D Printing Laboratory have been instrumental in preparing, processing and analysing samples - if not for their assistance with training and operation of equipment I would never have made it this far. In particular, I would like to thank Igor Dolbnya from the B16 beamline at DLS for his help on beamtime sessions, endlessly putting up with my last-minute changes to experiments and defending me when I12's furnace got coated in Nylon-12. My gratitude also to Apium GmbH and in particular Elena Reznikova for providing me with the P220 FFF printer and giving me the training I needed for its operation, and to iMakr for fixing it when I inevitably broke it. From Trinity, I must also thank Professor Justin Wark, my undergraduate Physics tutor, who firstly gave me the help I needed to salvage my degree at the end of Part A - without which I would never have attempted a DPhil, and who has been an enormously sage source of advice over the last 8 years.

Special mentions must go firstly to (now-)Drs Alasdair Morrison, Jakub Kwiecinski and Daniel Alanine, my cycling friends who were DPhil students when I was an undergraduate fresher. They gave me guidance on whether to apply for a DPhil myself and dispensed much sage advice which I have largely failed to follow, with the exception of Jakub's mantra that "a thesis written in Word is a thesis that deserves to be thrown in the bin." Secondly to my teammates from OULRC, particularly those from Nephthys 2020 and the victorious 2021 Blue Boat. Rowing has provided an invaluable outlet during my DPhil and it was a pleasure to race for Oxford with them. And last but most importantly, to my girlfriend Chloe, who single-handedly kept me sane during lockdown, during the Boat Race run-up and during difficult moments in my thesis. Her love has kept me motivated and has given me the strength to persevere.

Finally, I would like to thank my family for their support, both emotional and financial, and for their ability to keep me both motivated and grounded in the real world. Without them none of this would have been possible and I cannot thank them enough for everything they have helped me with over my lifetime and the last 4 years.

Nisi Dominus

Except the Lord build the house : their labour is but lost that build it.

Except the Lord keep the city : the watchman waketh but in vain.

It is but lost labour that ye haste to rise up early, and so late take rest, and eat the bread of carefulness : for so he giveth his beloved sleep.

Lo, children and the fruit of the womb : are an heritage and gift that cometh of the Lord.

Like as the arrows in the hand of the giant : even so are the young children.

Happy is the man that hath his quiver full of them : they shall not be ashamed when they speak with their enemies in the gate.

- *Psalm 127*

Abstract

This thesis is devoted to the investigation of the structure-property-relationships in additive manufacturing (AM). General thermodynamic and kinetic aspects that are peculiar for this manufacturing mode are considered, and made specific and applied by selecting a particular flavour of AM (FFF) and material (Nylon-12).

Fused Filament Fabrication (FFF) is an extrusion-based additive manufacturing method for thermoplastic polymers. Nylon-12 is a semi-crystalline thermoplastic polymer that is one of the most commonly used materials in FFF. The FFF process results in a unique spatially dependent thermal history, which has a considerable effect on the resultant microstructure. Crystallisation within the polymer proceeds via temperature-dependent nucleation and growth. In turn, the crystal structure relates to and determines the mechanical properties in semi-crystalline polymers.

This relationship can be referred to as the *processing-structure-property* relationship. This thesis focuses on a specific area of this relationship in FFF Nylon-12. These focused areas are the effect of the thermal history on the development of crystal morphology in Nylon-12 and degree of crystallinity, and the subsequent effect of the degree of crystallinity on tensile properties.

Precise control has not yet been achieved over the properties of FFF samples, which has provided a considerable barrier to industry adoption. Additionally, there have been comparatively few studies on Nylon-12 in the context of FFF compared to other polymeric materials, despite its extensive use in FFF. The aim of this thesis, therefore, is to build a quantitative link between thermal history, degree of crystallinity and tensile properties in Nylon-12 which can be used to provide more precise control and the ability to tailor the properties of FFF samples.

In situ X-ray diffraction was performed on FFF Nylon-12 samples, revealing that the orientation resulting from extrusion leads to a particular temperature-dependent crystal structure. Slower cooling rates from the melt were shown to result in a higher degree of crystallinity and higher lamellar density. It was shown that the thermal conditions during FFF lead to formation of the γ-form crystal structure, but with crystal structure differing from cast, sintered or moulded Nylon-12. A model of structural evolution was proposed to explain these observations.

The thermal properties of Nylon-12 filament and FFF samples produced under different processing conditions were examined through Differential Scanning

Calorimetry (DSC). It was found that Nylon-12 crystallises optimally at temperatures above 150 °C. Slower cooling rates and higher annealing temperatures were shown to result in a higher degree of crystallinity and more perfectly formed crystal structure. The processing-structure relationship between processing conditions and the degree of crystallinity was analysed. A model of the crystallisation behaviour was constructed based on this data. An alternative fit to model crystallisation behaviour was proposed, which has the ability to make quantitative predictions about evolution of crystallinity and rate of crystallisation based on thermal history.

Tensile testing of FFF-produced Nylon-12 samples revealed the relationships between processing conditions and tensile properties, specifically Young's Modulus, ultimate tensile strength, yield point and elongation at break. These data sets were fitted with a quantitative relationship. Finally, governing equations for the processing-structure-property relationship for FFF Nylon-12 were proposed based on the collected body of data.

This thesis sheds light on the processing-structure-property relationship in FFF Nylon-12, providing a full link from processing conditions to the mechanical properties. Additionally, the analysis and modelling of crystallisation behaviour has allowed for the data to be well-fitted to a set of governing equations that allow the prediction of tensile behaviour across a wider set of processing conditions. The methodology proposed, developed and used in this thesis provides the basis for further investigation into other components of the processing-structure-property relationship in Nylon-12, or for building similar relationships for other semi-crystalline thermoplastic polymers. Moreover, the present framework can be extended to other AM modalities, e.g., laser-based fabrication. This new understanding can lead to tailoring of structural and mechanical properties via alteration of the thermal history, eliminating the need for trial and error in AM and improving its performance compared to other manufacturing methods.

Contents

List of Figures **xi**

List of Abbreviations and Symbols **xxi**

1 Introduction and State of the Art **1**

1.1 Introduction . . . 3
1.2 Basic concepts . . . 4
1.2.1 Brief introduction to polymers . . . 4
1.2.2 Types of polymers . . . 5
1.2.3 Basic polymer physics . . . 7
1.2.3.1 Single chain physics . . . 7
1.2.3.2 System of chains . . . 7
1.2.4 Semi-crystalline polymers . . . 7
1.2.4.1 Structure of semi-crystalline polymers . . . 9
1.2.5 Kinetics of polymer crystallisation . . . 12
1.2.5.1 Nucleation and growth . . . 12
1.2.5.2 Avrami theory . . . 13
1.2.5.3 Hoffman-Lauritzen theory . . . 17
1.2.5.4 Lamellar thickening . . . 19
1.2.6 Polymer fibres . . . 20
1.2.7 Mechanical properties of semi-crystalline polymers . . . 22
1.2.7.1 Deformation behaviour . . . 22
1.3 Fused Filament Fabrication . . . 26
1.3.1 Introduction . . . 26
1.3.1.1 Basic principles of FFF . . . 28
1.3.1.2 Sample design and slicing . . . 30
1.3.2 Processing-structure-property relationship . . . 31
1.3.2.1 Processing . . . 32
1.3.2.2 Structure . . . 33
1.3.2.3 Property . . . 34
1.4 State of the art . . . 35
1.4.1 Thermal history of FFF . . . 36

1.4.2 Relationship between processing conditions and structural properties . . . 38
1.4.2.1 Dependence of microstructure on processing conditions 38
1.4.2.2 Dependence of mesostructure on processing conditions 41
1.4.3 Relationship between structural properties and mechanical properties . . . 43
1.4.3.1 Dependence of mechanical properties on microstructure . . . 43
1.4.3.2 Dependence of mechanical properties on mesostructure 48
1.5 Objectives of the current study . . . 49
1.5.1 Scope . . . 50
1.5.2 Objectives . . . 51

2 Materials and experimental methods 53
2.1 Introduction . . . 54
2.2 Structural characterisation . . . 54
2.2.1 Differential scanning calorimetry (DSC) . . . 54
2.2.1.1 Basic theory . . . 54
2.2.1.2 Experimental procedure . . . 57
2.2.2 X-ray diffraction (XRD) . . . 58
2.2.2.1 Basic theory . . . 59
2.2.2.2 Experimental procedure . . . 61
2.3 Mechanical characterisation . . . 64
2.3.1 Tensile testing . . . 64
2.4 Modelling . . . 64
2.4.1 Modelling of an individual filament . . . 64
2.4.2 Modelling of a series of contacted filaments . . . 66
2.5 Nylon-12 . . . 71
2.5.1 Introduction . . . 71
2.5.2 Structural properties . . . 72
2.5.2.1 WAXS studies on Nylon-12 . . . 75
2.5.2.2 Spherulitic structure . . . 76
2.5.3 Thermal properties . . . 78
2.5.3.1 Melting behaviour . . . 78
2.5.3.2 Equilibrium melting behaviour and heat of fusion . 80
2.5.3.3 Crystallisation behaviour . . . 80
2.6 Sample preparation . . . 82
2.6.1 3D printers used . . . 82
2.6.2 Print and sample parameters . . . 83

3 *In situ* Wide-Angle X-ray Scattering of Nylon-12 87
3.1 Introduction . . . 88
3.2 Results and discussion . . . 88
3.2.1 Nylon-12 samples produced under different printing conditions 89
3.2.2 *In situ* non-isothermal crystallisation of Nylon-12 filament . 96
3.2.3 *In situ* mechanical testing of Nylon-12 samples produced by FFF . . . 103

4 Thermal Analysis of Nylon-12 111
4.1 Introduction . . . 112
4.2 Results and discussion . . . 112
4.2.1 Isothermal crystallisation of Nylon-12 . . . 112
4.2.1.1 High temperature crystallisation . . . 113
4.2.1.2 Low temperature crystallisation . . . 118
4.2.2 Non-isothermal crystallisation of Nylon-12 . . . 124
4.2.3 DSC of FFF Nylon-12 samples with varying thermal history 128
4.2.3.1 Printed samples vs Nylon-12 filament . . . 129
4.2.3.2 Printed Nylon-12 samples with incrementally varying thermal history . . . 129
4.3 Analysis . . . 134
4.3.1 Isothermal crystallisation . . . 134
4.3.2 Non-isothermal crystallisation . . . 139
4.4 Conclusions . . . 141

5 Thermal and Crystallisation Modelling of FFF Nylon-12 145
5.1 Introduction . . . 146
5.2 Results and discussion . . . 147
5.2.1 Isothermal crystallisation model . . . 147
5.2.1.1 Methodology . . . 147
5.2.1.2 Results and analysis . . . 148
5.2.2 Non-isothermal crystallisation model . . . 150
5.2.2.1 Methodology . . . 150
5.2.2.2 Results and analysis . . . 151
5.2.3 Refinement of experimental data fitting . . . 153
5.2.3.1 Methodology . . . 153
5.2.3.2 Results and analysis . . . 156
5.2.3.3 Extension to the isothermal case . . . 159
5.2.4 Thermal modelling of Nylon-12 in FFF . . . 161
5.2.4.1 Modelling of an individual filament . . . 162
5.2.4.2 Modelling of a system of contacted filaments . . . 163

5.2.4.3 Modelling of the development of crystallinity . . . 165
5.2.5 Temperature-rate-crystallinity relation . . . 168
5.3 Conclusions . . . 174

6 Mechanical testing of FFF Nylon-12 samples 177
6.1 Introduction . . . 178
6.1.1 Samples tested . . . 179
6.2 Results and discussion . . . 179
6.3 Analysis . . . 182
6.3.1 Young's Modulus . . . 182
6.3.2 Ultimate tensile strength . . . 184
6.3.3 Yield point . . . 186
6.3.4 Elongation at break . . . 187
6.4 Conclusions . . . 188

7 Processing-Structure-Property Relationship 191
7.1 Processing-structure relationship . . . 192
7.2 Structure-property relationship . . . 197
7.3 Processing-structure-property relationship in FFF Nylon-12 . . . 198
7.3.1 Governing equations . . . 200
7.3.2 Conclusions . . . 201

8 Conclusions and future work 203
8.1 Conclusions . . . 204
8.1.1 Thermal properties of Nylon-12 . . . 204
8.1.2 On the viability of isothermal and non-isothermal crystallisation models for FFF . . . 206
8.1.3 Impact on the structure of Nylon-12 . . . 207
8.2 Outlook . . . 209

References 213

List of Figures

1.1 Chain configuration for amorphous and semi-crystalline polymers as a function of temperatures T_m and T_g. As the temperature falls, the chains move less before being frozen in place below T_g. 6

1.2 The reptation model for a random-coil chain in an entangled melt shows the chain relaxing from its original configuration or tube at times $0 < t_1 < t_2 \leq T_r$ where T_r is the relaxation time. The dotted tube represents the topological constraints to motion imposed by the neighbouring chains in the melt. [3] 8

1.3 Length scales of crystalline structures in a semi-crystalline polymer. 10

1.4 Polarised optical microscopy (POM) micrograph of the typical spherulitic structure of melt-crystallised PLA. The maltese cross structure is clearly visible. [9] 11

1.5 An illustration of the (a) nucleation and (b) growth process, showing the initial alignment of parallel polymer chains to form a nucleus followed by the folding of chains onto the crystal substrate surface to grow the crystal in the direction of thermal gradient. 13

1.6 An illustration of the radial growth rate maximum, driven by the degree of undercooling ΔT and retarded by the viscosity. 14

1.7 Melting temperature versus crystallisation temperature for laser-sintered Nylon-12, denoted here as PA12. PA2200 is the commercial name for the EOS white PA12 powder used in the experiment. [16] The data is projected onto the line $T_m = T_c$, from the intersection of which the equilibrium melting temperature T_m^0 is derived. 18

1.8 Lauritzen-Hoffman plot of $\ln G + U^*/R(T - T_{\text{inf}})$ vs $1/(T_c \Delta T)$ for PVDF [19]. 20

1.9 An illustration of the lamellar thickening process. Under energetically favourable conditions, parallel chains will move within the lamella, increasing the distance between chain folds and increasing the thickness. Note that no additional chains are added to the lamella during this process. 21

1.10 The hierarchical structure of a Nylon-6 fibre, showing the locations of inter-lamellar and inter-fibrillar amorphous polymer. A Nylon-12 fibre would differ only in terms of its unit cell and chain backbone length. [22] 22
1.11 A schematic stress-strain curve for a polymer, showing the elastic and plastic sections of the curve, as well as the yield point. 23
1.12 Working schematic of a generic Fused Filament Fabrication (FFF) printer. [43] 29
1.13 Detailed illustration of the FFF process and its related physical phenomena [45] 31
1.14 Temperature profile for a mid-sample layer during FFF demonstrating three distinct thermal phases. [50] 37
1.15 Illustration of the bond formation process between adjacent filaments. After two beads get in contact (1), a neck grows (2) and finally molecular diffusion happens at the interface and the polymer chains randomize (3). [45] 41
1.16 X-ray diffraction (XRD) data for (a) SLS vs (b) FFF Nylon-12. The highly crystalline nature of SLS Nylon-12 is visible, with minimal amorphous halo. FFF Nylon-12 shows more visible reflections than SLS Nylon-12 (data from the present study). The white dots resembling Bragg peaks seen in (b) were found to be due to background data. 44
1.17 Effect of percentage crystallinity on elongation at break for SLS Nylon-12, with increasing degree of particle melt (DPM) going as decreasing percentage crystallinity. 'Double phase' refers to parts containing both melted and unmelted material, whereas 'single phase' refers to parts containing only melted material. Fill scan count refers to the density of scan vectors in each transverse cross-section. [94] . 46
1.18 Relationship between crystallinity and (a) tensile strength, (b) tensile modulus, (c) flexural strength and (d) flexural modulus of carbon-fibre reinforced PEEK samples after heat treatment. [98] 47
1.19 Illustrated flowchart of the position of the links to be studied within the processing-structure-property relationship. 51

2.1 DSC schematic view: heat flux design, from the TA Instruments compendium. 56
2.2 Schematic temperature programme used in isothermal crystallisation DSC measurements. T_c symbolises the isothermal crystallisation temperature. 58

2.3 Schematic temperature programme used in non-isothermal crystallisation DSC measurements. Φ symbolises the cooling rate. 59
2.4 Schematic of the X-ray diffraction process, demonstrating Bragg's Law. 60
2.5 WAXS pattern of fully molten Nylon-12. With all crystalline structures having melted, the polymer is fully amorphous and a broad halo is visible. 61
2.6 The Linkam TS1500 furnace used in the *in situ* thermal characterisation experiments. 62
2.7 The Deben Microtest MT1000 tensile compression and horizontal bending stage used in the mechanical characterisation experiments. 63
2.8 (a) shows the experimental setup for *in situ* crystallisation using the Linkam TS1500 furnace, while (b) shows the setup for *in situ* mechanical testing using the Deben MT1000 stage. 63
2.9 The sample geometry used in the COMSOL model for a single filament's cooling behaviour. 65
2.10 Schematic of the model's thermal contact points on the filament geometry. 67
2.11 The computational procedure for modelling the temperature of the system of contacted filaments. 68
2.12 A schematic of the sample geometry used in the model. 70
2.13 The simulated thermal history for a given cross-section in a contacted system of filaments, with $T_{\text{inf}} = 120$ °C. 70
2.14 The basic repeating unit of Nylon-12. From Essential Chemical Industry 72
2.15 Unit cell of $\gamma-$ form Nylon-12. (a) is the projection on the *ab* plane, (b) on the plane perpendicular to the $a-$axis and (c) on the *ac* plane. The apparently differing angles between bonds in the backbone chain between (a) and (b) is a result of these projections. [120] 73
2.16 Summary of transformation behaviours of Nylon-12 [119] 74
2.17 The standard $\gamma-$form WAXS pattern. The 200 reflection is visible, with a surrounding amorphous halo. The white dots resembling Bragg peaks are due to background data. 76
2.18 The non-standard $\gamma-$form WAXS pattern. In addition to the 200 reflection, an additional reflection attributable to the $001(+20\bar{1})$ plane is visible. 76
2.19 Optical microscopy images acquired during isothermal crystallisation at 175 °C of Nylon-12 (20× magnification). Panel (a), (b) and (c) show the growth in space and time of spherulites with one spherulite highlighted with a yellow circle; panel (d) is the last frame after 4h at 175 °C. [124] 77

2.20 Melting endotherms of Nylon-1212, recorded at a heating rate of 10 °C/min after isothermal crystallisation at the specified temperature [114] 79
2.21 Melting endotherms of SLS Nylon-12, showing the second lower-temperature endotherm. [94] 80
2.22 Heat flow vs time during isothermal crystallisation of PA12 at different temperatures by DSC. [16] 81
2.23 A sample correlation function extracted from a SAXS pattern, along with a brief explanation of how the morphological parameters are calculated. L_p refers to the lamellar long period and L_c to the crystalline thickness, while the interlamellar amorphous thickness is calculated as the difference between L_p and L_c. 82
2.24 (a) shows the RS Pro Ideawerk 3D printer. (b) shows the Apium P220 3D printer. 83
2.25 (a) shows the design of the dogbone samples used for tensile testing, created in accordance with ASTM D-638 Type IV. (b) shows the sample print orientation used to create these samples. 84
2.26 The zone heater in an Apium P220, showing the Apium Adaptive Heating System in effect. 85

3.1 2D WAXS patterns (a-c) and 1D line profiles (d) of the Nylon-12 samples analysed. (a) shows the filament pattern, with only the $001(+20\bar{1})$ peak visible. (b) shows the FFF RS Pro sample, consisting of a main peak with an outer shoulder; (c) shows the Apium sample with two clearly resolved peaks visible. (d) shows the 1D line profiles of these patterns overlaid. The shadowing in (b) is due to the Deben Microtest tensile stage, while the white dots resembling Bragg spots in (a) and (c) are due to background data from the Linkam furnace setup. 90
3.2 The fitting of the 1D WAXS pattens for (a) the filament, (b) the FFF RS sample and (c) the FFF Apium sample. The amorphous halo was fitted with a Voigt curve while the semi-crystalline components were fitted with Lorentzian curves. 91
3.3 An illustration of the crystal planes in the unit cell of Nylon-12 that cause the reflections seen on the WAXS data. This illustration is in the $a-c$ plane. The b-axis, in the direction of the long backbone chains, is illustrated by the circles, where crosses and dots represent chains aligned perpendicular to each other [113, 120]. Ishikawa [121] noted that the 001 and $20\bar{1}$ reflections overlap due to their close d-spacing; these are both illustrated. 93

3.4 In (a), (i) shows a schematic of the lamellar sheet that is formed in the Nylon-12 filament, consisting of aligned chains bonded in the *c*-axis by H-bonds. (ii) shows the disoriented lamellae and (iii) the resulting diffraction pattern with only the single ring observed due to bulk isotropic alignment in *c*. In (b), lamellar sheets form energetically favourable planes along the *a*-axis, leading to a more complete unit cell and causing the emergence of the 200 diffraction ring. (i) shows the unit cell in full lamellar form, (ii) the crystallites formed as a result and (iii) the resulting diffraction pattern. 94

3.5 Figures (a) - (d) show the 2D and 1D WAXS patterns for Samples I - IV respectively after cooling from melt. It can be observed that the outer ring on the slower cooled Sample IV, corresponding to the 200 reflection, is better defined than on the more rapidly cooled Sample I. 97

3.6 Figures (a) - (d) show the evolution of the 1D WAXS pattern during cooling for all four samples. Each line on the figure represents the 1D WAXS pattern at the temperature represented by the colour map on the right of each figure. It can be observed that the inner $001(+20\bar{1})$ peak is seen first; this slowly moves towards a higher d-spacing during cooling. The 200 peak is seen subsequently and moves towards a lower d-spacing during cooling. 99

3.7 Evolution of the principal peaks in FFF Apium Nylon-12. Note the coalescence of the double peak into a single peak as T increases. (a) shows the pattern at T = 25 °C; (b) shows the ongoing peak coalescence at T = 65 °C; (c) shows the final pattern at T = 124 °C prior to the transition to an amorphous pattern. 100

3.8 d-spacing for all four samples during cooling. In line with the results seen in Figure 3.6, the 200 peak only becomes clearly resolvable later in the cooling process. It is notable that the peak appears at a higher temperature as the cooling rate falls. 101

3.9 Degree of crystallinity versus cooling rate for Samples I-IV. The degree of crystallinity increases as the cooling rate slows. Notably, the rate of increase of crystallinity increases with decreasing cooling rate, consistent with data seen elsewhere in literature [130]. 102

3.10 WAXS patterns of (a) the “slow-cooled” and (b) the “air-cooled” samples at 0N. Minimal differences are noticeable between the two peaks, with only minor differences in degree of crystallinity. 104

3.11 WAXS patterns of (a) the “slow-cooled” and (b) the “air-cooled” samples at 0N. Minimal differences are noticeable between the two peaks, with only minor differences in degree of crystallinity. 105

3.12 (a) shows the 2D WAXS pattern for the "slow-cooled" sample, while (b) shows the 2D WAXS pattern for the "air-cooled" sample after completion of tensile testing. The 200 reflection is no longer visible in the meridional direction, and the more faint 040 reflection has appeared. 106
3.13 The evolution of the WAXS patterns in the meridional ((b), (d)) and equatorial directions ((a), (c)) for the "slow-cooled" and "air-cooled" samples. Each line on the figure corresponds to a 1D WAXS pattern at a different force, corresponding to the force shown on the colour map to the right of the figure. Clear differences can be seen; in particular the 200 peak is no longer visible in the meridional direction (direction of tensile test) as the force increases. 107
3.14 The d-spacing of the $001(+20\bar{1})$ peak in the meridional direction during tensile testing. While minimal change is initially seen during the elastic component, the d-spacing then increases during the plastic region of the tensile test. 108
3.15 The stress-lattice strain curves for the 'slow-cooled" and "air-cooled" samples. The elastic region at the start of the tensile test can be observed, following by a levelling out of stress as strain continues to increase. This is proposed to be due to the fact that more of the strain is applied to the entangled chains in the amorphous region of the polymer. 109
3.16 The alignment of the unit cell during tensile testing is shown. In the meridional direction, the unit cell rotates along the $b-$axis, leading to the presence of the 040 reflection. In the equatorial direction, there is continued alignment in a and c over the bulk filament, hence the presence of the 200 and $001(+20\bar{1})$ rings in this orientation. . . 109

4.1 DSC thermograms for samples reheated at 10 °C/min after 60 minutes isothermal crystallisation at different T_c. 113
4.2 Melting temperature T_m as a function of isothermal crystallisation temperature T_c, projected onto the line $T_m = T_c$ to derive equilibrium melting temperature T_m^0. 114
4.3 (a) shows the crystallisation rate for the isothermal crystallisation. (b) shows the development of relative crystallinity $X(t)$ as a function of time. 115
4.4 The raw isothermal crystallisation DSC trace for the rapid cooling and isothermal crystallisation phase at 170 °C. Note the peak caused by instrumental inertia which serves to obscure the early phase of crystallisation. 116

4.5 Isothermal crystallisation half-time $t_{1/2}$ as a function of isothermal crystallisation temperature T_c. 117
4.6 (a) shows the double logarithmic plot of $\ln(-\ln(1-X(t)))$ vs $\ln t$. (b) shows the plot with a linear fit to obtain n and K. 118
4.7 DSC thermograms for samples reheated at 10 °C/min after 60 minutes isothermal crystallisation at different T_c. 119
4.8 Peak positions and magnitude ratios for the isothermal crystallisation. (a) shows the evolution of temperature values at peak maximum, and (b) shows peak heights as a function of isothermal crystallisation temperature T_c. 119
4.9 Relative crystallinity X(t) as a function of time for the isothermally crystallised samples. 121
4.10 The double logarithmic plot of $\ln(-\ln(1-X(t)))$ versus $\ln(t)$ for the isothermal crystallisation experiments. 122
4.11 An illustration of how different isothermal crystallisation temperatures affect the type of crystal structure formed, and how this relates to the growth activation energy and constraints on nucleation rate. Although the nucleation and growth rates may be below their peak at 176 °C, the increased internal energy given by the higher T_c can more readily overcome the activation energy for growth (illustrated in the rightmost curve), resulting in more well-formed crystal structures. 122
4.12 Degree of crystallinity vs T_c, fitted with an exponential function. . . 123
4.13 (a) DSC thermograms for samples reheated at 10 °C/min after non-isothermal crystallisation at different cooling rates. (b) shows the DSC thermograms during crystallisation. 124
4.14 Peak positions and magnitude ratios for the non-isothermal crystallisation. (a) shows the evolution of temperature values at peak maximum, and (b) shows peak heights as a function of cooling rate. 126
4.15 Relative crystallinity X(t) as a function of (a) time and (b) temperaturefor the non-isothermally crystallised samples. 126
4.16 The double logarithmic plot of $\ln(-\ln(1-X(t)))$ versus $\ln(t)$ for the non-isothermal crystallisation experiments. 127
4.17 An illustration of how different cooling rates affect the type of crystal structure formed, and how this manifests itself on the DSC and WAXS data. The parallel chain structures represent single layers of lamellae, which stack together at slower cooling rate. 128
4.18 DSC thermograms for the first heating cycle of all three samples. Note the presence of the shoulder at 184 °C corresponding to the presence of the 200 reflection. 130

4.19 DSC thermograms for the heating of all FFF samples printed at varying thermal history. The peaks and shoulder are identified. . . . 131
4.20 Overlay of the Apium FFF single peak from Figure 4.18 on a DSC trace from the FFF sample prepared at 170 °C. 132
4.21 Degree of crystallinity for all FFF samples, plotted against their preparation temperature. 133
4.22 The position of Peak I and Peak II in °C plotted against T_c 134
4.23 Plot of $\ln(1/t_{1/2}) + U^*/R(T - T_\infty)$ vs $(T + T_0)/(2T^2\Delta T)$. K_0 and K_g are calculated from the intercept and slope respectively. 135
4.24 Plot of $1/n \ln K$ vs $1/T_c$, determining the activation energy of isothermal crystallisation for Nylon-12. 136
4.25 Plot of $\ln t_{max}$ vs $1/(T_c^2\Delta T)$, verifying that the crystallisation behaviour of Nylon-12 in filament form fits the Avrami theory. 137
4.26 Time-temperature transformation (TTT) diagram for Nylon-12 filament. 139
4.27 Plot of $\ln(\Phi/T^{*2})$ vs $1/T^*$, determining the nucleation activation energy of non-isothermal crystallisation for Nylon-12. 140
4.28 The plots of $\ln \Phi$ vs $\ln t.$ from the combined Avrami and Ozawa equation for Nylon-12. 141
4.29 Continuous cooling transformation (CCT) diagram for Nylon-12 filament. 142

5.1 An overlay of the modelled data and the experimental data, showing the deviations between model and data. 148
5.2 The relative deviation in percent between the modelled and experimental data. 149
5.3 (a) shows the modelled crystal growth rate curves, and (b) shows the experimental crystal growth rate data for the non-isothermal crystallisation. 151
5.4 An overlay of the modelled data and the experimental data, showing the deviations between model and data. 152
5.5 The relative deviation in percent between the modelled and experimental data. 153
5.6 (a) shows an Avrami curve superposed on an arctan curve, while (b) shows an the same for a crystallisation rate curve and an arctangent derivative curve. The qualitative similarities are notable. 154
5.7 The non-isothermal data overlaid with arctangent fits. It is notable that the quality of fit is considerably better than with the Nakamura-Avrami model. 155

5.8 The relative deviation in percent between the modelled and experimental data. 156
5.9 Fitting of the data of $A(\Phi)$ vs Φ for the arctangent function 157
5.10 The non-isothermal data crystal growth rate data overlaid with arctangent fits. It is notable that the quality of fit is considerably better than with the Nakamura-Avrami model. 158
5.11 The isothermal data overlaid with arctangent fits. While the fit is imperfect, it represents a closer fit to the data than the Nakamura-Avrami fit did to the non-isothermal data. 159
5.12 The isothermal data crystal growth rate data overlaid with arctangent fits. The quality of fit for the lower isothermal temperatures, but deviates at higher isothermal temperatures. 160
5.13 The modelled cooling rate of a single filament in a simulated printing environment. 162
5.14 The simulated thermal history for a given cross-section in a contacted system of filaments, with T_{inf} ranging from 120 °C to 150 °C. 164
5.15 The simulated crystal growth rate as a function of temperature. . . 165
5.16 The simulated latent heat of crystallisation. 165
5.17 (a) shows the obtained data for $\ln G$. (b) shows data from the study of Plummer *et al* [125] on Nylon-12, as a qualitative comparison of curve shape. 166
5.18 The simulated isothermal crystallisation rate parameter K as a function of temperature. 166
5.19 The simulated nucleation density as a function of temperature. . . . 167
5.20 The simulated radius of a single crystal as a function of time derived from the contacted filament model. 168
5.21 The $T - Z(T) - X(T)$ plot for the experimental non-isothermal crystallisation data from Section 4.2.2. 169
5.22 The $T - Z(T) - X(T)$ plot for the arctangent function, plotted for 0.5°C/min$< \Phi <$ 100°C/min to form a discrete three-dimensional surface. 170
5.23 A phase contour line for the $T - Z(T) - X(T)$ arctangent plot, projected onto the $x - y$ and $x - z$ axes to show the degree of crystallinity and crystal growth rate. 171
5.24 (a) shows the temperature profile of the simulated non-constant cooling rate function, while (b) shows the associated cooling rate. . 171
5.25 The $T - Z(T) - X(T)$ plot of the simulated non-constant cooling rate crystallisation. 173

5.26 The $T-Z(T)-X(T)$ plot of the simulated non-constant cooling rate crystallisation, superimposed onto the $T-Z(T)-X(T)$ arctangent three-dimensional surface. 173

6.1 A sample stress-strain curve with annotations indicating the relevant metrics for mechanical analysis. 179
6.2 The stress-strain curves for the tested FFF samples. 181
6.3 A comparison of obtained values for (a) Young's Modulus and (b) UTS with data from the literature for Nylon-12. 182
6.4 The Young's Modulus E plotted against sample preparation temperature. 183
6.5 The ultimate tensile strength plotted against sample preparation temperature. 184
6.6 The yield point plotted against sample preparation temperature. . . 186
6.7 Young's Modulus, UTS and yield point plotted against crystallinity. 188

7.1 A summary of the findings relating to the processing-structure relationship. 193
7.2 A summary of the findings relating to the structure-property relationship. 197
7.3 Three graphs indicating the three components of the processing-structure-property relationship for fused filament fabrication of Nylon-12. 199
7.4 An extrapolation of the curve fit from the DSC data, allowing for predictions of degree of crystallinity across a broader range of FFF processing temperatures. 202

List of Abbreviations and Symbols

1D, 2D, 3D . . One-, two- or three-dimensional

A . . . . . Area

Å . . . . . Angstrom, unit of distance

ASTM . . . . . American Society for Testing and Materials

BJ . . . . . Binder Jetting

CAD . . . . . Computer Aided Design

CCT . . . . . Continuous cooling transformation

COMSOL . . . A physics-based simulation software package

C_p . . . . . Specific heat capacity, equal to 1700 kJ/kg·K

DED . . . . . Directed Energy Deposition

° . . . . . Degree, unit of angle

°C . . . . . Degree celsius, unit of temperature

ΔT . . . . . Refers to a temperature difference

DSC . . . . . Differential scanning calorimetry

e . . . . . Approximately equal to 2.718

E . . . . . Young's modulus, equal to stress divided by strain

ϵ . . . . . Strain, the ratio of extension to original length

FDM . . . . . Fused Deposition Modelling

FFF . . . . . Fused Filament Fabrication

G, G_0 . . . . . Crystal growth rate, pre-exponential growth rate constant

H . . . . . Hydrogen

h . . . . . Convective heat transfer coefficient

J . . . . . Joule, unit of energy

K . . . . . Kelvin, unit of temperature

K . . . . . Isothermal crystallisation rate constant

k . . . . . Thermal contact conductance

K_0 . . . . . Growth rate constant

kg . . . . . Kilogram, unit of mass

K_g . . . . . Nucleation rate constant

L . . . . . Latent heat of crystallisation, equal to 7000 J/kg for Nylon-12

LaB6 . . . . . Lanthanum hexaboride

l_c . . . . . Lamellar thickness

m . . . . . Metre, unit of distance

MATLAB . . . MATrix LABoratory, a numeric computing programming language

ME . . . . . Material Extrusion

min . . . . . Minute, unit of time

MJ . . . . . Material Jetting

mol . . . . . Mole, equal to 6.02×10^{23} molecules of a substance

MPa, GPa . . Mega- and gigapascal, unit of stress equal to N/m^2

N . . . . . Nitrogen

N . . . . . Newton, unit of force

N, N_0 . . . . . Nucleation rate, pre-exponential nucleation constant

n . . . . . Avrami parameter

O . . . . . Oxygen

P220 . . . . . The Apium P220 FFF 3D printer

PBF . . . . . Powder Bed Fusion

PCL . . . . . Polycaprolactone

PEEK . . . . . Polyether ether ketone

% . . . . . Percentage, measure of ratio

Φ . . . . . Cooling rate, measured in K/min

PLA . . . . . Polylactic acid

POM . . . . . Polarised optical microscopy

R . . . . . Universal gas constant = 8.314 J/mol

ρ . . . . . Density, equal to 1150 J/kg for Nylon-12

s . . . . . Second, unit of time

SAXS . . . . . Small-angle X-ray scattering

σ . . . . . Stress, equal to force over cross-sectional area

SL . . . . . Sheet Lamination

SLM . . . . . Selective Laser Melting

SLS . . . . . Selective Laser Sintering

STL . . . . . Stereolithography

T . . . . . Temperature

T^* . . . . . Temperature of peak crystallisation

τ . . . . . Instantaneous time

T_c . . . . . Crystallisation temperature

T_g . . . . . Glass transition temperature, below which no chain reptation can take place

T_∞ . . . . . Environment temperature, often refers to print chamber temperature

T_m^0 . . . . . Equlibrium melting temperature, melting point of an infinite stack of crystals. Equal to 203.7°C for Nylon-12

T_m . . . . . Melting temperature

TTT . . . . . Time temperature transformation

U^* . . . . . Diffusion activation energy = 6270 J/mol

UTS . . . . . Ultimate tensile strength

VP . . . . . Vat Photopolymerisation

W . . . . . Watt, unit of power equal to J/s

WAXS . . . . . Wide-angle X-ray scattering

X, X_c . . . . . Degree of crystallinity

XRD . . . . . X-ray diffraction

Z, Z_c . . . . . Rate of crystal growth for non-isothermal crystallisation

1

Introduction and State of the Art

Contents

1.1 Introduction 3
1.2 Basic concepts 4
1.2.1 Brief introduction to polymers 4
1.2.2 Types of polymers 5
1.2.3 Basic polymer physics 7
1.2.3.1 Single chain physics 7
1.2.3.2 System of chains 7
1.2.4 Semi-crystalline polymers 7
1.2.4.1 Structure of semi-crystalline polymers 9
1.2.5 Kinetics of polymer crystallisation 12
1.2.5.1 Nucleation and growth 12
1.2.5.2 Avrami theory 13
1.2.5.3 Hoffman-Lauritzen theory 17
1.2.5.4 Lamellar thickening 19
1.2.6 Polymer fibres 20
1.2.7 Mechanical properties of semi-crystalline polymers . . . 22
1.2.7.1 Deformation behaviour 22
1.3 Fused Filament Fabrication 26
1.3.1 Introduction 26
1.3.1.1 Basic principles of FFF 28
1.3.1.2 Sample design and slicing 30
1.3.2 Processing-structure-property relationship 31
1.3.2.1 Processing 32
1.3.2.2 Structure 33
1.3.2.3 Property 34
1.4 State of the art 35
1.4.1 Thermal history of FFF 36

1.4.2 Relationship between processing conditions and structural properties 38
1.4.2.1 Dependence of microstructure on processing conditions 38
1.4.2.2 Dependence of mesostructure on processing conditions 41
1.4.3 Relationship between structural properties and mechanical properties 43
1.4.3.1 Dependence of mechanical properties on microstructure 43
1.4.3.2 Dependence of mechanical properties on mesostructure 48
1.5 Objectives of the current study 49
1.5.1 Scope 50
1.5.2 Objectives 51

1.1 Introduction

Fused Filament Fabrication (FFF) is an extrusion-based additive manufacturing system for thermoplastic polymers. It constructs a sample from a 3D file by depositing successive layers of molten polymer filament which has been extruded through a nozzle. FFF's layer-wise manufacturing stands in contrast to conventional "subtractive" manufacturing methods such as casting or injection moulding and allows for bespoke and unique geometries to be produced rapidly.

FFF has been in use since 1988, and significant strides continue to be made in the field. However, the most prevalent use of the technology continues to be in rapid prototyping rather than full-scale manufacturing. At the core of this is the variability of the final product in FFF, which is further impacted by the large proliferation of competing standards in the field. Precise control of the properties of FFF samples has still not yet been fully attained. The strength of FFF as a manufacturing process is its ability to produce bespoke geometries without the need for special tooling, but the mechanical properties of these samples need to be controlled at least as well as their geometry for FFF to compete as a viable large-scale manufacturing process. Currently, the mechanical properties of FFF samples remain an uncertainty, with processing conditions being adjusted a *posteriori* to iron out poor performance and inhomogeneity via trial and error.

A greater understanding of the process-structure-property in FFF would therefore allow for a precise *a priori* link between a set of processing parameters and a set of mechanical properties which could be readily replicated across different FFF machines. This link can be referred to as the *processing-structure-property* link, which relates:

1. the processing conditions during sample production *(processing)*
2. the crystal structure or more general structure of the sample that results from these conditions *(structure)*
3. the bulk mechanical properties of the sample *(property)*.

Investigation into the processing-structure-property relationship therefore requires detailed study into firstly the relationship between processing conditions and the structure of the thermoplastic polymers used in FFF, and secondly how the sample's structure affects its mechanical performance. However, the large number of physical processes and processing parameters involved in FFF mean that full establishment of the processing-structure-property link requires a study of vast scope, and this thesis is only able to focus on a small number of these parameters.

In particular, this thesis focuses on developing the processing-structure-property relationship in the context of how the processing parameters affect the crystal structure of the polymeric materials used in FFF, and how that crystal structure in turn affects the tensile properties of the final product. This study is carried out using the conduit of Nylon-12, a semi-crystalline thermoplastic which is one of the most commonly used materials in FFF due to its ubiquity, ease of processability and resistance to wear.

In the proceeding sections, therefore, the basic concepts that underpin this thesis and the current state of the art of FFF are presented so that both the processing-structure-property relationship and this thesis' approach to understanding it are laid out.

1.2 Basic concepts

In this section, basic notions on polymers will be presented. The principal focus will be on the notions required for the characterisation of the materials used in this study and for the interpretation of results.

1.2.1 Brief introduction to polymers

A *macromolecular* substance is composed of molecules that have long sequences (chains) of one or more species of atoms or groups of atoms linked by covalent bonds. Polymer macromolecules are formed from the linking together of *monomers* through polymerisation, whereby linear or branched chains, or three-dimensional networks are formed. For example, polymerisation of ethylene yields polyethylene,

a typical sample of which may contain molecules with 50,000 carbon atoms in a linked chain [1]. Macromolecules are characterised by molar mass M related to the degree of polymerisation x, where x is the number of repeat units in the macromolecule and M_0 is the molar mass of the monomer [2]:

$$M = xM_0 \tag{1.1}$$

When the number of repeat units exceeds (typically) 100, the term *polymer* is applied. It is this long-chain nature which sets polymers apart from other materials and gives rise to their characteristic properties. If only one type of monomer is used the resulting polymer is called a *homopolymer* whereas if more than one type of monomer is used the polymer is termed a *copolymer*.

1.2.2 Types of polymers

Polymers are most commonly divided into three separate groups for classification: these are *thermoplastics*, *elastomers* and *thermosets*. This method of classification is based on the underlying molecular structure of the polymers. Thermoplastics melt on the application of heat; elastomers are cross-linked rubbery polymers that can be stretched to high extensions and rapidly recover their original dimensions; and thermosets which are rigid materials in which chain motion is limited by a high density of crosslinks. Unlike thermoplastics, thermosets and elastomers do not soften on the application of heat but degrade.

Thermoplastics, which make up the vast majority of polymers in commercial production, can be moulded into virtually any shape. Thermoplastics tend to consist of long linear or branched chains; due to this, they do not crystallise easily on cooling as the entangled chains of macromolecules resist complete ordering. They can therefore be subdivided further into *semi-crystalline*, which in their solid state contain both crystalline and amorphous regions, and *amorphous*, which do not form any crystalline regions on cooling.

Thermoplastics can be thus characterised by two principal temperatures. The first is the melting temperature T_m, above which crystalline regions become

disordered and amorphous, allowing for processing and moulding. The second is the glass transition temperature T_g, which is the temperature below which motion of macromolecule chains ceases, causing a transition from the soft *rubbery state* to the hard *glassy state*. Below T_g, the polymer behaves as a solid, with the chains held firmly in place by van der Waals forces. Amorphous polymers are characterised only by T_g while semi-crystalline polymers are characterised by T_g and T_m. The relationship between temperature and chain configuration for amorphous and semi-crystalline polymers is illustrated in Figure 1.1.

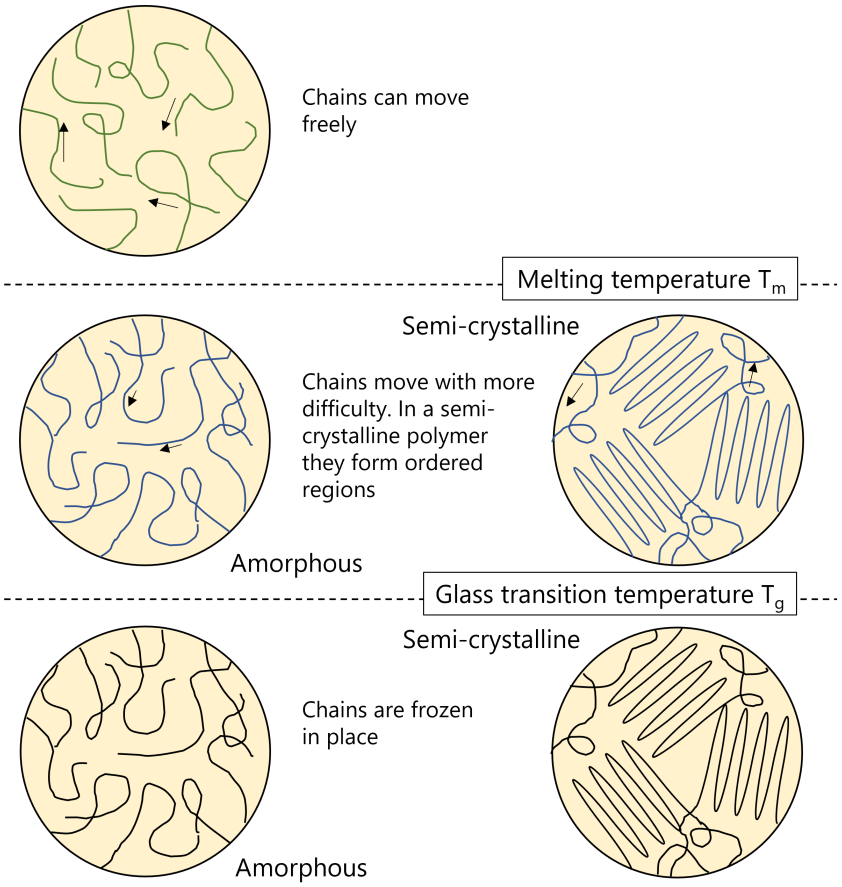


Figure 1.1: Chain configuration for amorphous and semi-crystalline polymers as a function of temperatures T_m and T_g. As the temperature falls, the chains move less before being frozen in place below T_g.

1.2.3 Basic polymer physics

1.2.3.1 Single chain physics

It is useful to consider the base unit of a polymer, the macromolecule chain, in order to understand its basic physical properties. A single polymer chain can be characterised by its *persistence length* P, quantifying its bending stiffness. Informally speaking, for length scales below the persistence length the polymer chain can be considered to behave like a rigid rod, whereas for much larger (orders of magnitude) length scales, the chain behaves in a manner that is best described statistically. Within a length scale that is smaller than the chain length but larger than the persistence length, a polymer chain is described as a segment chain with an infinite number of segments, which moves as a random walk on a periodic lattice.

1.2.3.2 System of chains

In the amorphous regions of a polymer, a dense system of chains persist. When a polymer is heated above T_g, the dynamics of the chains has been well described by the reptation model [3]. The chains can move by Brownian motion, but cannot intersect each other. They can therefore move in between obstacles in a worm-like fashion, called *reptation*. Edwards [4] introduced the notion of a tube that contains the chain, which is represented in Figure 1.2. The mean squared displacement of a polymer chain due to reptation in a system of chains is given by:

$$s(t)^2 = 2k_B T \mu_{tube} t \tag{1.2}$$

where k_B is Boltzmann's constant, and μ_{tube} is the coefficient of friction in the tube.

1.2.4 Semi-crystalline polymers

Some thermoplastics have the ability to form ordered crystalline domains when the polymer is heated to the range of temperatures in which crystallisation can take place. The extent to which this occurs is dependent on the type of polymer and its molecular microstructure. Polymers with the ability to crystallise are

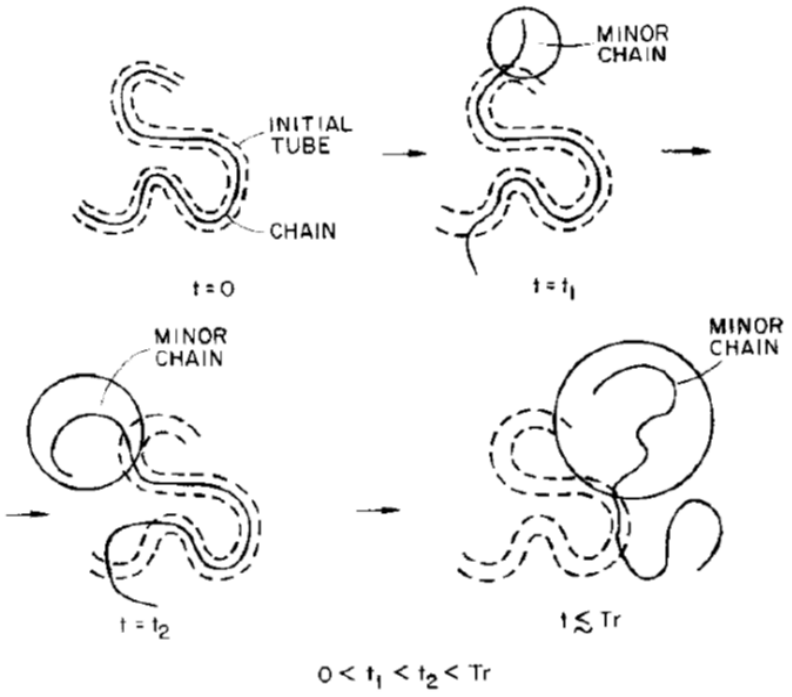


Figure 1.2: The reptation model for a random-coil chain in an entangled melt shows the chain relaxing from its original configuration or tube at times $0 < t_1 < t_2 \leq T_r$ where T_r is the relaxation time. The dotted tube represents the topological constraints to motion imposed by the neighbouring chains in the melt. [3]

distinguished from other crystalline solids by the fact that they are only semi-crystalline, having a density below that expected for a fully crystalline polymer. The chain entanglements in a polymer prevent full crystallisation; instead, a mix of ordered and disordered regions is obtained.

In polymers, a periodic crystal structure in three dimensions is obtained in the ideal case by choosing identical configurations for all polymers, orienting the helical axes of all chains parallel to each other and then packing the chains laterally in a regular manner [5]. For a polymer with uniform molar mass, this type of crystal with extended straight chains and end-groups assembled in planar interfaces would represent the equilibrium state with the lowest free energy. The crystallisation of polymers, therefore, is driven by thermodynamic considerations.

The Gibbs free energy G is related to the enthalpy H and the entropy S by

$$G = H - TS \tag{1.3}$$

The system is in equilibrium when G is minimised. A polymer melt consists of randomly coiled and entangled chains, which gives a much higher entropy than in the case of extended straight chains due to the increased number of conformations available. When the melt is cooled below T_m, there is corresponding enthalpy change ΔH_m, causing crystallisation and therefore a reduction in S (ΔS_m). If $\Delta H_m > T_m \Delta S_m$ then crystallisation is favoured thermodynamically [1]. Crystallisation also has a kinetic component; this is discussed in more detail in Section 1.2.5.

The crystallisation of polymers is of enormous importance, as the presence of crystals has a signficant effect on the polymer's thermal and mechanical properties. The crystalline regions can be thought of as reinforcing the polymer. As a consequence, most high-performance engineering polymers are semi-crystalline, as these offer certain advantages over amorphous polymers in terms of the ability to use the material at temperatures above T_g without significant loss in modulus [6], better resistance to creep deformation and excellent resistance to physical and chemical degradation. The relationship between polymer processing from the melt to crystallisation forms are the core focus of this study.

1.2.4.1 Structure of semi-crystalline polymers

The structure of any crystalline solid is specified by defining a regular pattern of repeating atomic arrangements in the structure, known as the *unit cell*. In the case of semi-crystalline polymers, the unit cells are made up of the repeating segments of the polymer chains packed together. There can be several segments in one unit cell. The atomic spatial arrangement is controlled by the covalent bonding within molecular segments, with inter-chain arrangement being held together due to weaker hydrogen bonds or van der Waals forces. This leads to high levels of directional anisotropy of physical properties. In polymers, the monomers are placed at the nodes of the unit cell, with the main axis of the chains typically lying along one side of the unit cell.

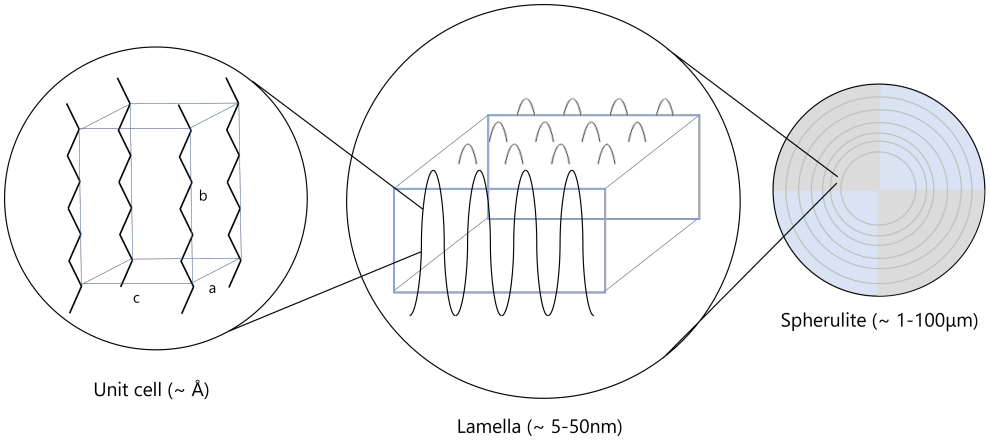


Figure 1.3: Length scales of crystalline structures in a semi-crystalline polymer.

Semi-crystalline polymers are comprised of crystalline domains separated by amorphous regions. The crystalline regions have different characteristic features depending on length scale. On the smallest length scale (c.Å) is the unit cell, the form of which is one of the seven basic crystal systems (monoclinic, hexagonal etc). The extended polymer chains that form the unit cell fold over to create a stacked lamellar structure (thickness length scale 5-50nm). The polymer chain is much longer than the lamellar thickness, and must fold over several times to enter and reenter the lamella. Multiple lamellae form a superstructure on the scale of 1-100μm, the nature of which is dependent on the thermal conditions experienced by the polymer on cooling. Sideways lamellar growth caused by temperature gradients causes the formation of planar *crystallites*, whereas growth in the absence of temperature gradients occurs radially in all directions, forming *spherulites*. The structures on these length scales are illustrated in Figure 1.3.

There are two principal models describing the way in which the chains form and interact with the lamellae. In the first of these, the *folded chain* model [7], the chain folds back and forth with hairpin turns, therefore entering and leaving the lamella in adjacent positions. The nature of the folds is unknown, and two models have been suggested whereby the folds are either regular and tight, or irregular and of variable length. In the second model, the *switchboard* model [8], chains enter and leave the lamellae, with re-entry being random like an old telephone

switchboard. Both models result in the same consequences for crystal density and lamellar thickness. The crystalline lamellae have a substructure which consists of blocks of aligned polymer chains, which fit together in a mosaic configuration.

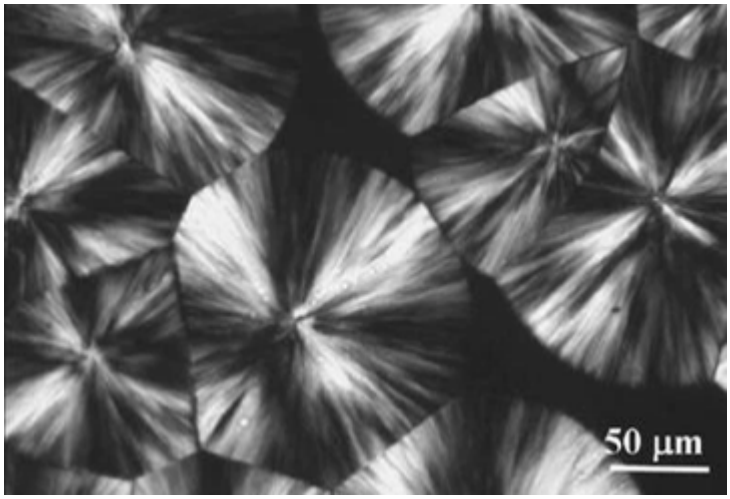


Figure 1.4: Polarised optical microscopy (POM) micrograph of the typical spherulitic structure of melt-crystallised PLA. The maltese cross structure is clearly visible. [9]

Chain folding to form lamellae, and subsequently larger crystal structures such as spherulites, is driven by the temperature gradients in the polymer during melt-crystallisation. Typical spherulites formed during the crystallisation of poly(L-lactic acid) (PLLA) are shown in Figure 1.4 [9]. Spherulites form by nucleation at different points in the sample and subsequently grow as spherical entities. Typically, spherulites grow at a constant rate until impingement of adjacent spherulites occurs. Examination of spherulites shows that the chain orientation is always perpendicular to the spherulite radius vector. This creates optical anisotropy when viewed under polarised optical microscopy (POM), as polarised light cannot travel through a crystalline polymer if the direction of the polarisation of the light is perpendicular to the direction of chain orientation. Only chains perpendicular to neither the microscope's polariser or the analyser are visible, which creates a pattern resembling a Maltese cross, as shown in Figure 1.4. In the case of directional temperature gradients, lamellar growth in the direction of the temperature gradients will be the principal mode of crystallisation. As growth in this case proceeds in fewer

dimensions than in the case of uniform temperature gradients, the crystallites formed may be smaller than spherulites.

1.2.5 Kinetics of polymer crystallisation

1.2.5.1 Nucleation and growth

As stated above, crystallisation is a process that proceeds by nucleation and growth, which can be separated into two distinct stages. During nucleation, the randomly entangled polymer chains become aligned. As the temperature falls below T_m, chains may either become aligned parallel to each other or fold randomly into a parallel arrangement and form small ordered regions called nuclei. When these small ordered nuclei have reached a critical size, growth can proceed. In the second stage, growth, these nuclei grow by the addition of further polymer chains, whereby additional chains from the melt or disordered lengths of existing chains in the nuclei will fold onto the energetically favourable surface of the crystal substrate. The nucleation and growth stages are illustrated in Figure 1.5. Nucleation tends to take place heterogeneously, dependent on the crystallisation temperature T_c and the presence of interfaces that may restrict degrees of freedom. Crystallisation can occur at a range of temperatures, which vary polymer to polymer, with the universal constraint $T_g < T_c < T_m$. Each discrete temperature T_c in the range of crystallisation temperatures will result in different nucleation and growth rates due to thermodynamic considerations. T_c in this thesis refers to the instantaneous temperature at which the polymer is being crystallised.

Both nucleation and radial growth rate are controlled by the competing thermodynamic forces driving crystallisation, which increase as the temperature is lowered, and viscosity η which acts against the transport of material to the growth point [2] and likewise increases faster with reducing temperature. Neither nucleation nor growth can take place above T_m or below T_g. Plots of nucleation and radial growth rate as a function of T_c will therefore display a maximum between T_m and T_g, illustrated for growth in Figure 1.6. The growth stage can take place in either one, two, or three dimensions.

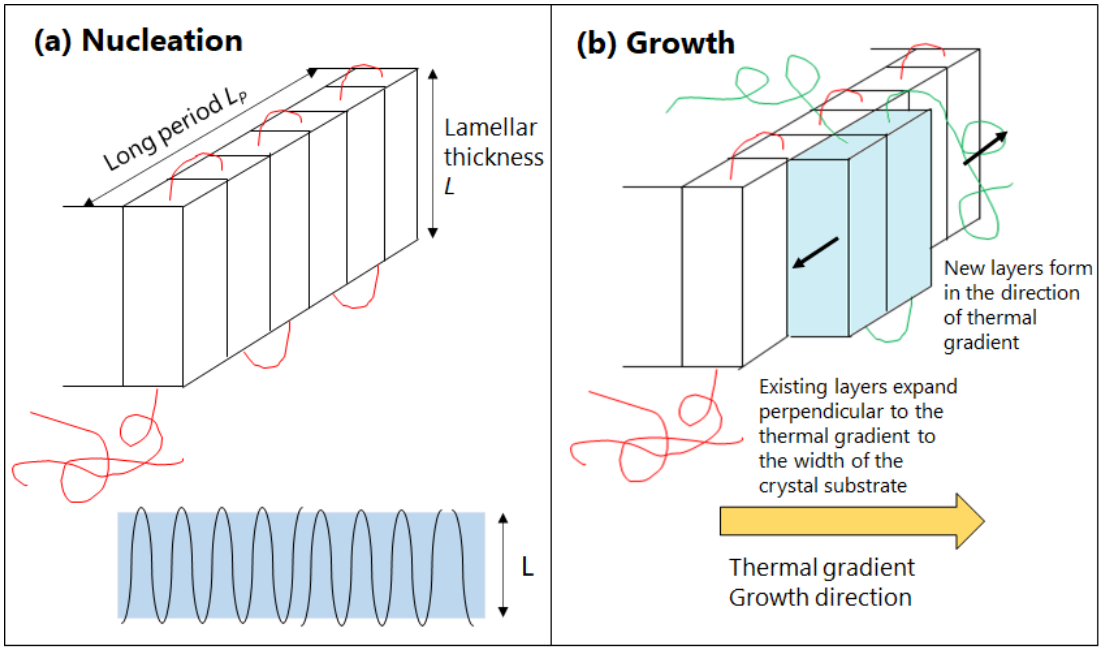


Figure 1.5: An illustration of the (a) nucleation and (b) growth process, showing the initial alignment of parallel polymer chains to form a nucleus followed by the folding of chains onto the crystal substrate surface to grow the crystal in the direction of thermal gradient.

1.2.5.2 Avrami theory

When a polymer melt of volume V is cooled below T_c, the number of nuclei N formed at a given temperature per unit time per unit volume can be considered to be constant. Therefore in an interval dt, $NVdt$ nuclei are formed. During the growth phase these nuclei grow into spheres with volume $\frac{4}{3}\pi r^3$. Since the growth rate is known to be constant in the unimpeded case, r can be written as Gt, with G the growth rate. Hence the total volume of spherulitic material present at time t is given by:

$$dV = \frac{4}{3}\pi G^3 t^3 NV dt \tag{1.4}$$

This term must be adjusted to account for the eventual impingement of spherulites during growth, as eventually some part V_c of V will be taken up by the already-crystallised material. Then, the actual crystalline volume that forms per unit time dV_c is proportional to the volume fraction of remaining uncrystallised material.

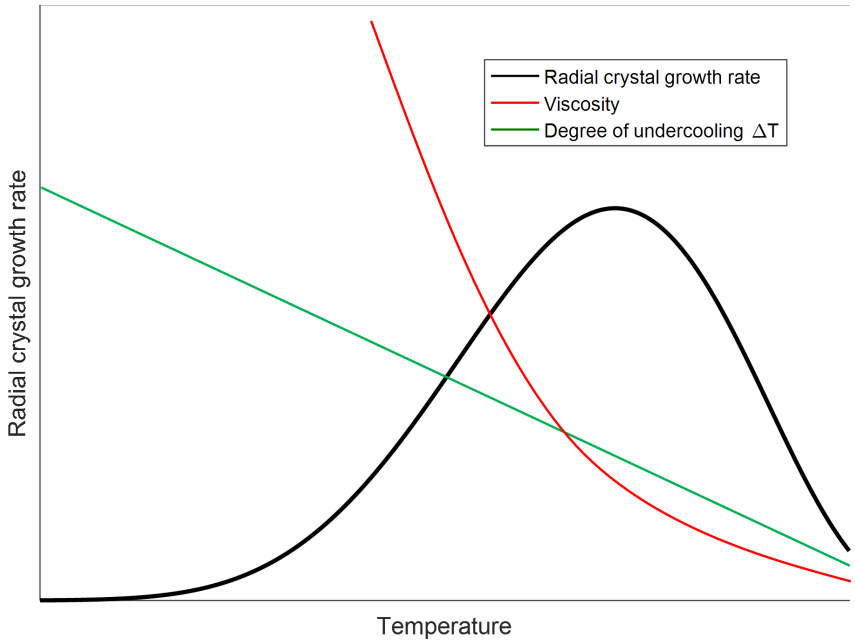


Figure 1.6: An illustration of the radial growth rate maximum, driven by the degree of undercooling ΔT and retarded by the viscosity.

The following relation is therefore obtained:

$$dV_c = dV\left(1 - \frac{V_c}{V}\right) \tag{1.5}$$

Then, the volume fraction of crystallised material $X(t)$ is given by $\frac{V_c}{V}$. This gives:

$$\frac{1}{1 - X(t)} dX(t) = \frac{dV}{V} = \frac{4}{3}\pi N G^3 t^3 \tag{1.6}$$

which integrates to:

$$X(t) = 1 - e^{-Kt^n} \tag{1.7}$$

where in this idealised case $n = 4$ and $K = \pi N G^3$. This is known as the Avrami equation [10], and n is known as the Avrami exponent, having a value between 1 and 4 depending on the number of dimensions in which spherulite growth is able to take place. As n derives from the integration of the volume fraction, $n - 1$ is therefore the number of dimensions in which crystallisation proceeds.

To determine the Avrami exponent n and the crystallisation rate parameter K, the Avrami equation is written in the form of the following relation in the case of constant crystallisation temperature (isothermal crystallisation):

$$\ln(-\ln(1 - X(t))) = \ln K + n \ln t \tag{1.8}$$

In the case of non-constant crystallisation temperature (non-isothermal crystallisation), a similar relation holds whereby

$$\ln(-\ln(1 - X(t))) = \ln Z_c + n \ln t \tag{1.9}$$

where Z_c is the non-isothermal crystallisation rate parameter.

Non-isothermal crystallisation was described by Ozawa [11], who modified the Avrami equation as follows:

$$X(t) = 1 - e^{-K(T)/\Phi^m} \tag{1.10}$$

where $K(T)$ is the Ozawa crystallisation rate constant, Φ is the cooling rate and m is the Ozawa parameter, analogous to the Avrami parameter. However, the maximum cooling rate utilised in the Ozawa study was 4K/min, which is considerably smaller than any cooling rate in the FFF process. Therefore, the more general modification to the Avrami equation developed by Nakamura [12] was used in this model. The exponent Kt^n can be written as:

$$e^{Kt^n} = e^{(tK^*)^n} \tag{1.11}$$

where $K^* = K^{1/n}$. But tK^*, for constant K^* and linearly increasing t, is given by the area under the K^* vs t curve.

For non-isothermal crystallisation, Nakamura's modification considers that the crystallisation rate parameter is constantly changing with temperature. For this non-constant rate parameter, the equivalent expression for tK^* is given by $\int_0^\tau K^* dt$. This therefore yields the following modification to the Avrami equation:

$$X(t) = 1 - e^{-\left(\int_0^\tau Z(T) dt\right)^n} \tag{1.12}$$

$Z(T)$ is a modification of the isothermal crystallisation rate parameter $K(T)$, which deviates from the isothermal parameter according to the following equation:

$$Z(T) = K(T)^{\frac{1}{n}} = (\ln 2)^{\frac{1}{n}} \frac{1}{t_{1/2}} \tag{1.13}$$

where n and $t_{1/2}$ are temperature dependent.

The temperature-dependence of $t_{1/2}$ is calculated from Hoffman-Lauritzen theory (1.2.5.3) using the equation proposed by Ziabicki [13], such that:

$$\frac{1}{t_{1/2}} = K_0 e^{-\frac{U^*}{R(T-T_\infty)}} e^{-\frac{K_g(T+T_m^0)}{2T^2\Delta T}} \tag{1.14}$$

where K_0 is the growth rate constant, $U^* = 6270$ J/mol is the activation energy for polymer diffusion, $R = 8.314$ J/mol·K is the universal gas constant, $T_\infty = T_g - 30$ K, K_g is the nucleation rate constant, $\Delta T = T_0^m - T$ and T_0^m is the equilibrium melting temperature.

An important parameter in crystallisation analysis is the half-time of crystallisation $t_{1/2}$, which is defined as the time taken from the onset of the crystallisation until 50% completion. Equation 1.7 shows that this can be extracted directly from the plot of $X(t)$ versus t, as follows:

$$t_{1/2} = (\ln 2/K)^{1/n} \tag{1.15}$$

The rate of crystallisation G can be described as the reciprocal of $t_{1/2}$, such that $G = (t_{1/2})^{-1}$.

The time for maximum crystallisation rate t_{max} is calculated from Equation 1.7 using the method proposed by Lin [14]. This time corresponds to the point of peak heat flow Q, such that $dQ/dt = 0$. t_{max} can therefore be calculated by taking the second derivative of $X(t)$, the extent of crystallisation at time t:

$$\frac{d^2X(t)}{dt^2} = (-nKt^{n-1})^2 e^{-Kt^n} + n(n-1)Kt^{n-2}e^{-Kt^n}$$

At the point t_{max},

$$\begin{aligned} \frac{d^2X(t)}{dt^2} &= 0 \\ nKt^n - (n-1) &= 0 \\ t_{max} &= \left(\frac{n-1}{nK}\right)^{1/n} \end{aligned} \tag{1.16}$$

1.2.5.3 Hoffman-Lauritzen theory

The Avrami equation provides a general guide for the bulk kinetics of the crystallisation process. However, an alternative approach is required to describe the kinetics of crystallisation at the molecular level. The most widely accepted approach is that of Hoffman *et al* [15]. Hoffman and Weeks introduce the concept of an *equilibrium melting temperature* T_m^0, which corresponds to the melting temperature of an infinitely large crystal. This is derived for a polymer by extrapolation of the plot of T_m against T_c, shown in Figure 1.7 [16] to the point where it meets the line $T_m = T_c$; this is the limit of melting behaviour, as the melting temperature can never be lower than the crystallisation temperature. At T_m^0, the change in free energy involved in laying down additional lamellae will be zero, thus

$$\Delta G = \Delta H - T_m^0 \Delta S \tag{1.17}$$

With a degree of undercooling from T_m^0 to temperature T, such that $\Delta T = T_m^0 - T$, it can be derived that

$$\Delta G = \frac{\Delta H \Delta T}{T_m^0} \tag{1.18}$$

Equation 1.13 gives us the overall change in free energy per unit volume due to the melting process. For a lamella of thickness b and surface energy σ_0, it was derived that

$$T_m = T_m^0 - \frac{2\sigma_0 T_m^0}{b\Delta H} \tag{1.19}$$

where ΔH is the enthalpy of fusion per unit crystal volume.

In the Hoffman and Lauritzen approach to modelling crystallisation [17], the polymer crystal is considered to grow on the surface of a pre-existing crystal, the kinetics of which are separated into two rates. In the initial step, the polymer grows onto the pre-existing crystal surface; in the second, the grown polymer from the initial step is itself the site of further nucleation.

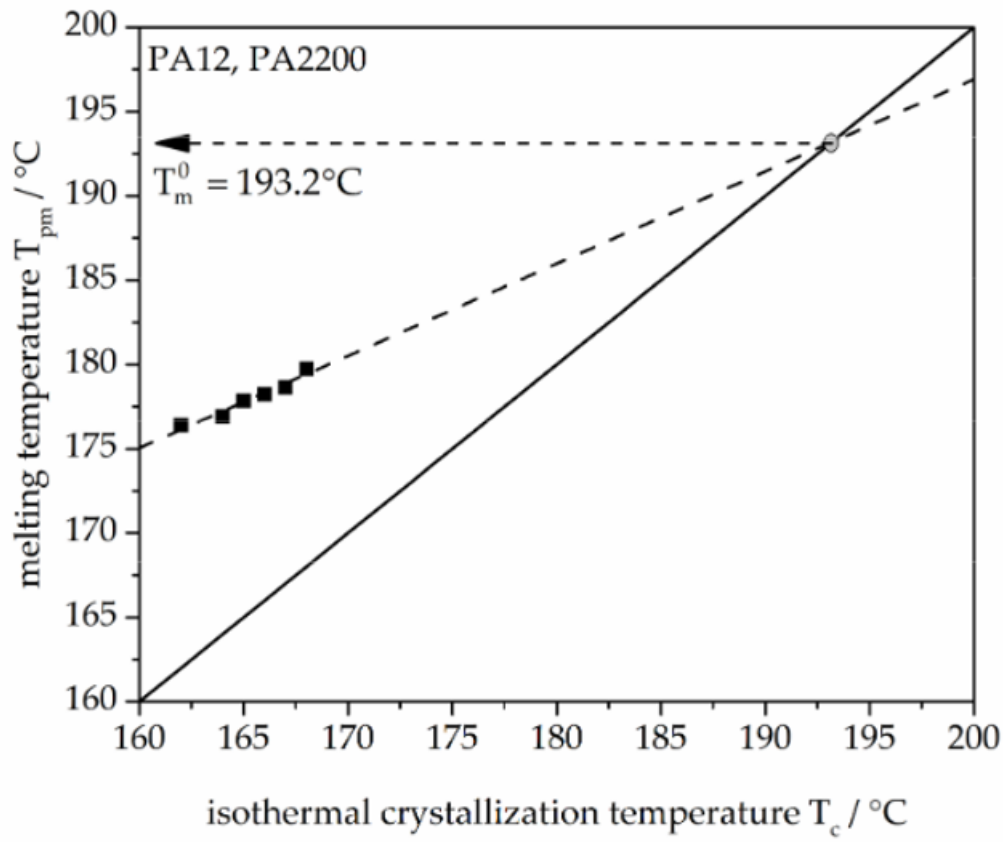


Figure 1.7: Melting temperature versus crystallisation temperature for laser-sintered Nylon-12, denoted here as PA12. PA2200 is the commercial name for the EOS white PA12 powder used in the experiment. [16] The data is projected onto the line $T_m = T_c$, from the intersection of which the equilibrium melting temperature T_m^0 is derived.

In the initial step, monolayers of new polymer chains are formed one at a time, such that for a substrate of length L_p, nucleation rate per unit length i and thickness b, the overall linear growth is given by Hoffman-Lauritzen theory, such that:

$$G_1 = biL_p \tag{1.20}$$

The nucleation rate in a specific area is then driven thermodynamically, such that

$$G_1 = e^{-K_g/T\Delta T} \tag{1.21}$$

where K_g is given by

$$K_g = nb_0\sigma_0\sigma_e T_0^m/\Delta h \tag{1.22}$$

where b_0 is the thickness of a monomolecular crystal layer, σ_0 and σ_e are the lateral and fold surface free energies respectively, k is the Boltzmann constant and

Δh is the bulk melting enthalpy per unit volume for a fully crystalline polymer. These monolayers consist of small areas where the polymer chain is folded to produce areas with parallel chains. σ_e denotes the free energy associated with the large lateral surface containing the chain folds while while σ_0 denotes the free energy associated with the surface containing the chain stems, which is the principal crystal growth front.

In the second step, where lateral growth is no longer consequential to the overall nucleation rate, which is instead driven by the nucleation rate per unit length i, the same equation applies as in the first step with additional thermodynamically driven pre-factors such that:

$$G = G_0 e^{-U^*/k(T-T_0)} e^{-K_g/T\Delta T} \tag{1.23}$$

where G_0 is a pre-exponential factor which can be experimentally determined through the Lauritzen-Hoffman plot [18], illustrated in Figure 1.8 [19], U^* is the transport activation energy usually equal to 6300 J/mol and $T_0 = T_g - 30$ is the temperature at which viscous flow is considered to have ceased. During the growth phase, rather than the lamella expanding laterally along the plane of chain folding, additional layers are deposited on the substrate formed by the initial monolayer. This layer growth takes place along the direction of the temperature gradient.

1.2.5.4 Lamellar thickening

For a given temperature of crystallisation T_c, the lamellar thickness l_c of a semi-crystalline polymer is given by:

$$l_c = \frac{2\sigma_e T_m^0}{\Delta H_m (T_m^0 - T_c}) + \delta l \tag{1.24}$$

Hoffman and Weeks [15] noted that the thickness of lamellae during nucleation increases from b_0 to thickness $b = b_0\beta$, with β given by:

$$T_m = \frac{T_c}{\beta} + \left(1 - \frac{1}{\beta}\right) T_m^0 \tag{1.25}$$

β is the thickening ratio, which is the ratio of the post-crystallisation thickness of the polymer crystal ($L*$) to its initial thickness (L) and is always greater than or

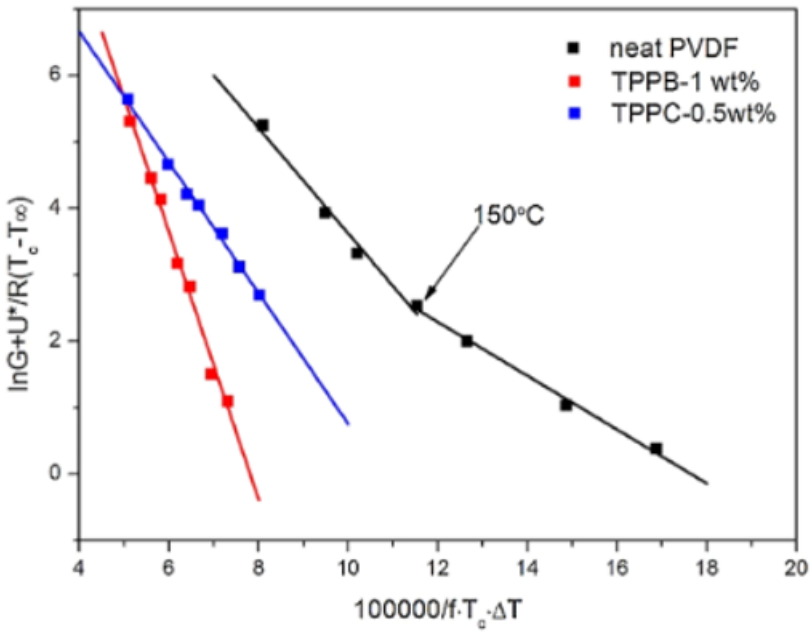


Figure 1.8: Lauritzen-Hoffman plot of $\ln G + U^*/R(T - T_{\text{inf}})$ vs $1/(T_c \Delta T)$ for PVDF [19].

equal to 1. The relationship between T_m and T_c observed by Hoffman and Weeks and illustrated in Figure 1.7 is related to β; it was observed that the melting point T_m of a polymer crystal that has thickened by a factor β is a linear function of T_c. Lamellar thickening is essentially a reorganisation process of chains within lamellae, whereby the length between chain folds increases along the chain axis direction, thus decreasing the surface area to volume ratio of the lamellae. This process is illustrated in Figure 1.9.

1.2.6 Polymer fibres

If polymer melts are crystallised under stress, morphologies are found that are distinct from those crystallised under ordinary conditions. This has important consequences as polymers are often found in fibre or extruded form, both of which involve the application of stress to the material during crystallisation. During the FFF process, the shear forces from extrusion through the nozzle result in morphologies that may resemble polymer fibre morphologies.

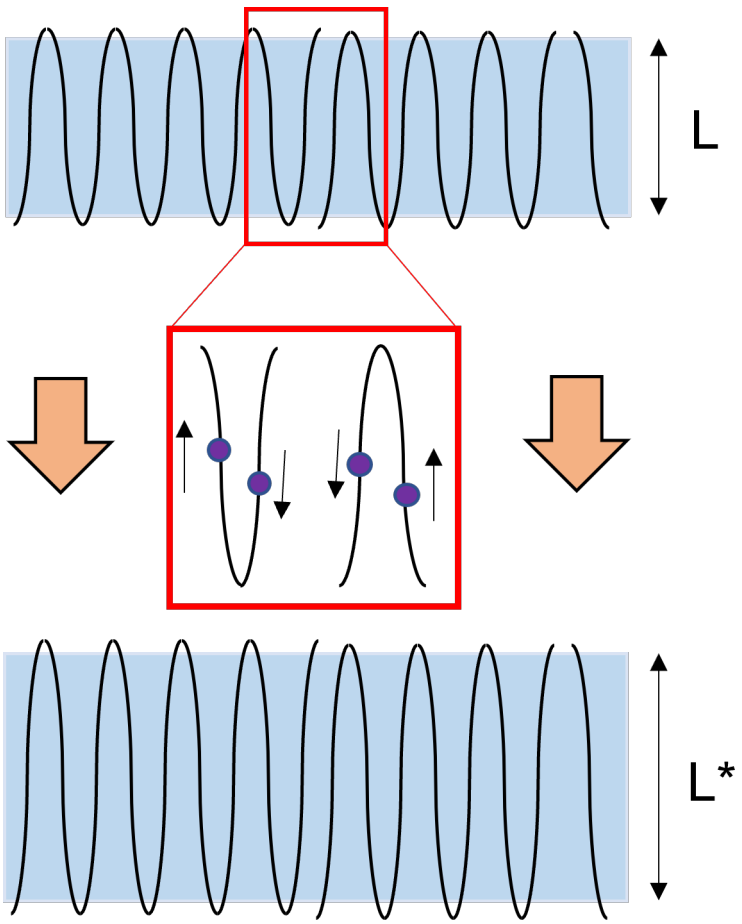


Figure 1.9: An illustration of the lamellar thickening process. Under energetically favourable conditions, parallel chains will move within the lamella, increasing the distance between chain folds and increasing the thickness. Note that no additional chains are added to the lamella during this process.

Studies of thin stretched films of natural rubber [20] showed that crystals formed transverse to the direction of applied stress, nucleating on a central backbone from which they grew in perpendicular directions [21]. This row-nucleated structure is termed *shish-kebab* morphology. In this morphology, the stress causes chain alignment, which allows for a nucleus to form as in Section 1.2.5. From this nucleus, chains fold onto the energetically favourable surface perpendicular to the aligned chains, creating the shish-kebab structure.

Polymer fibres are typically produced through spinning, followed by drawing. During spinning, the molten polymer is forced through the spinneret, and the molten stream of polymer is then cooled rapidly, causing it to quench in that molecular orientation. The fibre is often redrawn to increase alignment. The degree

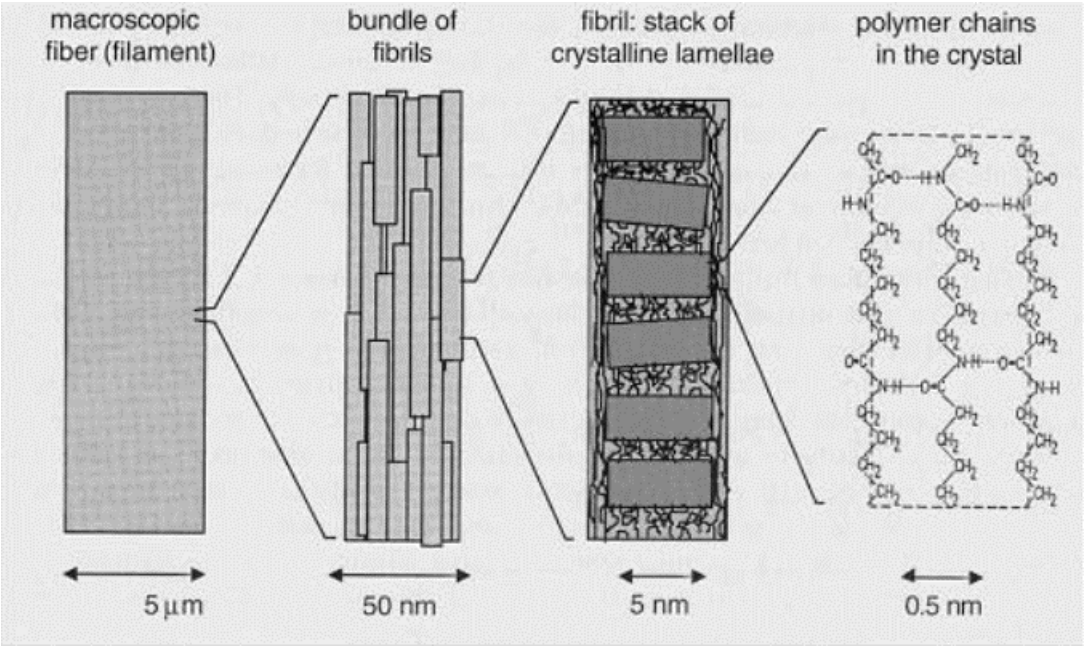


Figure 1.10: The hierarchical structure of a Nylon-6 fibre, showing the locations of inter-lamellar and inter-fibrillar amorphous polymer. A Nylon-12 fibre would differ only in terms of its unit cell and chain backbone length. [22]

of molecular orientation depends on the processing conditions, with a high degree of alignment being obtained through high extrusion rates and fast cooling. In nylon, for example, the fiber is stretched four times its spun length. The crystals formed during drawing are held together by hydrogen bonds between the amide hydrogens of one chain and the carbonyl oxygens of another chain. The orientation in the H-bonded sheets prevents splitting in the longitudinal direction without a sacrifice in tensile strength. Each fibre consists of sections of crystalline lamellae joined by sections of amorphous polymers; a structural characterisation of length scales of a nylon fibre is given by Rieger [22] and is shown in Figure 1.10.

1.2.7 Mechanical properties of semi-crystalline polymers

1.2.7.1 Deformation behaviour

In the majority of present day uses of polymers, the focus is on their mechanical performance. This differs from conventional crystalline solids because bulk polymers combine elastic and viscous properties. The mechanical response of all polymers can be classified into two segments: an elastic (reversible) part and a plastic (irreversible)

part. At low strains the polymer behaves elastically, while after the *yield point* the behaviour becomes plastic. This is illustrated in Figure 1.11.

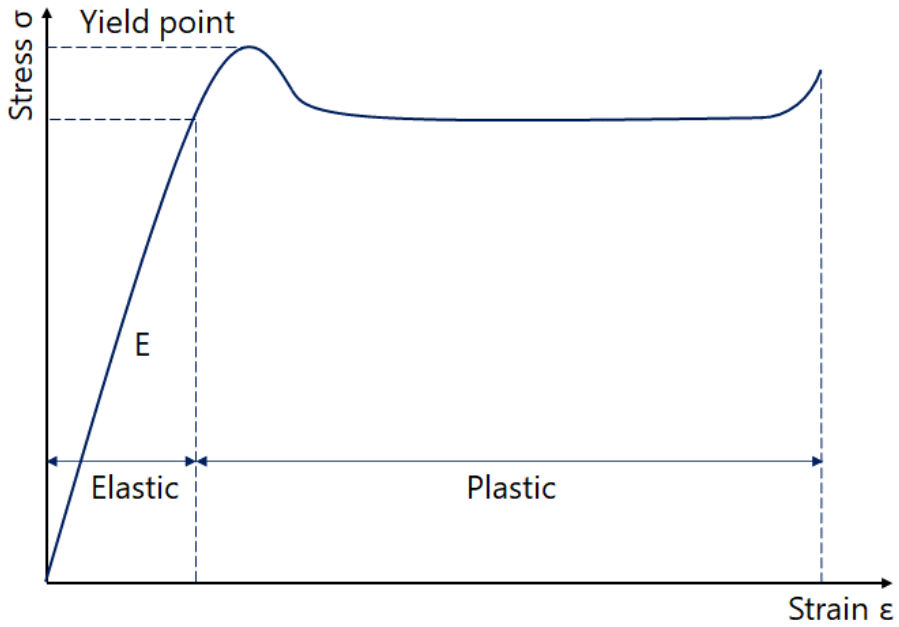


Figure 1.11: A schematic stress-strain curve for a polymer, showing the elastic and plastic sections of the curve, as well as the yield point.

In the elastic regime at low strain, the polymer behaves according to Hooke's Law, with the strain ϵ being nearly proportional to the applied stress σ. Young's Modulus E is generally taken from this region as the apparent slope on the stress-strain curve. For higher levels of strain, the deformation becomes plastic and preferential orientation can be induced in the sample. The maximum of the stress strain curve is called the yield point. When the plastically deformed and oriented part has extended to the whole sample being tested, a hardening (*strain hardening*) can occur till the breakage of the material.

The region of the stress-strain curve whereby the stress falls back below the yield point even as the strain increases, is known as cold drawing. This behaviour is due to the rearrangement of the chains, beginning with necking, whereby a portion of the stressed polymer is narrowed down to a smaller cross section. In the region of the neck, the polymer is extensively reorganised. The spherulites are broken up, causing the polymer to be oriented in the direction of the stretch such that the

number of chain folds decreases. In fact, the crystallisation of the total polymer is enhanced by this chain alignment, increasing the strength of the neck.

The strength of engineering polymers is sensitive to temperature, with the mechanism depending on how the operating temperature compares with T_g. For temperatures below T_g the amorphous portion of the polymer is glassy and so the response is brittle. Above T_g, the amorphous region becomes rubbery and so extensive plastic deformation can occur prior to failure. At temperatures significantly above T_g, a thermoplastic can deform extensively by viscous flow.

The granular substructure of crystal lamellae have nm-sized crystal blocks as the basic morphological elements. The blocks are able to slide against each other, which gives sufficient degree of freedom to accommodate externally imposed strain. At the beginning of the drawing process, block sliding is a local process, but becomes a collective process at the yield point.

This effect is observed in polymer fibres, in which the chains are already aligned prior to stretching. As a result there is large anisotropy of mechanical properties. The moduli parallel to the chain direction are $\sim 10^{11}$ Pa [1], on the order of metals; whereas in directions perpendicular to the chain axes, the modulus drops to $\sim 10^9$ Pa. The high modulus of polymer fibres parallel to the chain direction is due to the elastic behaviour of thermoplastics below T_g, which involves stretching of the covalent chain backbone bonds.

The stretching of the backbone bonds causes a change in the lattice parameter of the polymer unit cell. It can be assumed that in the elastic region of deformation, the stress on polymer crystals in the direction of the polymer chains is equal to the stress σ on the entire bulk, such that the chain-direction crystal modulus is given by

$$E_c = \frac{\sigma}{e_c} \tag{1.26}$$

where e_c is the axial crystal strain. This can be determined through wide-angle X-ray scattering (WAXS), which will be covered in Section 2.2.2. The calculated chain direction modulus E_c is higher than the experimentally measured values for even highly aligned fibres due to the presence of amorphous regions, which undergo

a higher strain for the same stress. The presence of amorphous regions causes a significant reduction in modulus, such that in general highly oriented semi-crystalline polymers tend to have moduli of less than 50% of the calculated values.

The variation of the polymer modulus with the proportion of amorphous and crystalline region can be predicted by two composite models, forming an upper and lower bound for the actual modulus. In the lower bound, due to Reuss [23], it is assumed that the elements in the polymer structure experience the same stress, with the Reuss modulus E_R being given by

$$\frac{1}{E_R} = \frac{V_c}{E_c} + \frac{(1 - V_c)}{E_a} \tag{1.27}$$

where V_p is the crystalline volume fraction, and E_c and E_a are the moduli of the crystalline and amorphous regions respectively. In the upper bound Voigt model [24], it is assumed that the elements all experience the same strain, such that the Voigt modulus E_V is given by

$$E_V = E_c V_c + E_a(1 - V_c) \tag{1.28}$$

The Reuss model assumes that the direction of loading is perpendicular to any crystal structure in the material, whereas the Voigt model assumes it to be parallel to the crystal structure. In the case of a fibre morphology where the loading direction is parallel to the fibre orientation, the Voigt model is more appropriate. In the case of more uniform spherulitic morphology, the Reuss model gives a better prediction of the observed behaviour.

Semi-crystalline polymers are therefore in effect two-phase composite materials, with observed moduli being a reflection of the combined moduli of the amorphous and crystalline regions. As a result, the deformation properties of semi-crystalline polymers are greatly dependent on the degree of crystallinity (the crystalline volume fraction) and the nature and arrangement of the crystal regions. It can therefore be seen that the mechanical properties of a semi-crystalline polymers derive directly from the thermal history that led to the formation of its specific crystal structure.

1.3 Fused Filament Fabrication

1.3.1 Introduction

Fused filament fabrication (FFF) is one of numerous advanced manufacturing technologies collectively known as *Additive Manufacturing* (AM). AM is an umbrella term encompassing any of the various processes that involve the joining of materials to make objects according to three-dimensional model data, usually layer upon layer. This "bottom-up" manufacturing process stands in contrast to traditional "subtractive" manufacturing methods such as machining, and therefore has the ability to generate complex structures without the need for special tooling, offering advantages from both time and direct cost points of view. In addition, it has the ability to make efficient use of raw materials and produces minimal waste while reaching satisfactory geometric accuracy [25, 26]. The topologically optimized designs that AM is capable of realizing could also increase a product's functionality and provide significant weight savings [27], thus reducing the amount of energy, fuel, or natural resources required for its operation [28].

Significant progress has been made since the initial development of the technology in the 1980s, and there persists an expectation that AM technology can revolutionise the industry and provide various benefits to society as a whole. It has been predicted that as AM technology continues to evolve, it will be able to compete with current mass production techniques such as injection moulding and casting [29]. The economic feasibility of using existing AM systems to manufacture parts in quantities up to 14,000 was already demonstrated by Hopkinson and Dickens in 2001 [30]. The possibility of on-demand manufacturing presents an opportunity to reconfigure the traditional supply chain to produce cheaper products faster. Furthermore, the ability of AM systems to produce bespoke products quickly allow it to break into industries such as healthcare, for instance through the production of implants and knee replacements customised to the needs of individual patients.

The International Organisation for Standardisation (ISO)/American Society for Testing and Materials (ASTM) 52900:2015 classify AM processes into seven categories as follows:

1. binder jetting (BJ);
2. directed energy deposition (DED);
3. material extrusion (ME);
4. material jetting (MJ);
5. powder bed fusion (PBF);
6. sheet lamination (SL);
7. vat photopolymerisation (VP).

Within this general list, more specific technologies can be highlighted. When manufacturing polymer-based samples, the most commonly used instance of ME is fused filament fabrication (FFF), also sometimes referred to as fused deposition modeling (FDM). For metal AM, methods such as selective laser melting and sintering (SLM and SLS respectively), both subsets of PBF, tend to be used.

FFF manufactures samples by heating an extruded filament of material before laying it down layer-wise to build up the desired shape, allowing the adjacent layers to cool and start to bond before the deposition of successive layers. Since the material layer is deposited in a fluidic state, the FFF process is currently limited to polymers and polymer-based composites owing to their relatively lower melting and glass transition temperatures, which makes extrusion comparatively easier [31].

FFF allows for the construction of bespoke complex geometries to generate geometric overhangs [32]. FFF allows for significant design flexibility and more efficient use of material compared to conventional methods, and has seen increasing uptake in industries such as aerospace and biomedical technology.

As stated in Section 1.1, FFF currently suffers from several drawbacks which present a barrier to wider industry adoption. FFF's low print speed results in a

lower rate of sample production compared to injection moulding and casting [33, 34], which is compounded by the small build volume of most commercially available FFF printers [35]. The layer-wise production of FFF samples also may result in void formation between adjacent layers or filaments. These voids are due to incomplete inter-layer bonding, which in turn lead to reduced mechanical performance [36], anisotropic mechanical properties [37, 38] and delamination [39, 40].

These anisotropic mechanical properties present a significant barrier to wider adoption of the technology. The extrusion of the molten filament from the nozzle results in a fibre-like morphology, as described in Section 1.2.6. The polymer chain alignment resulting from this results in different mechanical properties in the filament's parallel versus perpendicular direction. In addition to the effect of material properties, the mechanical properties of FFF parts in which the filaments are laid down perpendicular to the tensile direction will be dependent on the degree of inter-layer bonding between adjacent filaments. Parts manufactured by FFF therefore tend to possess better strength in the plane of the print bed as compared to the strength in the build direction [41, 42].

1.3.1.1 Basic principles of FFF

Figure 1.12 shows the working principle of a generic FFF machine. The FFF process can be summarised in the following steps [43]:

1. **Filament supply**: Filaments are stored on a rotating spool on the side of the machine, which uses a rotating gear mechanism (drive wheels) to control the intake into the extrusion head.

2. **Filament extrusion**: The drive wheels move the filament into the nozzle, which is heated until it reaches a near-molten state and extruded through the head of the filament.

3. **Filament Deposition**: The nozzle deposits the filament layer-by-layer on the print bed to create the desired shape. Parts that have free-hanging or

overhanging structures must have associated support structures which are removed once the print is finished.

4. **Layer-wise construction**: Following the completion of an individual layer, the nozzle or the print bed moves in the z-axis by a constant amount corresponding to the individual layer height, restarting the process in Step 3.

5. **Cooling**: Following print completion, the part is cooled to room temperature, at which point it is removed from the print bed.

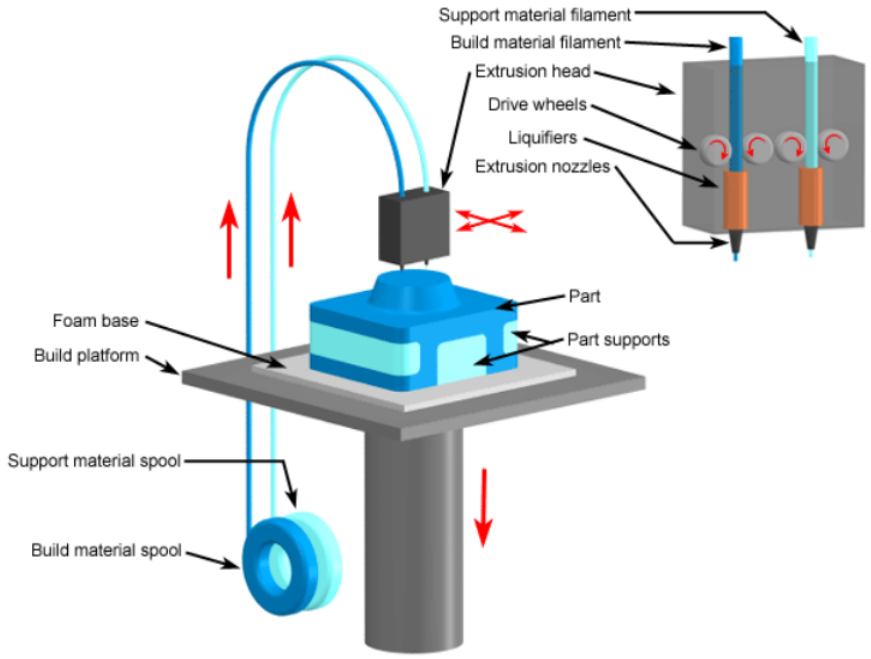


Figure 1.12: Working schematic of a generic Fused Filament Fabrication (FFF) printer. [43]

FFF printers control the properties of their printed samples through a number of parameters, the most important of which are listed below.

1. **Nozzle diameter**: In most modern high-end printers, the nozzle diameter is 0.2-0.3mm. In practice, the filament is usually deposited with an ellipsoidal shape due to gravitational forces and the reaction force from the layer below, which compress the molten filament from the cylindrical shape with which it exits the nozzle.

2. **Extrusion temperature**: This ranges from 200-600 °C, with a higher maximum temperature allowing for a wider range of polymers to be processed. The extrusion temperature is typically set considerably above the melting temperature T_m of the polymer to ensure more complete melting despite the relatively short exposure time.

3. **Bed temperature**: The print bed temperature can be varied depending on the polymer to be printed in most high-end modern printers. This can be kept low (70 °C for PLA [44]) to prevent warping at the edges of the print due to crystallisation-induced stresses and increase adhesion force. It can also be raised to control the thermal history in the build, namely the materials cooling rate after deposition.

4. **Chamber temperature**: In certain high-end printers, the chamber temperature can be varied which reduces porosity and aids interlayer adhesion.

The significance of the chamber and bed temperature is discussed in more detail in Section 1.4.1.

1.3.1.2 Sample design and slicing

A 3D model is first drawn in a computer aided design (CAD) program such as SolidWorks. This is output as a stereolithography (STL) file, which is widely used in AM processes. STL file describes the surface geometry of an object without any representation of colour, texture or other attributes. Surfaces are subdivided into triangular planar structures.

To prepare for printing, the STL file is 'sliced' using specific FFF software packages. This will define a further set of printing parameters, which are listed below:

1. **Infill**: The percentage volume infill can be controlled, as well as the type of infill. A solid structure, cross-hatched or honeycomb structure are examples of infill types.

2. **Extrusion speed**: Extrusion speed is calculated by the slicing software based on the geometry of the STL file. This can also be edited manually depending on the needs of the sample.

3. **Print orientation**: The orientation of the deposited filaments is dependent on the scan strategy, whereby filaments can be laid down along different sample axes or diagonally. The print orientation has a significant effect on sample properties, which will be elucidated in Section 1.4.3.2.

The sliced file is then converted to GCODE format, which encodes the file in a set of spatial coordinates along with commands to define the print parameters in Section 1.3.1.1. The FFF printer then fabricates the part.

1.3.2 Processing-structure-property relationship

FFF is a complex and dynamical process, during which a variety of associated physical phenomena affect the structure and properties of the final product. A schematic diagram of the various physical processes that take place during FFF is shown in Figure 1.13.

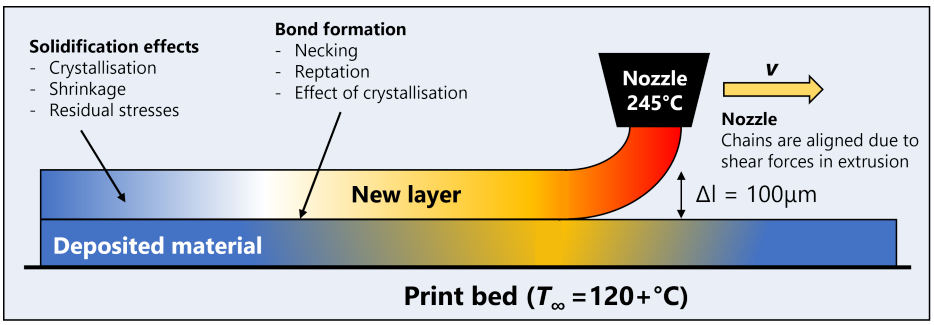


Figure 1.13: Detailed illustration of the FFF process and its related physical phenomena [45]

Core to the understanding of the FFF process is the *processing-structure-property relationship*. As per Section 1.1, this is defined as the relationship between

1. the processing conditions during sample production (*processing*)

2. the crystal structure or more general microstructure of the sample that results from these conditions (*structure*)

3. the bulk mechanical properties of the sample (*property*), which is a function of the crystal structure of the material as well as the overall part geometry.

The large number of processing parameters presented in Section 1.3.1.1 gives an insight into the scale of this relationship. In this section, a brief discussion of the processing-structure-property relationship in FFF is presented.

1.3.2.1 Processing

The processing conditions during FFF are controlled by the printer settings as elucidated in Section 1.3.1.1, namely the *extrusion temperature*, *extrusion rate*, *print orientation*, and *bed and chamber temperature*. The extrusion speed controls the shear forces that the filament undergoes on exit from the nozzle, controlling the degree of chain alignment induced in the filament. In addition, it controls the exposure time to the heated nozzle, and therefore the degree of melt in the filament on deposition. The extrusion speed is therefore a principal driver for the structural anisotropy in the build.

The print orientation causes alterations to the time period T of the print, which is defined as the time taken for the nozzle to return to the same spot on different layers. In particular, the larger the projection of the part onto the print bed, the longer it will take for the nozzle to return to the same spot on the subsequent layer. Since the hot nozzle is the main thermal force that reheats already-deposited layers, samples with a larger base will have a longer period between reheatings. Part geometry therefore has a significant effect on thermal history, therefore helping to determine the formation of the crystal structure. This spatially-dependent thermal history is unique to 3D printing processes. In addition, the direction of filament deposition has a significant effect on mechanical properties due to the propensity of the crystal structure to form perpendicular to the direction of chain alignment, as described in Section 1.2.6, and therefore the direction of filament deposition. A more detailed discussion about crystal structure of FFF samples is undertaken in Section 1.4.2.1.

The bed and chamber temperatures control the post-extrusion cooling rates, the minimum temperature of the filament in between successive reheatings by the nozzle and therefore the degree of crystallisation that can occur during the print. The chamber temperature drives the degree of undercooling experienced by filaments on exposure to air, while the bed temperature becomes the principal driver of thermal history once sufficient layers separate a given part of the sample and the print nozzle. If the bed temperature differs from the chamber temperature, the sample may have spatially varying crystal structure and therefore mechanical properties as a vertical thermal gradient is produced in the sample. In addition, lower layers in the centre of a sample will tend to retain heat longer than outer or higher layers. In the situation where the print bed and chamber are equally elevated to minimise thermal gradients within the print chamber, this effect can be mitigated.

1.3.2.2 Structure

The previous discussion of the key physical phenomena in the FFF process underlines the complexity of the process. A complete characterisation of the FFF process therefore requires careful consideration of these phenomena both individually and also as a sum total. To this end we consider a set of length scales on which the processing conditions affect the end product's structure:

1. microstructural
2. mesostructural
3. macrostructural.

The microstructure of an FFF sample can be defined as its crystal structure. The mesostructure encompasses the individual filaments and their bonding in a cross-section of the sample. The inter-filament bond area, which governs sample porosity, can be considered to be the mesostructure. Finally, the macrostructure encompasses the length scale of the entire sample.

The crystal structure of semi-crystalline thermoplastics and its dependence on thermal history has been discussed in detail in Section 1.2.5. Variation of any

of the processing parameters in the above section will affect the thermal history and will therefore also lead to changes in the microstructure, which in turn will affect the mechanical properties. However, the mechanical properties of an FFF sample are not wholly governed by material properties, and the mesostructure must also be taken into consideration.

The microstructure and mesostructure interact at the interfacial bond, where the bond area due to filament wetting and bond strength due to interfacial crystallisation both drive the mechanical properties of the sample. The strength of interlayer bond is driven by the thermal history and therefore the processing parameters, which will be discussed in more detain in Section 1.4.2.2. In a complex FFF sample, filaments may be aligned parallel, perpendicular or at an angle to the direction of applied stress. If all filaments were aligned parallel to the direction of applied stress, then the tensile properties of the sample would be primarily dependent on the tensile properties of the constituent filaments, which are dependent on the microstructure (e.g. degree of crystallinity and degree of chain alignment). By contrast, the mechanical properties of an FFF sample in which all the filaments were oriented perpendicular to the direction of tensile stress would depend both on the mechanical properties of the constituent filaments in that direction and on the degree of interlayer bonding between adjacent filaments. In order to optimise the mechanical properties of a complex FFF sample, part geometry and print orientation must be considered on top of optimisation of the microstructural properties.

1.3.2.3 Property

The bulk mechanical properties of an FFF-produced sample may encompass a large number of parameters. Some of the most primary parameters used to define the strength of a polymer are [38]:

1. the **tensile properties**, comprising the Young's Modulus E, the ultimate tensile strength (UTS), the yield strength and the elongation at break (EAB). These are typically determined through tensile testing of a sample with dogbone geometry.

2. the **flexural properties**, comprising the flexural strength and modulus. These are determined typically through three-point bending testing.

3. the **compressive properties**, comprising the compressive yield strength and modulus of elasticity.

4. the **hardness**, which quantifies a material's resistance to localised plastic deformation and depends on other parameters including elastic modulus and yield strength. It is typically determined through nanoindentation testing.

5. the **impact strength**, which measures the amount of energy absorbed by a specimen during its deformation and failure upon the application of an impact.

6. the **fracture toughness**, which is a measure of a material's resistance to crack propagation. It is typically determined through measurement of a crack propagation in a pre-notched sample under applied load.

7. **fatigue life**, which defines the time to failure under given cyclic loading conditions. It is typically determined through cyclic loading of a dogbone sample.

These properties will be affected by the structure of an FFF part, as the degree of inter-layer bonding, part geometry and material microstructural properties will drive the mechanical response over the macrostructural length scale of an FFF part.

1.4 State of the art

In this section, a review of studies on elements of the processing-structure-property relationship for thermoplastic polymers both in and out of the context of FFF is presented.

1.4.1 Thermal history of FFF

Each filament that is deposited cools on exposure to the air in the print chamber, with the minimum temperature reached governed in the first instance by the print chamber temperature. During the deposition, subsequent filaments are then laid down adjacent to and on top of the initial filament, thereby wetting and re-heating or re-melting it. The wetting process determines the interfacial contact area between adjacent filaments, while the higher temperatures that an already-deposited filament is exposed to promotes inter-filament coalescence and interdiffusion of polymer chains across the interface.

A strong dependence of temperature on the viscosity of the polymer limits the range of temperatures for forming a bond between layers. High temperatures are needed for a diffusion based fusion of the adjacent filaments after an interface has formed. At lower temperatures, the molecular mobility decreases and the diffusion process is hindered. Hence, the temperature history at the inter-filament interface is the crucial factor for the bond formation [46].

Following deposition, the filaments begin to cool, which starts the process of crystallisation. As discussed in Section 1.2.5, crystallisation is a process that proceeds through both nucleation and growth with a high dependence on the temperature of crystallisation T_c and the degree of undercooling ΔT. There are several principal physical sub-processes to consider within the scope of crystallisation of FFF. Firstly, the crystallisation behaviour of a single filament, and secondly the nature of inter-filament bonding in the case of semi-crystalline polymers.

Considering firstly the case of the single filament, the resulting structure is governed by the thermal history. The nature of this thermal history has been studied by several groups [46–49]. Bellehumeur *et al* [46] and Kousiatza *et al* [47] investigated the temperature profiles in different sizes of specimen using embedded thermocouples, finding that filaments underwent a series of fluctuations in temperature due to the reheating process, resembling a damped quiescent sinusoidal wave. The reasons for this are clear: as the nozzle deposits more layers on top of the filament being examined, the effect of its thermal radiation is lessened. It was additionally

found that the minimum temperature ΔT_{min} achieved during this temperature profile was affected by several factors, such as the size of the sample [46] and the print speed [48]. As the time period between the deposition of successive layers decreases, ΔT_{min} increases.

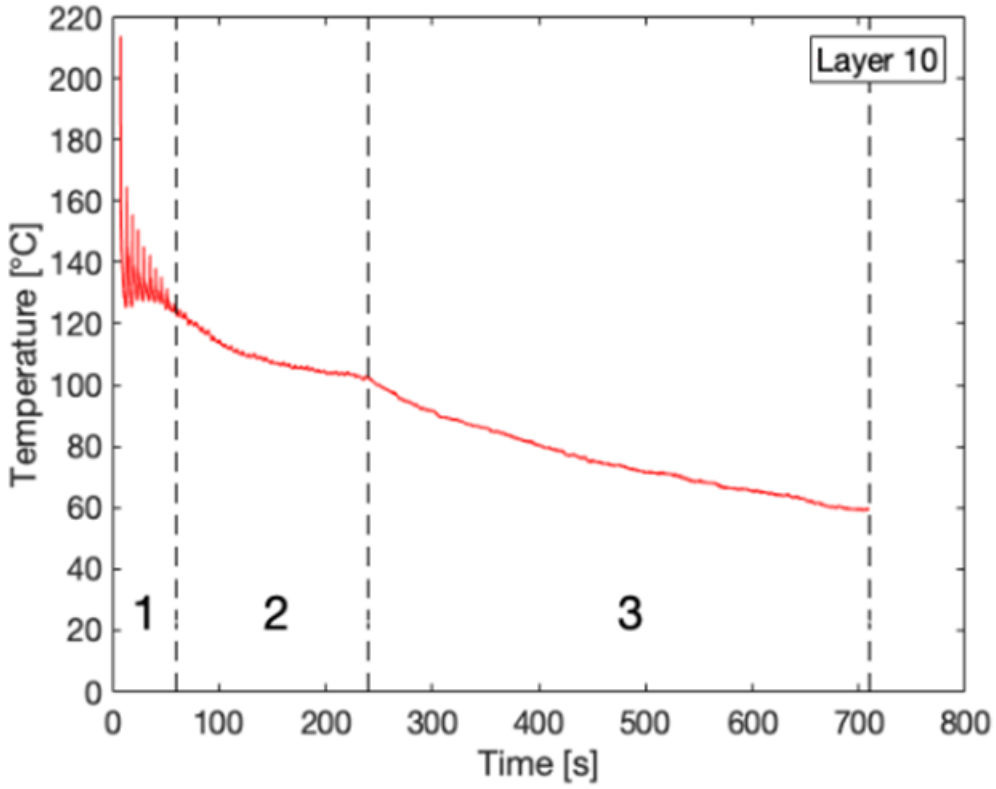


Figure 1.14: Temperature profile for a mid-sample layer during FFF demonstrating three distinct thermal phases. [50]

Furthermore, the thermal history of a deposited filament can be separated into phases. Vaes *et al* [50] studied the thermal history of filaments on Nylon-6/66 using infrared thermometry. It was found that initially, the pseudo-sinusoidal temperature profile seen in [47] and Figure 1.14 was observed. However, after the deposition of sufficient layers, the effect of the thermal radiation of the printer nozzle became negligible. Thereafter, the filament cooled from ΔT_{min} to the temperature of the build plate, which becomes the driving force of thermal history. After the print is completed, there is a third cooling phase whereby the filament cools to room temperature. The thermal gradients of the second and third phase are driven entirely by the degree of undercooling; here, the difference between ΔT_{min}

and the plate temperature, and the difference between the plate temperature and room temperature respectively.

Subsequent investigation by fast scanning chip calorimetry (FSC) in [50] further revealed that a significant part of the obtained crystallinity is acquired during the initial heating and reheating cycles. It is also notable that these studies into the thermal history reveal that the repeated reheating due to the printer nozzle passage during the first phase does not reheat the filament to its melting temperature. Although the temperature of the filament may be raised high enough to induce further crystallisation, a significant proportion of crystallisation can be inferred to take place during the initial cooling from the nozzle on deposition, highlighting the importance of this stage in the sample's highly non-isothermal thermal history.

1.4.2 Relationship between processing conditions and structural properties

1.4.2.1 Dependence of microstructure on processing conditions

Considerable work has been done on studying the dependence on the crystal structure of semi-crystalline polymers on their processing conditions. The effect of the cooling rates experienced by the polymer on its resultant microstructure has been well-established. A rapid cooling experienced during FFF results in a lower degree of crystallinity, resulting in a semi-crystalline material with more amorphous parts and therefore different mechanical properties. Pourali *et al* and Doumeng *et al* [51, 52] both note in studies on Nylon-6 and polyether ether ketone (PEEK) respectively that the rate of crystallisation increases with faster cooling rate. In the study of Van de Voorde *et al* [53], slow cooling of poly(ethylene terephthalate) (PET) increased the degree of crystallinity from 1.4% to 21.2% versus rapid fan cooling.

This low degree of crystallinity produced by fast cooling rates in [53] is supported by the results of Yu *et al* [54], which note that the cooling rates experienced during FFF in excess of 100 °C/min may be too fast for crystallisation to occur in polylactic acid (PLA). Samples produced by FFF in this study remained amorphous, in contrast to samples cooled at 10 °C from the melt which had a degree of crystallinity in

excess of 30%. Further studies on PLA have revealed that the crystallinity of samples produced through FFF is higher than that of the filament [55, 56]. This is proposed by Lay *et al* [57] to be due to the repeated heating and cooling that a filament undergoes during FFF; as stated in Section 1.2.5, this thermodynamic driving force induces more nucleation, leading to more and smaller crystals.

Teo *et al* [58] investigated the effect of cooling rate on degree of crystallinity and spherulite size in Nylon-12. It was noted that a slower cooling rate resulted in a higher degree of crystallinity, with a cooling rate of 0.2 °C/min corresponding to 24.9% crystallinity, versus 19.1% crystallinity at 10 °C/min. In addition, a slower cooling rate resulted in larger but fewer crystals. Cooling at 1 °C/min resulted in a mean spherulite diameter of 40 μm, versus 21 μm for a cooling rate of 10 °C/min. In a rapid crystallisation study of poly(vinylidene flouride) (PVF) by Gradys *et al* [59], crystallinity decreased from 25% to 0% as cooling rate increased from 10 °C/s to 2000 °C/s.

A period of annealing within the thermal history has also been shown to have a beneficial effect on the crystal structure. It has been reported in [60–63] that increasing the build plate temperature has an annealing effect on FFF samples, increasing the part crystallinity as the sample is kept above T_g for a longer period of time. Studies on this thesis' material of choice Nylon-12 [64] also demonstrated a higher degree of crystallinity as well as larger crystallites in a more ordered arrangement after heat treatment. In a study on SLS Nylon-12 by Hejmady *et al* [65], it was noted that the mean crystallite thickness was increased from 11 μm to 15 μm by increasing the chamber temperature from 70 °C to 155 °C; however, no change in overall degree of crystallinity was observed between these chamber temperatures.

Felder *et al* [66] noted that annealing Nylon-6 samples for 60 min at 160 °C increases the degree of crystallinity from 23% to 28 %. Reis *et al* [67] studied the effect of annealing on PLA, noting that annealing samples at 90 °C for a longer period resulted in a higher degree of crystallinity than samples annealed for a shorter period at 120 °C. It was noted that the spherulite size increased with annealing temperature, from 6.4 μm at 80 °C to 9.7 μm at 110 °C.

In addition, the extrusion processing parameter affects the microstructure. During this process, the diameter of the filament is reduced from 1.75mm to 0.2mm, and the polymer is heated to a molten state and pushed through the head of the nozzle. This has an effect on the chain alignment within the filament, as it represents a repeating and refinement of the initial extrusion process that produced the filament initially. The effect of extrusion on chain alignment was discussed in Section 1.2.6.

The chain alignment caused by extrusion during the FFF process is known as the *deposition-induced effect*. The deposited molten materials undergo external stretching during the nozzle scanning process of printing, causing the orientation of macromolecules [68]. These can be frozen in place during cooling, and may enhance the tensile properties along the filament direction. Zhou *et al* [69] found that strain-at-break values of FFF-produced tensile test samples based on PC/ABS/EMA were higher than that of conventional injection moulded samples.

Nogales *et al* [70] found that the degree of crystallinity close to the inter-layer boundary in FFF was lower, which was proposed to be due to limitations on crystal growth imposed by the inter-layer boundary. Levenhagen *et al* [71] propose that high shear rates applied to the filament during extrusion may lead to shear induced crystallisation, leading to a higher degree of crystallinity for a faster extrusion speed. In the study of Shmueli *et al* [72], orientational effects were observed in the filament which created a shish-kebab crystalline microstructure. Studies on the effect of chain alignment on crystallisation have shown that a more ordered configuration considerably facilitates and enhances crystallisation [73–76].

A higher degree of polymer chain alignment may lead to a higher degree of crystallinity on cooling; it was found by Leng *et al* [68] that in polyurethane parts reinforced with polylactic acid microfibres, a higher degree of crystallinity was attained through FFF compared to injection moulding. Mitchell *et al* [77] found that alteration of the extrusion speed resulted in a higher degree of chain anisotropy in the extruded filament, contributing to an earlier onset of crystallisation, as well as improved mechanical properties in the direction of the filament.

1.4.2.2 Dependence of mesostructure on processing conditions

The relationship between the mesostructure and the processing conditions is primarily driven by the interfacial adhesion between adjacent filaments, leading to the reinforcement of a semi-crystalline polymer interface. This is achieved through either chain entanglement (via reptation across the interface) or through the incorporation of polymer chains on both sides of the interface in the same crystallite (*co-crystallisation*) [2]. This process is shown in Figure 1.15. The microstructure of the filament near the interface strongly influences the way in which inter-filament bonding will take place, thereby governing its fracture toughness and plastic deformation properties.

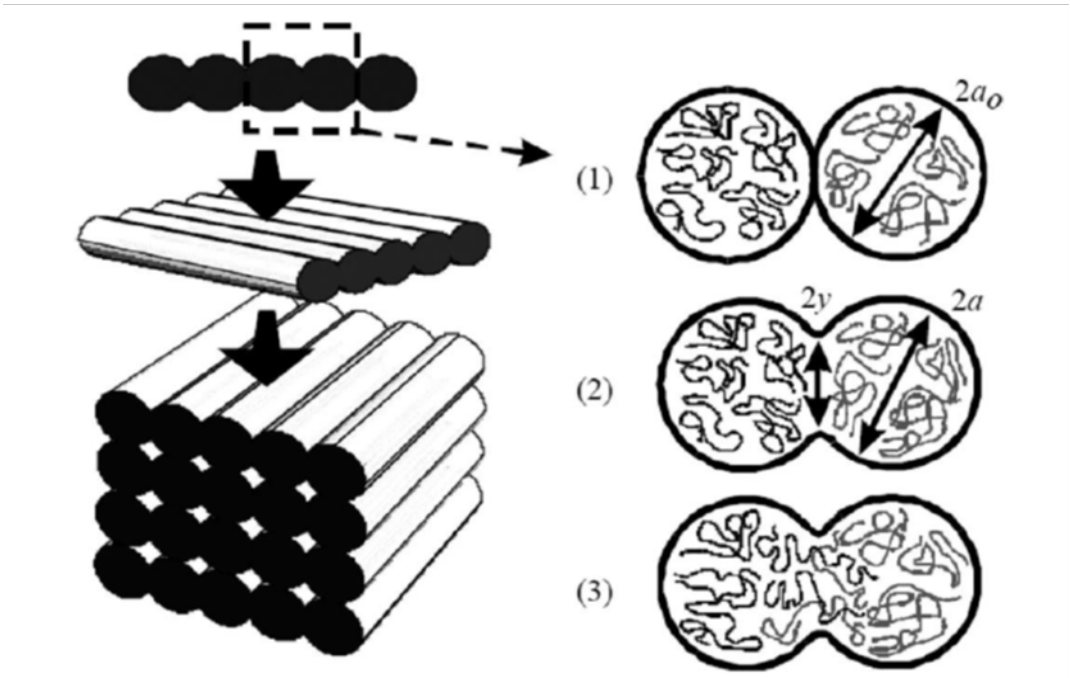


Figure 1.15: Illustration of the bond formation process between adjacent filaments. After two beads get in contact (1), a neck grows (2) and finally molecular diffusion happens at the interface and the polymer chains randomize (3). [45]

The spatially varying microstructure in an individual filament was investigated by Wang *et al* [78]. It was found that varying the layer height and plate temperature affected the distribution of crystallites within a filament. It was noted that the non-isothermal pulse-like conditions of the first phase of cooling led to small, poorly formed crystallites. Furthermore, a more dense distribution of crystallites was

observed close to the interfacial region. This is hypothesised to be due to the fact that the edges of the filament undergo the greatest shear strain during extrusion. The crystals formed in the interfacial area were found to orient perpendicular to the interface, which was attributed to the molecular diffusion occurring at the interface.

The self-adhesion component of semi-crystalline polymers has been extensively studied. Several groups investigated the specificities of the self-adhesion of semi-crystalline polymers by studying in particular the influence of the temperature gradient (Smith *et al* [79]) and co-crystallisation (Xue *et al* [80], Gent *et al* [81]). Furthermore, in studies done by Jarrousse on self-adhesion of semi-crystalline polymers, it was shown that co-crystallisation can be an effective method to reinforce interfaces if preceded by some interdiffusion of chains prior to recrystallisation [2].

In the context of FFF, the inter-filament interface is the most fragile region of manufactured parts. A single filament has nearly the same mechanical properties as a die-formed part when it is melted, solidified and continuously distributed in its X-direction, but has discontinuous properties in the Y and Z direction where the interfaces exist. The thermal history is essential to determining the interface strength; rapid cooling may cause poor interface bonding through lack of polymer chain diffusion across the interface, leading to poor mechanical properties. Previous studies have been conducted on altering the local thermal history of parts in order to achieve more optimal inter-filament bonding. Partain *et al* [82] used localised application of hot air via a secondary nozzle and Ravi *et al* [83] used localised laser heating to decrease the thermal gradients across the interfacial adhesion area. A maximum interface strength increase of 66% was achieved in the former case [82], and in the latter case more than a 60% increase in strength and 100% increase in elasticity was achieved versus parts printed with the same parameters but no localised heating. However, a high level of localised heating may lead to dimensional inaccuracy in the printed part [83].

Furthermore, the crystal structure of FFF samples is affected by controlling the thermal history at the interfacial boundary. Basgul *et al* [84] used annealing to control the cooling rate of deposited PEEK filaments and therefore decreased the

thermal gradients across the inter-layer boundary. Annealing at 300 °C was found to result in a marginal increase in ultimate load under certain printing conditions, and simultaneously a different morphology was observed, explained by a thickening of the crystal phases [84]. Luo *et al* [85] used a CO_2 laser to locally heat FFF samples during printing. It was observed that with laser assistance, the crystallinity of the PEEK samples increased from less than 15% to 34.5%, demonstrating that precise control of the thermal history also results in control over the crystal structure. The inter-layer shear strength was in the same study shown to increase by more than 45% with laser application compared to without [85]; as a result of this an optimisation zone in which the microstructure and mechanical properties can be optimised as a function of thermal history was obtained.

1.4.3 Relationship between structural properties and mechanical properties

1.4.3.1 Dependence of mechanical properties on microstructure

The crystallinity of a semi-crystalline polymer increases strength, because in the crystalline phase the intermolecular bonding is regular and has a more significant effect on the overall response. The relationship between percentage of crystallinity and tensile properties has been evaluated repeatedly in a large range of studies since the advent of polymer science. As far back as 1956, Starkweather *et al* [86] studied unoriented Nylon-610 crystallised through thermal treatment, and found that the stiffness, yield point and tensile strength of Nylon-610 all increase linearly with increasing crystallinity in the range from 7% to 40%. A further study of Nylon-66 by the same authors revealed a similar linear relationship between tensile properties and crystallinity.

Wright *et al* [87] studied the effect of crystallinity on the properties of injection-moulded polypropylene (PP). It was firstly noted that the crystallinity was directly linked to the thermal history, as when the processing temperature was increased from 12 °C to 105 °C, the size of the spherulites increased from 10µm to 60µm.

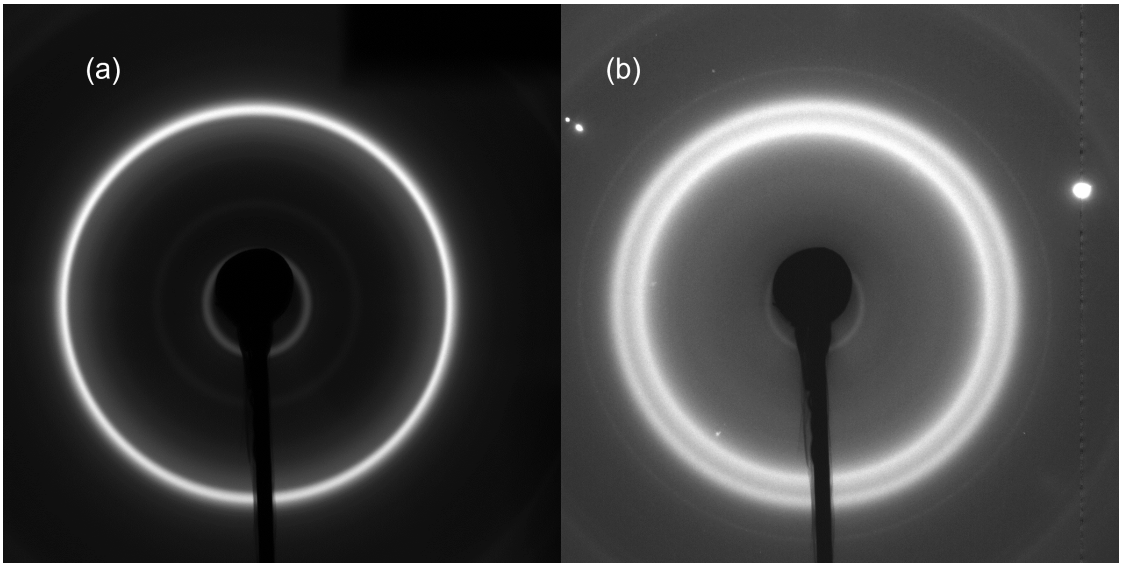


Figure 1.16: X-ray diffraction (XRD) data for (a) SLS vs (b) FFF Nylon-12. The highly crystalline nature of SLS Nylon-12 is visible, with minimal amorphous halo. FFF Nylon-12 shows more visible reflections than SLS Nylon-12 (data from the present study). The white dots resembling Bragg peaks seen in (b) were found to be due to background data.

Increasing the degree of crystallinity from 43% to 51% increased the tensile strength from 34.4 MPa to 35.8 MPa, nearly a 5% increase.

The effect on annealing, shown in the previous section to increase degree of crystallinity, on the mechanical properties has also been studied. Samples that have undergone annealing [44, 88–91] have been shown to have a higher tensile strength and Young's Modulus. Kumar *et al* [92] found that annealing polyethylene terephthalate glycon (PETG) sampes improved the hardness, tensile strength, impact strength and bending strength by 21, 25, 23 and 18 % respectively. Studying the same material, Valvez *et al* [93] found that annealing for 480 minutes at 130 °C improved the flexural strength by 31.8 % and the flexural modulus by 61.1 % versus an un-annealed control group.

Various studies have been conducted on the material of choice, Nylon-12, to assess the relationship between the degree of crystallinity and mechanical properties. In addition, much work has been done on other nylons. Nylon-66 and Nylon-610 were shown by Starkweather *et al* [86] to display a largely linear relation between stiffness and percentage crystallinity below 35% crystallinity. Multiple studies have

been done on laser-sintered (SLS) Nylon-12. Although SLS of Nylon-12 results in a different microstructure (more highly crystalline) and more homogeneous mechanical properties versus FFF, the results are nevertheless applicable to the current study. The different XRD patterns of SLS vs FFF Nylon-12 obtained in the present investigation are shown in Figure 1.16.

The relationship was studied by Zarringhalam *et al* [94], who looked at laser sintered Nylon-12. Whilst the sintered samples are anisotropic, testing Z-orientation 3D-printed samples in the X-Y plane yields useful results. The relationship was found to be linear between the degree of crystallinity, the elongation at break and tensile strength, such that a higher degree of crystallinity resulted in a lower elongation at break but a higher tensile strength. The relationship is illustrated in Figure 1.17. These findings are in accordance with the theory outlined in the previous section, as ordered crystalline regions have a higher modulus than disordered amorphous regions. It must also be noted that the crystal arrangement and morphology also have an effect on mechanical properties. A study on Nylon-12/carbon black composites manufactured through various means by Athreya *et al* [95] showed that although sintered samples had a lower degree of crystallinity than injection-moulded samples, their tensile strength was greater. This was attributed to there being larger but fewer spherulites due to the slower cooling in SLS.

A higher degree of crystallinity has been shown to beneficially affect the bulk mechanical properties of FFF samples. Wang *et al* [78] found that smaller crystal size and higher degree of crystallinity improved the toughness of printed polylactic acid (PLA), such that its Izod impact strength was up to 114% higher than injection moulded PLA. Furthermore, annealing to improve degree of crystallinity was shown to improve the tensile strength of PLA [89, 96].

In addition, the bulk mechanical properties of FFF samples are highly anisotropic. It has been shown that the formation of microfibres [49] and the presence of high chain alignment are beneficial to tensile properties in the filament direction [77]. A higher degree of alignment in PCL filaments was shown to improve the load at break by 40%. However, this tensile strength in the filament direction comes

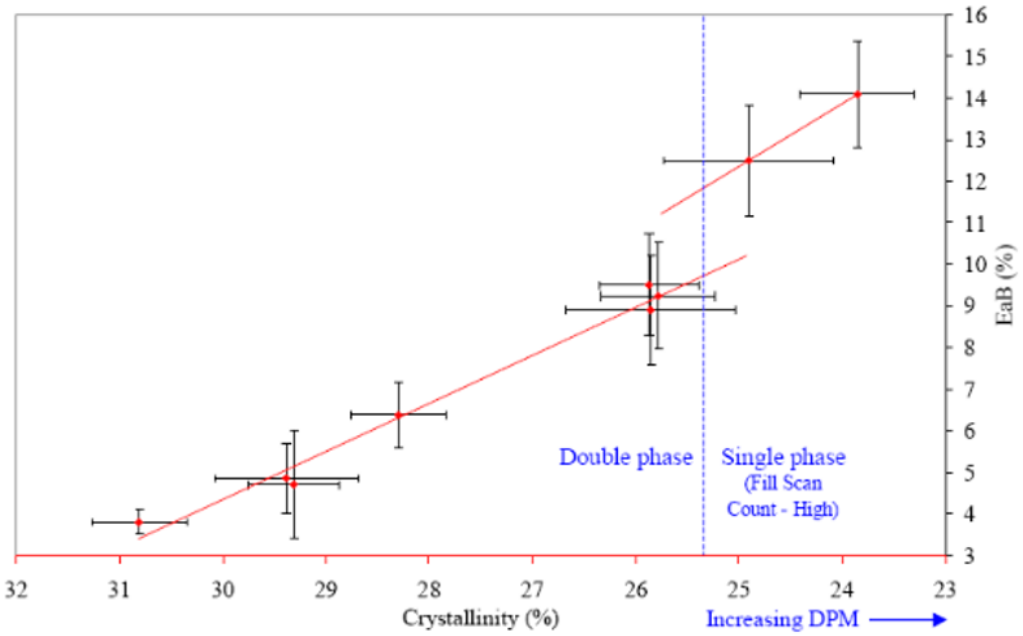


Figure 1.17: Effect of percentage crystallinity on elongation at break for SLS Nylon-12, with increasing degree of particle melt (DPM) going as decreasing percentage crystallinity. 'Double phase' refers to parts containing both melted and unmelted material, whereas 'single phase' refers to parts containing only melted material. Fill scan count refers to the density of scan vectors in each transverse cross-section. [94]

at the cost of reduced mechanical properties along other sample axes. Reduction of mechanical anisotropy can be achieved through annealing [97]; this reduced structural anisotropy but therefore reduces tensile strength in the filament direction.

Valerga *et al* [99] studied the mechanical properties and crystallisation of additively manufactured PLA samples. It was noted that when the percentage crystallinity of the samples increased above 25%, there was a significant increase in elongation at break. Based on this experimental data, fitting equations were proposed to define the tensile behaviour according to the percentage crystallinity X_c of the sample:

$$T_{max} = A + BX_c \tag{1.29}$$

$$EAB = C(e^{DX_c} - 1) \tag{1.30}$$

where A-D are material constants, T_{max} is tensile strength and EAB is elongation at break. It is notable that the latter governing equation implies that EAB =

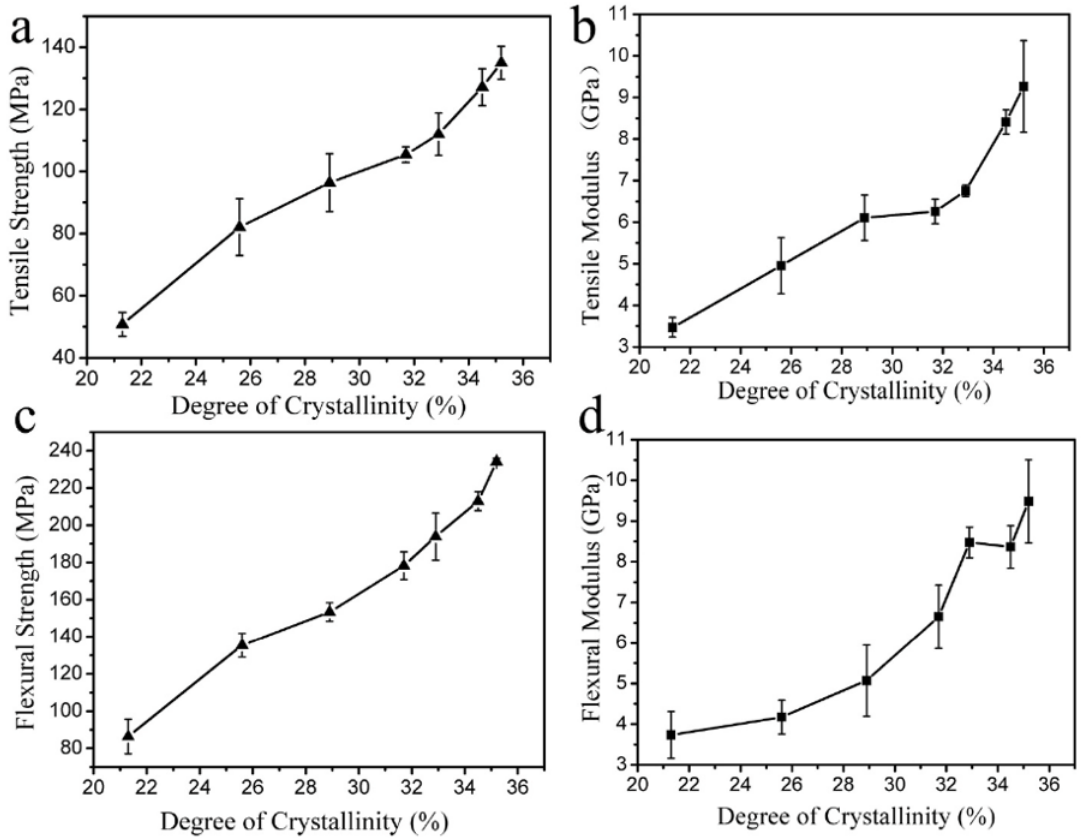


Figure 1.18: Relationship between crystallinity and (a) tensile strength, (b) tensile modulus, (c) flexural strength and (d) flexural modulus of carbon-fibre reinforced PEEK samples after heat treatment. [98]

0 at $X_c = 0$, whereas in actual fact the data showed a very small but non-zero EAB for a fully amorphous sample. Based on the close relation between degree of crystallinity and mechanical properties, control over mechanical properties via control of degree of crystallinity is possible. Yang *et al* [98] used heat treatment to control the degree of crystallinity in fibre-reinforced PEEK samples, annealing at different temperatures to obtain the desired degree of crystallinity. The results of the study are shown in Figure 1.18; large variation in the tensile modulus (from 3.5 GPa to 9 GPa) was observed by varying the crystallinity from 21.3% to 35.2%. In addition, it was noted by Wach *et al* that the thermal history and type of crystallinity are essential to consider. Different crystallisation conditions can lead to different sizes of spherulites in the sample, with larger spherulites leading to slightly higher strain and flexural modulus [96].

1.4.3.2 Dependence of mechanical properties on mesostructure

The mechanical performance is also affected by the mesostructure of the sample, parameters of which may include print orientation, infill raster angle and layer thickness. Arjun *et al* [100] investigated the effect of layer height on the tensile strength of PLA specimena, finding that tensile strength was reduced as layer height increased; it was proposed that this was due to increased voids in the sample. Likewise, Chen *et al* [101] found that a decrease in void space in polyetherimide (PEI) resulted in an improvement in tensile strength. Other authors [102, 103] have similarly found that a decrease in layer height results in an increase in Young's Modulus.

The effect of infill raster angle on mechanical properties has been investigated by several authors. In the study of Mohan *et al* [104], it was found that a raster angle of ± 45 ° resulted in an increase in impact strength of 41 % and in flexural modulus of 14 % compared to a raster angle of 0 or 90 °. Likewise, Ayatollahi *et al* [105] found in a study of samples with infill raster angles varied from 0 to 90 ° that a raster angle of ± 45 ° resulted in the highest fracture load. Milenkovic *et al* [106] found that a raster angle of ± 45 ° increased the Young's Modulus, yield point and elongation at break compared to a raster angle of 0 or 90 °, however decreased the ultimate tensile strength. It has been found by several authors [38, 107–109] that a cross-hatched pattern at raster angle of ± 45 ° results in better tensile and impact properties than other cross-hatched pattern angles, but has lower tensile properties than dogbone samples in which the filament is oriented parallel to the direction of applied stress.

The quality of the mesostructural interlayer bond has been shown to have a significant effect on properties. The interlayer adhesion is thus particularly weak in the vertical direction, limiting toughness and robustness [110]. Previous studies have indicated that this anisotropy can reduce the impact strength by as much as 90% [111] and the tensile strength by as much as 85% [112].

1.5 Objectives of the current study

It can be seen from the above sections that considerable work has been done on studying components of the processing-structure-property relationship in FFF. Historically, there has been a focus on linking the processing parameters that affect the mesostructure - namely part geometry, layer height and orientation - to mechanical properties, to the extent that this component of the processing-structure-property relationship has been well-established. Many recent studies have focused on developing the relationship between degree of crystallinity and thermal history, with particular emphasis on cooling rate and post-processing via annealing. The use of X-ray diffraction (XRD) and differential scanning calorimetry (DSC) to investigate the crystallisation behaviour has also seen an increased focus. In turn, the effect of annealing on degree of crystallinity and mechanical properties has also been well-investigated. Studies have also focused on the effect of extrusion on chain alignment, degree of crystallinity and mechanical properties.

However, while many of these studies investigate in detail the crystallisation behaviour or mechanical properties of a given material, comparatively few have established a quantitative processing-structure-property relationship. Much research has focused on establishing a qualitative link - for instance, that a faster cooling rate results in a lower degree of crystallinity, or that a higher annealing temperature tends to improve mechanical performance for a given material. Where research into the quantitative relationship between, say, thermal history and crystallisation behaviour has been done, it has tended to be in the context of materials characterisation and not in the context of FFF.

There therefore exists a gap in the literature for the establishment of a full quantitative processing-structure-property link which links together conventional polymer characterisation methods such as DSC or XRD with the *a posteriori* parametric studies of processing parameters on either structure or mechanical properties.

1.5.1 Scope

As stated in Section 1.1, the large number of physical processes and processing parameters involved in FFF mean that full establishment of a quantitative processing-structure-property link falls outside the scope of a single thesis. On the basis of the considerable work done on parametric studies of part geometry and the direct effect of processing parameters such as layer height on mechanical properties, it was decided to focus the scope of this thesis on the microstructural component of the processing-structure-property link.

In particular, this thesis focuses on development of the following quantitative links:

1. The effect of the thermal history. specifically the crystallisation temperature and cooling rate, on formation of crystal structure, degree of crystallinity and thermal properties in Nylon-12. Examined via X-ray diffraction (XRD) and differential scanning calorimetry (DSC).

2. The relationship between the degree of crystallinity and tensile properties, specifically Young's Modulus, ultimate tensile strength, yield point and elongation at break. Examined via ASTM-standard dogbone tensile testing.

3. Establishment of a direct link between the thermal history and the tensile properties of FFF-manufactured Nylon-12 using the above data.

The position of these links in the processing-structure-property relationship is illustrated in Figure 1.19.

The above links represent a small subset of the possible parameters investigable in a wider study of the processing-structure-property relationship. However, they represent a significant contribution to the processing-structure-property relationship in FFF. Literature reviewed in Section 1.4.3.1 has noted the significant variations in mechanical properties (up to 61% [93]) associated with a change in thermal history and an increase in degree of crystallinity. Establishment of a quantitative link between thermal history and degree of crystallinity would potentially allow

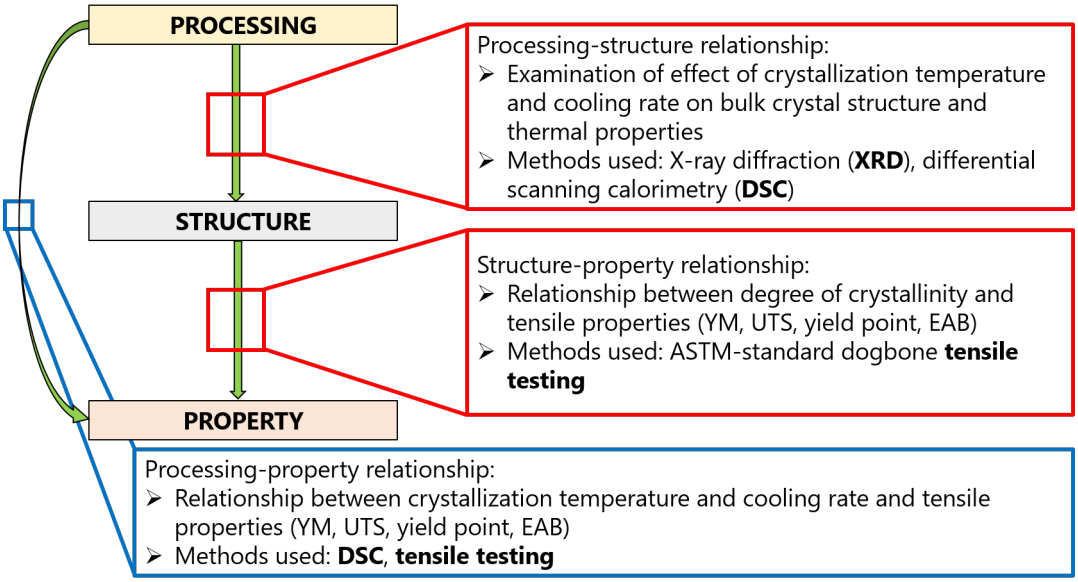


Figure 1.19: Illustrated flowchart of the position of the links to be studied within the processing-structure-property relationship.

for more precise control over the latter, and therefore for more precise control over the large variation in mechanical properties associated with it.

Although there are a large range of mechanical parameters for a potential analysis, the tensile properties were chosen for study in this thesis. This was firstly due to the existing well-established links and mathematical relations between degree of crystallinity and tensile properties, which therefore provide a basis for the construction of a full quantitative link between the thermal history and the tensile properties. Secondly, it allows for direct comparison of the results of this study and the bulk of literature on the subject, which has tended to focus on tensile testing.

1.5.2 Objectives

Whilst individual links between the thermal history and the crystal structure and between the crystal structure and the tensile properties have been previously in literature, as discussed in Section 1.4, precise control of the properties of FFF samples has still not yet been fully attained. The strength of FFF as a manufacturing process is its ability to produce bespoke geometries without the need for special tooling, but the mechanical properties of these samples need to be controlled at least as well as their geometry for FFF to compete as a viable large-scale manufacturing

process. Currently, the mechanical properties of FFF samples remain an uncertainty, with processing conditions being adjusted *a posteriori* to iron out poor performance and inhomogeneity via trial and error.

A greater understanding of the process-structure-property in FFF would therefore allow for a precise *a priori* link between a set of processing parameters and a set of mechanical properties which could be readily replicated across different FFF machines. This would additionally allow for bespoke control over the 3D distribution of mechanical properties within the sample, thus unlocking the full potential of layer-wise manufacturing.

The objective of the current study is to investigate the relationship between the processing conditions, in particular the cooling rate from the melt, on the resulting crystalline structure and mechanical properties of FFF-produced Nylon-12. Extended research activities have increased our understanding of the complex phenomena that accompany crystallisation under FFF conditions, however there are still key questions to be answered.

By elucidating these links above, and using a quantitative model to predict the consequence of thermal history on crystal structure during FFF, this study aims to establish a firm quantitative link between the processing conditions, the crystalline structure and the tensile properties of Nylon-12 samples produced via FFF. This will allow for the establishment of a processing-structure-property relationship for FFF-produced Nylon-12. Using the experimental and modelling data obtained in this study, this processing-structure-property relationship will be established such that reliable models can be delivered to tailor the characteristics of FFF-produced Nylon-12.

2

Materials and experimental methods

Contents

2.1 Introduction 54
2.2 Structural characterisation 54
2.2.1 Differential scanning calorimetry (DSC) 54
2.2.1.1 Basic theory 54
2.2.1.2 Experimental procedure 57
2.2.2 X-ray diffraction (XRD) 58
2.2.2.1 Basic theory 59
2.2.2.2 Experimental procedure 61
2.3 Mechanical characterisation 64
2.3.1 Tensile testing 64
2.4 Modelling 64
2.4.1 Modelling of an individual filament 64
2.4.2 Modelling of a series of contacted filaments 66
2.5 Nylon-12 71
2.5.1 Introduction 71
2.5.2 Structural properties 72
2.5.2.1 WAXS studies on Nylon-12 75
2.5.2.2 Spherulitic structure 76
2.5.3 Thermal properties 78
2.5.3.1 Melting behaviour 78
2.5.3.2 Equilibrium melting behaviour and heat of fusion 80
2.5.3.3 Crystallisation behaviour 80
2.6 Sample preparation 82
2.6.1 3D printers used 82
2.6.2 Print and sample parameters 83

2.1 Introduction

This chapter serves the dual purpose of introducing the materials used in this study and to describe precisely the experimental procedures applied in their analysis.

The experimental procedures are firstly presented that are linked to the determination of the crystal structure and its dependence on the thermal history, with particular implications for FFF. The relevant mechanical properties are identified, and the approaches to their determination outlined. The material of choice for this study, Nylon-12, is introduced and a review of existing studies on it is presented.

2.2 Structural characterisation

In this section, an overview of the bulk structural characterisation techniques utilised over the course of this thesis are elucidated.

Bulk characterisation methods provide a view of the overall structural properties of a sample within a certain area or volume. Differential scanning calorimetry (DSC), which measures the thermal properties of a sample on the millimetre scale, is a bulk characterisation method and provides an view of a sample's overall thermal properties. X-ray diffraction (XRD) allows for better spatial resolution than DSC, as its beam spot size is in the range of 1-300 μm. However relative to the structural length scales of FFF Nylon-12, XRD is a bulk characterisation method. Multiple lamellae and crystallites, which may lie in different orientations, will fall within the beam cross-section and thus XRD data can only provide an overall view of the structural properties of the sample, albeit on a significantly finer scale than DSC.

Table 2.1 shows the structural length scales of FFF Nylon-12.

2.2.1 Differential scanning calorimetry (DSC)

2.2.1.1 Basic theory

Differential scanning calorimetry (DSC) is a thermoanalytical technique in which the difference in heat flow between a given sample and an inert reference is measured as a function of temperature and time. Both the sample and reference are subjected

Dimension	Characteristic length
Sample dimensions	30 x 10 x 2.5 mm
FFF layer thickness	100 μm
Spherulite radius	$\leq$ 100 μm
Crystallite length	$\leq$ 25 μm
Lamellar thickness	10 nm
Crystalline volume fraction	10-30%

Table 2.1: Characteristic length scales for FFF Nylon-12. Sample dimensions, layer thickness and crystalline volume fraction taken from this study; other values from [94] [113].

to a controlled environment in terms of temperature and pressure. A schematic of the DSC apparatus is shown in Figure 2.1.

A metallic disc made of constantan, a copper-nickel alloy consisting of 55% copper and 45% nickel, is the primary means of heat transfer to and from the sample and reference [2]. Constantan is used as it has a very low thermal variation of resistivity whilst having a good temperature sensitivity. A thermocouple is formed by the junction of the constantan disc and a disc on its underside made from chromel, a nickel-chrome alloy consisting of approximately 90% nickel and 10% chromium by weight. This measures the heat fluxes to the sample and reference. The thermocouples measure the heat flux as follows:

$$\frac{dQ}{dt} = \frac{\Delta T}{R_D} \tag{2.1}$$

where ΔT is the temperature difference between the sample and the reference, and R_D the coefficient of thermal resistance of the constantan disc.

The underlying principle of DSC is that during the phase transitions of a sample. More or less heat will need to flow to it than the reference to maintain both at the given temperature, depending on whether the process in the sample is endothermic or exothermic, respectively. For instance, during melting, the breakdown of the bonds requires more heat flow to increase its temperature to the same level as the reference, as the sample absorbs heat.

The resultant heat flow at any point during a DSC experiment is given by

$$\frac{dQ}{dt} = C_p \frac{dT}{dt} + f(T, t) \tag{2.2}$$

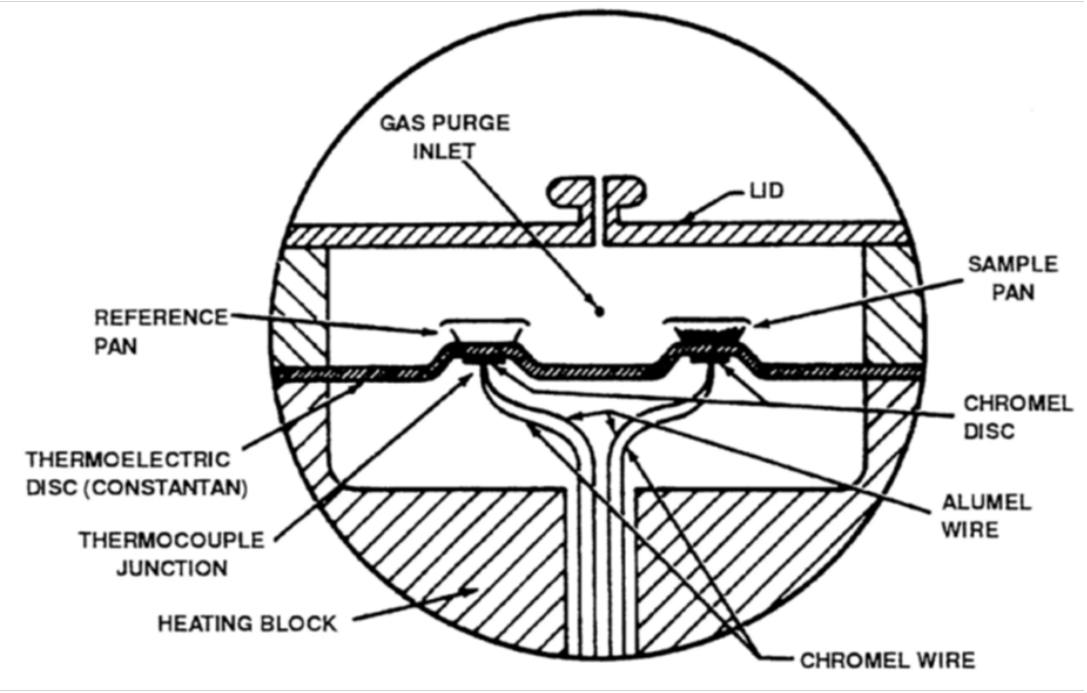


Figure 2.1: DSC schematic view: heat flux design, from the TA Instruments compendium.

where C_p is the sample specific heat capacity and $f(T,t)$ the heat flow from kinetic processes. The heat flow is therefore composed of two terms; the *reversing* heat flow and the *non-reversing* heat flow. The reversing heat flow is calculated by the determination of the heat capacity, which is determined by dividing the heat flow amplitude by the magnitude of the heating ramp.

The heat evolved during crystallisation leads to exothermic peaks in DSC, which represent the rate of heat evolution dQ/dt. The extent of crystallisation can therefore be expressed as:

$$X(t) = \frac{\int_0^t \frac{dQ}{dt} dt}{\int_0^\infty \frac{dQ}{dt} dt} \tag{2.3}$$

DSC results can be analysed according to the Avrami theory detailed in Section 1.2.5. The percentage of crystallinity in a sample is given by dividing the heat of melting (indicated on the DSC curve) by the known heat of melting for a 100% crystalline specimen.

2.2.1.2 Experimental procedure

DSC analysis was carried out under nitrogen atmosphere using Q2000 DSC apparatus (TA Instruments, DE 19720, USA).

Three principal experimental methods were used during the course of this thesis:

1. **Thermal cycling**: the sample is heated to melt, cooled and reheated at constant rate.

2. **Isothermal crystallisation**: the sample is heated to melt before being cooled rapidly to a set T_c and subsequently reheated.

3. **Non-isothermal crystallisation**: the sample is heated to melt before being cooled back to room temperature at a constant rate Φ, and is subsequently reheated.

For thermal cycling, a small amount of Nylon-12 was placed in the DSC pan and heated to 230 °C at a ramp rate of 10 °C/min, held there for 5 minutes to eliminate residual crystals and ensure full melting, and then cooled back to 25 °C at a ramp rate of 10 °C/min. This procedure was selected so as to be consistent with DSC analysis performed in polymer analysis literature.

The isothermal crystallisation process was performed as follows: samples were heated at 10 °C/min to 230 °C, held for 5 minutes, then cooled at 60 °C/min to the designated crystallisation temperature (T_c) in the range of 120-170 °C for isothermal crystallisation for 60 minutes. The samples were subsequently heated to 230 °C at 10 °C/min so that the melting endotherms could be obtained and the effect of isothermal crystallisation temperature on crystal structure could be ascertained. The thermal profile of the tests is shown in Figure 2.2.

Non-isothermal crystallisation experiments were performed as follows: filament feedstock was heated at 10 °C/min to 230 °C and held for 5 minutes to eliminate residual crystals. Then, the melt was cooled at different cooling rates: 2, 5, 10, 20 and 40 °C/min to 40 °C before being heated to 230 °C at 10 °C/min. The exothermic curves of heat flow as a function of time and temperature were recorded

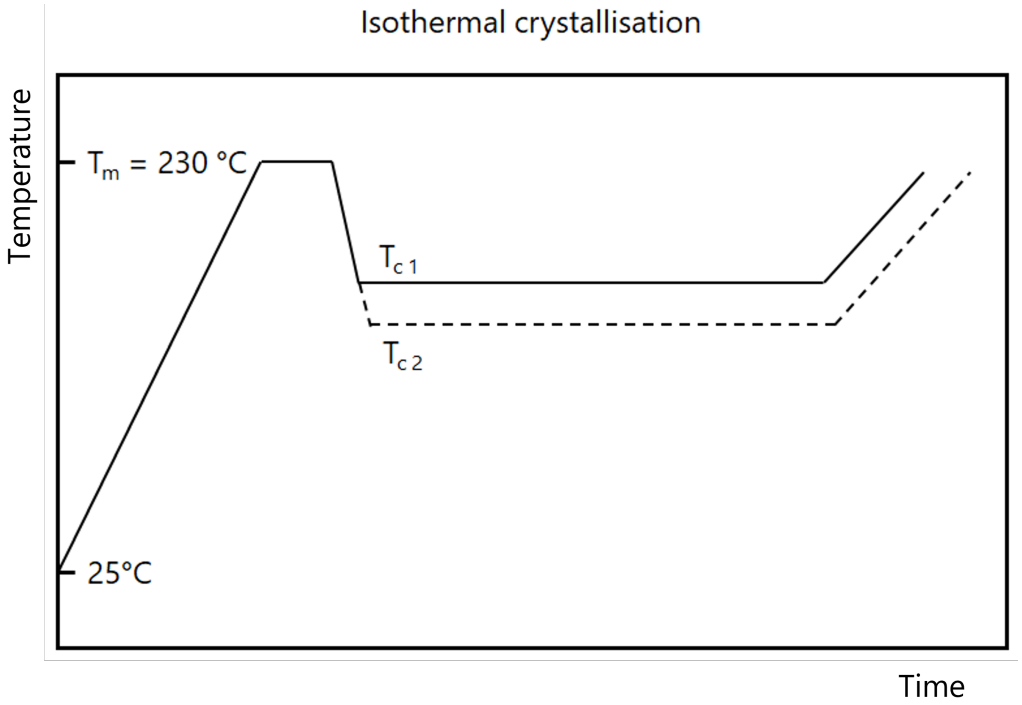


Figure 2.2: Schematic temperature programme used in isothermal crystallisation DSC measurements. T_c symbolises the isothermal crystallisation temperature.

and investigated. The thermal profile of the tests is shown in Figure 2.3. This range of temperatures was selected to be consistent with non-isothermal studies in the literature on SLS- and FFF-produced polymer samples. Although samples may undergo faster cooling rates during FFF, 40 °C/min was found to be the fastest cooling rate at which reliable data could be obtained from the DSC apparatus.

The isothermal and non-isothermal crystallisation procedures were designed to be in line with the TA Instruments standard procedure for isothermal and non-isothermal crystallisation as well as other DSC experiments performed in the literature [16, 114].

2.2.2 X-ray diffraction (XRD)

Synchrotron wide-angle X-ray scattering (WAXS) was used to characterise the crystalline structure and to calculate the degree of crystallinity of the Nylon-12 samples.

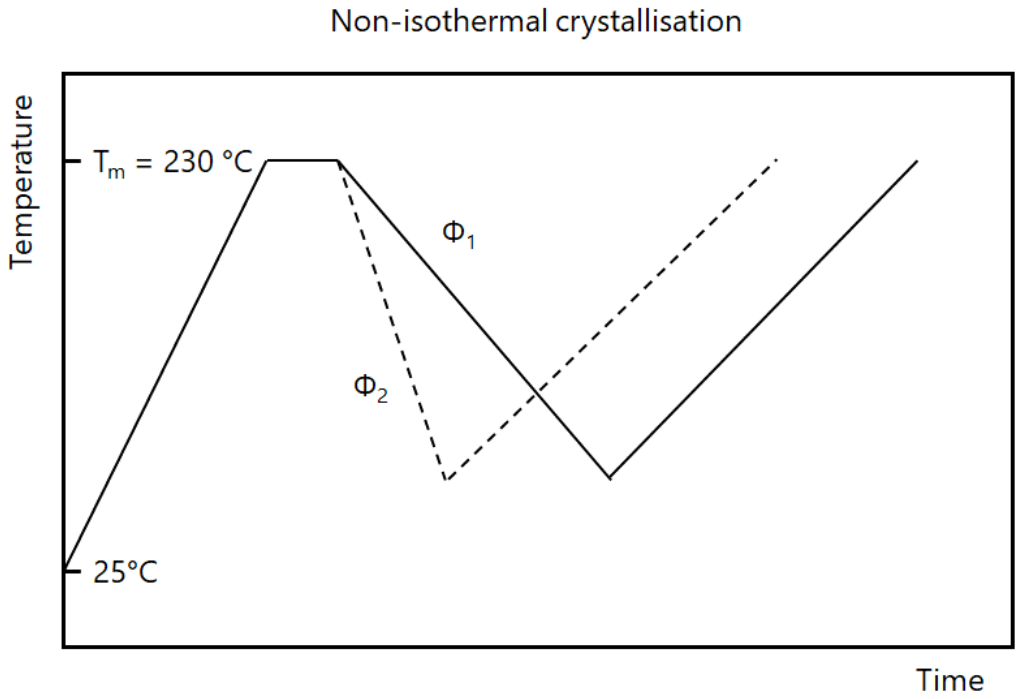


Figure 2.3: Schematic temperature programme used in non-isothermal crystallisation DSC measurements. Φ symbolises the cooling rate.

2.2.2.1 Basic theory

Incident X-rays on a crystalline solid produce intense peaks of scattered radiation. This can be explained at the basic level by modelling the crystalline component of the solid as a set of discrete parallel planes separated by a constant distance d. The path difference between two waves undergoing interference is given by $2d\sin\theta$, where θ is the angle between the diffracting plane, on the one hand, and the incident and scattered beams. The geometry of diffraction from a crystal is illustrated in Figure 2.4.

Based on the obtained patterns, therefore, the crystal structure of a material can be calculated using the relation

$$n\lambda = 2d\sin\theta \tag{2.4}$$

This is known as the Bragg condition. In polymers, the crystalline regions form a regular lattice due to the periodicity of the polymer unit cell within spherulite

lamellae. The process of diffraction from a polycrystal produces cones with semi-angles of 2θ corresponding to different families of crystal planes. If a two-dimensional detector is placed perpendicular to the incident X-ray beam, then diffraction patterns are formed that are known as Debye-Scherrer rings. From the scattering angle θ of the observed diffraction patterns, the respective lattice parameter d is obtained. In a semi-crystalline polymer, periodicity may be observed due to regions of parallel chains within a lamella, in which case d refers to the dimensions of the polymer unit cell, or due to stacks of lamellae, in which case d refers to the lamellar spacing. The amorphous region, consisting of tangled polymer chains, has minimal periodicity and therefore the incident X-rays are scattered over a broad range of 2θ forming an amorphous halo which is not present in purely crystalline samples. This is demonstrated in Figure 2.5.

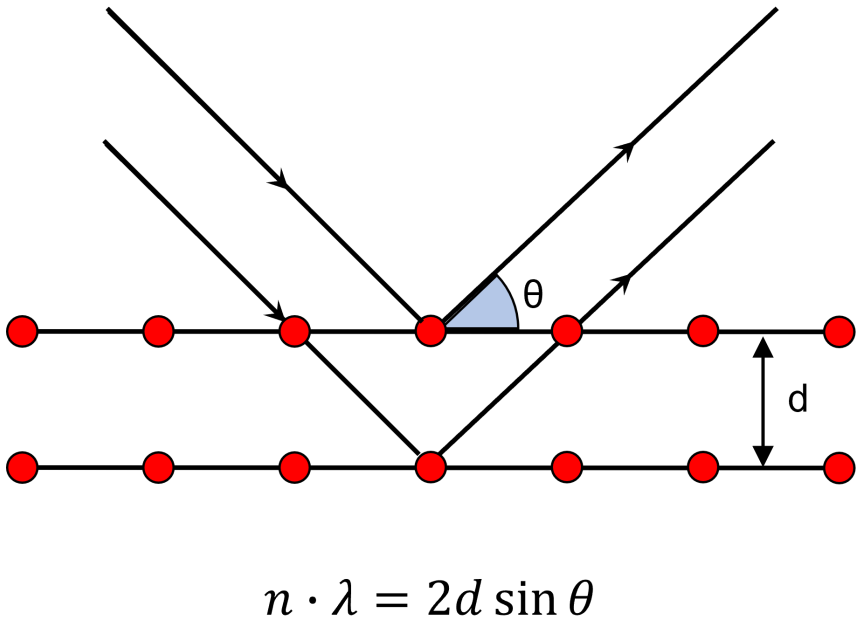


Figure 2.4: Schematic of the X-ray diffraction process, demonstrating Bragg's Law.

The degree of crystallinity X_c of a semi-crystalline sample can be calculated as a function of scattering intensities, whereby:

$$X_c = \frac{I_C}{I_A + I_C} \tag{2.5}$$

where I_A and I_C are the amorphous and crystalline scattering intensities respectively and are calculated as being the area under the amorphous halo and crystalline Debye-Scherrer peaks respectively.

2.2.2.2 Experimental procedure

In situ WAXS experiments were carried out on beamline B16 at Diamond Light Source Synchrotron (Harwell Campus, UK). ImageStar 2D diffraction detector (Photonic Science Ltd., Hastings, UK) was used to register the scattering patterns from the X-ray beam. The experiments used wavelengths and sample-detector distance of 0.8277 Å (15 keV) and 170 mm respectively for the first session in 2019, and 0.6898 Å (18 keV) and 110 mm respectively for the second session in 2020. During the first session diffraction patterns for filament and previously-printed Nylon-12 samples were obtained, while *in situ* isothermal crystallisation and mechanical testing were carried out in the second session as a result of data gathered in the first session. A collimated beam was used with a multi-layer monochromator (MLM), with slit diameter 0.2 mm.

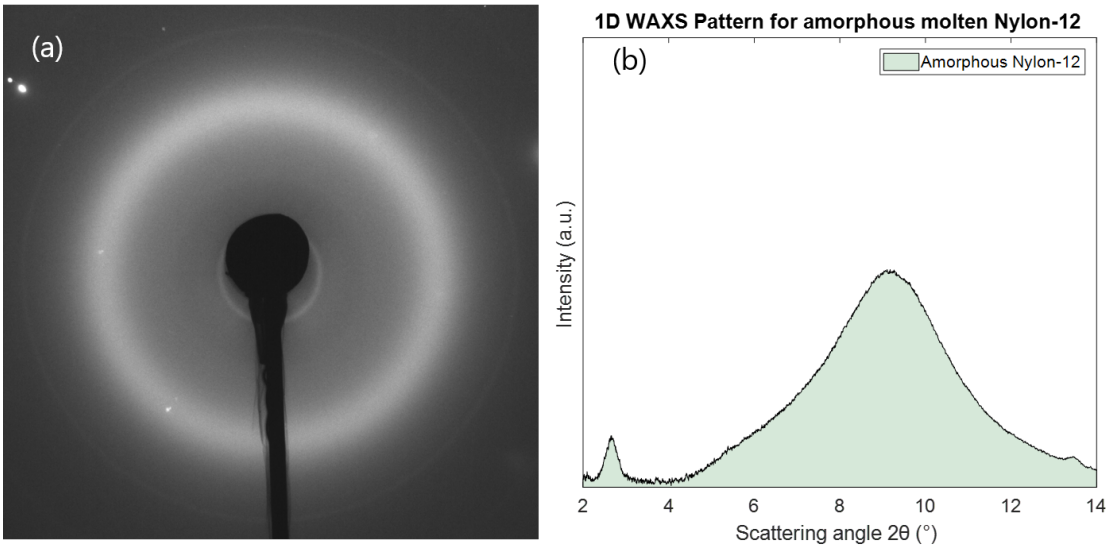


Figure 2.5: WAXS pattern of fully molten Nylon-12. With all crystalline structures having melted, the polymer is fully amorphous and a broad halo is visible.

A Linkam TS1500 furnace (Linkam Scientific, Epsom, UK) was used to heat the Nylon-12 filament from room temperature to 230 °C at a ramp rate of 10

°C/min. A custom aluminium sample holder fastened by Kapton was used to mount the samples in the furnace. Following this, the filament samples were cooled at the prescribed rates of 5, 10, 20 and 40 °C/min analogous to DSC testing. In these experiments, WAXS patterns were taken at regular temperature intervals, with the heating and cooling process being briefly paused to acquire the patterns. Nylon-12 samples produced by FFF under differing thermal conditions were also characterised *in situ* using WAXS.

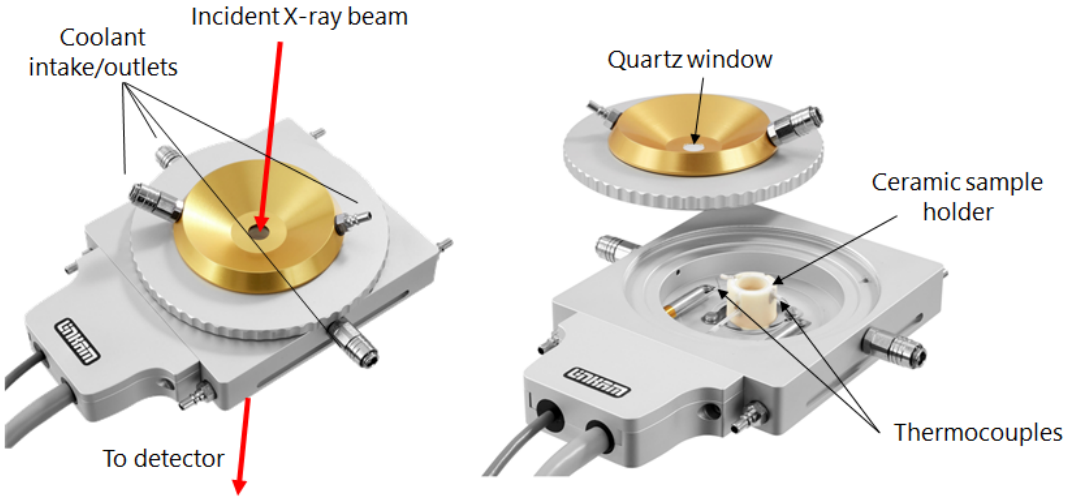


Figure 2.6: The Linkam TS1500 furnace used in the *in situ* thermal characterisation experiments.

Additionally, a small number of samples were tested to maximum extension *in situ* during the WAXS investigation using a Deben Microtest MT1000 tensile compression and horizontal bending stage (Deben Ltd., UK) with a 1kN load cell shown. The samples were stretched at 0.2 mm/min to 100% extension, with WAXS patterns being taken every 30 seconds.

The WAXS setup for the Linkam furnace and the Deben microtest are shown in Figure 2.8(a) and (b) respectively.

WAXS data were processed using DAWN Science sotware (Diamond Light Source). The pixel to angle conversion was obtained through calibration with LaB_6 sample. As the beam centre was not perfectly aligned on the beam stop, caking was carried out in the azimuthal range of -45 ° to 45 ° and in the radial range of 2 ° $< 2\theta <$ 15 ° to best capture the features of the diffraction pattern.

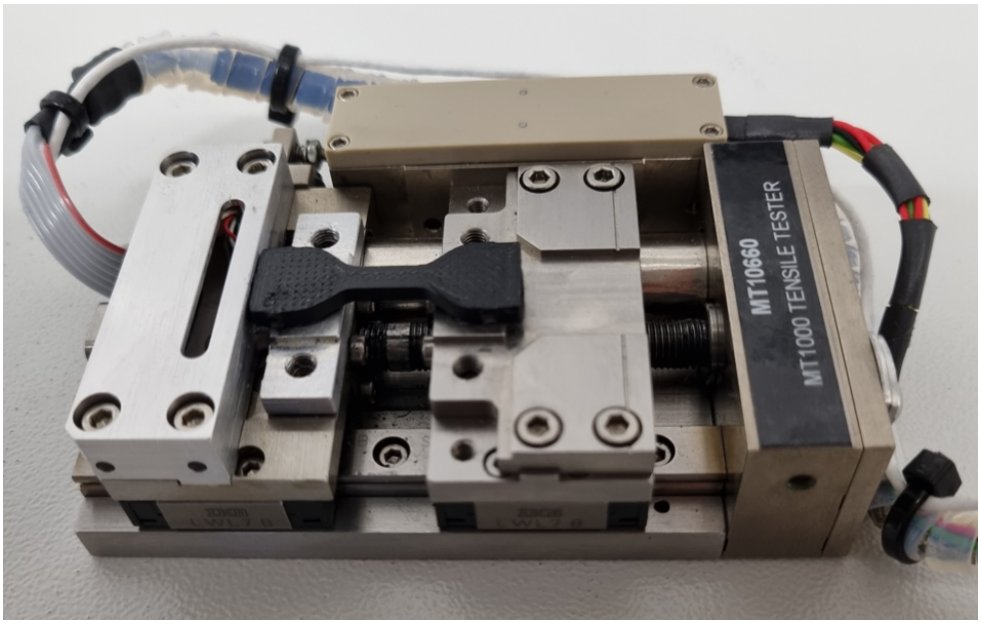


Figure 2.7: The Deben Microtest MT1000 tensile compression and horizontal bending stage used in the mechanical characterisation experiments.

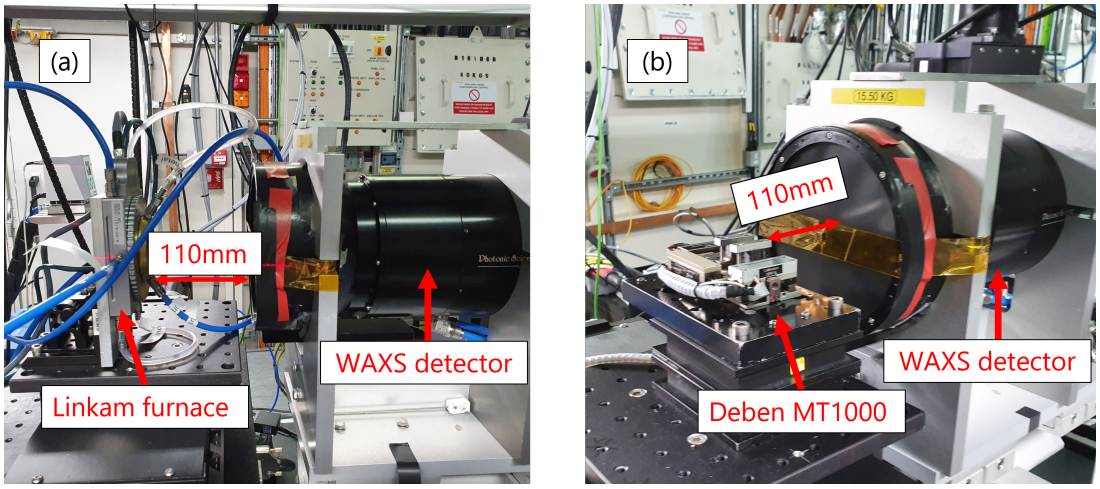


Figure 2.8: (a) shows the experimental setup for *in situ* crystallisation using the Linkam TS1500 furnace, while (b) shows the setup for *in situ* mechanical testing using the Deben MT1000 stage.

The background data was subtracted from *in situ* WAXS data, and the peaks were then fitted as follows. The amorphous halo was obtained in isolation from the WAXS patterns of fully amorphous Nylon-12, and fitted using a Voigt peak. This peak was subsequently subtracted from the data for semi-crystalline Nylon-12, the peaks of which were fitted with Lorentzian peaks. The curve fitting was performed using the *peakfit* function in MATLAB [115]. The areas of these semi-crystalline

and amorphous peaks were then computed analytically and used to calculate the degree of crystallinity of the samples as per Equation 2.5.

2.3 Mechanical characterisation

The mechanical properties of the FFF Nylon-12 samples were analysed using tensile testing.

2.3.1 Tensile testing

Tensile testing was carried out using a Deben Microtest MT1000 tensile compression and horizontal bending stage (Deben Ltd., UK) with a 1kN load cell shown in Figure 2.7. Data was acquired using proprietary stage control software. The maximum extension of the sample was 10 mm, allowing for strain ϵ of up to 1.17.

The rate of extension during the tensile testing was set to 1.0 mm/min for all samples. This rate of extension was selected to ensure good quality of data; it was found during trial tests that slower rates of extension often resulted in the load cell stopping short of full extension. The Microtest device was set to move to its maximum extension at the set rate, with the load cell recording force data at every point. The sampling time during the tensile tests was set at 500 ms. The cross-section and gauge length of the sample were measured prior to tensile testing using a Homyl Stainless Hardened digital micrometer (Homyl, China), allowing the stress σ and strain ϵ to be computed from the force and extension data.

2.4 Modelling

Thermal history was modelled using both MATLAB (MathWorks, United States) and COMSOL (COMSOL AB, Sweden).

2.4.1 Modelling of an individual filament

The modelling of the thermal history of an individual printed filament of Nylon-12 was conducted using COMSOL. Figure 2.9 shows the geometry of the filament used in the model. The cross-section of the filament was based on the printing

parameters used in the layer height of the Apium P220, which was 0.1 mm. The nozzle diameter was 0.2 mm^2; on the basis of this the filament cross-section was calculated to be consistent with this on the principle of conservation of mass.

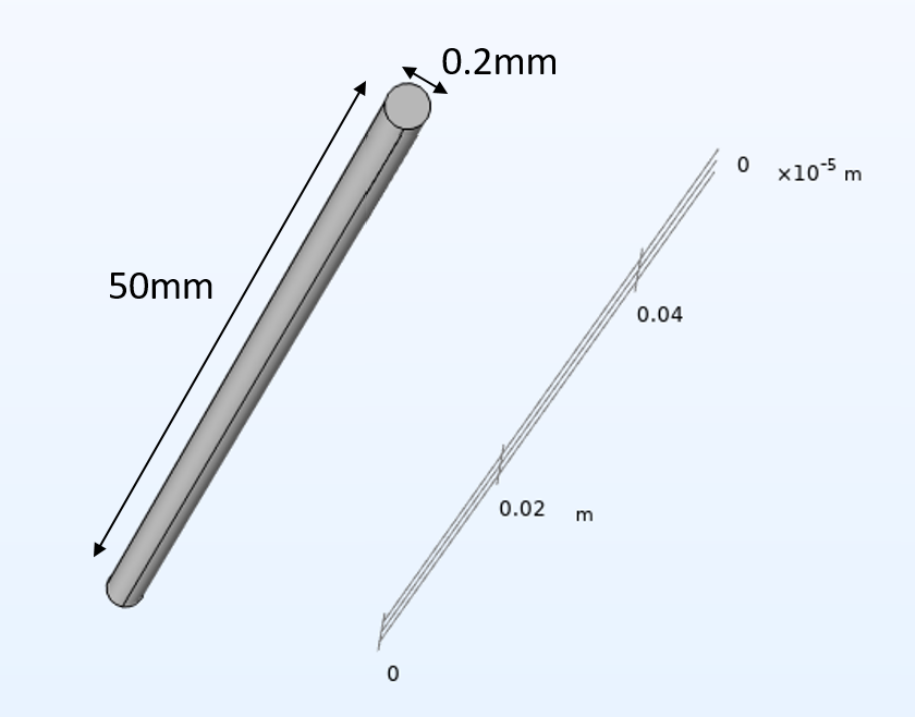


Figure 2.9: The sample geometry used in the COMSOL model for a single filament's cooling behaviour.

The filament surroundings were modelled to be consistent with those of the base settings of an Apium P220, whereby the print bed and zone heater created an ambient temperature of 120 °C surrounding the filament. The nozzle temperature was 245 °C. The nozzle velocity was taken as 360 mm/s. As a result, the nozzle was projected to have moved >100 mm from the end of the extruded filament within 300 μs. The far end of the filament was held to be still in contact with the nozzle, at 245 °C. The thermal conductivity of the bed was taken from that of glass, being 0.96 W/m^2K. The material parameters for thermal conduction and convection were taken from literature values from Nylon-12, being 200 and 75 W/m^2K respectively. These parameters are shown in Table 2.2.

The sample was meshed using a mesh of 41951 tetrahedra, with tetrahedron size 3.7×10^{-14} m^3. Heat flow within the filament was modelled as behaving according

to the 3D transient heat equation:

$$\rho c_p \frac{\partial T}{\partial t} = \frac{\partial}{\partial x}\left(k\frac{\partial T}{\partial x}\right) + \frac{\partial}{\partial y}\left(k\frac{\partial T}{\partial y}\right) + \frac{\partial}{\partial z}\left(k\frac{\partial T}{\partial z}\right) + q_v \tag{2.6}$$

where k is the thermal conductivity, ρ is the density, c_p is the specific heat capacity and q_v is the rate at which energy is generated per unit volume. Convective heat flow across the boundary of the filament was modelled according to:

$$q = hA(T - T_\infty) \tag{2.7}$$

where h is the heat transfer coefficient, and T_∞ is the ambient temperature outside the filament. The print chamber of the Apium P220, which has size 0.0048 m^3, is kept at constant temperature via controlled airflow and heating elements. Temperature is recorded and kept constant via a built-in thermocouple, exposed to the air below the zone heater 7.5 mm above the sample. On this basis, the model assumes that T_∞ remains constant throughout the cooling process.

2.4.2 Modelling of a series of contacted filaments

The modelling of a series of contacted filaments was modelled using MATLAB. The model for a system of contacted filaments was developed based on the Costa *et al.* method [116]. In this model, all filaments are subjected to the same heat transfer mechanism but with time-dependent boundary conditions. These boundary conditions will change based on part geometry and deposition sequence. The energy balance for the r^{th} filament (of N) at instantaneous time t is therefore:

Energy in at one face - heat loss by convection - heat loss by conduction = change in internal energy + energy out at opposite face.

This is expressed by Costa *et al.* as a differential equation [116]; namely the sum of the simplified forms of the conductive and convective heat equations in Equations 2.6 and 2.7:

$$\frac{\partial T}{\partial t} = -\frac{P}{\rho c_p A}\left(k\left(1 - \sum_{i=1}^{n} a_i\lambda_i\right)(T - T_\infty) + \sum_{i=1}^{n} h a_i \lambda_i (T - T_i)\right) \tag{2.8}$$

where P is the filament perimeter, A is filament cross-sectional area, n is the number of contacts with adjacent filaments, λ_i is the fraction of P in contact with an adjacent

filament and T_i is the temperature of the adjacent filament at contact i. a_i is defined as being 1 if the filament has a contact with an adjacent filament at position i, and 0 otherwise. The positions of the contact points i are shown in Figure 2.10.

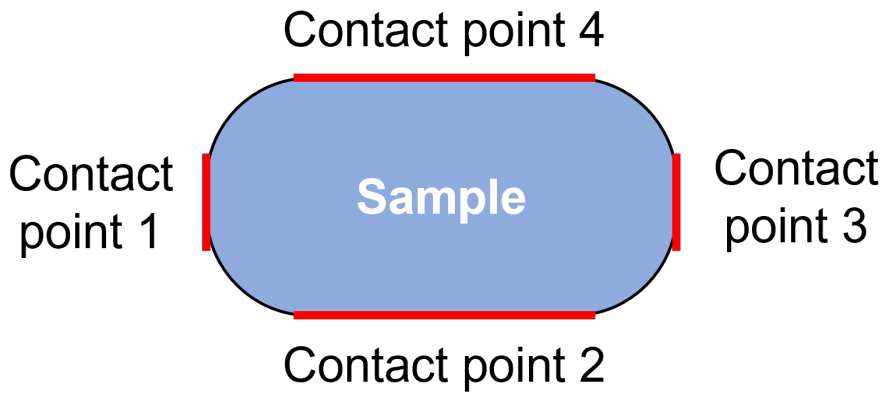


Figure 2.10: Schematic of the model's thermal contact points on the filament geometry.

Equation 2.8 holds for an amorphous polymer; however in the case of a semi-crystalline polymer a modification must be made to account for the latent heat of crystallisation during the cooling phase [117]. This is expressed by:

$$q = L\frac{A_c}{A} \tag{2.9}$$

where A_c is the area fraction transformed between times t and $t + \delta t$ and L is the latent heat of fusion of Nylon-12, given as 7000 J/kg. The development of volume fraction transformed is modelled using Hoffman-Lauritzen theory (from Section 1.2.5.3), where the crystal growth rate is given by:

$$G = G_0 e^{-\frac{U^*}{R(T-T_\infty)}} e^{-\frac{K_g}{T_c \Delta T f}} \tag{2.10}$$

where G_0 is a temperature-independent pre-exponential factor, K_g is the surface nucleation constant and f is equal to $2T/(T_m^0 + T)$ [117].

The radial growth rate of the crystal is given by:

$$\Delta r = \Delta t \cdot G_n(T) \tag{2.11}$$

such that the accumulative radius at time t is given by:

$$r_i = \sum_0^t \Delta t \cdot G_n(T) \tag{2.12}$$

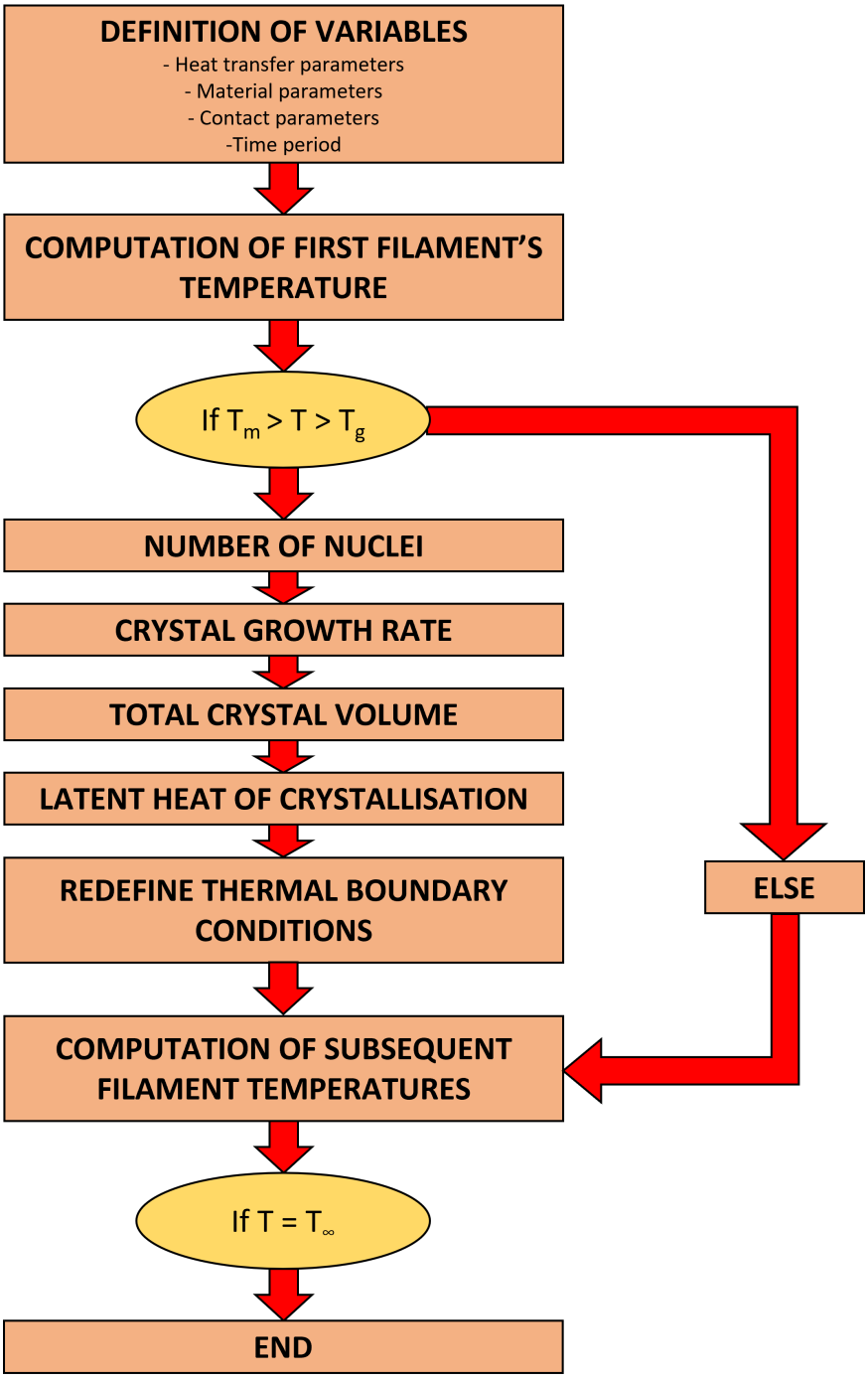


Figure 2.11: The computational procedure for modelling the temperature of the system of contacted filaments.

and the area is therefore given by:

$$A_c = \pi r_i^2 = \pi \left(\sum_0^t \Delta t \cdot G_n(T) \right)^2 \tag{2.13}$$

The number of nucleations N formed under temperature T is given by:

$$N = N_0 e^{-\frac{1/k}{T_c \Delta T}} \tag{2.14}$$

where N_0 is the final reference number of nucleation per unit volume at a specific temperature [117]. The accumulative area transformed is therefore given by:

$$A_c = \sum_0^N \pi \left(\sum_0^t \Delta t \cdot G_n(T) \right)^2 \tag{2.15}$$

The full differential equation for the contacted filament model is therefore given by:

$$\frac{\partial T}{\partial t} = -\frac{P}{\rho c_p A} \left(k \left(1 - \sum_{i=1}^{n} a_i \lambda_i \right) (T - T_\infty) + \sum_{i=1}^{n} h a_i \lambda_i (T - T_i) \right) + L \frac{A_c}{\rho c_p A^2} \tag{2.16}$$

This can be reduced to a readily soluble form using the substitution [116]:

$$b = k \left(1 - \sum_{i=1}^{n} a_i \lambda_i \right) + \sum_{i=1}^{n} h a_i \lambda_i \tag{2.17}$$

$$Q = \frac{k \left(1 - \sum_{i=1}^{n} a_i \lambda_i\right) T_\infty + \sum_{i=1}^{n} h a_i \lambda_i T_i}{b} \tag{2.18}$$

thereby reducing Equation 5.34 to:

$$\frac{\rho c_p A}{P b} \frac{\partial T}{\partial t} + T = Q + L \frac{A_c}{A} \tag{2.19}$$

yielding the characteristic polynomial solution:

$$T = (T_0 - Q) e^{-\frac{Pb}{\rho c_p A}} + Q + L \frac{A_c}{A} \tag{2.20}$$

where T_0 is the temperature of the filament at the instant at which it begins to cool down or comes into contact with another filament. In order to account for the non-zero size of the nozzle and the thermal field it generates, the temperature of the most recently deposited filament is kept at 245 °C for the time it takes the nozzle to move away from the deposition region.

Figure 2.11 shows the flow chart for the general computational procedure for evaluating the temperature of each filament at time t. All filaments are extruded from the nozzle at $T_0 = 245$ °C. After the filament temperature drops below T_m, the crystallisation process begins, and continues until the filament temperature drops below T_g according to the Hoffman-Lauritzen theory. As the temperature of the filament evolves over time, the data is gradually output. The boundary conditions are updated as more filaments are deposited, with three key variables:

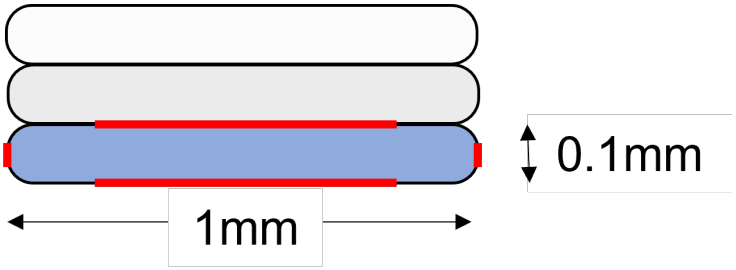


Figure 2.12: A schematic of the sample geometry used in the model.

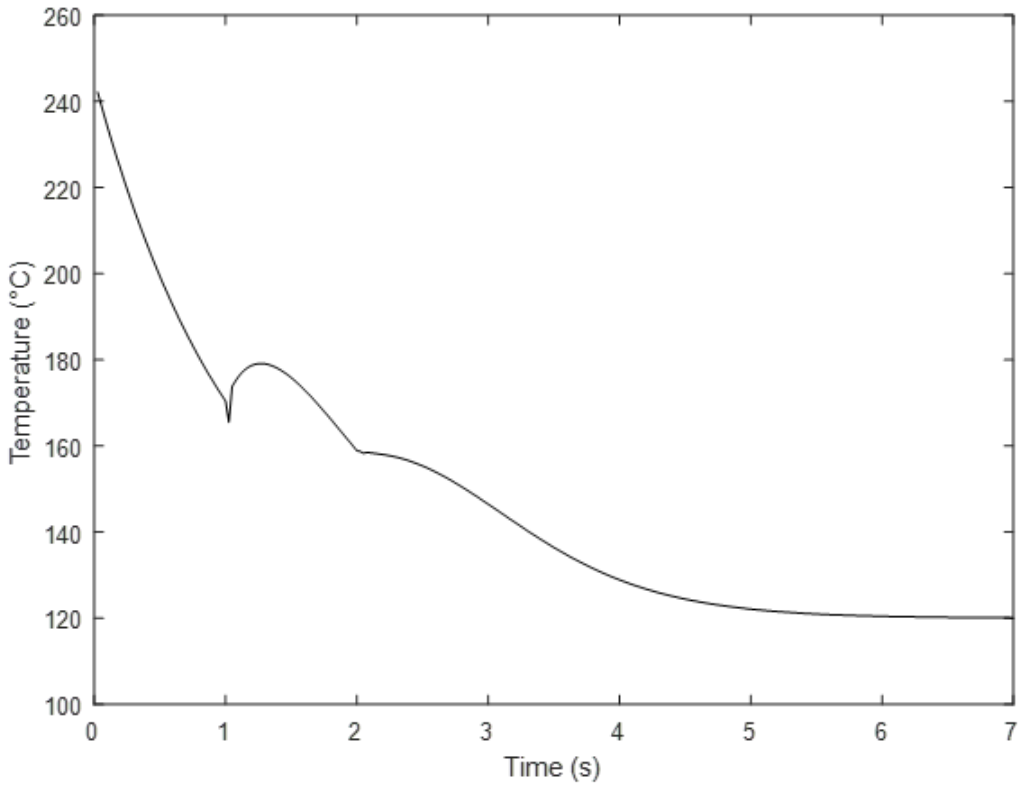


Figure 2.13: The simulated thermal history for a given cross-section in a contacted system of filaments, with $T_{\text{inf}} = 120$ °C.

1. Time t_i at which the i^{th} filament begins to cool or comes into contact with another filament;

2. Temperature T_0^i at t_i;

3. The vector a_i which sets the filament contacts.

The sample geometry is shown in Figure 2.12. Each filament is defined as being a rectangle with filleted corners in line with the layer geometry seen in a real FFF

sample. The tower geometry was chosen due to the dominance of the horizontal inter-layer cross section, meaning that the dominant inter-filament contact is in the vertical direction. The model was finally simplified into the form shown in Figure 2.12. The sample parameters used in this model are shown in Table 2.2.

2.5 Nylon-12

2.5.1 Introduction

Nylons, or polyamides, are a family of synthetic polymers that can be melt-processed into fibres, films or 3D bulk shapes. First synthesised by DuPont in 1935, Nylon was the first commercially successful synthetic thermoplastic and has found widespread use in fibre and filament form, from food packaging films to the engine compartments of modern vehicles.

Nylons are named according to the number of carbons in each monomer unit. For nylons consisting of a single monomer type, only one number suffix is used (e.g., Nylon-6). Two numbers separated by a comma (e.g., Nylon-6,6) indicate a homopolymer formed from two monomers, with the two suffixes indicating the number of carbons in each, while two numbers separated by slashes indicate a copolymer, with the number of carbons in each comonomer indicated by the suffixes.

Nylon-12, also known as polyamide 12 (PA12), is a semicrystalline engineering thermoplastic polymer with a broad range of applications. Nylon-12 has a lower concentration of amide groups than any other polyamide, and has a relatively long hydrocarbon chain length, which confers its dimensional stability and low water absorption.

Nylon-12 has low moisture absorption, high resistance to chemical wear and high impact strength. Its industrial uses therefore include precision parts such as gears, bearings and bespoke screws, housings and watertight applications such as covering cables and oil resistant tubes, and structural parts which include thin walls. It has also found use in the food industry where it is used as films for packing, as well as in sterilised bags in the medical industry.

Nylon-12 is also one of the most commonly used advanced semicrystalline polymeric materials used in FFF. It is readily available in filament form, easy to process and has the lowest melting temperature among the principal nylons, as well as a high strength and stiffness. In particular, it was selected for this study due to its specific thermal behaviour, which is characterized by a relatively large temperature interval between the start of melting, typically at 190 °C, and the start of crystallisation, between 160 and 170 °C [118]. This allows the material to be maintained at an elevated temperature after the melting of the filament during extrusion, which minimises material warping.

Nylon-12 has seen considerable previous study in terms of characterisation of its crystal structure and mechanical behaviour [113, 119–122], however this has not been in the context of FFF. Conversely, Nylon-12 has seen renewed interest in the context of selective laser sintering (SLS), whereby recent studies have focused on its behaviour in powder form and under sintering conditions [16, 64, 65, 94, 95, 123]. Despite its widespread use both in wider industry and in FFF, there has been comparatively little focus on Nylon-12 in filament form and in the context of FFF. This gap in the literature has provided motivation for the selection of Nylon-12 as the material of focus for this study.

2.5.2 Structural properties

Nylon-12 has the formula $[(CH_2)_{11}C(O)NH]_n$, with its repeating unit shown in Figure 2.14. Depending on the processing conditions, Nylon-12 shows a complex

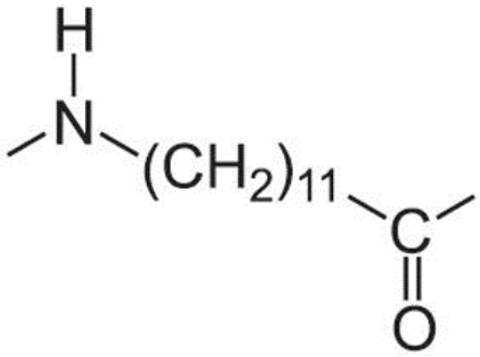


Figure 2.14: The basic repeating unit of Nylon-12. From Essential Chemical Industry

polymorphism, whereby the $\gamma-$, $\gamma'-$ and $\alpha-$ forms can be obtained. The most stable form of Nylon-12, obtained by slow cooling from the melt at atmospheric pressure, is the $\gamma-$form, which is characterised by a pseudohexagonal unit cell. The unit cell of the $\gamma-$form is shown in Figure 2.15 [120]. The $\gamma'-$form consists of smaller crystals of the same structure as the $\gamma-$form with many defects and transforms into the $\gamma-$form on annealing.

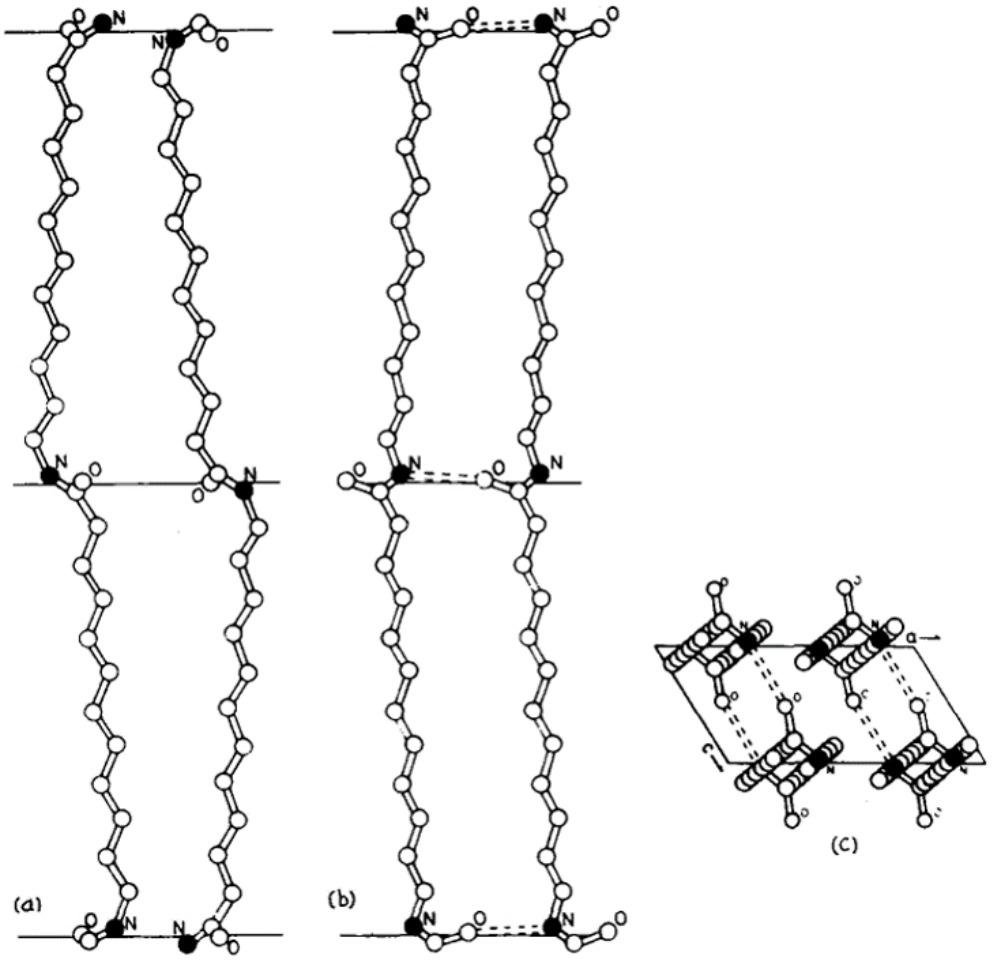


Figure 2.15: Unit cell of $\gamma-$ form Nylon-12. (a) is the projection on the ab plane, (b) on the plane perpendicular to the $a-$axis and (c) on the ac plane. The apparently differing angles between bonds in the backbone chain between (a) and (b) is a result of these projections. [120]

The $\gamma-$form unit cell dimensions were calculated by Inoue and Hoshino [120] as having $a = 9.33$Å, $b = 16.88$Å, $c = 4.78$Å. The $\alpha-$form, which can only be obtained under specific conditions such as high-pressure crystallisation, has a monoclinic

structure. Fast quenching from the melt leads to formation of a mesomorphic melt that irreversibly transforms into $\gamma-$form upon annealing [119]. The transformation behaviour of Nylon-12 is schematically summarised in Figure 2.16.

Studies into the crystal structure of Nylon-12 have concluded that the $\gamma-$form consists mainly of a planar zigzag chain conformation in which the $CONH_2$ groups are tilted and the CH_2 groups are arranged in the planar zigzag fashion. In this structure hydrogen bonds can exist between parallel running chains. The bond angle in the polymer chain remains constant, however there may be a degree of tilting in the individual amide groups [120]. When the tilting angle is varied, it results in a variation of the chain length such that a decrease in tilting angle results in a shorter chain length.

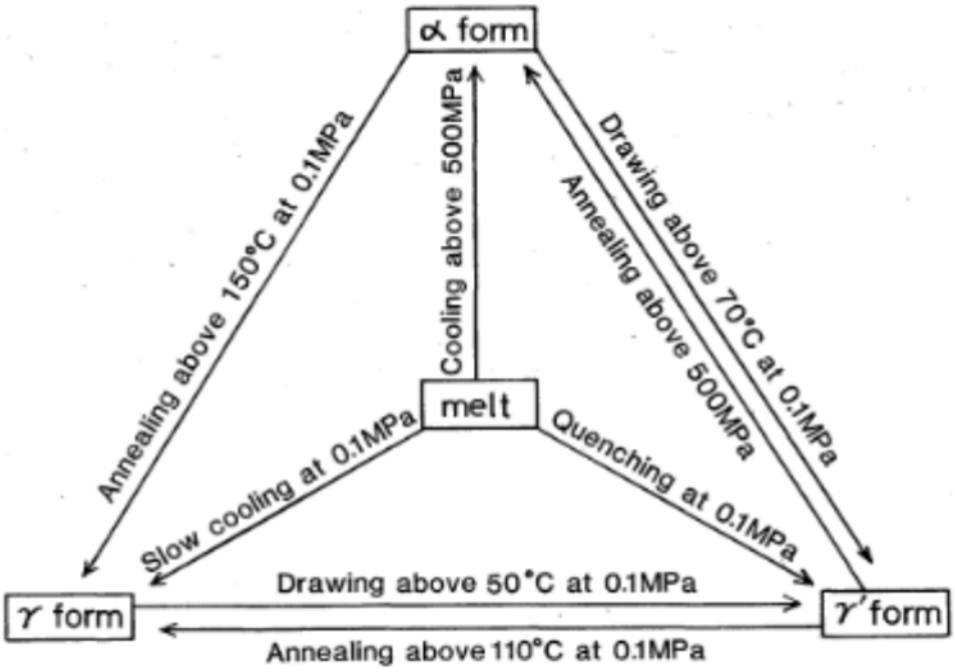


Figure 2.16: Summary of transformation behaviours of Nylon-12 [119]

During the FFF process, the melted extruded filament experiences rapid cooling according to the temperature of its surroundings, before being repeatedly reheated by the deposition of subsequent layers. Following the completion of the build process, the completed sample is cooled to room temperature. The low pressure

and temperature environment of AM processes mean that the molten Nylon-12 tends to crystallise into the $\gamma-$form.

2.5.2.1 WAXS studies on Nylon-12

The crystalline structure of Nylon-12 has been investigated by wide-angle X-ray scattering (WAXS) experiments [113, 121–124]. Wide-angle X-ray scattering (WAXS) studies of Nylon-12 polymorphs show that the $\alpha-$form, produced by cooling from the melt at high pressure, tends to have two strong reflections at 3.7 and 4.4 Å respectively [122]. By contrast, the $\gamma-$form tends to have only one strong reflection corresponding to a spacing of about 4.2 Å, which is due to the repeating unit cell along the *c*-axis. This corresponds to the lamellar spacing.

A sample WAXS pattern of a Nylon-12 sample used in this study is shown in Figure 2.17. A single reflection at 4.2 Å is shown, indicating that this is the $\gamma-$form and that the data in this study is consistent with literature data. In addition to these principal reflections, studies in the literature have shown that other reflections in the $\gamma-$form may appear depending on processing conditions. Ishikawa and Nagai [122] studied the behaviour of Nylon-12 under high-temperature drawing, and noted that further reflections attributable to the $\gamma-$form at 7.2 Å and 12.7 Å appeared. In addition, Ishikawa *et al* [121] further observed the presence of a second principal reflection of the $\gamma-$form in drawn Nylon-12.

Figure 2.18 shows a sample WAXS pattern of an FFF-produced Nylon-12 sample used in this study, with some of these additional reflections visible. These reflections have been indexed according to the unit cell dimensions of Nylon-12. The physical origin of these additional reflections and physical meaning of the Miller indices will be further discussed in Chapter 3. The inner principal $\gamma-$form reflection shown in Figure 2.18 is the 200 reflection at 4.2 Å, as per Figure 2.17. Based on previous literature studies and position of the reflection, the outer principal $\gamma-$form reflection is indexed as being due to the $001(+20\bar{1})$ plane. The lower intensity inner reflections at 7.2 Å and 12.7 Å are indexed as being due to the 040 and 020 reflections respectively.

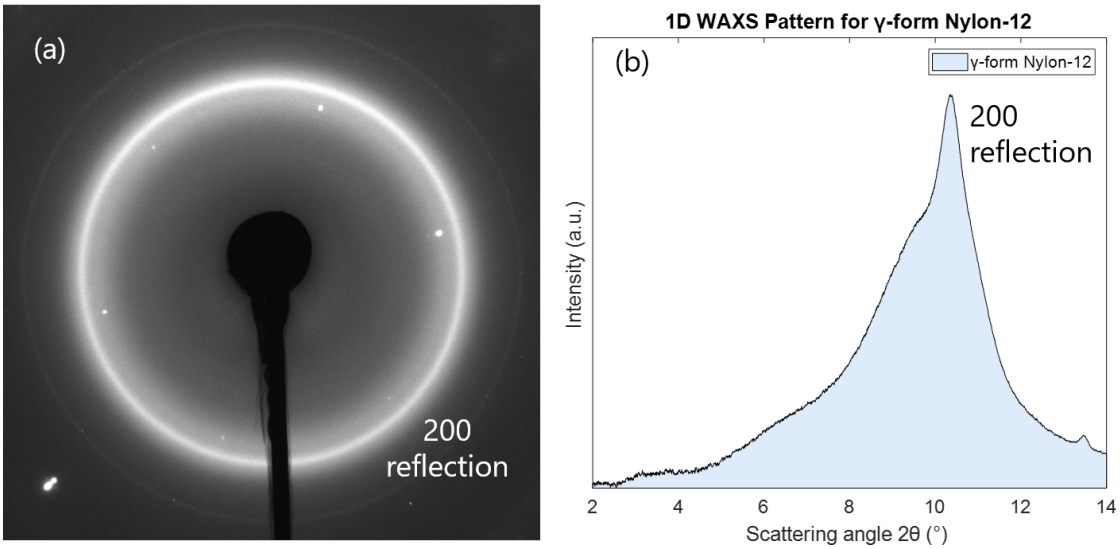


Figure 2.17: The standard $\gamma-$form WAXS pattern. The 200 reflection is visible, with a surrounding amorphous halo. The white dots resembling Bragg peaks are due to background data.

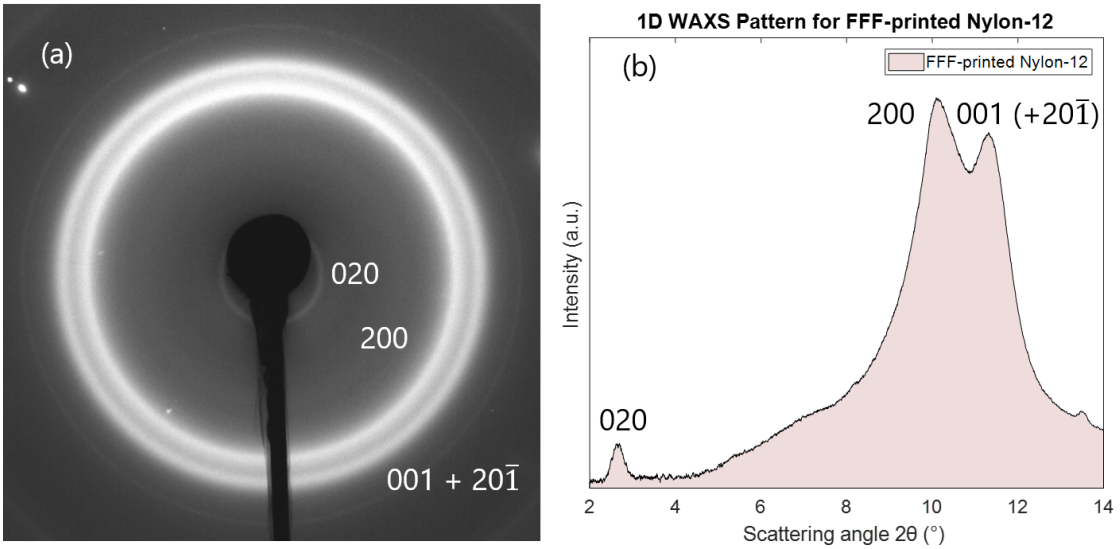


Figure 2.18: The non-standard $\gamma-$form WAXS pattern. In addition to the 200 reflection, an additional reflection attributable to the 001(+20$\bar{1}$) plane is visible.

2.5.2.2 Spherulitic structure

Various authors have studied the spherulitic structure of Nylon-12 obtained under a variety of processing conditions. Plummer *et al* [125] and Paolucci *et al* [124] used hot stage microscopy to observe spherulite formation under isothermal crystallisation conditions. Spherulites were found to nucleate with a relatively low density, growing

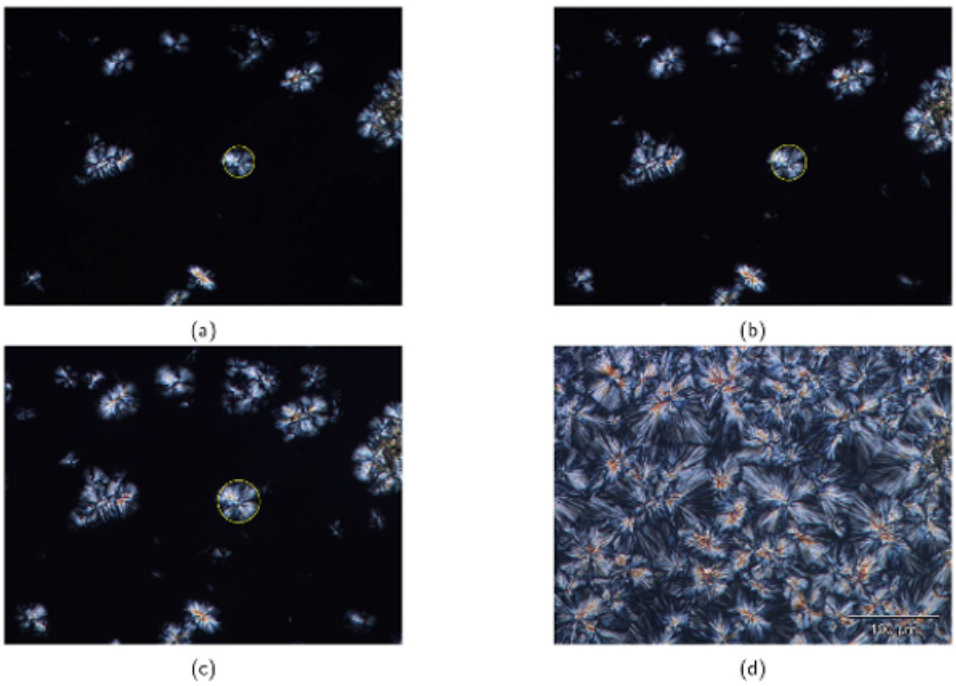


Figure 2.19: Optical microscopy images acquired during isothermal crystallisation at 175 °C of Nylon-12 (20× magnification). Panel (a), (b) and (c) show the growth in space and time of spherulites with one spherulite highlighted with a yellow circle; panel (d) is the last frame after 4h at 175 °C. [124]

with a time-independent constant growth rate to a scale of hundreds of microns. Figure 2.19 shows a polarised optical microscopy (POM) micrograph from the isothermal crystallisation of Nylon-12 at 175 °C [124]. A typical Maltese cross structure is visible.

Further investigation into the spherulite formation and spherulitic structure of Nylon-12 was carried out in the context of selective laser sintering (SLS) [94, 118], another additive manufacturing method. The spherulite structure was observed, with fineness of lamellae being governed by powder age. In addition, Majewski *et al* [94] noted that in SLS, larger crystal structures in the print feedstock powder do not receive sufficient energy to melt completely, such that the structure of SLS parts consisted of unmelted particle cores surrounded by melted areas.

It should be noted that the spherulitic structure observed in these studies is of limited utility when considering the spherulitic structure of FFF Nylon-12 components, as the high degree of chain alignment is not taken into account.

Furthermore, the unique thermal history of FFF does not necessarily allow for the same sort of steady unconstrained crystallisation as hot stage isothermal crystallisation. Nevertheless, the presence of spherulites in the SLS parts, which also undergo only partial melting during layerwise construction, is of utility when considering the possibility of observing spherulitic structures in FFF parts.

2.5.3 Thermal properties

Nylon-12 has a relatively large interval between its melting point and the temperature of the onset of crystallisation. The basic thermal properties are shown in Table 2.2. The values for T_m and T_g are taken from the Nylon-12 used in this study, while C_p and λ are average values from the literature on Nylon-12. The exact values shown for T_m, T_c may vary between physical forms (filament, powder, etc).

Property	Symbol	Value
Density	ρ	1150 kg/m^3 [94]
Specific heat capacity	C_p	1.7 kJ/kg·K [117]
Thermal contact conductance	k	200 [116]
Convective heat transfer coefficient	h	75 [116]
Glass transition temperature	T_g	60 °C
Nozzle temperature	T_{noz}	245 °C
Diffusion activation energy	U^*	6270 J/mol
Universal gas constant	R	8.314 J/mol
Equilibrium melting temperature	T_0^m	203.7 °C
Growth rate constant	G_0	0.013 [117]
Nucleation constant	N_0	0.175 [113]
Latent heat of fusion	L	7000 J/kg [94]

Table 2.2: Thermal properties of Nylon-12.

2.5.3.1 Melting behaviour

When analysed by differential scanning calorimetry (DSC), Nylon-12 typically shows a single endothermic melting peak at around 190 °C, which corresponds to the melting point of the main crystal structure. However, the shape and position of the melting peak has been shown to change depending on the thermal history.

Studies on Nylon-12 produced through SLS [94, 118] showed that the SLS process introduced a second lower-temperature melting endotherm when samples

were heated to melt. The magnitudes of the two endotherms varied with processing conditions. A schematic illustration of these endotherms is shown in Figure 2.21. The lower temperature endotherm was proposed to originate from the the early melting of molten and crystallised spherulite chains, whilst the second peak resulted from to the aggregated polymer molecules in the core regions of spherulites that can remain unmolten during laser melting. In a study of the similar polyamide Nylon-1212, Liu *et al* [114] noted that isothermal crystallisation at lower temperatures resulted in the appearance of an additional peak, the presence of which was hypothesised to be due to melting of crystals with different perfection. The magnitude of the second melting peak increased as the isothermal crystallisation temperature decreased. This is demonstrated in Figure 2.20. It can therefore be seen that the differences in the crystal structures of Nylon-12 samples can be elucidated through DSC.

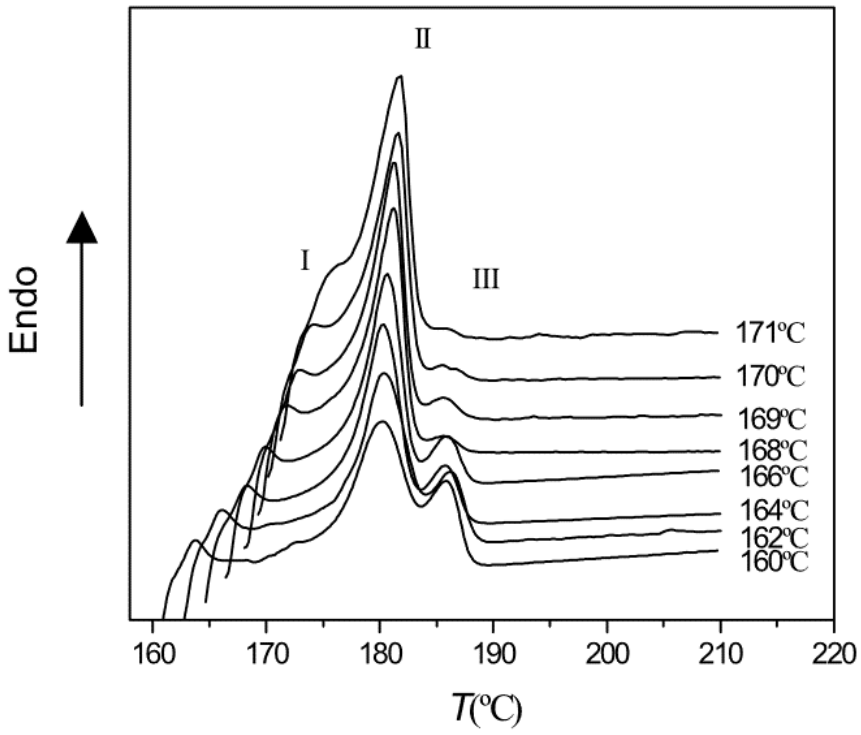


Figure 2.20: Melting endotherms of Nylon-1212, recorded at a heating rate of 10 °C/min after isothermal crystallisation at the specified temperature [114]

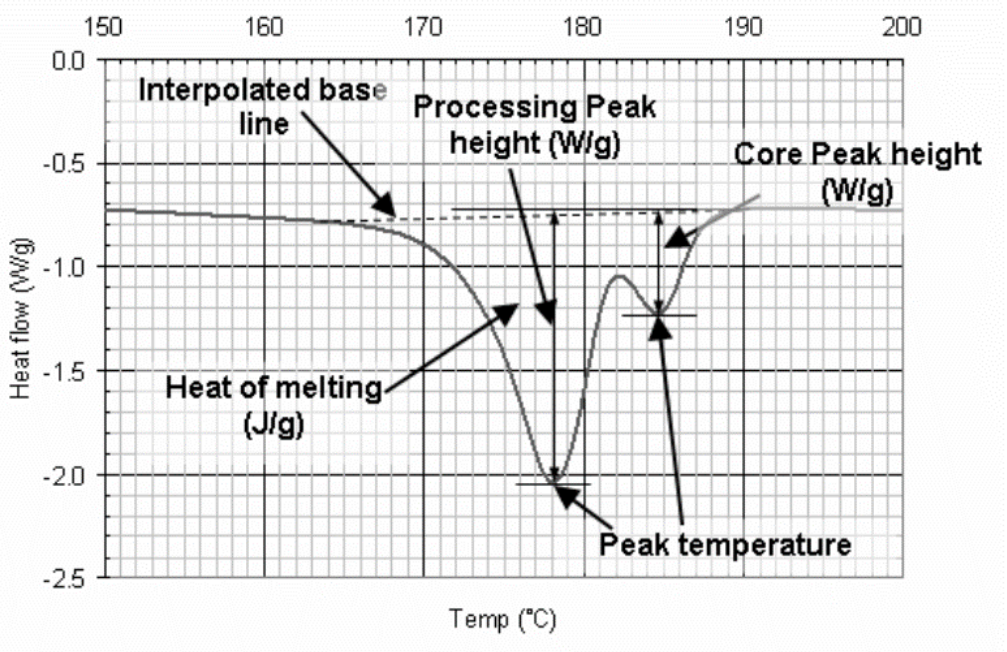


Figure 2.21: Melting endotherms of SLS Nylon-12, showing the second lower-temperature endotherm. [94]

2.5.3.2 Equilibrium melting behaviour and heat of fusion

The stable crystal of Nylon-12 follows the classical rules of crystallisation. The principal melting peak in the DSC thermogram is therefore used to determine the equilibrium melting temperature from the intersection of the melting line with the $T_m = T_c$ line as shown in Section 1.2.5 (Figure 1.7). The equilibrium melting temperature T_m^0 was reported to be 460.2 K (187 °C) by Aharoni [126] and 463.2 K (190 °C) by Plummer *et al* [125].

The heat of fusion of a pure crystal of Nylon-12 was reported by Gogolewski *et al* [127] to be 209.3 J/g. The degree of crystallinity can be computed from the DSC traces via dividing the area under the melting endotherm by this figure.

2.5.3.3 Crystallisation behaviour

The typical range of crystallisation of Nylon-12 is 160-170 °C. The rate of crystallisation increases as the temperature of crystallisation T_c decreases, with the exothermic crystallisation peak changing position depending on T_c. The exothermic peak also alters its shape and position depending upon cooling rate, such that a

slower cooling rate results in a smaller higher temperature peak. This is shown by Zhao *et al* [16] and is illustrated in Figure 2.22.

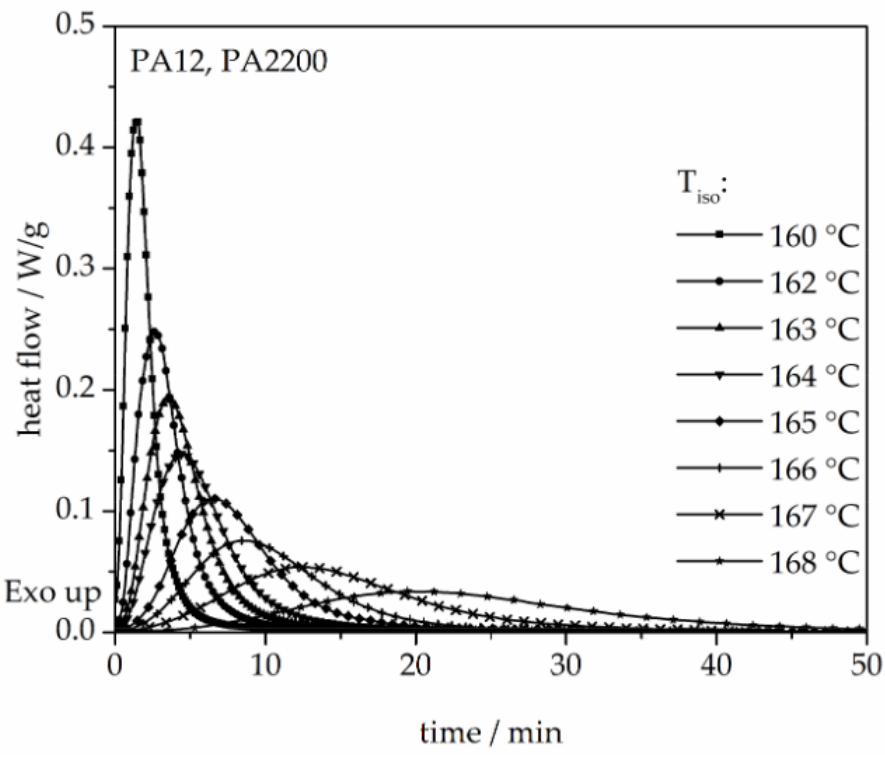


Figure 2.22: Heat flow vs time during isothermal crystallisation of PA12 at different temperatures by DSC. [16]

The Avrami constant (Avrami exponent) n introduced in Section 1.2.5 was calculated by several authors [16, 128]. Values ranging from 2.24 at 148 °C [128] to 2.71 at 160 °C to 2.94 at 170 ° were obtained. Most authors obtain values between 2.0 and 3.0 in the typical crystallisation range, indicating that the crystallisation process is characterised by 1-2 dimensional spherulitic growth and heterogeneous nucleation. Nevertheless, as an outcome of the present study it was reported by de Jager *et al* [129] that at $T_c < 150$°C the values of n drop below 2.0.

The lamellar structure was studied using small-angle X-ray scattering (SAXS) by Li *et al* [113], who extracted correlation functions from the SAXS patterns and used these to determine the following morphological parameters. A sample SAXS correlation function is shown in Figure 2.23, along with a brief explanation as to how the morphological parameters are calculated from it. It was found that the

lamellar long period was in the range of 11-12 nm, the crystalline thickness in the range of 8 nm and the interlamellar amorphous thickness 2-4 nm. All morphological parameters were found to increase with heating during thermal cycling.

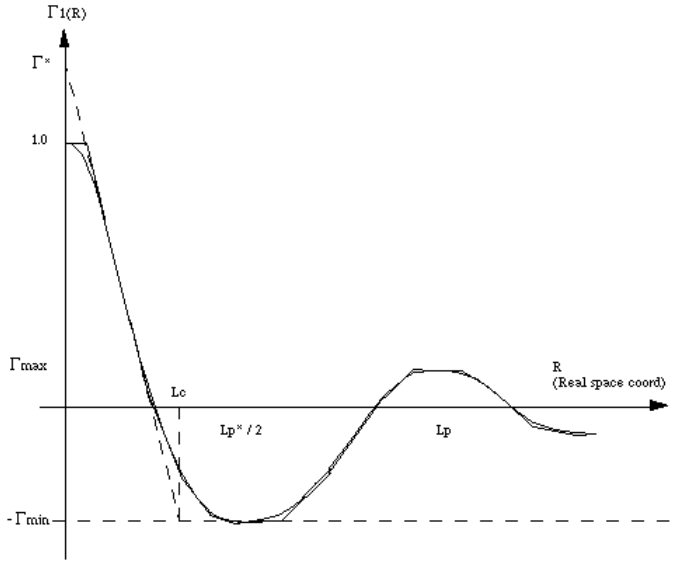


Figure 2.23: A sample correlation function extracted from a SAXS pattern, along with a brief explanation of how the morphological parameters are calculated. L_p refers to the lamellar long period and L_c to the crystalline thickness, while the interlamellar amorphous thickness is calculated as the difference between L_p and L_c.

2.6 Sample preparation

2.6.1 3D printers used

Nylon-12 filament manufactured by Breathe3DP was used to produce samples using an RS Pro Ideawerk 3D printer (RS Components, Corby, UK) and a P220 printer (Apium GmbH, Karlsruhe, Germany). The two printers are shown in Figure 2.24.

The P220 has an advanced heating system, with nozzle temperatures of up to 540 °C being attainable, and a zone heater installed in the area around the nozzle above the printing surface, which is illustrated in Figure 2.26. This allows a thin hot air film to form, which acts as a secondary means of controlling the thermal history in addition to the control of the heated print bed temperature. The print bed and zone heater can attain temperatures up to 150 °C. The nozzle diameter selected was 0.2 mm; this is the standard nozzle on a P220 and is consistent with

standard nozzle size used on FFF printers across the industry. During the printing process, the P220's heated bed moves in the z-axis, while x- and y-axis movement is performed by the nozzle and zone heater setup. The P220 was selected as it offers a higher range of nozzle, print bed and zone heater temperatures compared to many FFF machines commercially available on the market.

The P220, as an advanced manufacturing printer, has the ability to control the bed and chamber temperature to optimise the structural and mechanical properties of the printer. The RS Pro Ideawerk, as a basic model, has neither of these options with both bed and chamber temperature being set to room temperature, however was used to test the effect of rapid cooling rates on the structural and mechanical properties.

The RS Pro Ideawerk can attain a nozzle temperature up to 230 °C, with a nozzle diameter of 0.2 mm. During the printing process, z- and x-axis movement is performed by the print bed, while the nozzle moves in the y-axis only. It was selected due to its widespread availability and open air design, which makes it a useful representation for many commercially available FFF printers, which neither operate within a closed temperature-controlled chamber nor utilise a high-temperature heated bed.

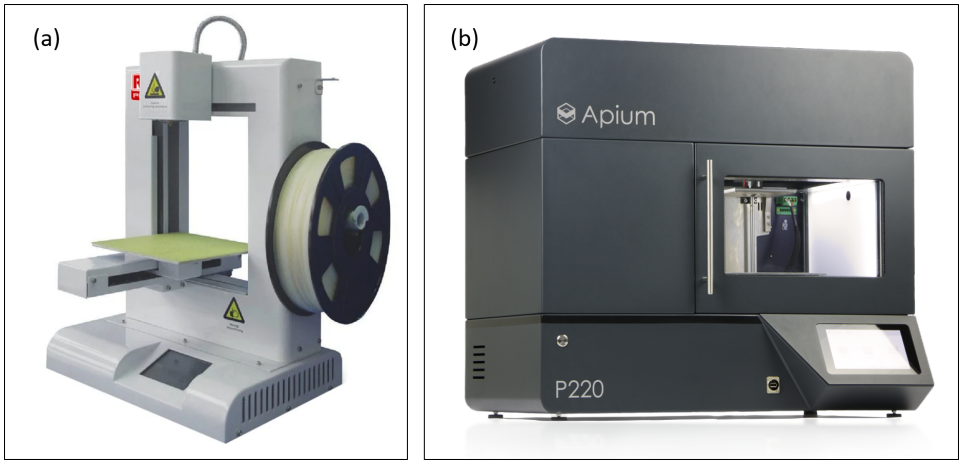


Figure 2.24: (a) shows the RS Pro Ideawerk 3D printer. (b) shows the Apium P220 3D printer.

2.6.2 Print and sample parameters

A list of key processing temperatures is presented below.

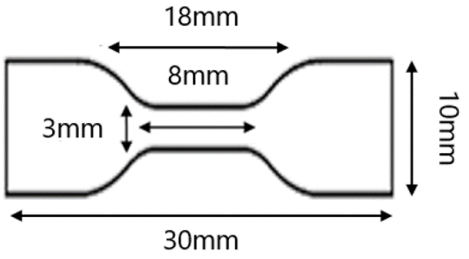


Figure 2.25: (a) shows the design of the dogbone samples used for tensile testing, created in accordance with ASTM D-638 Type IV. (b) shows the sample print orientation used to create these samples.

Print parameter	Apium P220	RS Pro Ideawerk
Nozzle temperature (°C)	230	230
Bed temperature (°C)	120	25
Chamber temperature (°C)	120	25

Table 2.3: Thermal print parameters for the two printers used.

The nozzle temperature was selected as 230 °C in line with standard FFF processing conditions for Nylon-12. The bed temperature was selected as 120 °C for consistency across samples produced and to allow a large range of post-processing temperatures to be applied to the samples. In addition, many commercially available FFF printers have bed temperatures capable of reaching 100-120 °C, and thus a value that allowed for overlap with this range was selected.

Samples were designed in SolidWorks CAD software and sliced using Simplify3D software, from which they were outputted into GCODE files. The samples were produced in a tensile dogbone design such that bulk mechanical properties and microstructure would be preserved across samples, with only the print parameters altered in any given print. The design of the dogbone used had the length 30 mm, width of 10 mm and depth 2.5 mm. The gauge length was set to 10 mm. Sample design is shown in Figure 2.25.

The infill was maintained at 100% for all samples, using a cross-hatching fill pattern. GCODE remains constant across all printers as it is output directly from Simplify3D software. An alternating ± 45 ° raster angle was chosen for the cross-hatching so that the mechanical properties were not biased towards one

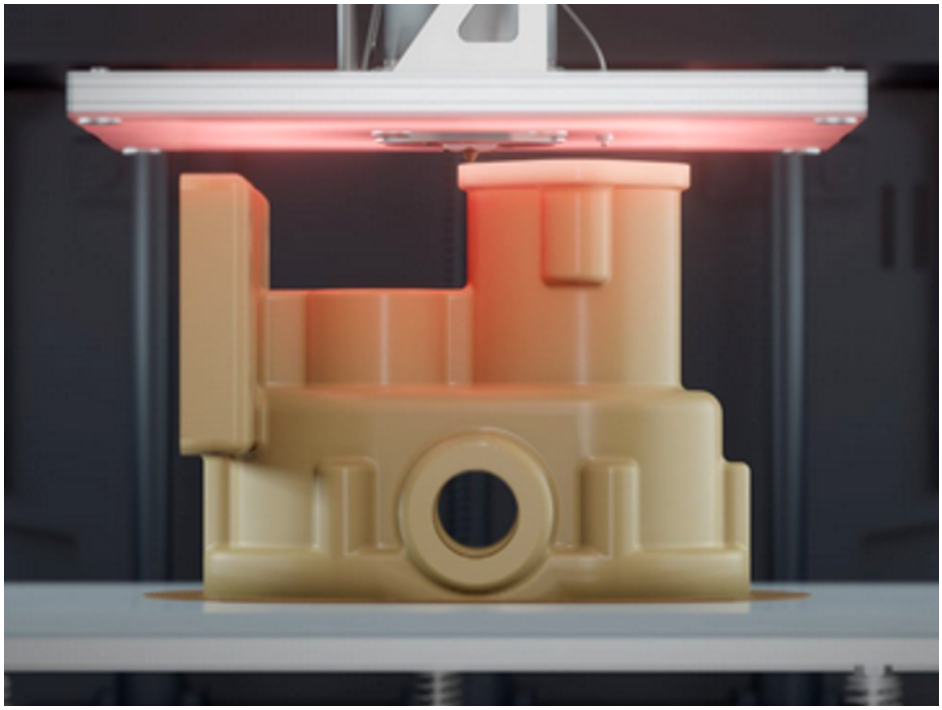


Figure 2.26: The zone heater in an Apium P220, showing the Apium Adaptive Heating System in effect.

side of the sample. A 0 or 90 ° raster angle would have resulted in bias towards either the tensile properties of a Nylon-12 fibre or the strength of the interlayer boundary respectively, rather than providing a representative result for the tensile properties of FFF Nylon-12.

A list of samples produced and the thermal conditions under which they were produced is presented at the beginning of each results section. The cooling rates, bed and chamber temperatures are varied between these prints.

3

In situ Wide-Angle X-ray Scattering of Nylon-12

Contents

3.1 Introduction 88
3.2 Results and discussion 88
3.2.1 Nylon-12 samples produced under different printing conditions 89
3.2.2 *In situ* non-isothermal crystallisation of Nylon-12 filament 96
3.2.3 *In situ* mechanical testing of Nylon-12 samples produced by FFF 103

3.1 Introduction

The results obtained from the *in situ* WAXS study of Nylon-12 are presented in this chapter. The main focus of this study was to use WAXS to elucidate the crystalline structure of FFF Nylon-12 and how it is affected by the cooling rate from the melt.

Firstly, the results of an initial study whereby samples produced under different FFF conditions were analysed via WAXS are presented. The reflections that appear are indexed and an interpretation of their physical origin is proposed. Then, the results from an *in situ* non-isothermal crystallisation study on Nylon-12 filament are presented. The evolution of the interplanar spacing d as a function of temperature as well the position and intensity of the major WAXS reflections are tracked and quantitatively analysed. The impact of different cooling rates on the formation of the crystal structure on Nylon-12 is quantitatively analysed based on this data.

Subsequently, the results from an *in situ* tensile testing study are presented. This study was performed on dogbone samples produced under different cooling conditions. Following sample build completion, the samples were either left in the printer to cool at a rate of 2 °C/min ("slow-cooled") or removed from the machine to cool rapidly to room temperature ("air-cooled"). These samples were tested using a Deben Microtest MT1000 1 kN tensile stage to ascertain their tensile properties and whether the difference in cooling rates post print affected either the crystalline structure or mechanical properties. These two samples, which represent the extremes of post-build cooling rates, were selected to ascertain whether there was a significant difference which could be further investigated with a set of parametric mechanical tests.

3.2 Results and discussion

The results are split into three sections, as follows:

1. **Section 3.2.1: Nylon-12 samples produced under different printing conditions**

2. **Section 3.2.2: *In situ* non-isothermal crystallisation of Nylon-12**

3. **Section 3.2.3: *In situ* mechanical testing of Nylon-12 samples produced by FFF**

3.2.1 Nylon-12 samples produced under different printing conditions

Samples produced under different FFF printing conditions were analysed via WAXS. These samples are listed in Table 3.1:

Sample	Production conditions
Filament	Unprocessed Nylon-12 filament
FFF RS	Printed in the RS Pro Ideawerk FFF printer with bed and chamber at 25 °C
FFF Apium	Printed in the Apium P220 FFF printer with bed and chamber at 120 °C

Table 3.1: Samples analysed via WAXS in Section 3.2.1

The differing print bed and chamber temperatures associated with the FFF RS and FFF Apium samples will have a significant effect on their respective thermal histories. The FFF RS is expected to have undergone faster cooling rates from the melt, and the sample will have remained under T_g of Nylon-12 after extrusion. The FFF Apium is expected to have undergone slower cooling rates, and spent more time above T_g. The results of previous studies on semi-crystalline polymers described in Section 1.4.2.1 indicate that differences in the crystal structure may arise as a consequence of this.

Figure 3.1 shows the 2D WAXS data from (a) the filament feedstock, (b) FFF RS and (c) FFF Apium samples, and the three overlaid 1D WAXS patterns in (d). Figure 3.1(a) shows a clear single peak at 4.57 Å surrounded by an amorphous halo. Comparison with studies in Section 2.5.3.3 suggests that this principal peak corresponds to the pseudohexagonal $\gamma-$form.

Figure 3.1(b) shows the 2D WAXS data from the Nylon-12 sample produced by the RS Pro FFF printer, which was allowed to cool to room temperature immediately on leaving the printer nozzle at 230 °C. It is observed that the single

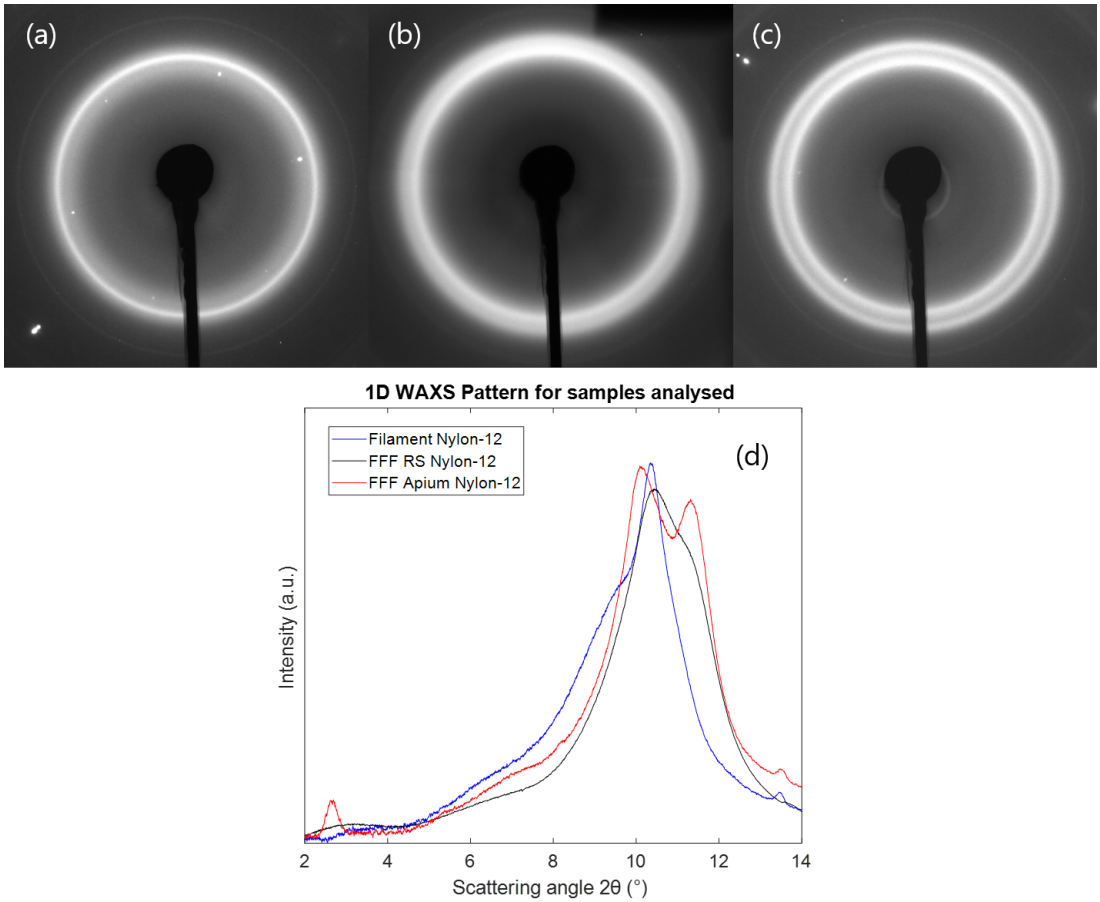


Figure 3.1: 2D WAXS patterns (a-c) and 1D line profiles (d) of the Nylon-12 samples analysed. (a) shows the filament pattern, with only the $001(+20\bar{1})$ peak visible. (b) shows the FFF RS Pro sample, consisting of a main peak with an outer shoulder; (c) shows the Apium sample with two clearly resolved peaks visible. (d) shows the 1D line profiles of these patterns overlaid. The shadowing in (b) is due to the Deben Microtest tensile stage, while the white dots resembling Bragg spots in (a) and (c) are due to background data from the Linkam furnace setup.

principal peak that was seen in the filament is now a broader peak with an outer shoulder. The principal of these two separate peaks is shifted by $2\theta = 0.42°$ from the principal peak in the feedstock data.

Figure 3.1(c) shows the 2D WAXS data from the Nylon-12 sample produced by the Apium P220 printer, which has an ambient print chamber temperature of 120 °C and subsequently gradually cools printed samples to room temperature after the process has finished. In this sample two clearly separated peaks can be observed; the principal (inner) peak at 4.74 Å corresponds to the position of the principal peak in the filament, whereas the minor (outer) peak at 4.19 Å corresponds in position to

the outer peak in the RS Pro-produced sample, as can be seen in the overlay in (d).

The peaks were fitted according to the methodology described in Section 2.2.2.2. The peak fitting is shown in Figure 3.2, in which (a) shows the fitting for the filament, (b) the FFF RS and (c) the FFF Apium. Table 3.2 shows the d-spacing associated with the fitted peaks, along with the calculated degree of crystallinity X_c for all three samples.

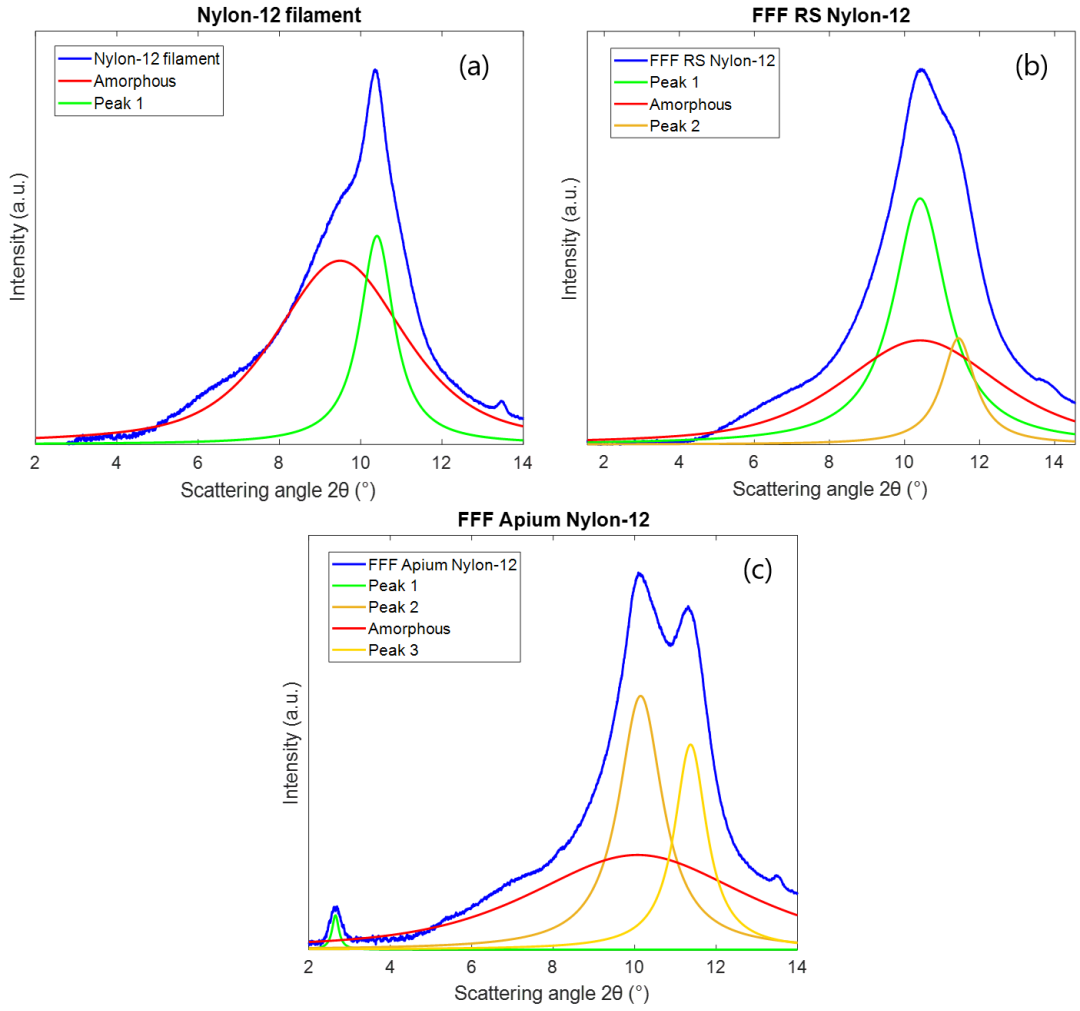


Figure 3.2: The fitting of the 1D WAXS pattens for (a) the filament, (b) the FFF RS sample and (c) the FFF Apium sample. The amorphous halo was fitted with a Voigt curve while the semi-crystalline components were fitted with Lorentzian curves.

The unit cell dimensions of Nylon-12 as indexed by Inoue and Hoshino [120] are $a = 9.33$Å, $b = 16.88$Å, $c = 4.78$Å. Prevalence of the $\gamma-$form in these samples is expected due to how the filament is produced; by being pulled through an extruder

Sample	Inner peak (Å)	Principal peak (Å)	Outer peak (Å)	X_c (%)
Filament	-	4.57	-	17.6
FFF RS	-	4.53	4.27	24.1
FFF Apium	18.05	4.69	4.19	32.1

Table 3.2: Samples analysed via WAXS in Section 3.2.1

before being cooled to room temperature in a series of water tanks. As reviewed in Section 2.5.2.1, the $\gamma-$form Nylon-12 expected to be produced under the conditions of FFF typically shows only one reflection at 4.2 Å, which has been indexed in the literature as the 200 reflection. This corresponds to a repeating structure along the $a-$axis of the unit cell, which is in the direction of the hydrogen-bonded sheets. Based on the d-spacing calculated from the WAXS data in Table 3.2, this is proposed to correspond to the outer peak in this data. Based on a comparison between the d-spacings of the principal peak in Table 3.2, the principal peak was initially proposed to correspond to alignment in the $c-$axis of the unit cell, indexed as 001.

Two principal peaks for $\gamma-$form Nylon-12 have not been widely reported in literature, however Ishikawa [121, 122] noted that two principal reflections in $\gamma-$form Nylon-12, separated by 0.2 Å appeared after uniaxial drawing at high temperatures. Ishikawa's analysis via Weissenberg photograph determined that the inner of the two principal reflections was the overlap of the 001 and $20\bar{1}$ reflections. This is in rough agreement with the proposal for the indexing of the principal peak above. These reflections identified by Ishikawa correspond respectively to alignment in the $c-$axis of the unit cell in the direction of bonding between adjacent backbone chains, and to alignment in the direction of multiple lamellar sheets. This is illustrated in Figure 3.3.

It was proposed that the findings of Ishikawa could be applied to the data above, as the extrusion process during both FFF and filament production resemble the high-temperature uniaxial drawing experienced by Ishikawa's samples. It was therefore decided that the principal peak should be indexed as $001(+20\bar{1})$.

The filament has a lower degree of crystallinity than either of the FFF-produced samples. This is in alignment with literature data on polylactic acid (PLA)

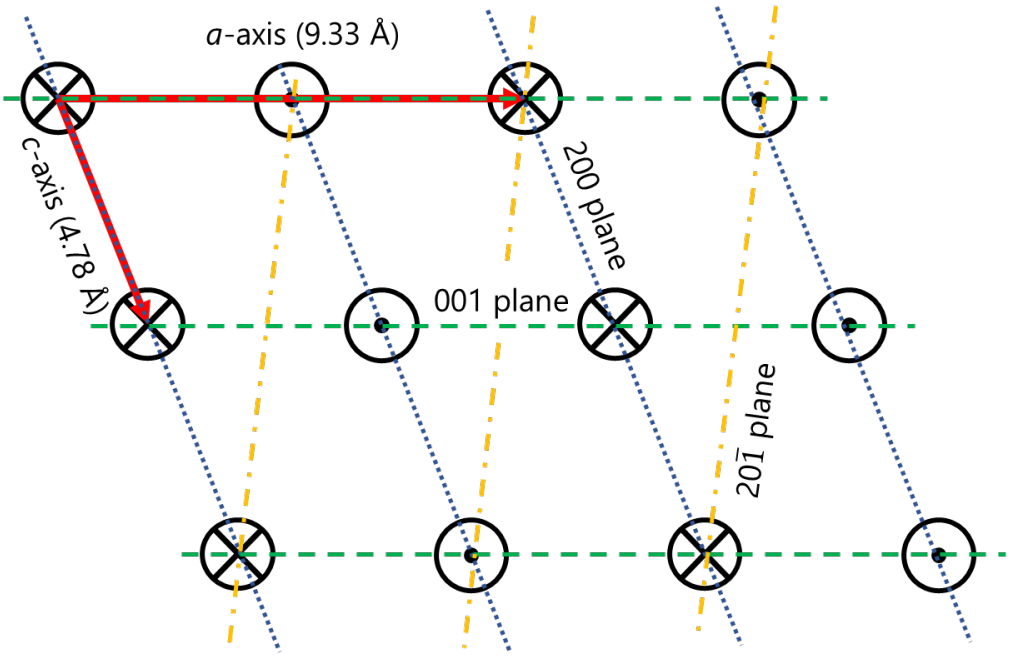


Figure 3.3: An illustration of the crystal planes in the unit cell of Nylon-12 that cause the reflections seen on the WAXS data. This illustration is in the $a-c$ plane. The b-axis, in the direction of the long backbone chains, is illustrated by the circles, where crosses and dots represent chains aligned perpendicular to each other [113, 120]. Ishikawa [121] noted that the 001 and 20$\bar{1}$ reflections overlap due to their close d-spacing; these are both illustrated.

[55–57] which noted that the repeated heating and cooling during FFF favoured the formation of crystal structure compared to the rapid quenching associated with filament production.

The data in Figure 3.1 show that all three samples display the 001(+20$\bar{1}$) reflection, but that the 200 reflection only appears in the samples that have been produced through FFF. In addition, the 001(+20$\bar{1}$) and 200 reflections overlap considerably more in the FFF RS sample (Figure 3.1(b)) than in the FFF Apium sample (Figure 3.1(c)). The 200 diffraction ring of the FFF RS sample is less sharp than that of the FFF Apium sample, and the FFF RS sample has a lower degree of crystallinity (24 % vs 32 %). It was noted by Ma *et al* on a study of cast Nylon-12 that melt-quenching resulted in a less sharp diffraction ring and a lower degree of crystallinity, caused by the freezing of molecular chains and imperfect crystallisation. The FFF Apium and FFF RS samples have undergone different thermal histories and different cooling rates during their preparation; based on

the above, it is proposed that the difference in degree of crystallinity and WAXS patterns between these two samples is caused by variations in thermal history and in particular variations in cooling rate.

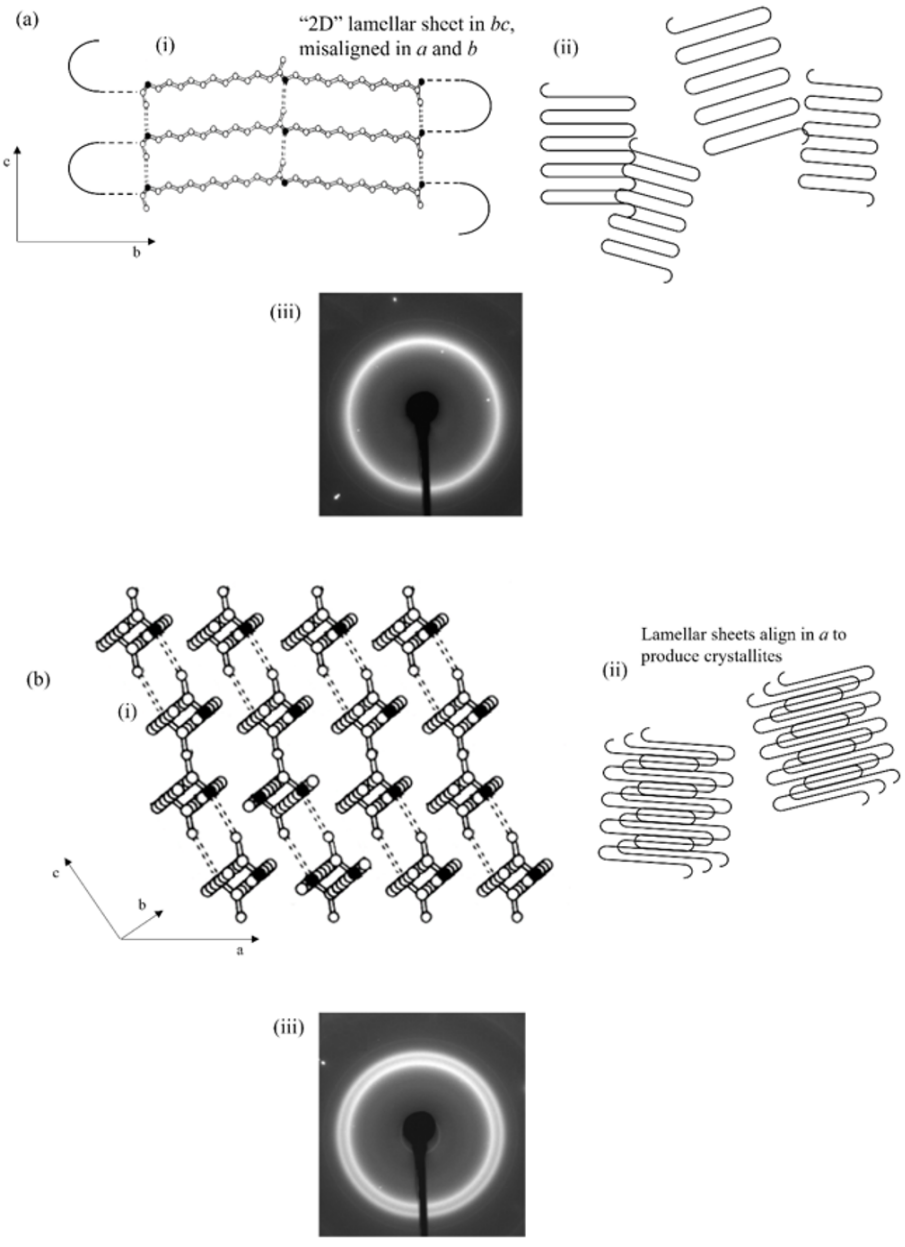


Figure 3.4: In (a), (i) shows a schematic of the lamellar sheet that is formed in the Nylon-12 filament, consisting of aligned chains bonded in the *c*-axis by H-bonds. (ii) shows the disoriented lamellae and (iii) the resulting diffraction pattern with only the single ring observed due to bulk isotropic alignment in *c*. In (b), lamellar sheets form energetically favourable planes along the *a*-axis, leading to a more complete unit cell and causing the emergence of the 200 diffraction ring. (i) shows the unit cell in full lamellar form, (ii) the crystallites formed as a result and (iii) the resulting diffraction pattern.

The appearance of the 200 reflection only in the FFF-produced samples demonstrates that the FFF process has a clear effect on the crystalline structure of filament Nylon-12. In particular, the emergence of a second diffraction ring after melting demonstrates a realignment of the crystalline structure. It is proposed that this alteration in the Nylon-12 WAXS pattern post-melt is the result of bulk isotropic alignment and realignment of the unit cell.

The unit cell of Nylon-12 depicted in Figure 2.15 shows that its structure is formed of parallel polymer chains with H-bonds between the N and O atoms. These H-bonded chains form a sheet; the arrangement of these sheets in a 3D structure forms the full unit cell. The H-bonds between chains exist along the c-axis. In Figure 3.1(a), a single diffraction ring with d-spacing 4.34 Å corresponding to the $001(+20\bar{1})$ reflection is observed; this corresponds to the 4.78 Å spacing of the unit cell's c-axis. This indicates that there is bulk isotropic alignment with a selective uniplanar orientation along the c-axis. This alignment is due to the extension of the long-chain Nylon-12 molecules in the flow field associated with filament production, whereby the chains (corresponding to the b-axis) orient themselves parallel to the filament direction, acting as row nuclei for subsequent lamellar growth [77].

Based on these observations, a possible picture of the internal structure evolution is proposed. Following melting and subsequent crystallisation during FFF, the chain alignment within the filaments is preserved; however the lamellae are reorganised into a more energetically favourable state such that the lamellar sheets are realigned. This causes additional planar orientation along the a-axis of the unit cell, causing the appearance of the 200 reflection. This alignment and realignment of the unit cell is illustrated in Figure 3.4.

It is notable that the position of both peaks change dependent on the cooling rates. The inter-sheet 200 reflection's position is governed by the lamellar properties; according to Hoffman-Lauritzen theory, less perfect lamellae would be formed at faster cooling rates, leading to a higher inter-sheet spacing. This is in alignment with the data, in which the faster-cooled FFF RS sample has its 200 reflection at 4.27 Å versus 4.19 Å for the FFF Apium sample.

3.2.2 *In situ* non-isothermal crystallisation of Nylon-12 filament

The initial conclusion drawn from the data in Section 3.2.1 was that the FFF process had an effect on the crystalline structure of Nylon-12, and in particular that the cooling rates affected the positions of the 001(+20$\bar{1}$) and 200 reflections. In order to more fully investigate this, *in situ* non-isothermal crystallisation was performed on Nylon-12 filament in accordance with the procedure in Figure 2.3. Filament samples were heated using a Linkam TS1500 furnace at 10 °C/min to melt, held for 5 minutes to eliminate residual crystals, and cooled at various cooling rates to room temperature, before being reheated to melt.

Four samples were analysed, denoted in descending order of cooling rate as Samples I-IV in Table 3.3. The irregular values of cooling rate are due to the necessity of pausing the cooling temperature ramp in order to acquire WAXS patterns.

Figure 3.5 shows the 2D and fitted 1D WAXS patterns for all four samples after cooling to room temperature from melt at their respective cooling rates.

Two diffraction peaks are present for all cooling rates: a principal peak at 2θ = 9.2 ° (corresponding to the interplanar lattice spacing d of 4.34 Å), attributed to the 001(+20$\bar{1}$) reflection, along with a second lower intensity peak at higher 2θ, attributed to the 200 reflection. A small inner peak at 2θ = 2.6 ° is attributable to background diffraction from the sample holder. Both peaks are surrounded by a broad halo corresponding to the presence of amorphous regions in the sample.

Significant differences can be observed regarding the shape and position of the second peak depending on the cooling rate. In Sample I, the second peak manifests as a shoulder; this is fitted with a Gaussian with peak at 2θ = 10.16 ° (3.89 Å).

Sample	Cooling Rate (°C/min)
Sample I	33.16
Sample II	12.38
Sample III	6.29
Sample IV	1.47

Table 3.3: Actual cooling rates for the four Nylon-12 samples tested non-isothermally *in situ*.

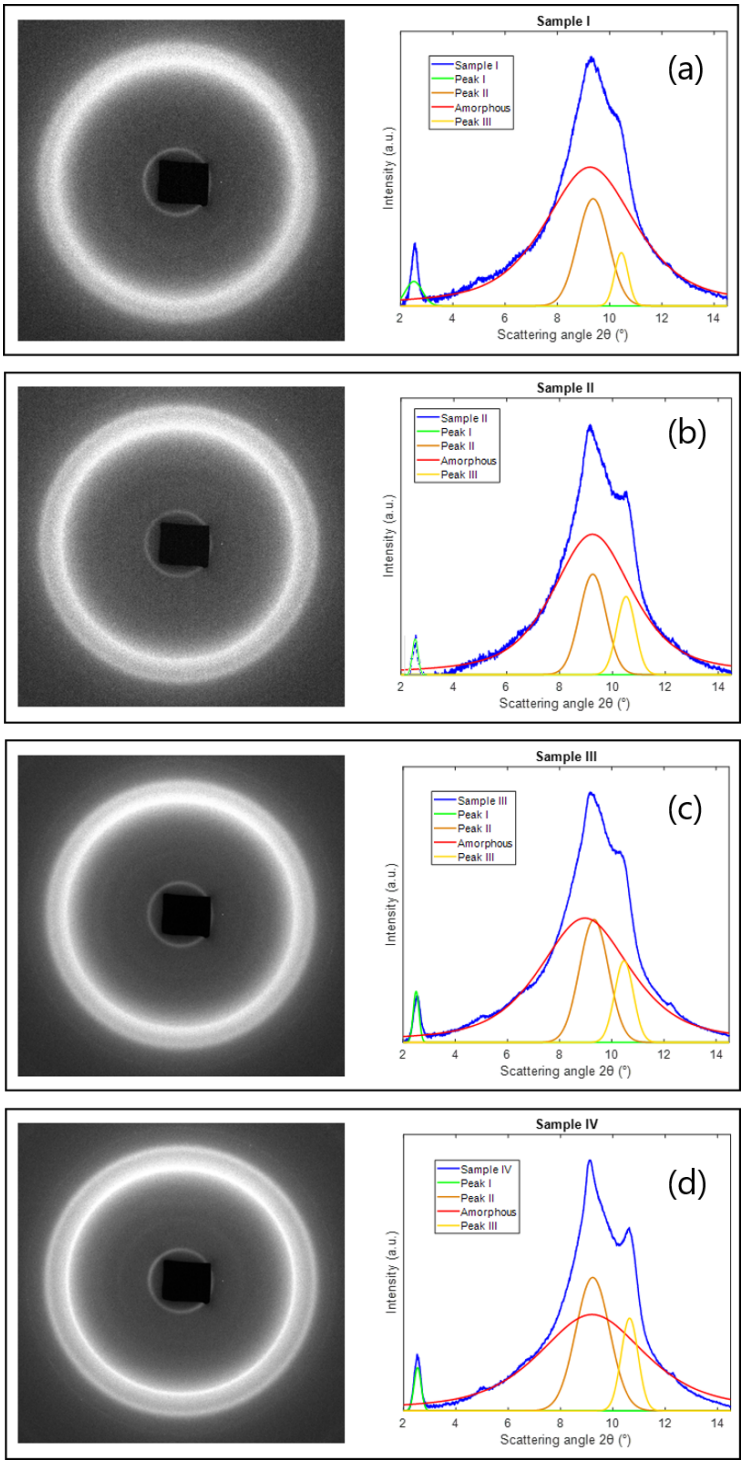


Figure 3.5: Figures (a) - (d) show the 2D and 1D WAXS patterns for Samples I - IV respectively after cooling from melt. It can be observed that the outer ring on the slower cooled Sample IV, corresponding to the 200 reflection, is better defined than on the more rapidly cooled Sample I.

Sample II in a more pronounced second peak with position at 2θ = 10.48 ° (3.77 Å); in Sample III, the second peak appears again as a shoulder with peak at 10.28 ° (3.84 Å). Finally, in Sample IV the second peak is more pronounced still and is positioned at 2θ = 10.62 ° (3.72 Å).

The evolution of the WAXS patterns for all four samples during cooling is shown in Figure 3.6. Each line on the plot of a respective sample corresponds to the 1D WAXS pattern at the temperature indicated by the colour map to the right of each plot.

Following cooling below T_m, a single sharp peak is seen across all samples at 2θ = 9.52 °(4.15 Å). As the samples cool, this single peak decomposes to two separate peaks, forming the patterns seen in Figure 3.6. Sample IV, with the slowest cooling rate has the best-resolved peaks with the highest inter-peak separation. Sample I, with the fastest cooling rate, has the least well defined outer peak.

In addition, it can be observed that Sample IV displays different peak behaviour during cooling. The position of the primary crystalline peak is shifted towards low-θ, and the secondary peak is observed to become prominent at a higher temperature compared to the other samples. With the exception of Sample IV, during cooling the d-spacing decreases with temperature in line with thermal contraction before the formation of the secondary peak. Thereafter the d-spacing corresponding to the $001(+20\bar{1})$ steadily increases whilst the d-spacing corresponding to the secondary 200 peak continues to decrease in line with thermal contraction.

The position of the second peak is likely due to the more complete crystals formed; as the degree of crystallinity due to the second peak increases, the lamellar density will also increase, shifting the peak towards high θ. The secondary peak, indexed as the 200 reflection, is the dominant peak for non-filament based Nylon-12 samples as it is the plane in which hydrogen bonds are aligned [26]. The effect of more complete crystallisation will therefore manifest itself more strongly on this peak, while the principal peak, due to the $001(+20\bar{1})$ reflection, will thereby shift inwards as a consequence.

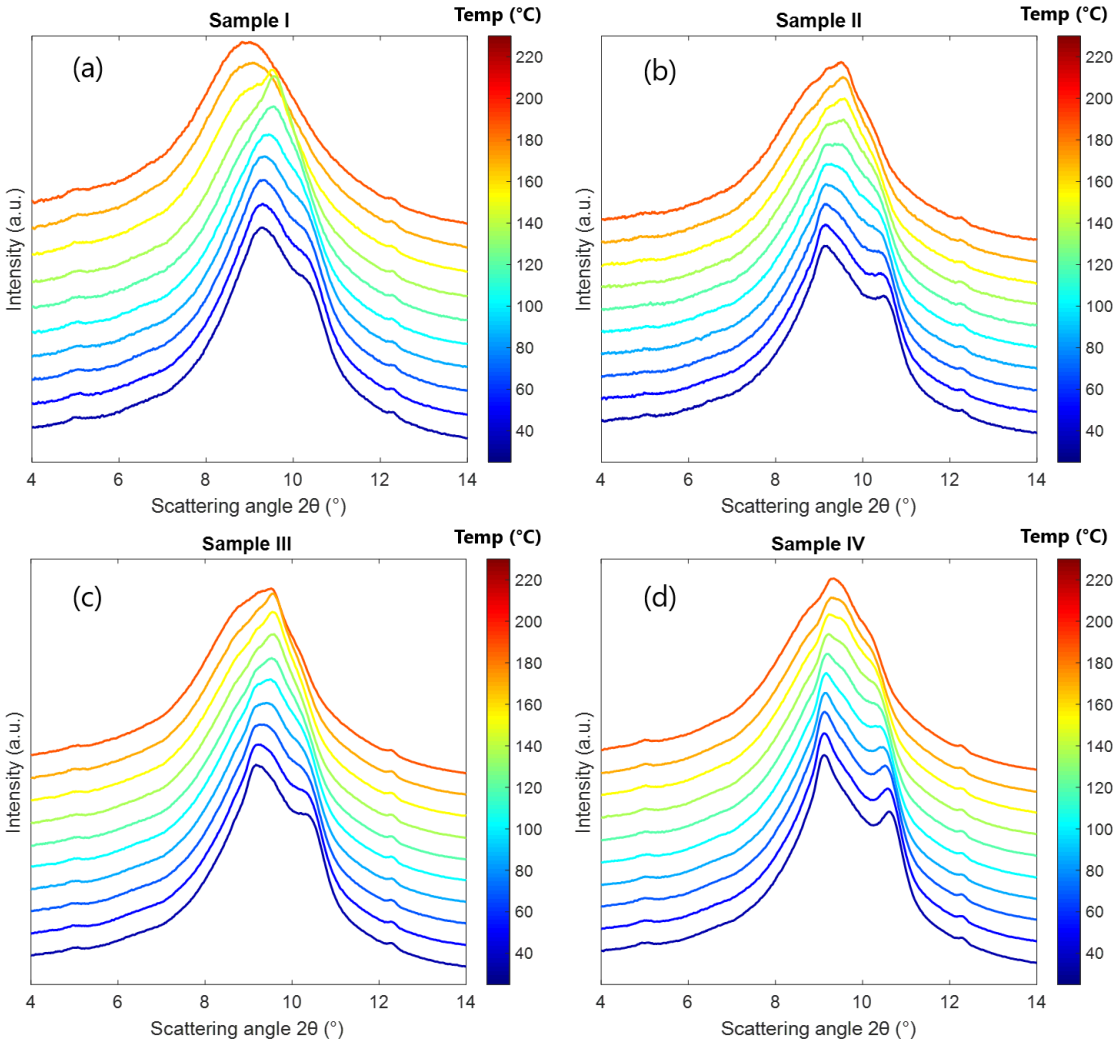


Figure 3.6: Figures (a) - (d) show the evolution of the 1D WAXS pattern during cooling for all four samples. Each line on the figure represents the 1D WAXS pattern at the temperature represented by the colour map on the right of each figure. It can be observed that the inner 001(+20$\bar{1}$) peak is seen first; this slowly moves towards a higher d-spacing during cooling. The 200 peak is seen subsequently and moves towards a lower d-spacing during cooling.

Following cooling to room temperature from melt, the samples were then reheated to melt at 10 °C/min. Figure 3.7 shows 2D WAXS patterns from Sample IV during the heating process. It can be observed that the 200 peak coalesces with the 001(+20$\bar{1}$) peak as the temperature increases above T_g, indicating a gradual increase in d-spacing before the merger of the two peaks. It remains unclear as to whether this represents a melting of the lamellar sheet crystal structure associated with the 200 peak, or whether it represents a change in the unit cell parameters

due to lamellar reorganisation such that the two peaks overlap.

Figure 3.8 shows the evolution of the d-spacing of the 001(+20$\bar{1}$) and 200 peaks of Samples I-IV during cooling and reheating, while Figure 3.9 shows a plot of the degree of crystallinity of the samples versus cooling rate. The degree of crystallinity for each sample is given in Table 3.4.

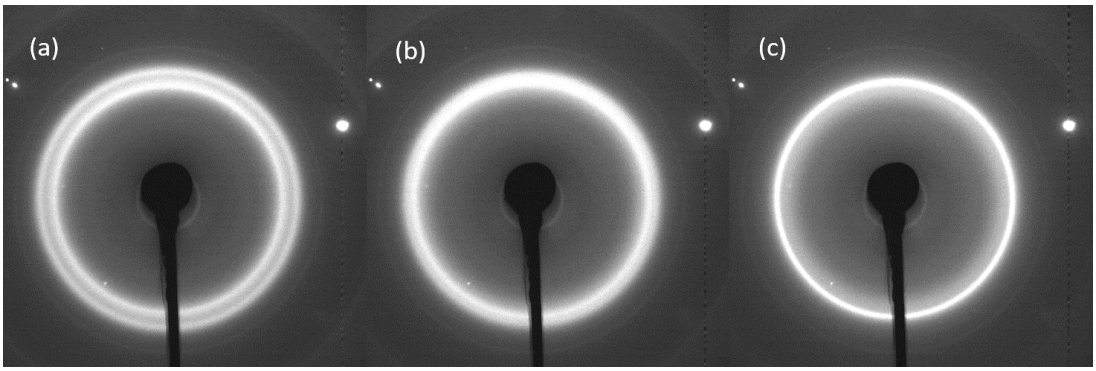


Figure 3.7: Evolution of the principal peaks in FFF Apium Nylon-12. Note the coalescence of the double peak into a single peak as T increases. (a) shows the pattern at T = 25 °C; (b) shows the ongoing peak coalescence at T = 65 °C; (c) shows the final pattern at T = 124 °C prior to the transition to an amorphous pattern.

The slower cooling rate can be seen in Figure 3.9 to result in a higher degree of crystallinity. Simultaneously, Figure 3.6 shows that the 200 reflection, corresponding to lamellar stacks, appears at a higher temperature at a slower cooling rate, while Figure 3.5 shows a more clearly defined 200 reflection at a slower cooling rate. Based on these three data points, it is proposed that the slower cooling rate leads to more perfectly formed crystal structures, such as a larger and more densely formed lamellar stack. The slower cooling rate means that these structures can form earlier during the crystallisation process.

The above data supports the preliminary conclusions drawn in Section 3.2.1 that the difference in WAXS patterns is related to the cooling rates undergone during

Sample	Degree of Crystallinity (%)
Sample I	24.6
Sample II	26.3
Sample III	30.1
Sample IV	37.2

Table 3.4: Degrees of crystallinity for all for samples on completion of cooling from melt.

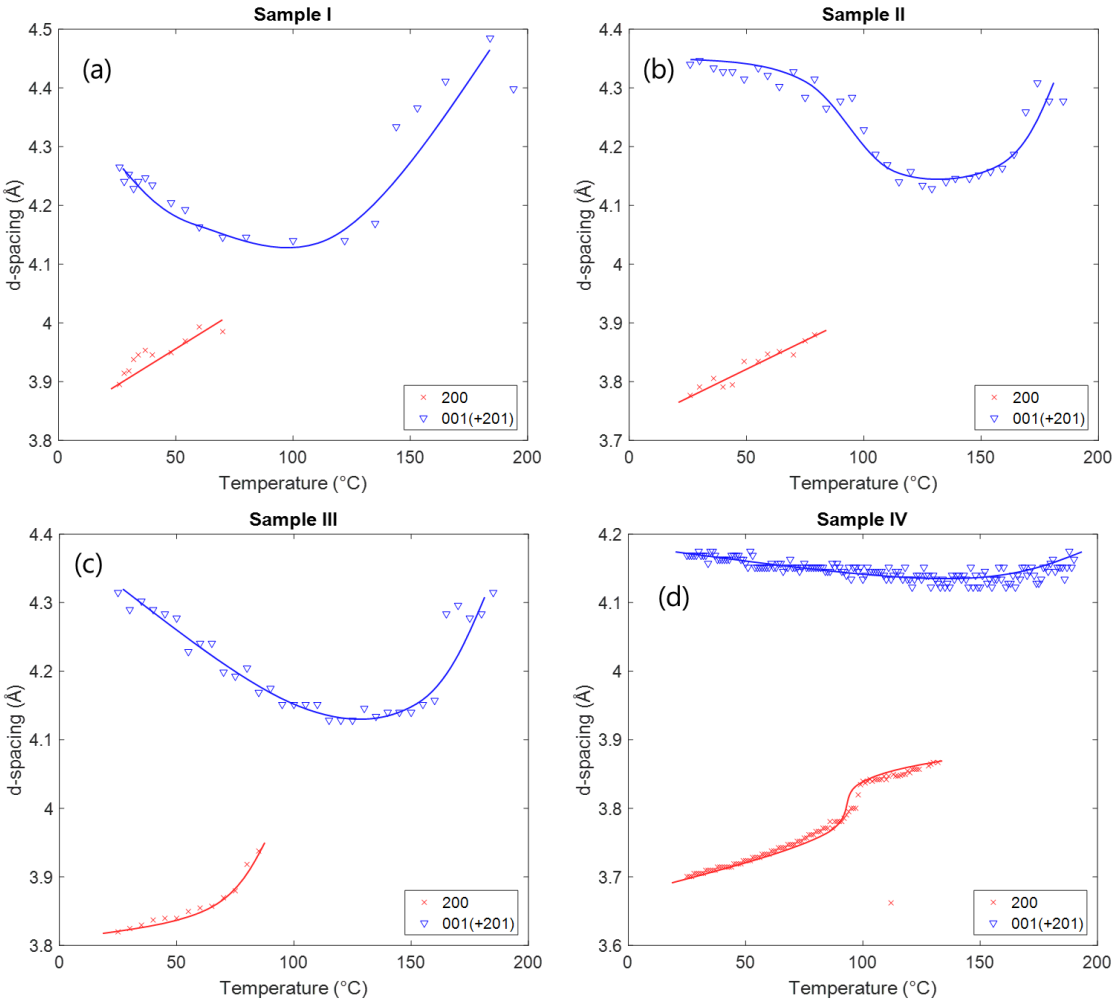


Figure 3.8: d-spacing for all four samples during cooling. In line with the results seen in Figure 3.6, the 200 peak only becomes clearly resolvable later in the cooling process. It is notable that the peak appears at a higher temperature as the cooling rate falls.

sample preparation. In addition, the 200 reflection appears in all four samples during the crystallisation from melt. This additionally supports the conclusions drawn in Section 3.2.1 that the realignment of crystalline structure that leads to the appearance of the 200 reflection takes place during the crystallisation from melt. In Section 3.2.1 this was seen only in FFF samples, which had undergone melting in the nozzle of the FFF printer; here it is seen in Samples I-IV which have undergone melting in the furnace.

It is therefore proposed that the position and intensity of the 200 reflection is dependent on the size and formation of crystallites. This is based on the fact that the 200 reflection is produced by periodicity of the hydrogen bonding surface in the

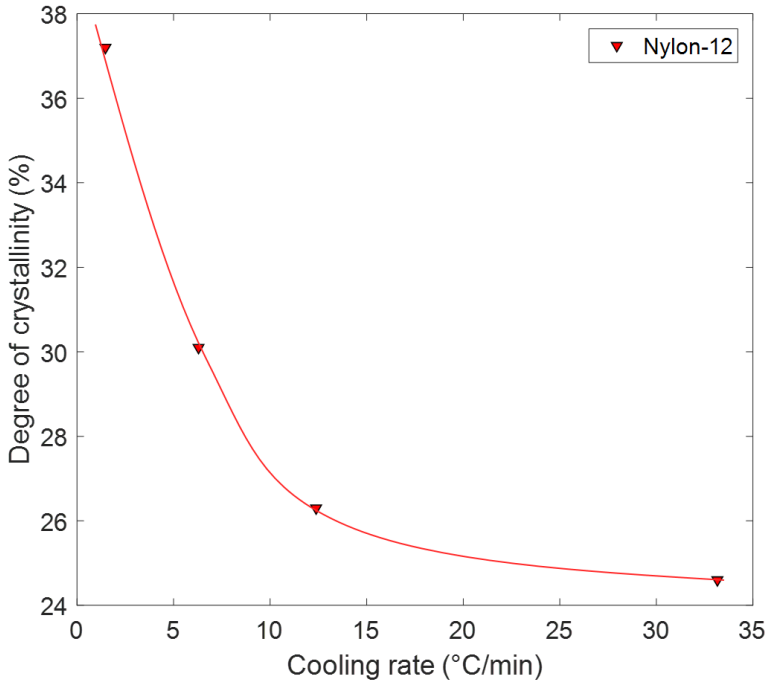


Figure 3.9: Degree of crystallinity versus cooling rate for Samples I-IV. The degree of crystallinity increases as the cooling rate slows. Notably, the rate of increase of crystallinity increases with decreasing cooling rate, consistent with data seen elsewhere in literature [130].

unit cell [131]. As the sample temperature rises causing the lamellar stack period to increase, the d-spacing increases. The "disappearance" of the 200 reflection during heating occurs at a lower temperature for more rapidly cooled samples; this is proposed to be due to the less perfect formation of the lamellar structures in these samples, which melt at a lower temperature. Further corroboration of this conceptual picture will be required.

The principal distinction between the WAXS patterns of the printed samples and the raw filament at room temperature, therefore, is the presence of the γ (200) phase which is suggested to be induced by the printing process. Furthermore, the slower the attendant cooling rate of the sample after production appears to affect the ratio of this phase present. Previous WAXS analysis of Nylon-12 samples produced by selective laser sintering (SLS), which has extremely slow attendant cooling rates compared to FFF, show a strong predominance for the 200 peak, which is shown in Figure 1.10. These XRD results reveal that the attendant cooling rate from melt

after extrusion has a clear effect on the crystalline phases present in the sample, with the degree of presence of the (200) form being correlated to the rate of cooling.

3.2.3 *In situ* mechanical testing of Nylon-12 samples produced by FFF

In situ tensile testing was performed on two dogbone samples. Both samples were produced by the Apium P220 printer in order to keep associated print parameters the same. The first sample, denoted as "slow-cooled", was printed at a bed and chamber temperature of 120 °C and then cooled slowly to room temperature on completion of build at a rate of 5 °C/min. The second sample, denoted as "air-cooled", was also printed at a bed and chamber temperature of 120 °C, but was then immediately removed from the print chamber and quenched to room temperature.

This test was intended to serve a number of purposes:

1. To investigate the impact of tensile testing on crystalline structure in FFF-produced Nylon-12 samples.

2. To determine whether the cooling rate post-build had an effect on the resultant crystalline structure of the samples. Currently, FFF has no guidelines for cooldown, being left to the user's discretion; in addition, most commercially available FFF printers lack the ability to control the cooldown cooling rates.

3. To determine whether the differences in crystalline microstructure, should they be found to be present, induced by the different cooling rates post-build had an impact on mechanical properties.

Figure 3.10 shows the 2D and fitted 1D WAXS data at zero extension for the "slow-cooled" and "air-cooled" samples. Table 3.5 shows the d-spacing and degree of crystallinity associated with these samples. Minimal differences are observable between the two samples, indicating that the cooling rate post-build below 120 °C has little observable effect on degree of crystallinity or crystalline structure. Based on this, it is concluded that the impact of thermal history on crystal structure in FFF takes place above 120 °C during the initial cooling from the melt.

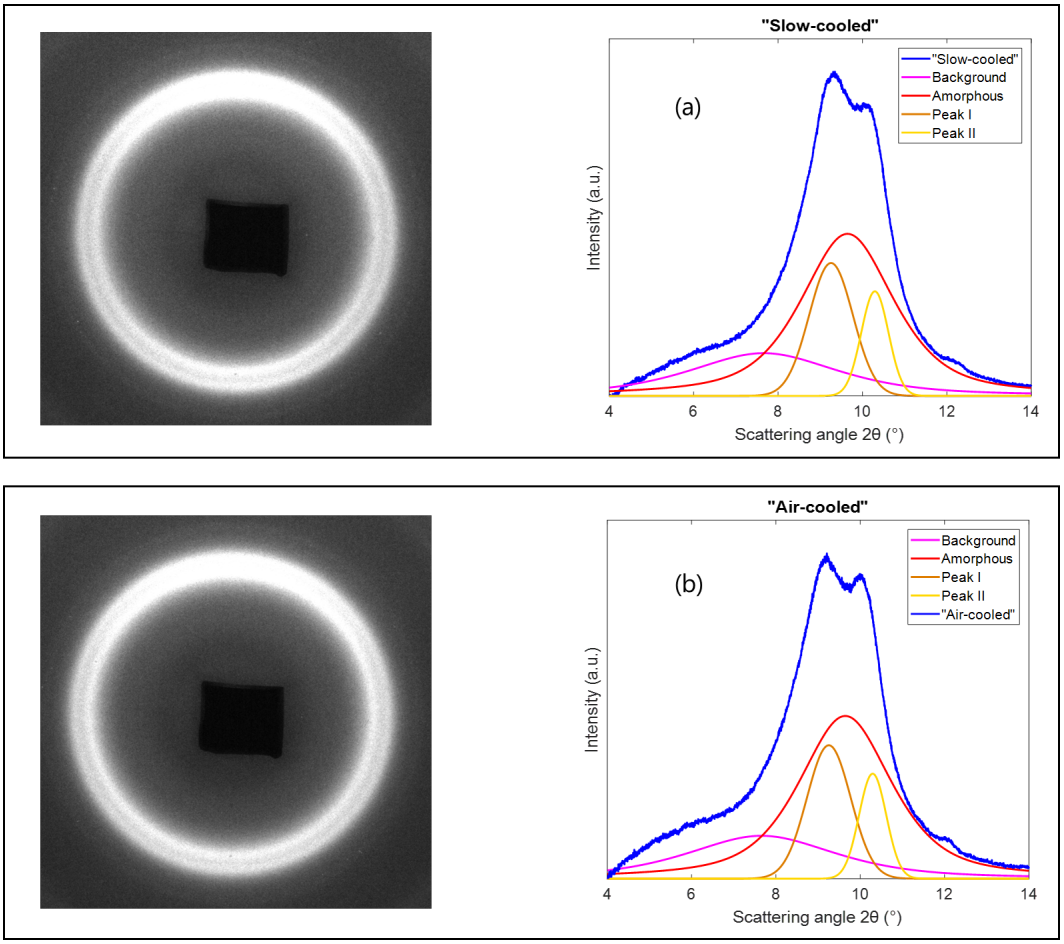


Figure 3.10: WAXS patterns of (a) the "slow-cooled" and (b) the "air-cooled" samples at 0N. Minimal differences are noticeable between the two peaks, with only minor differences in degree of crystallinity.

Figure 3.11 shows the stress-strain curves for both "slow-cooled" and "air-cooled" samples, while Table 3.5 shows the calculated Young's Modulus for the samples. Although significant difference is observed between the Young's Moduli of the respective samples, over-interpretation of this result is to be cautioned due to issues with the Deben MT1000 tensile stage *in situ*.

Sample	"slow-cooled"	"air-cooled"
Young's Modulus E (MPa)	859.7	839.5
Degree of crystallinity (%)	26.6	25.9

Table 3.5: Young's Modulus E for the preliminary testing of Nylon-12 tensile samples *in situ*.

Figure 3.12 shows the 2D WAXS patterns at the end of the tensile test. Figure

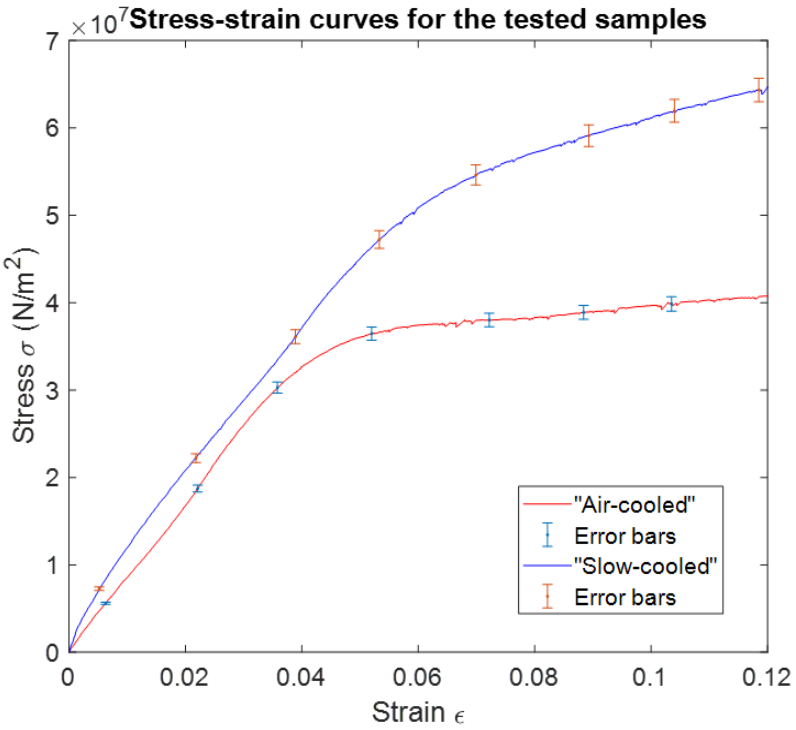


Figure 3.11: WAXS patterns of (a) the "slow-cooled" and (b) the "air-cooled" samples at 0N. Minimal differences are noticeable between the two peaks, with only minor differences in degree of crystallinity.

3.13 shows the evolution of the 1D WAXS pattern as the sample is stretched. Each line on a sample's respective curve in Figure 3.13indicates the 1D WAXS pattern at a given force, corresponding to the colour map to the right of each figure. The printing orientation of all samples was such that the filaments were oriented in plane with the tensile direction.

As the tensile test progresses, the double-ring pattern alters such that there are two meridional and two equatorial reflections observed. In particular, whilst the position of the 001(+20$\bar{1}$) reflection is unchanged outside of lattice strain, the 200 reflection becomes solely equatorial. In the meridional direction, a distinct inner reflection with d-spacing of 7.18 Å indexed as 040 becomes visible. This is in alignment with previous data obtained on drawn Nylon-12 by Ishikawa *et al* [122] and Hiramatsu *et al* [119], who noted that the 040 reflection was present only in the meridional direction whereas the 200 reflection was present only in the equatorial direction. These results are proposed to demonstrate the occurrence of uniaxial

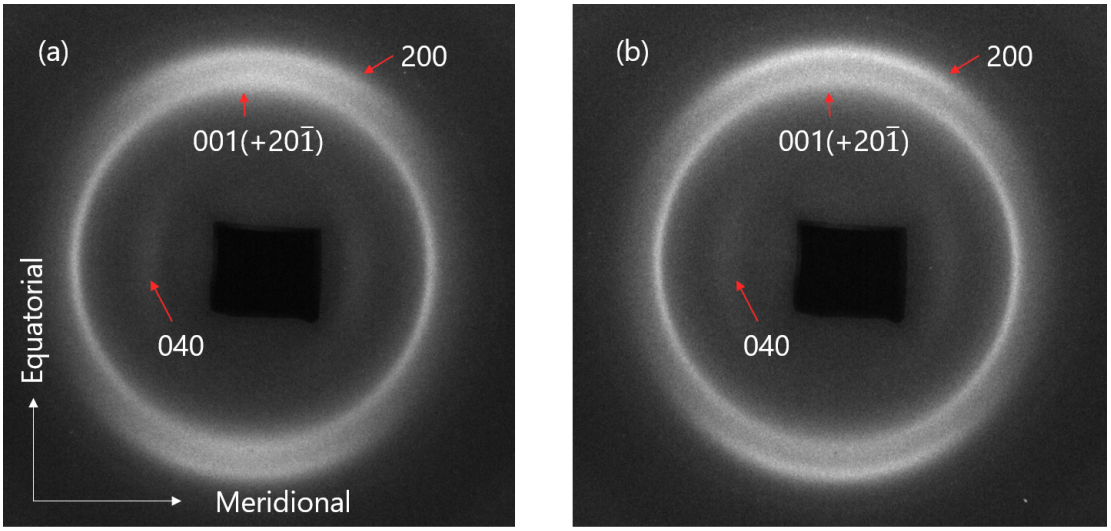


Figure 3.12: (a) shows the 2D WAXS pattern for the "slow-cooled" sample, while (b) shows the 2D WAXS pattern for the "air-cooled" sample after completion of tensile testing. The 200 reflection is no longer visible in the meridional direction, and the more faint 040 reflection has appeared.

orientation of crystallites along the tensile direction [132].

Figure 3.14 shows the d-spacings in the meridional direction (direction of tensile testing) as a function of applied load. Figure 3.15 plots the lattice strain in the meridional direction. The results are similar to those seen in Figure 3.11. The lattice modulus for both samples are very similar even though the move from elastic to plastic behaviour occurs at a much lower stress.

The elastic behaviour seen in semi-crystalline polymers is due to the mechanical behaviour of the crystalline structures. It is notable that after the initial period of elastic behaviour, increase in the d-spacing in the tensile testing direction continues to increase albeit at a lower rate. No lattice strain is observed above 0.06, indicating that above this strain the chain entanglement in the amorphous regions of the samples dominates the tensile behaviour.

The difference between the patterns in the equatorial and meridional directions indicate an orientational change in which crystallites not already ordered along the fibre axis are rotated into the tensile direction. A potential model for crystal structure evolution under tensile testing is therefore proposed as follows. The filament production process and secondary extrusion due to FFF preserve the

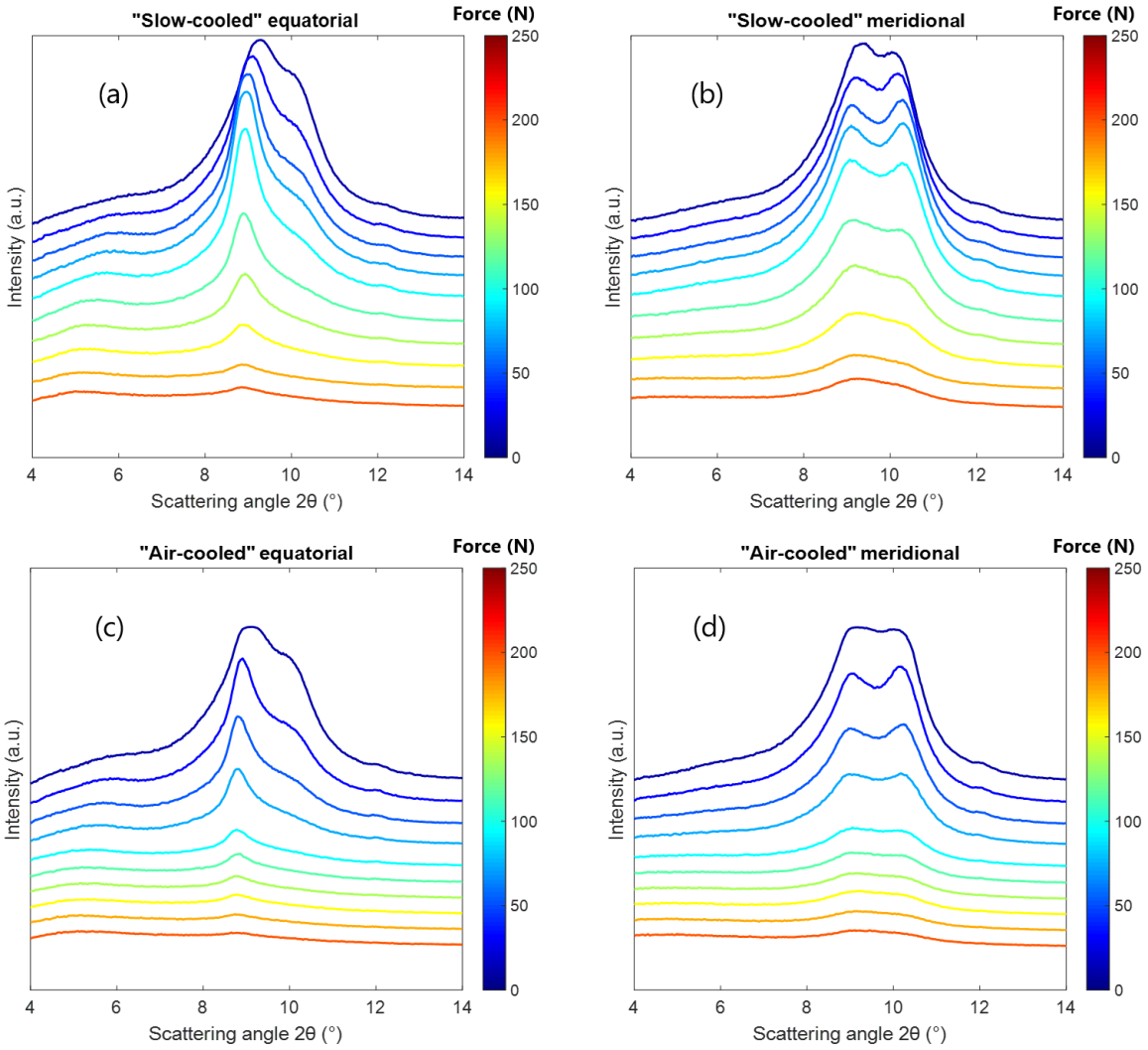


Figure 3.13: The evolution of the WAXS patterns in the meridional ((b), (d)) and equatorial directions ((a), (c)) for the "slow-cooled" and "air-cooled" samples. Each line on the figure corresponds to a 1D WAXS pattern at a different force, corresponding to the force shown on the colour map to the right of the figure. Clear differences can be seen; in particular the 200 peak is no longer visible in the meridional direction (direction of tensile test) as the force increases.

alignment of the Nylon-12 chains along the filament axis; as the tensile test proceeds, further unit cell rotation along this axis takes place. This allows for bulk alignment in the meridional direction of the *b*-axis of the unit cell, leading to the presence of the 040 reflection in this direction. This proposed process is shown by schematic in Figure 3.16.

The sharpening of the $001(+20\bar{1})$ reflection in the meridional direction is proposed to indicate a mechanism of additional crystallisation in the direction of alignment

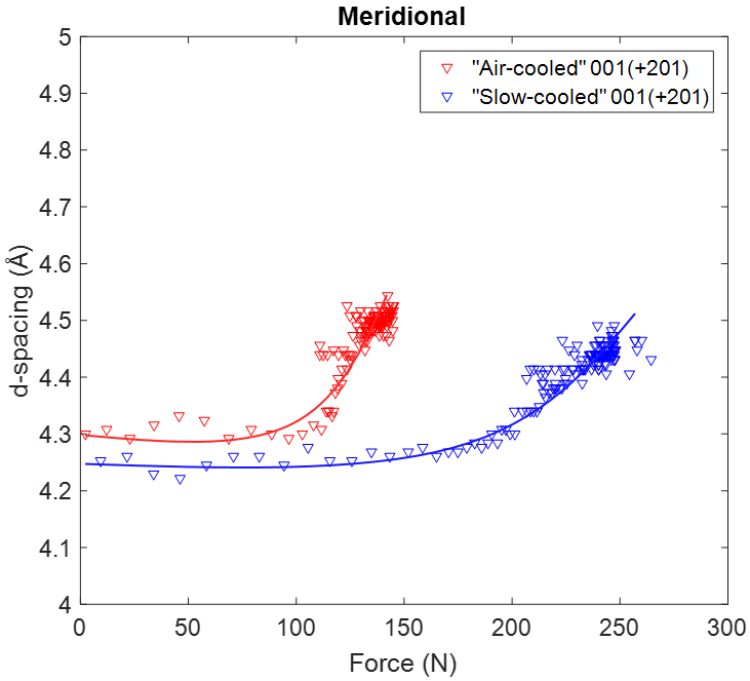


Figure 3.14: The d-spacing of the 001(+20$\bar{1}$) peak in the meridional direction during tensile testing. While minimal change is initially seen during the elastic component, the d-spacing then increases during the plastic region of the tensile test.

as disordered lamellae are reoriented. This is followed by a mechanism of crystallite breakup and disorientation, corresponding to peak broadening and decrease in intensity during plastic behaviour.

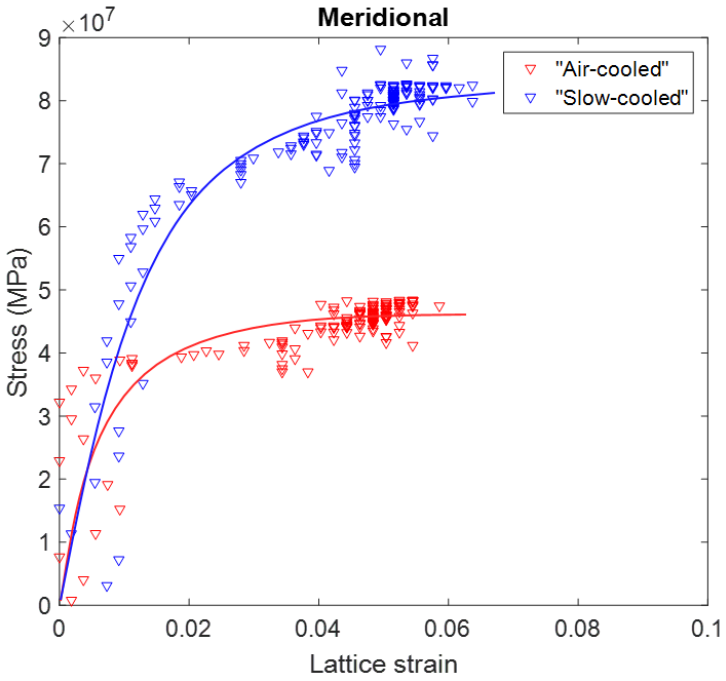


Figure 3.15: The stress-lattice strain curves for the 'slow-cooled" and "air-cooled" samples. The elastic region at the start of the tensile test can be observed, following by a levelling out of stress as strain continues to increase. This is proposed to be due to the fact that more of the strain is applied to the entangled chains in the amorphous region of the polymer.

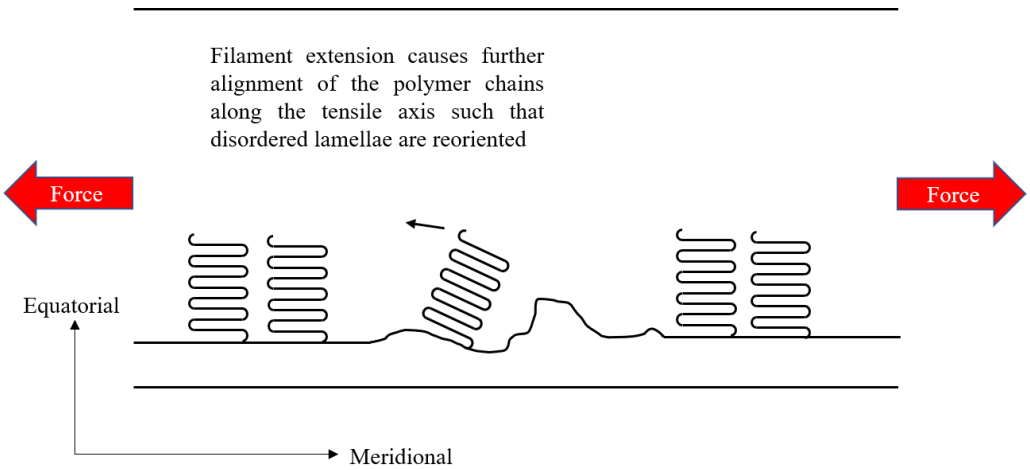


Figure 3.16: The alignment of the unit cell during tensile testing is shown. In the meridional direction, the unit cell rotates along the $b-$axis, leading to the presence of the 040 reflection. In the equatorial direction, there is continued alignment in a and c over the bulk filament, hence the presence of the 200 and 001$(+20\bar{1})$ rings in this orientation.

4

Thermal Analysis of Nylon-12

Contents

4.1 Introduction 112
4.2 Results and discussion 112
4.2.1 Isothermal crystallisation of Nylon-12 112
4.2.1.1 High temperature crystallisation 113
4.2.1.2 Low temperature crystallisation 118
4.2.2 Non-isothermal crystallisation of Nylon-12 124
4.2.3 DSC of FFF Nylon-12 samples with varying thermal history 128
4.2.3.1 Printed samples vs Nylon-12 filament 129
4.2.3.2 Printed Nylon-12 samples with incrementally varying thermal history 129
4.3 Analysis 134
4.3.1 Isothermal crystallisation 134
4.3.2 Non-isothermal crystallisation 139
4.4 Conclusions 141

4.1 Introduction

This chapter presents the results obtained from the DSC testing of Nylon-12. The main focus of this study is two-fold: firstly, to quantify the WAXS results described in the previous section as a function of the cooling rate, and secondly to quantify the crystallisation kinetics and behaviour of Nylon-12 filament under different thermal conditions. Isothermal and non-isothermal crystallisation experiments were performed on Nylon-12 filament. The latter were carried out under conditions that circumscribe the range of cooling rates that might be experienced during FFF. The percentage crystallinity and Avrami parameters were calculated from these data sets. Isothermal and non-isothermal testing were performed according to the experimental parameters given in Section 2.4.1.3.

Subsequently, DSC was performed on samples printed via FFF and then annealed at different temperatures. This was in order to examine the dependence of crystalline structure and thermal properties on annealing temperature in samples that had already undergone FFF thermal history. The DSC data from these samples was examined and compared to the isothermal and non-isothermal data to quantify the effect of thermal history on the thermal properties and crystal structure.

4.2 Results and discussion

4.2.1 Isothermal crystallisation of Nylon-12

The results for the second heating of the isothermally crystallised Nylon-12 samples are presented and discussed below, along with various derived crystallisation kinetics curves. The results are split into two sections, as follows:

1. **Section 4.2.1.1: High temperature crystallisation**
2. **Section 4.2.1.2: Low temperature crystallisation**

Section 4.2.1.1 deals with high temperature crystallisation (above 170 °C), and Section 4.2.1.2 deals with low temperature crystallisation (120-170 °C). The purpose of the high temperature crystallisation is to explore the thermal and crystallisation

properties of Nylon-12, which may differ from the literature due to its method of production. The purpose of the low-temperature crystallisation is to explore the behaviour of Nylon-12 when crystallised at temperatures more resembling those routinely achievable in FFF printers.

4.2.1.1 High temperature crystallisation

The DSC traces for the high-temperature isothermal measurements are shown in Figure 4.1. These traces are obtained from the reheating to melt of the samples at 10 °C/min after isothermal crystallisation. Samples were isothermally crystallised at different T_c between 168 and 176 °C. A single melting peak is observed for all samples, indicating that larger and more perfect crystals have been formed. Variation in the magnitude of the melting peak is minimal across the samples. It is notable that even at T_c = 168 °C, the crystallisation process is rapid (in the order of 5 minutes).

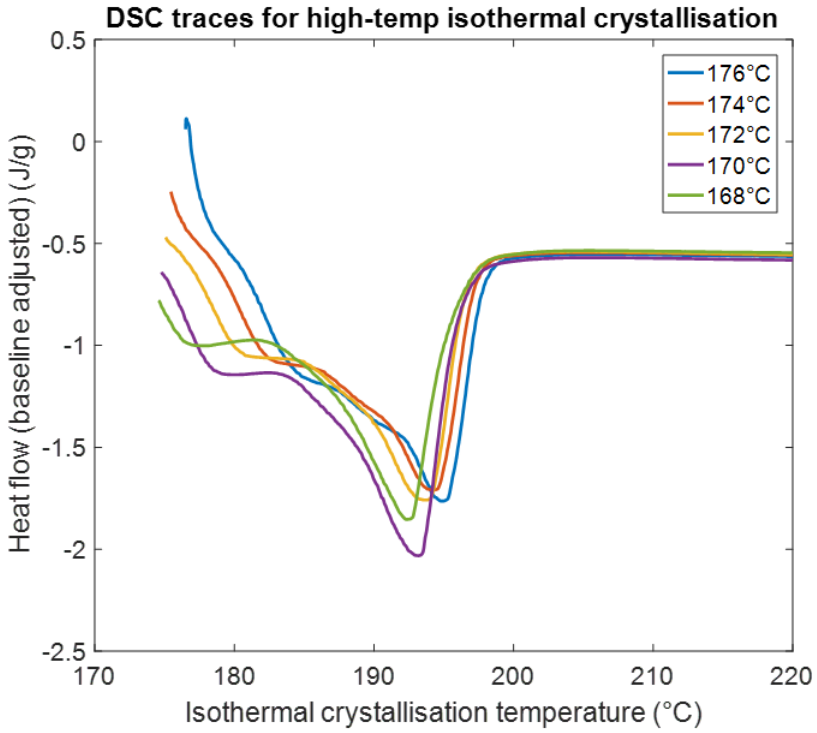


Figure 4.1: DSC thermograms for samples reheated at 10 °C/min after 60 minutes isothermal crystallisation at different T_c.

The peak position of the melting endotherms, which gives the melting point of the samples, also increases with increasing T_c. The positions of these peaks are

T_c (°C)	176	174	172	170	168
n	2.02	2.08	2.13	2.16	2.16
K (s^{-1})	2.47×10^{-6}	3.36×10^{-6}	3.36×10^{-6}	5.42×10^{-6}	8.83×10^{-6}
t_{max} (s)	422.9	309.9	274.1	204.1	163.7
$t_{1/2}$ (s)	537.1	380.7	325.5	224.3	177.6
G (s^{-1})	0.0019	0.0026	0.0031	0.0045	0.0056

Table 4.1: The kinetic parameters for the high-temperature isothermal crystallisation of Nylon-12.

displayed in Table 4.2 and plotted against T_m in Figure 4.2. As the isothermal crystallisation temperature T_c increases from 168 °C to 176 °C, the T_m melting peak position increases from 191.91 °C to 195.23 °C. The plot of T_c against T_m is well-fitted with a linear fit, which is consistent with the literature data showing a relationship of direct proportionality between T_m and T_c in semi-crystalline polymers.

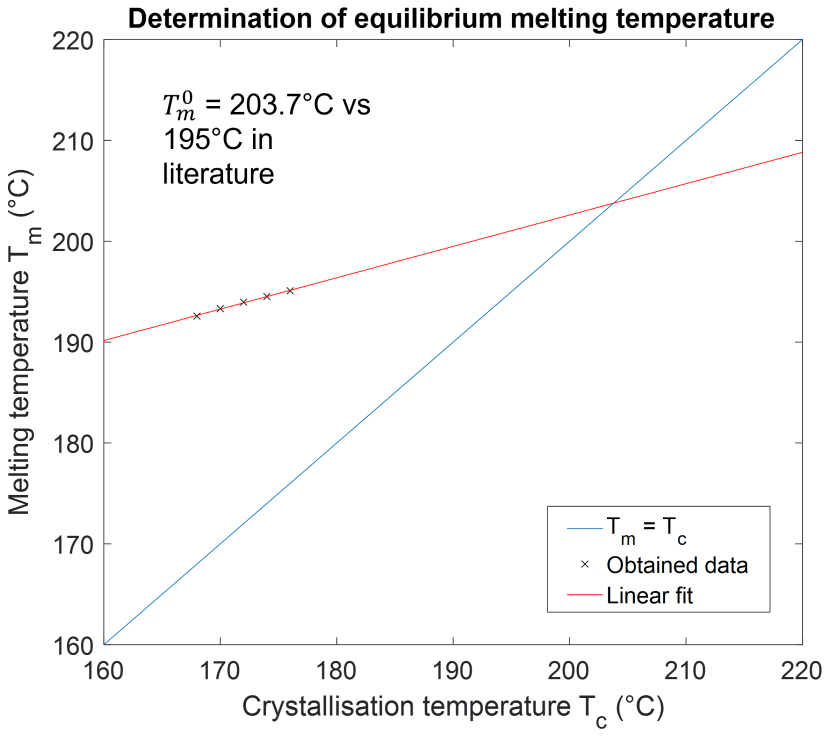


Figure 4.2: Melting temperature T_m as a function of isothermal crystallisation temperature T_c, projected onto the line $T_m = T_c$ to derive equilibrium melting temperature T_m^0.

As shown in Section 2.5.3.2, the equilibrium melting temperature T_m^0 can be obtained from the intersection of the T_m-T_c relation and the $T_m = T_c$ line in Figure

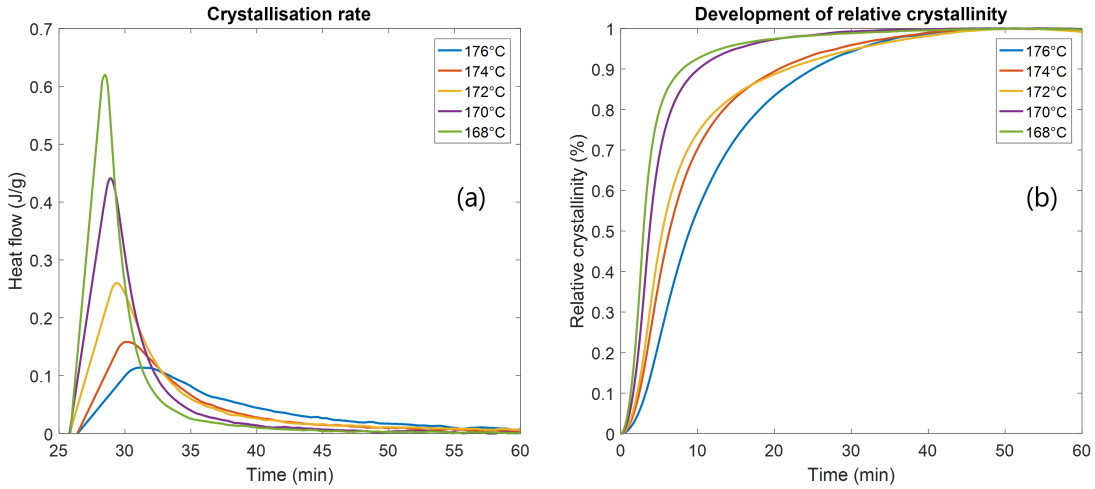


Figure 4.3: (a) shows the crystallisation rate for the isothermal crystallisation. (b) shows the development of relative crystallinity $X(t)$ as a function of time.

4.2. T_m^0 was found from the obtained data to be 203.7 °C, which significantly exceeds the value of 195 °C found in most literature. It is unknown whether this is due to an alteration to base Nylon-12 thermal properties due to the filament manufacturing process or a shift in the apparatus thermal readings. However, based on the data from Chapter 3, in which the Linkam TS1500 furnace registered similar melting points for Nylon-12 as were obtained by the DSC apparatus, and as no reliability issues have previously or since been recorded for either apparatus, the latter theory is considered to be unlikely.

T_c (°C)	176	174	172	170	168
T_m (°C)	195.04	194.52	193.96	193.32	192.58

Table 4.2: T_m and T_c values for the high-temperature isothermal crystallisation of Nylon-12.

The degree of relative crystallinity X_c is given by the derivative of the heat flow curve, as described in Section 2.2.1.1, and is plotted in Figure 4.3(a) as a function of time t. (b) shows the second derivative of the heat flow curve, corresponding to the crystallisation rate. It can be seen that the characteristic sigmoidal isotherms associated with polymer crystallisation are progressively stretched along the time axis as T_c increases, indicating a progressively slower crystallisation rate. This is

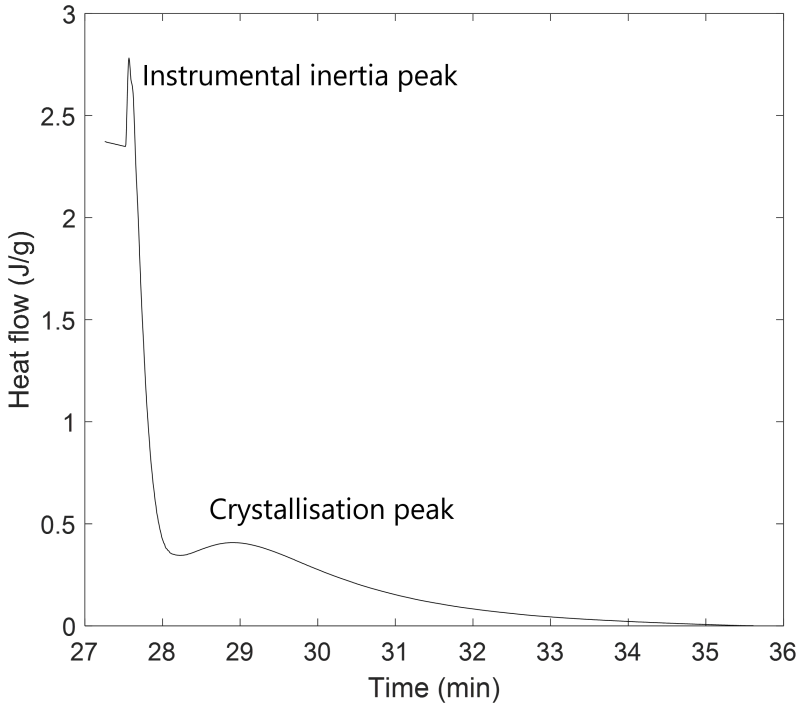


Figure 4.4: The raw isothermal crystallisation DSC trace for the rapid cooling and isothermal crystallisation phase at 170 °C. Note the peak caused by instrumental inertia which serves to obscure the early phase of crystallisation.

reflected in the shape of the rate curves in (a), which become longer and lower-magnitude with increasing T_c.

The rate curves in Figure 4.3(a) are projected at low values of t. Figure 4.4 shows the raw data from the isothermal crystallisation; it can be noted that due to the rapid cooling from melt to T_c and the associated change in the thermal profile that accompanies the transition from cooling to isothermal crystallisation, the DSC data shows a pre-isothermal crystallisation peak that obscures the first part of the heat flow curve. This is due to the instrumental thermal inertia switching between experimental phases. As a result, the low-t values of rate are calculated by extrapolating until the base line with a linear curve to take into account the overall crystallisation process, as per Choupin *et al.* [133]. The Avrami equation is given as:

$$X(t) = 1 - e^{-Kt^n} \tag{4.1}$$

Its derivative, which gives the rate of crystallisation is therefore given by:

$$\frac{dX}{dt} = nKt^{n-1}e^{-Kt^n} \tag{4.2}$$

such that at small t, Equation 4.2 tends towards:

$$\frac{dX}{dt} \propto nKt^{n-1} \tag{4.3}$$

For values of n close to 2, which is in line with the results shown in Table 4.1, this therefore corresponds to the equation of a linear curve with slope equal to nK [134].

The half-time of crystallisation $t_{1/2}$ is calculated as the time taken for 50% of crystallisation to occur; this is when $X_c = 0.5$. This is extracted directly from the $X(t)$ vs t plots in Figure 4.3(b), and is plotted against T_c in Figure 4.5. $t_{1/2}$ increases with T_c increasing, corresponding to the lower degree of super-cooling [114]. As described in Section 1.2.5, the reciprocal $t_{1/2}$ gives the crystallisation rate G. The time of maximum crystallisation rate t_{max} is also calculated as described in Equation 1.16.

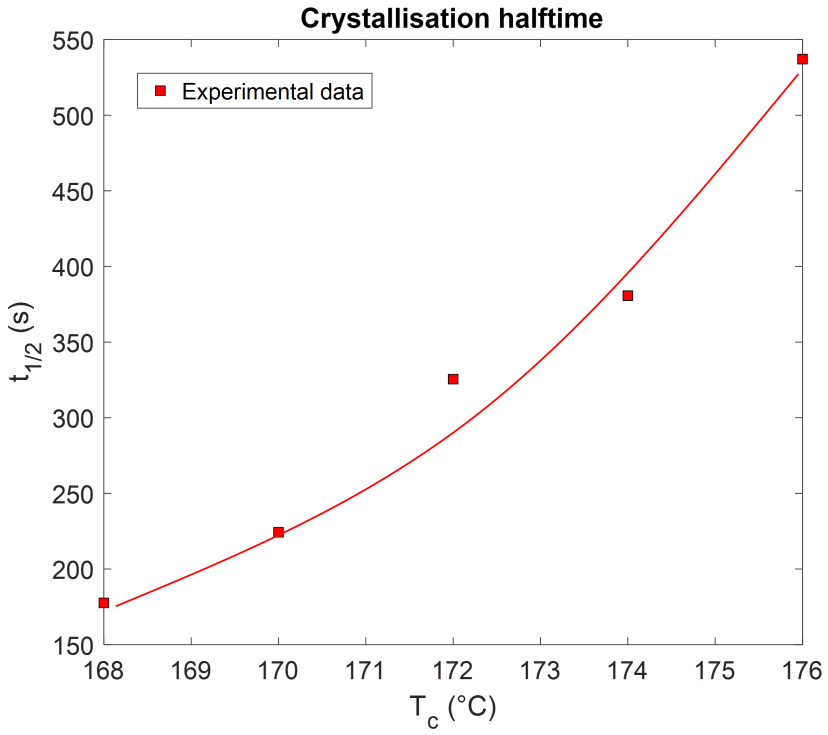


Figure 4.5: Isothermal crystallisation half-time $t_{1/2}$ as a function of isothermal crystallisation temperature T_c.

The Avrami parameter n and rate parameter K are calculated from the double logarithmic plot as described in Section 1.2.5. This double logarithmic plot of $\ln(-\ln(1-X(t)))$ vs $\ln t$ is shown in Figure 4.6(a). The Avrami parameter n and rate parameter K can be derived from Equation 1.8 by fitting the linear components of the double logarithmic plot using a least squares fit. This is shown in Figure 4.6(b). The values of the Avrami parameter and rate parameter are shown in Table 4.1. It can be observed that n increases with increasing T_c, while K decreases. This is in line with the lower magnitudes shown in Figure 4.3(a) for higher T_c.

The kinetic parameters associated with isothermal crystallisation n, K, t_{max}, $t_{1/2}$, G are calculated for this dataset as described above are listed in Table 4.1.

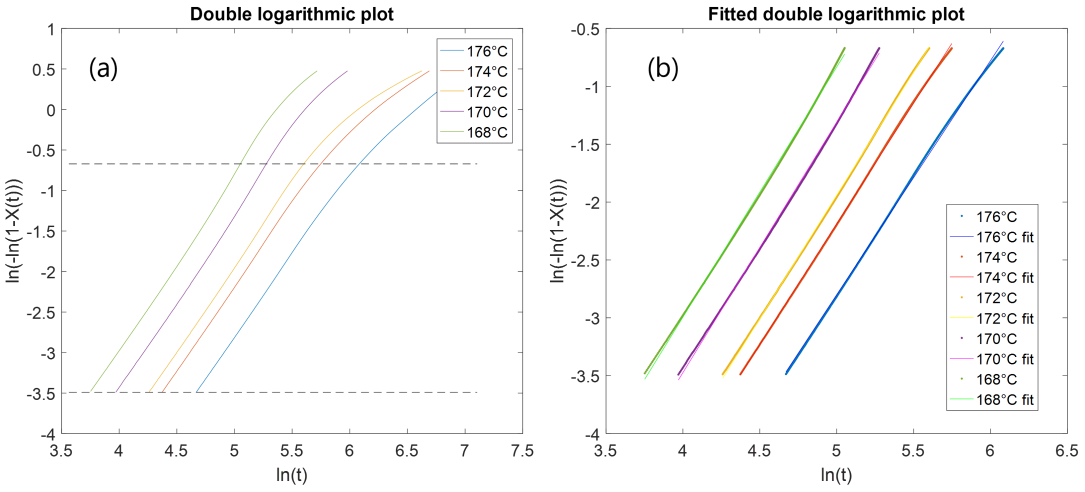


Figure 4.6: (a) shows the double logarithmic plot of $\ln(-\ln(1-X(t)))$ vs $\ln t$. (b) shows the plot with a linear fit to obtain n and K.

4.2.1.2 Low temperature crystallisation

The results obtained for the low-temperature isothermal measurements are shown in Figure 4.7, which demonstrate the second heating of the samples at 10 °C/min. It can be observed in Figure 4.7 that the isothermal temperature has a clear effect on the position of the principal melting exotherm. In addition, the shape of the melting exotherm is significantly altered between the samples. One melting peak corresponds to the melting of the crystal structure on a particular length scale.

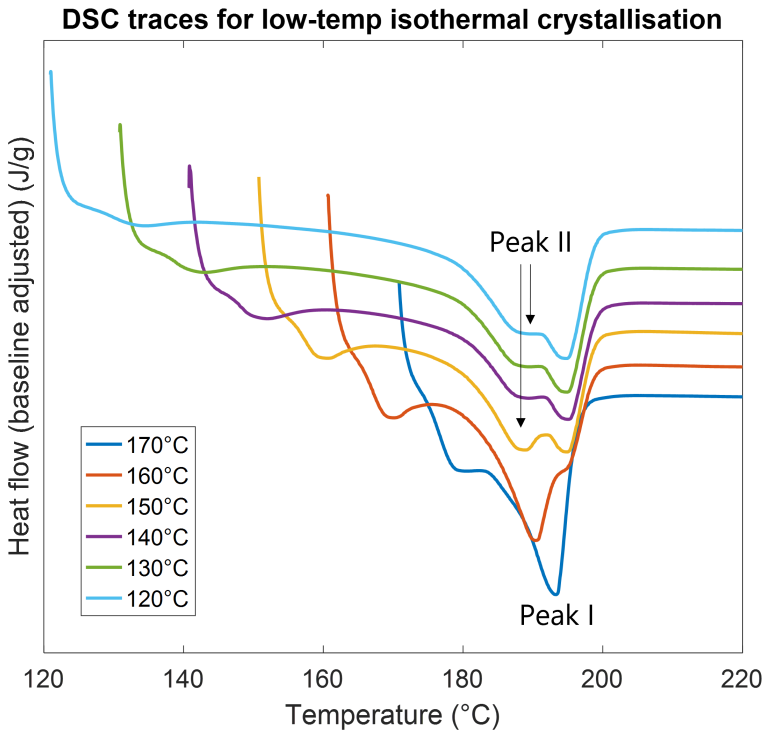


Figure 4.7: DSC thermograms for samples reheated at 10 °C/min after 60 minutes isothermal crystallisation at different T_c.

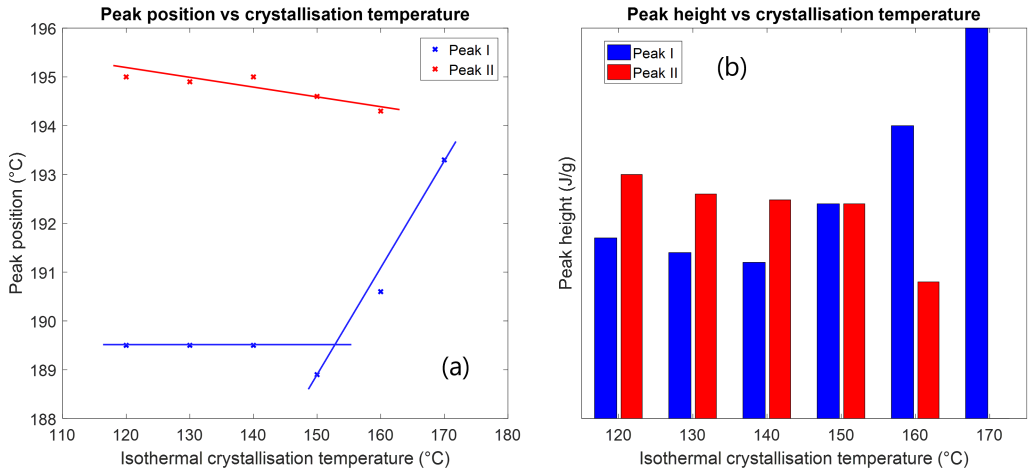


Figure 4.8: Peak positions and magnitude ratios for the isothermal crystallisation. (a) shows the evolution of temperature values at peak maximum, and (b) shows peak heights as a function of isothermal crystallisation temperature T_c.

Since larger and more perfect crystals are expected at a high T_c the larger magnitude of the melting endotherm for the 170 °C samples corresponds to this. At lower temperatures the crystallisation completes very rapidly, and smaller and less perfect crystals are expected. The presence of the lower-temperature shoulder

on the DSC trace for samples crystallised at low T_c is proposed to be due to the melting of these less well-formed crystal structures, in line with results obtained by Majewski *et al* [94] and Liu *et al* [114].

It can be noted that for isothermal temperatures of 120 °C, 130 °C and 140 °C, the melting endotherm has the same characteristic shape with a lower temperature shoulder (peak I) starting at around 188 °C and a principal endotherm (peak II) at around 195 °C. However, at higher isothermal temperatures the endotherm's shape progressively alters, with the lower temperature shoulder becoming the dominant endotherm. At an isothermal temperature of 170 °C, there is a single melting endotherm at 193 °C. The peak positions as a function of isothermal crystallisation temperature are plotted in Figure 4.8.

T_c (°C)	170	160	150	140	130	120
n	2.64	2.21	1.99	1.88	1.59	1.45
K (min^{-1})	0.02	0.06	0.43	1.35	1.87	2.69
t_{max} (min)	4.06	2.67	1.08	0.57	0.36	0.22
$t_{1/2}$ (min)	3.08	2.04	0.84	0.45	0.32	0.22
$\tau_{1/2}$ (min)	0.32	0.49	1.20	2.23	3.15	4.54

Table 4.3: The kinetic parameters for the low-temperature isothermal crystallisation of Nylon-12.

Figure 4.9 shows the values of $X(t)$ vs t for the isothermal crystallisation. It can be seen that the characteristic sigmoidal isotherms are shifted along the time axis as T_c increases, indicating a progressively slower crystallisation rate. It is notable that below $T_c = 150$ °C, the actual temperature at which the samples crystallise does not change. Therefore, even for samples isothermally crystallised at $T_c = 120 - 140$°C, the actual crystallisation temperature (T_c^{actual}) barely drops below 150 °C. This is shown in Table 4.4; the reasons for this phenomenon are discussed in more detail in Section 4.2.2.

The half-time of crystallisation $t_{1/2}$ is extracted directly from the $X(t)$ versus t plots in Figure 4.9. $t_{1/2}$ increases with T_c increasing for lower super-cooling degree [114]. The rate of crystallisation $G = (t_{1/2})^{-1}$ and time of maximum crystallisation rate t_{max} are also calculated from this data, as per Section 1.2.5.

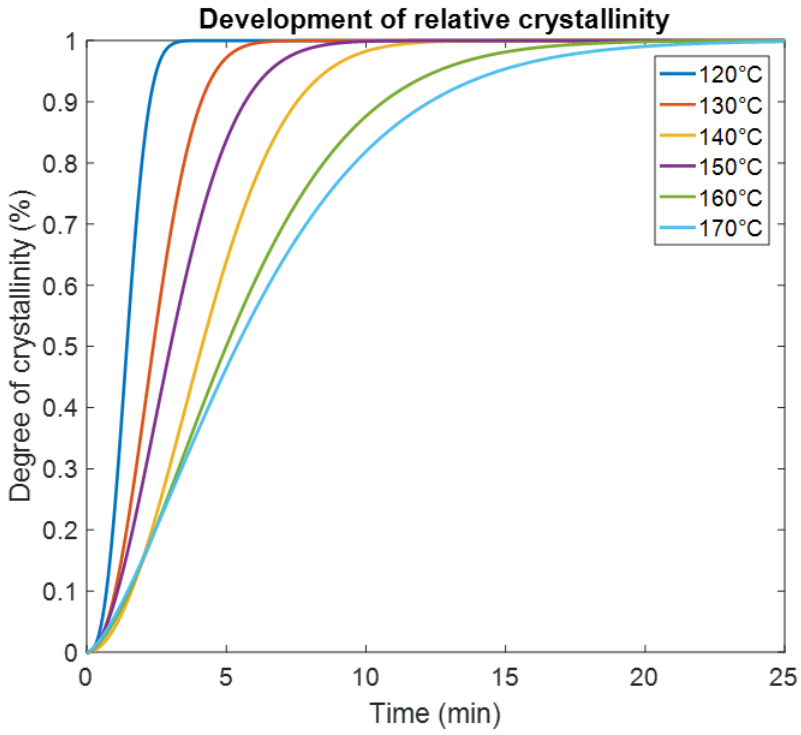


Figure 4.9: Relative crystallinity X(t) as a function of time for the isothermally crystallised samples.

T_c (°C)	170	160	150	140	130	120
T_m (II) (°C)	193.05	190.56	195.01	195.10	194.89	194.86
T_c^{actual} (°C)	178.81	168.13	155.68	148.22	151.31	150.28

Table 4.4: Melting temperatures for peak II (T_m (II)) and actual crystallisation temperatures (T_c^{actual}) for the low-temperature isothermal crystallisation experiments

The Avrami parameter n and rate parameter K are calculated from the double logarithmic plot as described in Section 1.2.5. This double logarithmic plot of $\ln(-\ln(1-X(t)))$ vs $\ln t$ is shown in Figure 4.10. The Avrami parameter n and rate parameter K can be derived from Equation 1.8 by fitting the linear components of the double logarithmic plot using a least squares fit. It can be seen that the Avrami parameter n varies from 1.44 to 2.64 depending on crystallisation temperature T_c, while the rate constant K increases as T_c decreases. A higher T_c results in higher n but lower K. The latter is to be expected as the crystallisation process is shown in Figure 4.9 to take place considerably quicker as T_c decreases. n drops below 2 as T_c drops below 150 °C. It is therefore hypothesised that at higher T_c the growth is

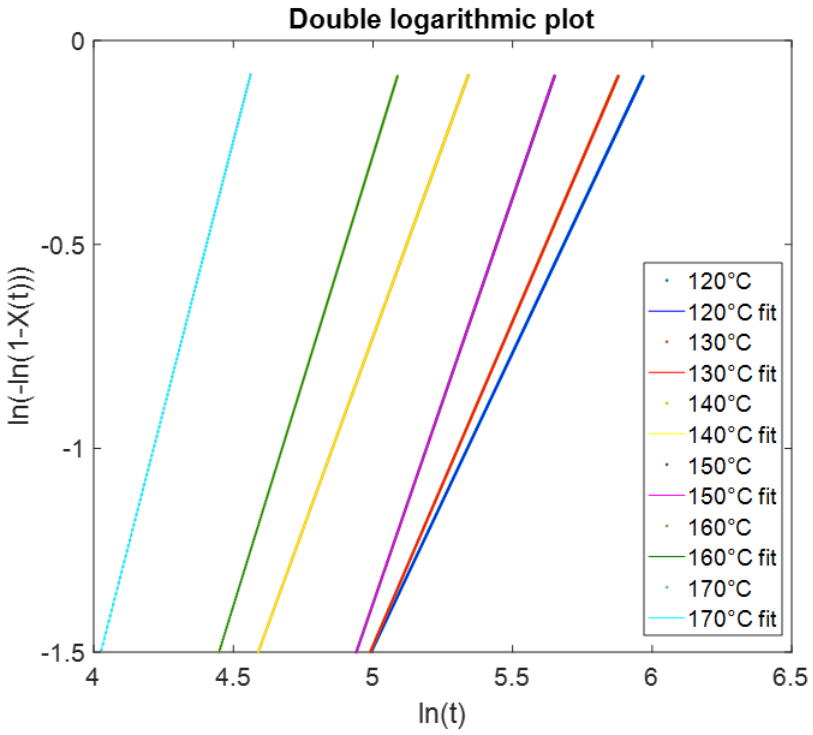


Figure 4.10: The double logarithmic plot of $\ln(-\ln(1-X(t)))$ versus $\ln(t)$ for the isothermal crystallisation experiments.

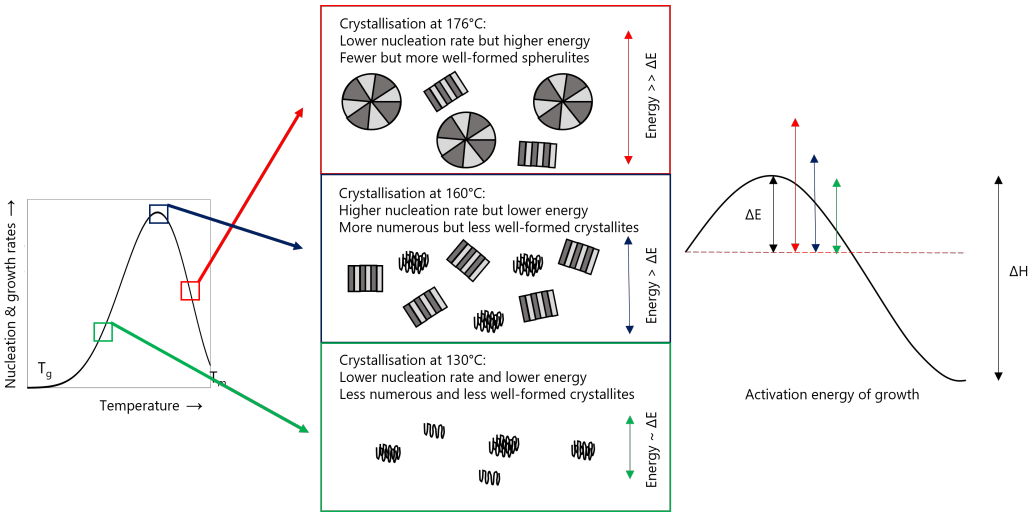


Figure 4.11: An illustration of how different isothermal crystallisation temperatures affect the type of crystal structure formed, and how this relates to the growth activation energy and constraints on nucleation rate. Although the nucleation and growth rates may be below their peak at 176 °C, the increased internal energy given by the higher T_c can more readily overcome the activation energy for growth (illustrated in the rightmost curve), resulting in more well-formed crystal structures.

two-dimensional diffusion-controlled growth with some spatial restriction, whereas at lower T_c the growth is constrained to one-dimensional needle-like growth. The hypothesised nature of the nucleation and growth of the crystal structure at different isothermal crystallisation temperatures is illustrated in Figure 4.11.

The kinetic parameters associated with isothermal crystallisation n, K, t_{max}, $t_{1/2}$, G are calculated for this dataset as above and as described in Section 4.2.1.1, and are listed in Table 4.3.

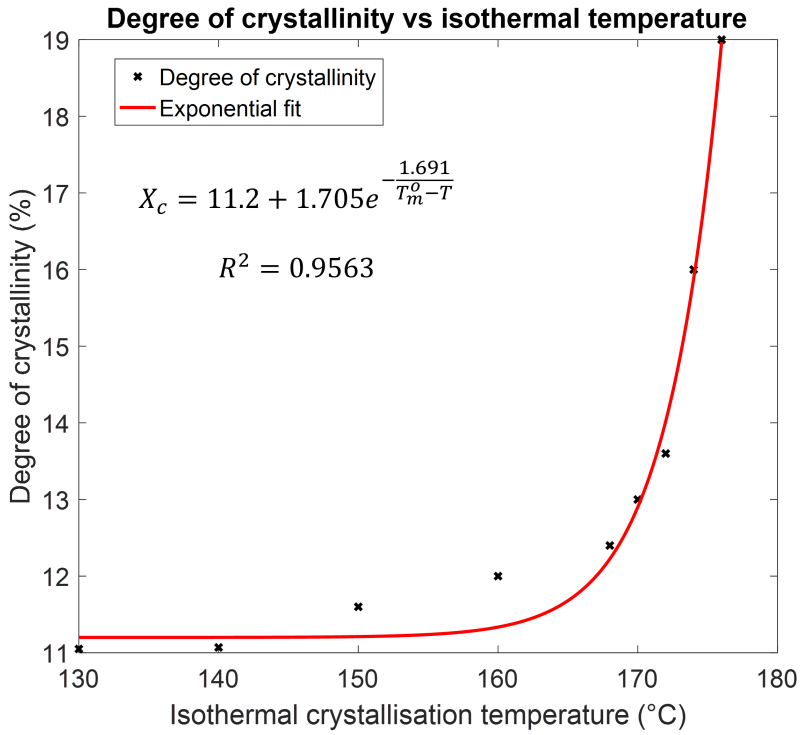


Figure 4.12: Degree of crystallinity vs T_c, fitted with an exponential function.

Figure 4.12 show the degree of crystallinity for all isothermally crystallised samples plotted against the temperature of isothermal crystallisation T_c. The results show that between 130 °C and 168 °C, the degree of crystallinity increases steadily, with a rapid increase occuring between 168 °C and 176 °C. This is in line with the shape of the melting endotherms for the isothermal crystallisation experiments, as $T_c = 130 - 150$°C crystallisation shows similar melting endotherms, with a characteristic double peak.

The single peak observed in the high temperature isothermal crystallisation experiments and at 170 °C in the low temperature isothermal crystallisation experiments is therefore correlated with a considerably higher degree of crystallinity, and the change in gradient of X_c vs T_c occurs around 168 °C, where the transition from double peak to single peak is expected to have fully occurred. The values of degree of crystallinity for each T_c are shown in Table 4.5 and are plotted in Figure 4.12. The plot is fitted with an exponential function based on the Hoffman growth model described in Section 1.2.5.

T_c (°C)	130	140	150	160	168	170	172	174	176
X_c (%)	11.1	11.0	11.6	12.0	12.4	13.0	13.6	16.0	19.1

Table 4.5: The degree of crystallinity for the samples crystallised via both high- and low-temperature isothermal crystallisation.

4.2.2 Non-isothermal crystallisation of Nylon-12

The DSC heat flow traces obtained for the non-isothermal measurements between 2 and 40 °C/min are depicted in Figure 4.13.

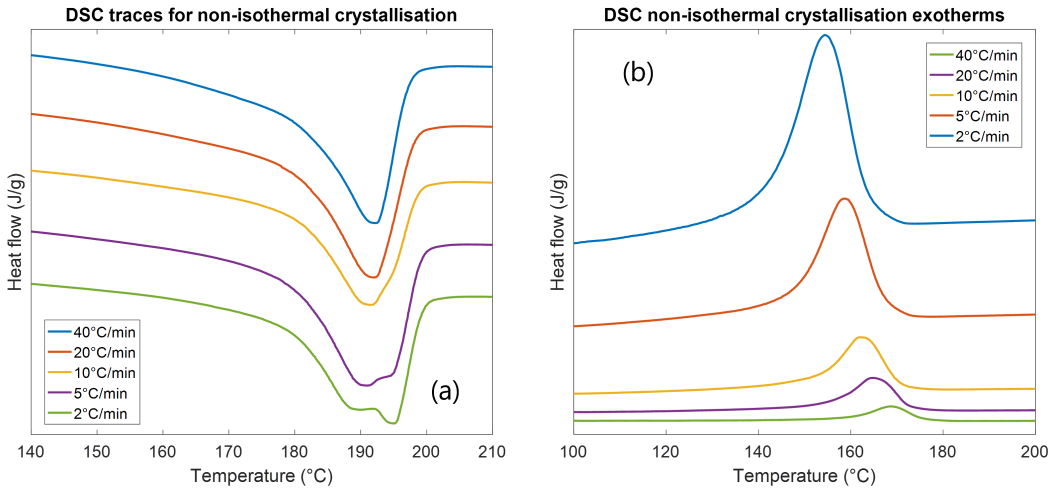


Figure 4.13: (a) DSC thermograms for samples reheated at 10 °C/min after non-isothermal crystallisation at different cooling rates. (b) shows the DSC thermograms during crystallisation.

Figure 4.13(a) shows the melting endotherms during sample reheating after non-isothermal crystallisation. The melting enthalpy ΔH_c is calculated as being

the area under this heat flow trace. It can be observed that there is a continual evolution of the shape depending on the attendant cooling rate. At 2 °C/min the endotherm shows a single peak, whereas a double peak appears at faster cooling rates. The primary melting endotherm, as shown most clearly in the curve obtained at 2 °C/min, is designated as Peak I. This can be seen to shift to a progressively lower temperature as the cooling rate increases to 40 °C/min. The secondary melting endotherm which manifests itself at cooling rates above 10 °C/min, is designated Peak II. In particular, the ratio of the magnitudes of the peaks within the doublet alters as a function of the cooling rate. The characteristic double peak with principal exotherm at 195 °C and lower temperature shoulder only appears at the cooling rates equal to or in excess of 40 °C/min. This is plotted as a function of the cooling rate in Figure 4.14.

Figure 4.13(b) shows the DSC traces during non-isothermal crystallisation between 2 and 40 °C/min from melt. It can be observed that a slower cooling rate leads to a shift of the crystallisation onset temperature T_{ic} towards a higher temperature. The peak of the crystallisation exotherm is also shifted considerably towards higher temperatures, whilst the magnitude of the exotherm decreases.

Φ (cooling rate)	2 °C/min	5 °C/min	10 °C/min	20 °C/min	40 °C/min
T^* (°C)	168.7	164.8	162.2	158.8	154.5
$t_{1/2}$ (min)	10.1	4.17	1.56	0.91	0.69
ΔH_c (J/g)	36.5	36.8	35.5	33.6	30.1
n	2.04	2.61	2.21	2.30	3.16
Z_c (min^{-1})	0.02	0.02	0.28	0.97	2.53

Table 4.6: The kinetic parameters for the non-isothermal crystallisation of Nylon-12.

A clear comparison can be made between the melting endotherms from the second heating cycle in both the isothermal and non-isothermal crystallisation experiments. The isothermal 170 °C peak resembles the peak obtained from crystallising non-isothermally at 2 °C/min peaks. Correspondingly, the isothermal 160 °C peak resembles the non-isothermal 20 °C/min peak, and lower isothermal temperatures resemble to the non-isothermal 40 °C/min peak. It can therefore

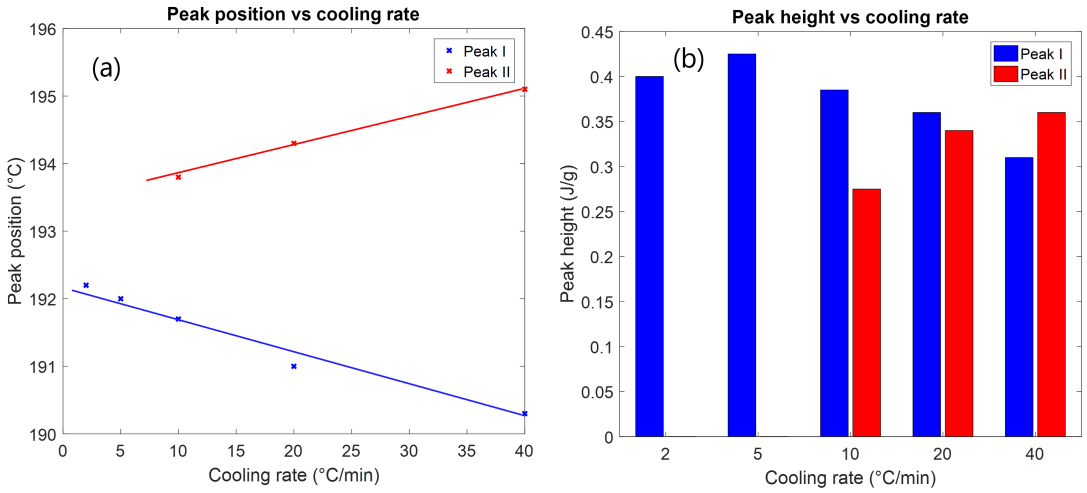


Figure 4.14: Peak positions and magnitude ratios for the non-isothermal crystallisation. (a) shows the evolution of temperature values at peak maximum, and (b) shows peak heights as a function of cooling rate.

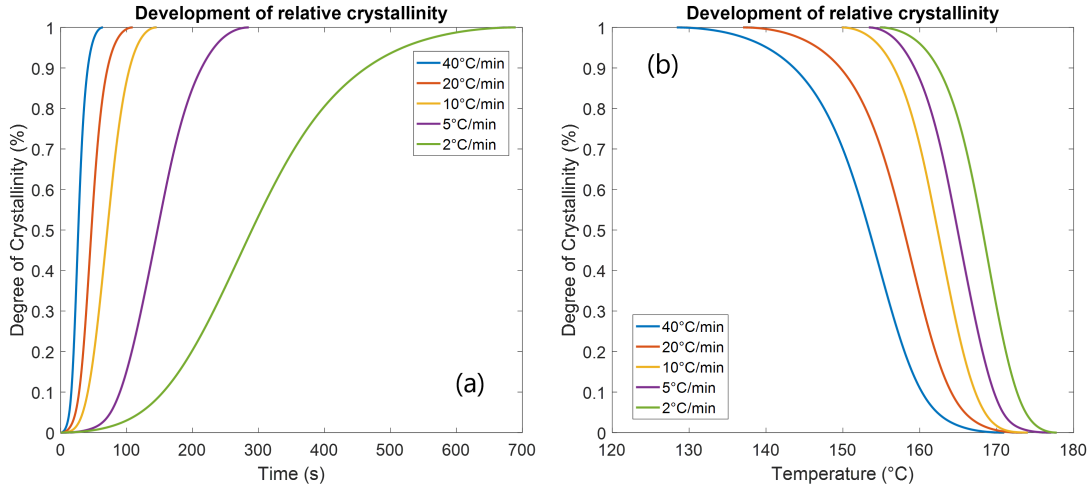


Figure 4.15: Relative crystallinity X(t) as a function of (a) time and (b) temperaturefor the non-isothermally crystallised samples.

be concluded that low-temperature isothermal crystallisation has the same effect on the crystal microstructure as non-isothermal rapid cooling. The emergence of a lower temperature shoulder as the cooling rate increases is concluded to be due to the presence of less well formed crystal structure at higher cooling rates, analogous to the conclusions drawn in Section 4.2.1.2.

Figure 4.15(a) and (b) show the $X(t)$ values obtained as functions of T and t. It is clear that a higher cooling rate leads to a shorter time of crystallisation completion.

Figure 4.16 shows the double logarithmic plot of $\ln(-\ln(1-X(t)))$ versus

$\ln(t)$ for the non-isothermal crystallisation. Linearity is observed for the non-isothermal crystallisation, from the gradient of which the rate parameter Z_c and Avrami parameter n can be calculated. It can therefore be concluded that the non-isothermal case results in a single-phase crystallisation.

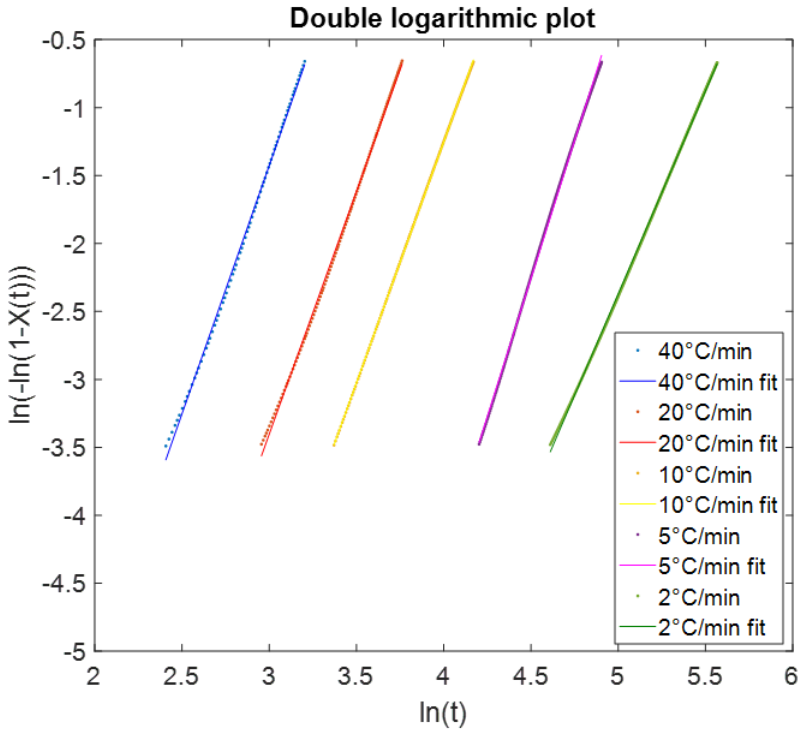


Figure 4.16: The double logarithmic plot of $\ln(-\ln(1-X(t)))$ versus $\ln(t)$ for the non-isothermal crystallisation experiments.

The range of the Avrami parameter, from 2.04 to 3.16 in the primary crystallisation stage, shows that the mode of nucleation and growth may be one- and two-dimensional space extension, diffusion controlled growth with thermal nucleation. The higher values of n compared to the isothermal crystallisation case indicates that the crystal growth process has become more complicated. Notably, the values of n and Z_c decrease with the cooling rate. This indicates that per unit time, a greater proportion of crystallisation is complete at a higher cooling rate. Furthermore, it indicates that a higher cooling rate results in random nucleation sites, whereas at a slower cooling rate the nucleation and growth sites are non-random and restricted. This hypothesised crystal growth is illustrated in Figure

4.17, where it is also compared with the XRD data and model of crystallisation behaviour proposed in Chapter 3.

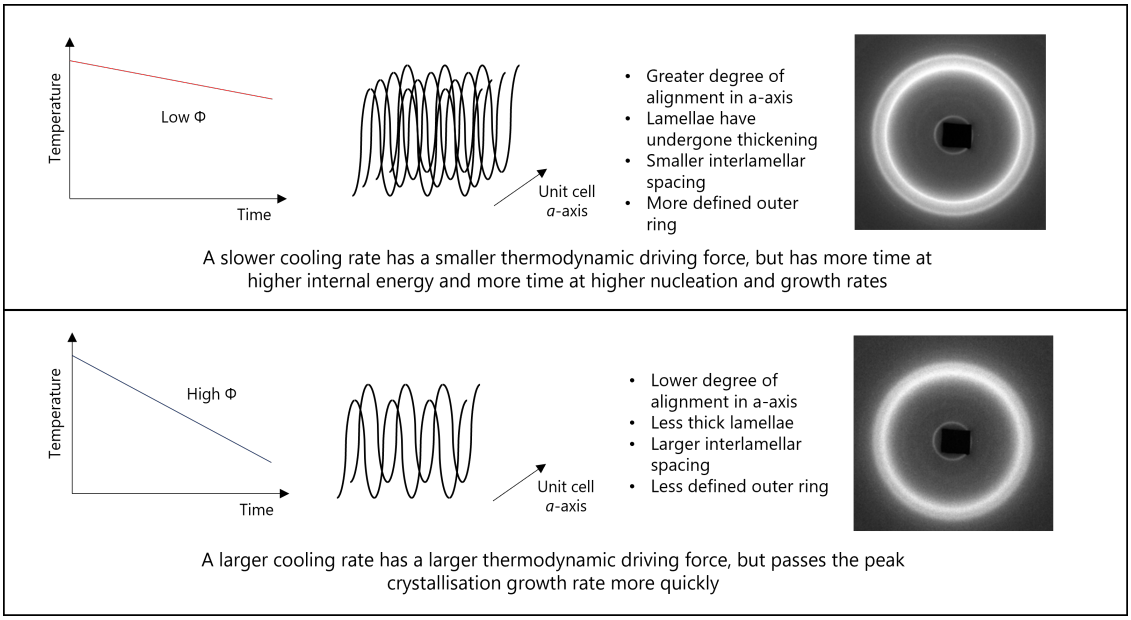


Figure 4.17: An illustration of how different cooling rates affect the type of crystal structure formed, and how this manifests itself on the DSC and WAXS data. The parallel chain structures represent single layers of lamellae, which stack together at slower cooling rate.

The temperature of peak crystallisation rate T^*, crystallisation half-time $t_{1/2}$ and melting enthalpies ΔH_c, along with Avrami parameter n and rate parameter Z_c for the different cooling rates are listed in Table 4.6.

4.2.3 DSC of FFF Nylon-12 samples with varying thermal history

The results of the second heating of the DSC thermal cycling of Nylon-12 samples with varying thermal history are presented below. This is split into two sections, as follows:

1. **Section 4.2.3.1: Printed samples vs Nylon-12 filament**

2. **Section 4.2.3.2: Printed Nylon-12 samples with incrementally varying thermal history**

Section 4.2.3.1 presents a comparison between the DSC data for raw Nylon-12 filament and FFF Nylon-12 samples printed with two different ambient temperatures (T_{amb}): (i) T_{amb} = 25 °C (referred to below as FFF RS) and (ii) T_{amb} = 120 °C (referred to below as FFF Apium). This section examines the thermal properties that FFF imparts on Nylon-12, and considers the difference in the crystalline structure that variation in T_{amb} can impart.

Section 4.2.3.2 presents the DSC data for FFF Nylon-12 samples produced with T_{amb} varying from 120 to 190 °C, in increments of 10 °C. Post-print annealing was used to simulate the effect of printing at such a high T_{amb}.

4.2.3.1 Printed samples vs Nylon-12 filament

Figure 4.18 demonstrates the DSC thermal behaviour of the FFF parts and filament. A clear distinction can be drawn between the melting endotherms for each sample. A large endothermic peak can be seen at a temperature of around 197 °C; the magnitude of the endotherm becomes larger for the samples produced by FFF compared to the filament feedstock. In addition, a shoulder is seen on the low-temperature side for the FFF-produced samples, which is not present for the filament.

The shoulder and principal endotherm are due to the melting of γ-form crystals, as shown by the XRD results. In addition, XRD analysis showed that the FFF samples show the 200 reflection peak in different proportions, whereas the raw filament does not. It is therefore proposed that the large shoulder that appears in the melting endotherms of the FFF samples is due to the same crystal morphology that leads to the appearance of the 200 XRD reflection. The principal endotherms are likewise proposed to be due to the melting of the crystal morphology corresponding to the $001(+20\bar{1})$ peak.

4.2.3.2 Printed Nylon-12 samples with incrementally varying thermal history

The DSC melting endotherms for the samples printed with incrementally varying thermal history are shown in Figure 4.19.

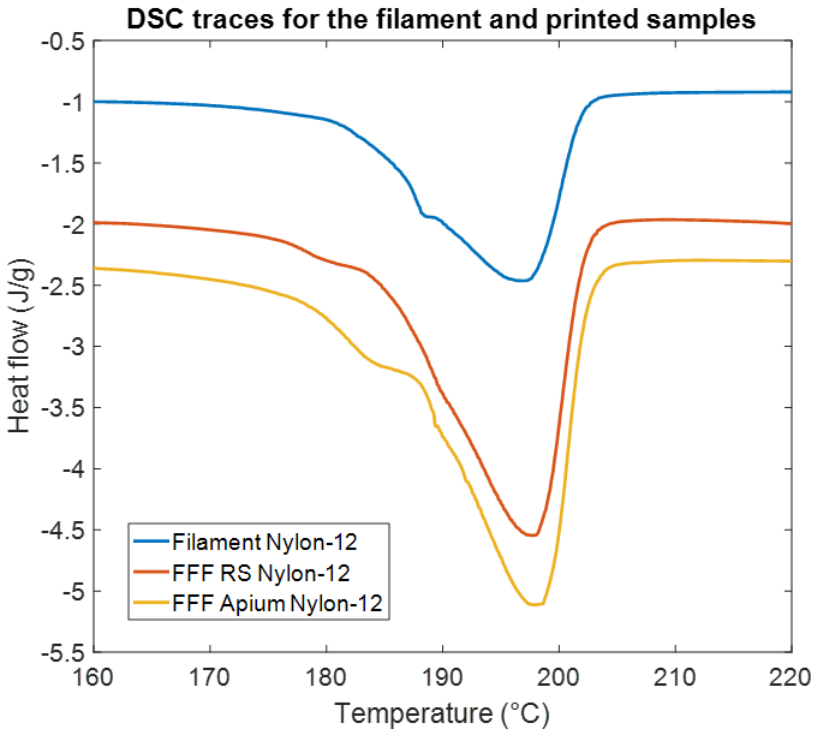


Figure 4.18: DSC thermograms for the first heating cycle of all three samples. Note the presence of the shoulder at 184 °C corresponding to the presence of the 200 reflection.

T_c (°C)	120	130	140	150	160	170	180	190
Peak I (°C)	197.1	196.3	196.8	197.7	197.1	197.1	197.1	200.3
Peak II (°C)	-	-	180.3	182.1	184.3	187.6	186.7	187.3
X_c (%)	17.8	18.3	18.7	19.1	19.9	22.7	24.6	28.7

Table 4.7: Melting temperatures for peak I and II and degree of crystallinity X_c for the FFF Nylon-12 samples

The samples were printed at a chamber and bed temperature of 120 °C and immediately annealed for 60 minutes at temperatures between 130 and 190 °C. The peak positions and degree of crystallinity for these samples are shown in Table 4.7.

It can be observed that between T_c = 120 and 150 °C, a single peak with a shoulder is seen on the DSC trace. This is the same single peak seen in the Apium sample in Figure 4.18; an overlay of the Apium single peak on a DSC trace from the printed samples is shown in Figure 4.20. The appearance of the single peak with shoulder between 120 and 150 °C is consistent with the data from the low temperature isothermal crystallisation experiments, where it was established that crystallisation had taken place by 155 °C, resulting in highly similar DSC melting

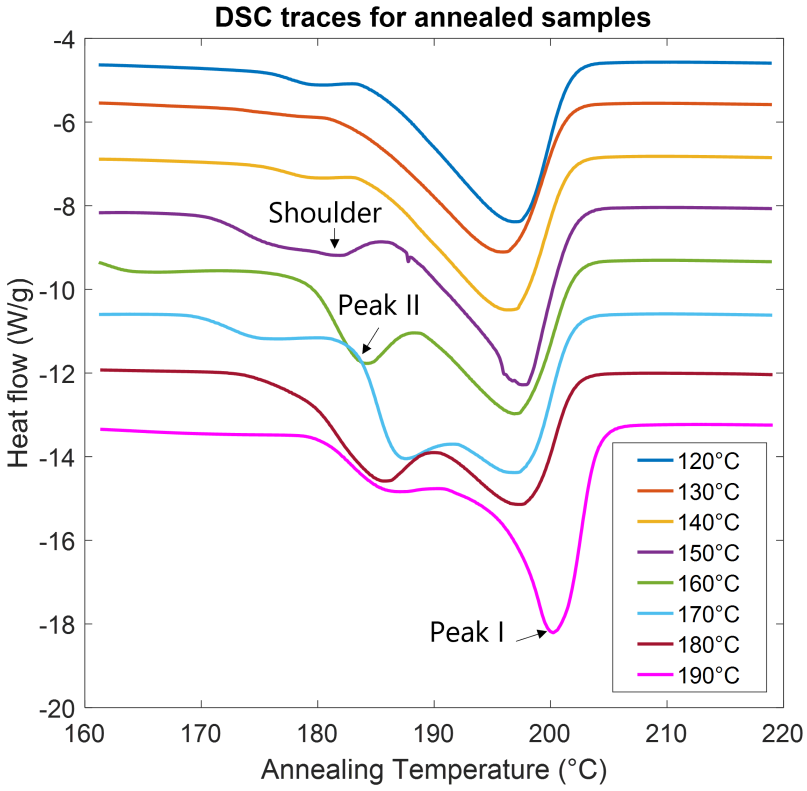


Figure 4.19: DSC thermograms for the heating of all FFF samples printed at varying thermal history. The peaks and shoulder are identified.

endotherms for samples isothermally crystallised at 150 °C.

However, the reason for the single rather than double DSC peak in FFF-produced samples remains unclear. It is hypothesised that the reheatings due to deposition of subsequent layers may contribute to the formation of larger crystallites, which are resolved into a single peak during melting. This is borne out by an analysis of the degree of crystallinity of the samples, which is shown in Figure 4.21 and Table 4.7. It can be observed that the degree of crystallinity of the FFF-produced samples is considerably higher at the same T_c than those of the isothermally crystallised samples.

Based on this, it was decided to fit the degree of crystallinity data with the following relation:

$$X_c = A + Be^{\frac{C}{T_m^0 - T}} \tag{4.4}$$

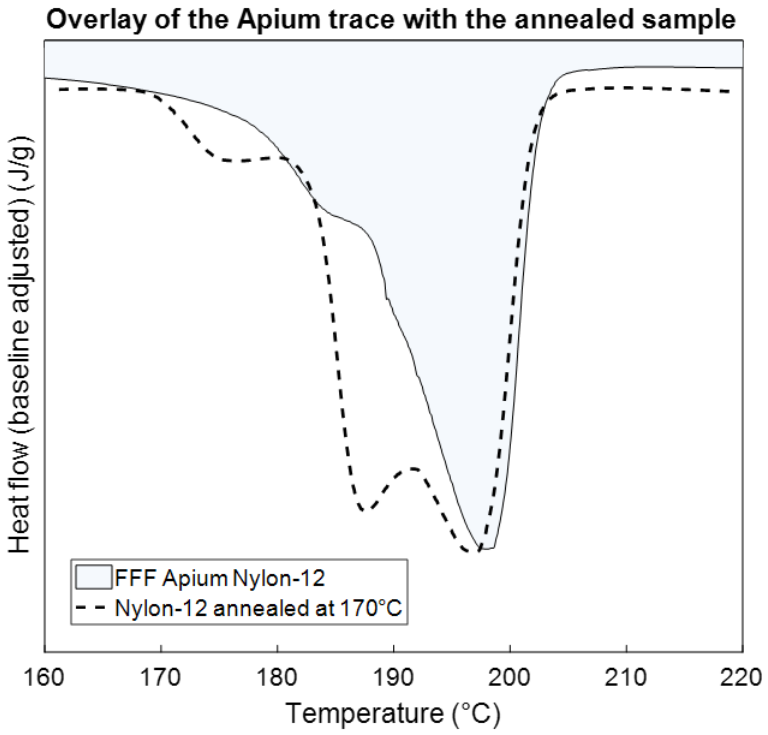


Figure 4.20: Overlay of the Apium FFF single peak from Figure 4.18 on a DSC trace from the FFF sample prepared at 170 °C.

The coefficients were calculated as $A = 35.2, B = -21.35, C = -16.33$ with $R^2 = 0.9787$. The value for A represents the theoretical maximum attainable crystallinity obtainable via FFF/heat treatment under the conditions for these experiments. Figure 4.21 shows a 61% increase in degree of crystallinity over a 58% increase in print chamber temperature.

At 150 °C, the low-temperature shoulder characteristic of the FFF samples becomes more prominent, and is classified as a peak in its own right. This is described in Table 4.7 and Figure 4.19 as Peak II. This peak becomes progressively more prominent as T_c increases, and also increases in temperature. However, above 170 °C, the peak position does not change and in fact decreases whilst also becoming less prominent in magnitude. As the sample preparation temperature rises, Peak I once again becomes more prominent, dominating at 190 °C. This is shown in Table 4.7 and is plotted in Figure 4.22. The behaviour of the position of the two peaks is similar to that seen in the isothermal crystallisation experiments, which is plotted in Figure 4.8(a).

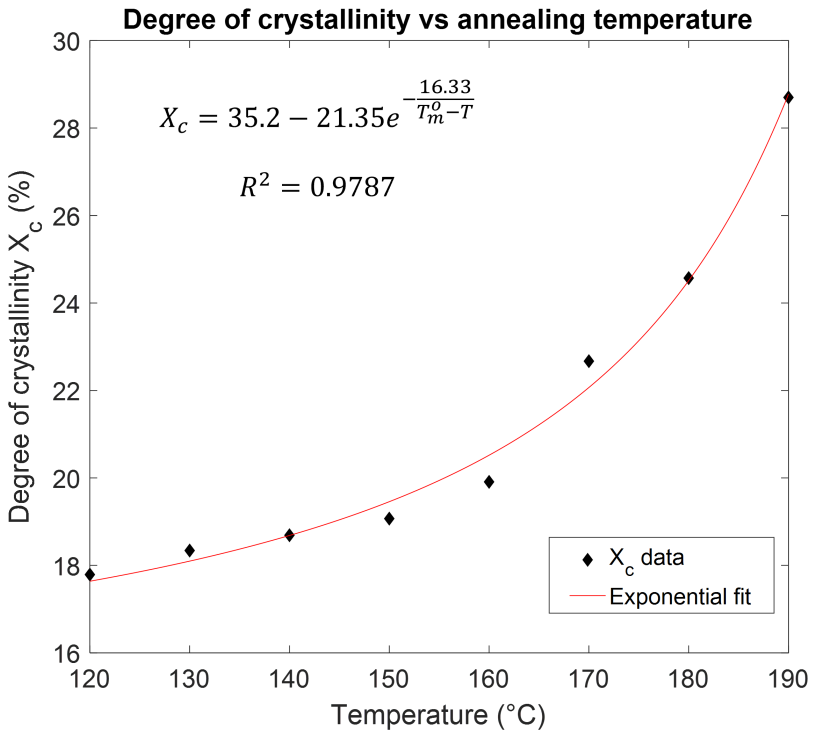


Figure 4.21: Degree of crystallinity for all FFF samples, plotted against their preparation temperature.

It is notable that while Peak II increases in temperature as T_c rises, the values of the temperatures for this peak are lower than that seen in the isothermal crystallisation experiments. This may be due to the fact that the samples prominently displaying Peak II had already undergone some crystallisation prior to their annealing during the FFF process. This is borne out by the fact that the two peaks seen for the 170 °C sample are a convolution of the FFF peak, formed from printing at 150 °C, and the 170 °C peak due to the isothermal post-annealing. This is shown in Figure 4.20. In addition, it is notable that the 190 °C sample has a significant shift in Peak I position, from 197 °C to 200 °C, accompanied by a jump in degree of crystallinity. This may indicate that at very high operating temperatures close to T_m, there is significant reformation of the crystal structure.

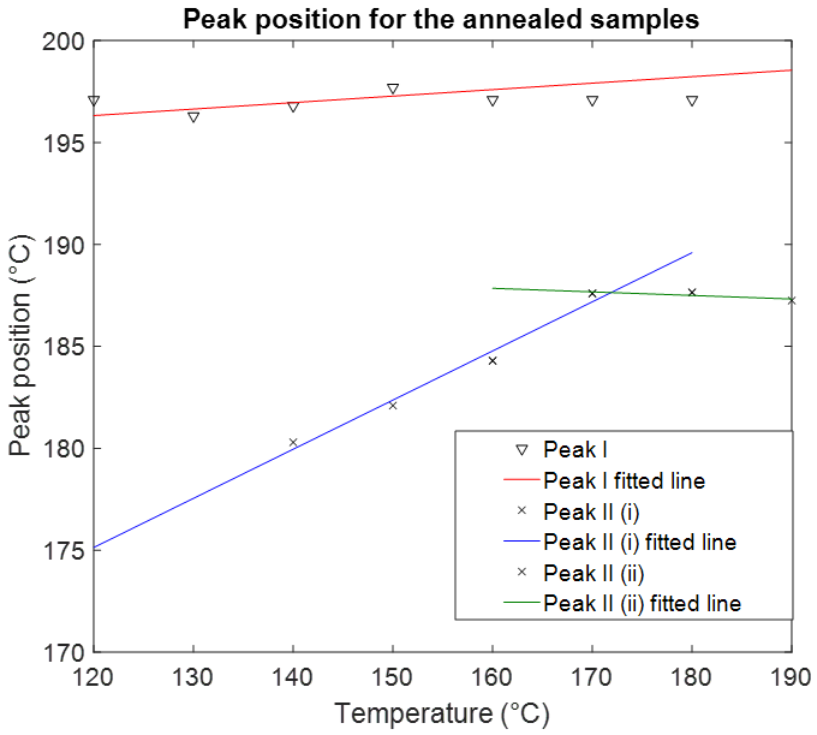


Figure 4.22: The position of Peak I and Peak II in °C plotted against T_c

4.3 Analysis

4.3.1 Isothermal crystallisation

Analysis of the data was undertaken using Hoffman-Lauritzen theory [15]. The growth rate constant K_0 and the nucleation rate constant K_g were obtained from the isothermal measurements using the temperature dependence of $t_{1/2}$:

$$\ln\left(\frac{1}{t_{1/2}}\right) + \frac{U^*}{R(T - T_\infty)} = \ln K_0 - \frac{K_g(T + T_m^0)}{2T^2\Delta T} \tag{4.5}$$

The double logarithmic plot of $\ln(1/t_{1/2}) + U^*/R(T - T_\infty)$ vs $(T + T_0)/(2T^2\Delta T)$ is shown in Figure 4.23. K_g is given by the straight line slope, and K_0 is determined from the y-axis interception. K_0 was found to be 30,981 s^{-1} and K_g was found to be 83283 K^2. The comparable values from Zhao's [16] study on powderised Nylon-12 are 37,869 s^{-1} and 136,235 K^2, which fall within an order of magnitude of these results. These obtained values form the basis of modelling in Chapter 5.

Analysis of the nucleation activation energy for the crystallisation process of Nylon-12 was performed in accordance with Arrhenius theory, using the method

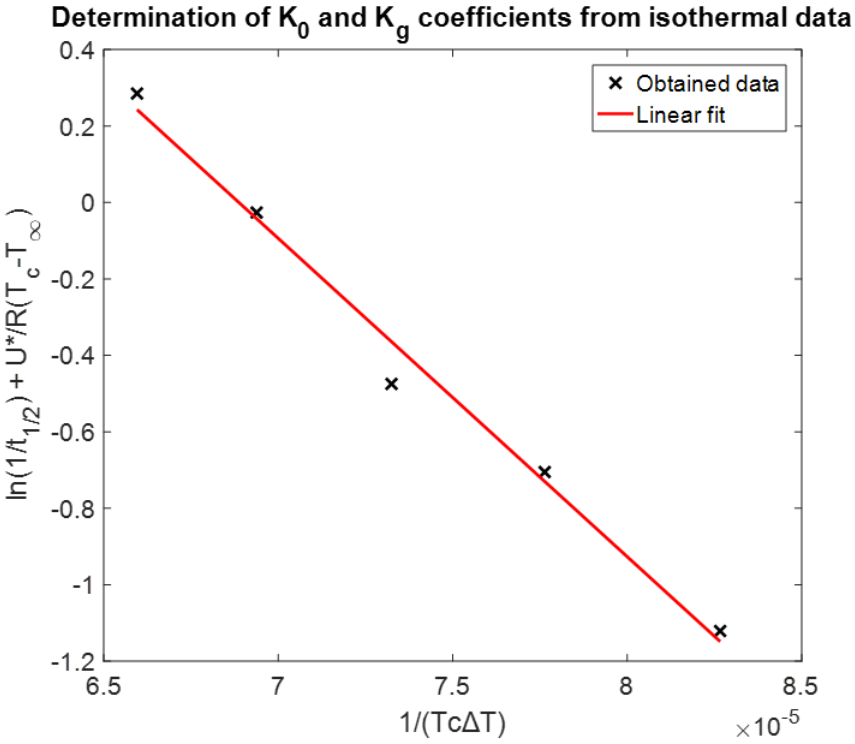


Figure 4.23: Plot of $\ln(1/t_{1/2}) + U^*/R(T - T_\infty)$ vs $(T + T_0)/(2T^2\Delta T)$. K_0 and K_g are calculated from the intercept and slope respectively.

in Liu *et al.* [114]. The crystallisation process is thermally activated, as both the nucleation and growth stages are temperature dependent. The Arrhenius equation [135] therefore applies:

$$K^{\frac{1}{n}} = k_0 e^{-\frac{\Delta E}{RT_c}} \tag{4.6}$$

where k_0 is a temperature-independent pre-exponential factor, R is the ideal gas constant and ΔE is the crystallisation activation energy. Taking the logarithm of Equation 4.6 yields the following relation:

$$\frac{1}{n} \ln K = \ln k_0 - \frac{\Delta E}{RT_c} \tag{4.7}$$

ΔE can therefore be obtained from a plot of $1/n \ln K$ vs $1/T_c$, which is shown in Figure 4.24. The value of the nucleation activation energy was found to be -201.12 kJ/mol.

Crystallisation is an exothermic reaction with negative enthalpy as the bonding of chain folds onto lamellar sites is energetically favourable, and the heat released is

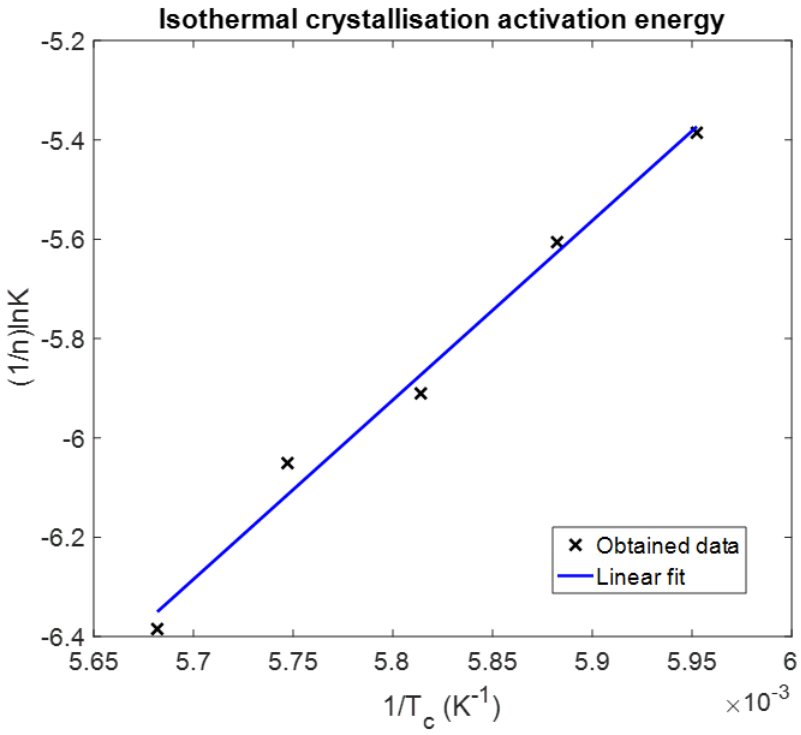


Figure 4.24: Plot of $1/n \ln K$ vs $1/T_c$, determining the activation energy of isothermal crystallisation for Nylon-12.

the latent heat of crystallisation. However, the nucleation activation energy ΔE is also negative, which is a trait unique to polymer crystallisation. It may be recalled from Figure 1.6 that the crystal growth rate displays a maximum, driven by both degree of supercooling and viscosity. In general, decreasing temperature causes a reaction rate to slow down in accordance with the Arrhenius equation, which also occurs in polymer crystallisation after the crystallisation rate maximum has been passed. However, at higher crystallisation temperatures, the crystallisation rate increases with decreasing temperature. This is sometimes known as anti-Arrhenian behaviour and means that the corresponding activation energy is negative.

Due to the variance between obtained values of T_m and T_m^0 and literature values for Nylon-12, additional verification was necessary to ensure that the Nylon-12 filament used in this experiment underwent a primary crystallisation which could be well-described by the Avrami equation. This analysis was performed based

on the Turnbull-Fisher equation[136]:

$$\ln G = \ln G_0 - \frac{\Delta E}{kT_c} - \frac{\Delta F}{kT_c} \tag{4.8}$$

where G is the spherulitic growth rate, k is the Boltzmann constant and ΔF is the free energy barrier to formation of a nucleus. $\Delta E/kT_c$ can be described as the transportation term, and $\Delta F/kT_c$ as the nucleation term.

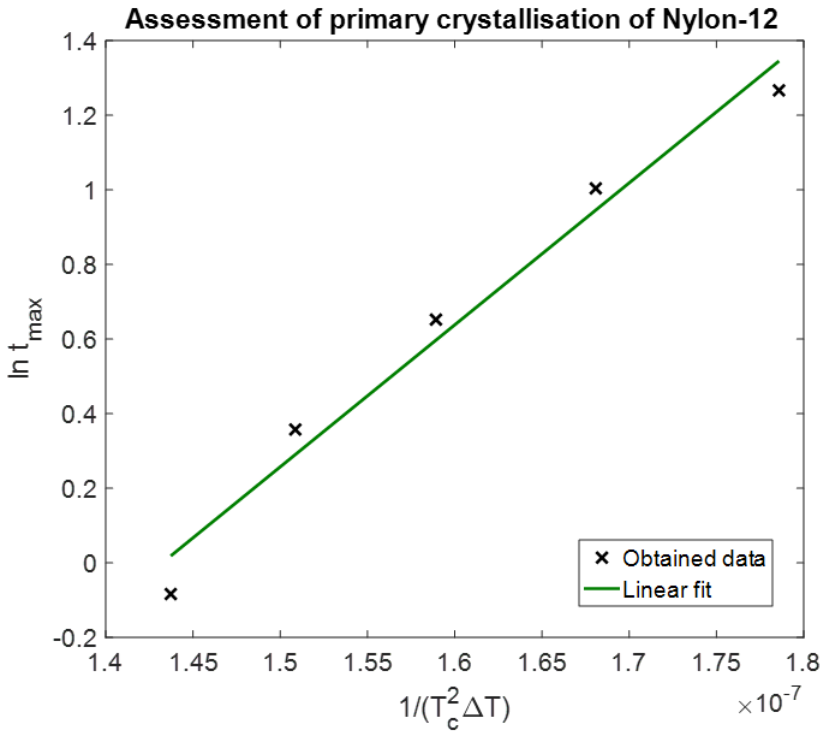


Figure 4.25: Plot of $\ln t_{max}$ vs $1/(T_c^2\Delta T)$, verifying that the crystallisation behaviour of Nylon-12 in filament form fits the Avrami theory.

At low temperatures, the transportation term is dominant, while as T_c approaches T_m, the nucleation term dominates. The relationship of these two terms as a function of T_c leads to a theoretical maximum value of crystallisation rate as a function of temperature, which is discussed further in Chapter 5. For T_c close to T_m, as in the high-temperature isothermal crystallisation case, the nucleation term dominates, giving:

$$\ln G = \ln G_0 - \frac{\Delta F}{kT_c} \tag{4.9}$$

The free energy barrier to the formation of a nucleus ΔF was calculated for substances with a glass transition temperature by Hoffman [137]], and for temperatures high above T_g such as those used in this study was approximated by Van Antwerpen *et al* [138] to give:

$$\ln G = \ln G_0 - \frac{\chi T_m^0}{T^2(T_m^0 - T_c)} \tag{4.10}$$

Lin [14] used the expression for t_{max} shown in Equation 2.7 to demonstrate that $t_{max} \propto K^{-1/n}$. Since G is related to rate parameter K by $G \propto K^p$ where p is a constant, it was obtained that $t_{max} \propto G^{-p/n}$. Therefore, it was derived [14, 139] that:

$$\ln t_{max} = B - \frac{C}{2.3T_c^2\Delta T} \tag{4.11}$$

where B and C are constants, and $\Delta T = T_m^0 - T_c$.

Then, Avrami-compatible primary crystallisation can be verified by plotting $\ln t_{max}$ vs $1/(T_c^2\Delta T)$. This is shown in Figure 4.25. The plot is fitted closely by a linear function, indicating that the behaviour of the Nylon-12 filament is nevertheless compatible with the linear relation in Equation 4.11, and thus primary crystallisation at t_{max} can be assumed for the operational limits of the thermal analysis.

Although the low-temperature isothermal crystallisation falls significantly below obtained values for T_m, thereby bringing the transportation term into play and altering this relation, the lowest T_c used is still sufficiently above obtained values of T_g that Avrami primary crystallisation can still be assumed to dominate. The impact of the transportation term and additional modes of crystallisation can be seen in the DSC curves in Figure 4.7, where the second melting endotherm indicates the presence of microcrystallites.

The isothermal transformation dynamics of a materials can be understood through plotting its time-temperature transformation (TTT) diagram. This is a plot of the percentage volume transformation of the material's crystal phases over time, with phase contour lines being plotted on time-temperature axes [140]. Here, the TTT diagram for Nylon-12 is plotted for 10%, 50% and 90% relative crystallinity conversion, as shown in Figure 4.26. As the heat flow peak for the

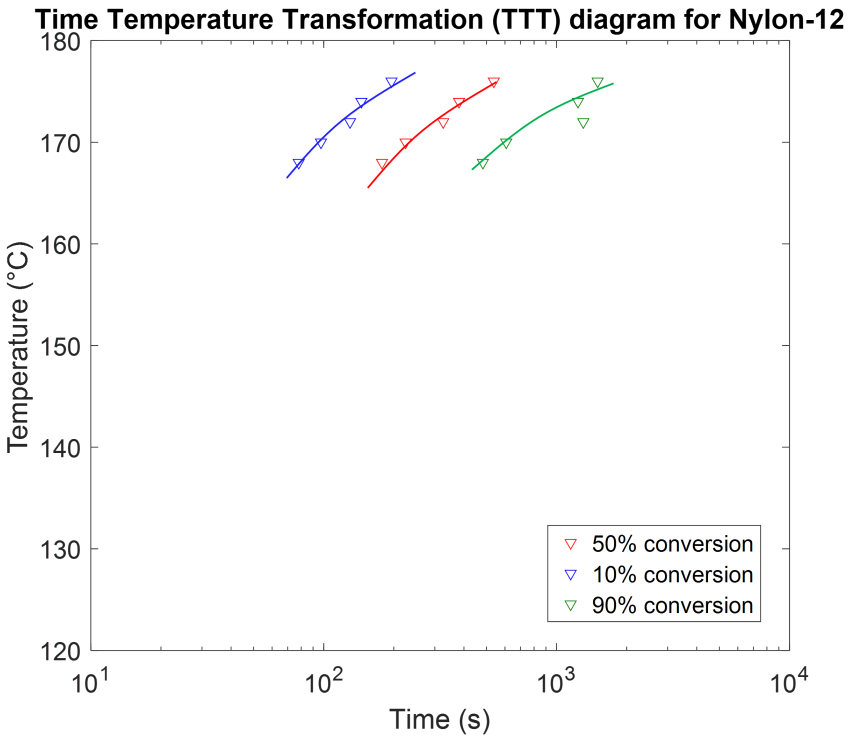


Figure 4.26: Time-temperature transformation (TTT) diagram for Nylon-12 filament.

isothermal crystallisation experiments is extrapolated for small t, as per Equation 4.3, data for $X(t) < 10\%$ is not included on the TTT diagram.

4.3.2 Non-isothermal crystallisation

The crystallisation activation energy for non-isothermal crystallisation was analysed according to Kissinger's method [141], which reported that nucleation activation energy ΔE could be determined by:

$$\frac{d(\ln(\Phi/T^{*2}))}{d(1/T^*)} = -\frac{\Delta E}{R} \tag{4.12}$$

where T^* is the temperature at peak crystallisation rate, and Φ is the cooling rate. The plot of $\ln(\Phi/T^{*2})$ vs $1/T^*$ is shown in Figure 4.27. According to equation 4.12, the slope is given by $-\Delta E/R$, therefore giving ΔE = T-340.71 kJ/mol for Nylon-12.

Analysis of the non-isothermal crystallisation process via a combination of the Avrami equation and the Ozawa equation was undertaken. This relates the cooling rate Φ to time t, using the kinetic approach taken by Zhang and Mo

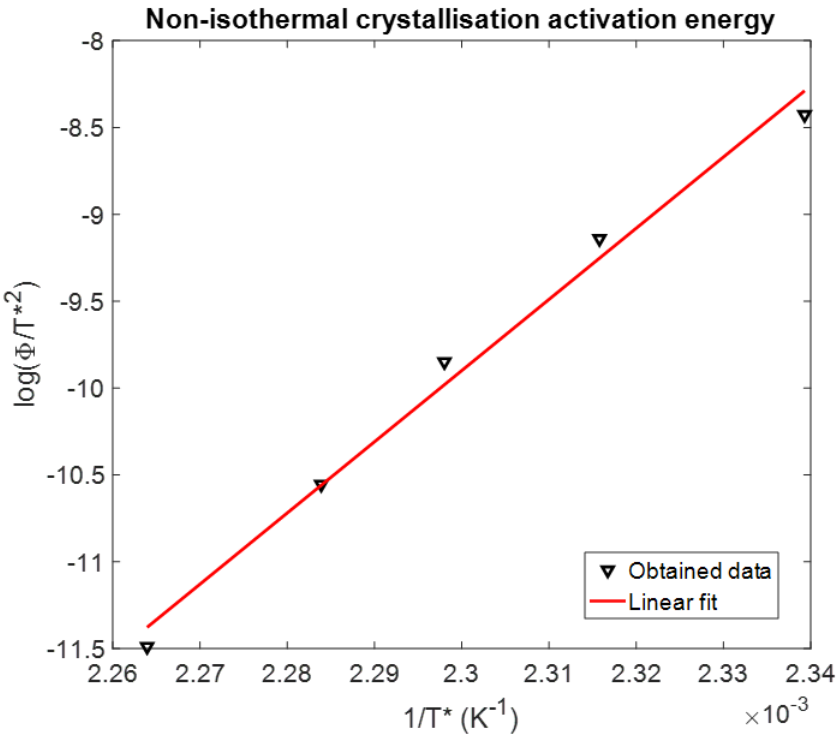


Figure 4.27: Plot of $\ln(\Phi/T^{*2})$ vs $1/T^*$, determining the nucleation activation energy of non-isothermal crystallisation for Nylon-12.

[142] in dealing with Nylon-66:

$$m \ln \Phi = \ln K(T) - n \ln t - \ln Z_c \tag{4.13}$$

which yields a simplified form:

$$\ln \Phi = \ln F(T) - a \ln t \tag{4.14}$$

where $F(T) = (K(T)/Z_t)^{1/m}$ and $a = n/m$. $F(T)$ corresponds to the value of the cooling rate at crystallisation time τ when the material has a certain degree of crystallinity [114]. Figure 4.28 shows the plot of $\ln \Phi$ vs $\ln t$. $F(T)$ corresponds to the y-intercept. It can be observed that the value of $F(T)$ rises with increasing relative crystallinity; therefore at time τ, a slower cooling rate should be used to obtain a higher degree of crystallinity. The values of gradient a are constant across all values of $X(t)$.

The non-isothermal analogue to TTT diagrams is the continuous cooling transformation (CCT) diagram. This plots the phase contour lines for non-isothermal crystallisation on time-temperature axes. Figure 4.29 shows the 1%, 20%,

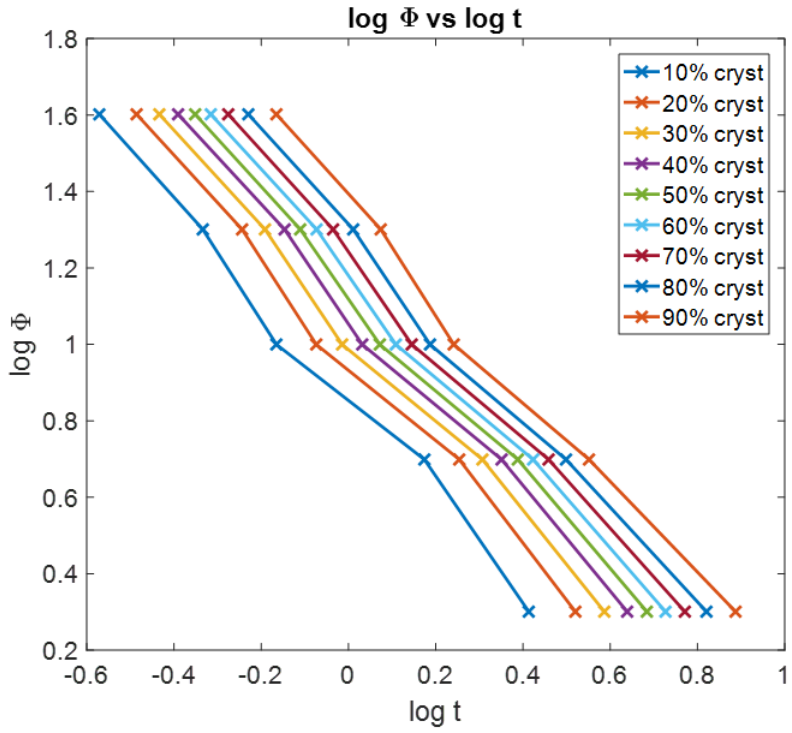


Figure 4.28: The plots of $\ln \Phi$ vs $\ln t$. from the combined Avrami and Ozawa equation for Nylon-12.

50% and 99% relative crystallinity conversion contour lines, along with additional dashed contour lines corresponding to the time-temperature relationship of the five cooling rates used.

4.4 Conclusions

The DSC results demonstrate the limitations of the isothermal and non-isothermal crystallisation regimes as a way of describing the FFF process. The results from the non-isothermal crystallisation show that a faster cooling rate results in a lower initial melting temperature due to poorly formed crystallites. The single endotherm observed for the slower cooled samples indicates the presence of a well-formed primary crystal structure, whereas the double endotherm corresponds to the presence of poorly formed crystals. The lower temperature endotherm indicates a lamellar reordering process whereby thicker crystals are formed by the partial melting and recrystallisation of the thin lamellae.

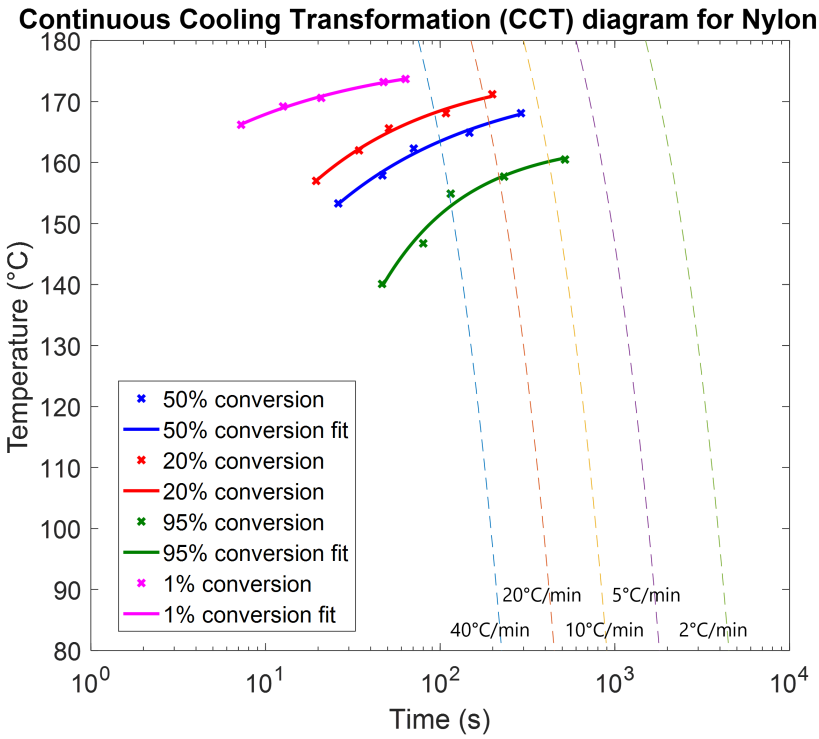


Figure 4.29: Continuous cooling transformation (CCT) diagram for Nylon-12 filament.

Based on the estimates of cooling rates for the FFF RS and FFF Apium samples, it was expected that the FFF RS sample would display a qualitatively similar DSC trace to the sample cooled at 40 °C/min. However, the FFF RS sample displays instead a single melting endotherm with a small shoulder. Furthermore, the FFF RS sample is found to melt at 197 °C, whereas the 40 °C/min sample melts at 195.03 °C. Furthermore, the FFF Apium sample, which experiences slower cooling rates throughout the process, shows a melting endotherm at 197.90 °C with a small lower-temperature endotherm that is quantitatively similar to that of the FFF RS. These observations highlight the fact that further differences may be present between samples in the nanoscale internal arrangement of the crystalline and amorphous phases which may induce significant disparity in the macroscopic thermal and mechanical properties.

The data from Table 4.4 shows that the crystallisation process completes by 150 °C even for samples isothermally crystallised at temperatures of 120-140 °C. Furthermore, the melting endotherms on reheating were quantitatively identical for

the sample non-isothermally crystallised at 40 °C/min and the samples isothermally crystallised at 120-140 °C. Since the highest chamber temperature attained by the FFF Apium sample is 120 °C, it is therefore suggested that both samples undergo an initial crystallisation at $T_c \approx 150$ °C. This accounts for some variation in the DSC patterns of the FFF Apium and FFF RS samples, as the difference in chamber temperatures (120 °C vs 25 °C respectively) leads to a significant difference in cooling rate following initial deposition. This can be considered on its own as being a non-isothermal crystallisation. However, as evidenced by the difference in the shape of the melting endotherms in the DSC data for the non-isothermally crystallised samples and the FFF-produced samples, it is not sufficient to describe the crystallisation processes during FFF. It is hypothesized that this is due to the effect of subsequent reheating and melting steps during layer deposition.

The DSC results from the FFF samples show that the chamber temperature has an effect on the thermal properties of the sample. The single peak at 197 °C that results from FFF sample preparation merits further study; however the presence of a more prominent shoulder in the 150 °C sample shows the effect of the higher temperature. Additionally, the post-annealing, while an imperfect approximation of a higher chamber temperature, shows the effect of exposure to higher temperatures even without remelting the sample. Further studies preparing samples at these temperatures if the equipment allows it may be able to shed light on the nature of the DSC peaks. However, the effect of the higher temperature is more clearly shown through the degree of crystallinity, which increases significantly as the temperature rises according to a power law.

5

Thermal and Crystallisation Modelling of FFF Nylon-12

Contents

5.1 Introduction 146
5.2 Results and discussion 147
5.2.1 Isothermal crystallisation model 147
5.2.1.1 Methodology 147
5.2.1.2 Results and analysis 148
5.2.2 Non-isothermal crystallisation model 150
5.2.2.1 Methodology 150
5.2.2.2 Results and analysis 151
5.2.3 Refinement of experimental data fitting 153
5.2.3.1 Methodology 153
5.2.3.2 Results and analysis 156
5.2.3.3 Extension to the isothermal case 159
5.2.4 Thermal modelling of Nylon-12 in FFF 161
5.2.4.1 Modelling of an individual filament 162
5.2.4.2 Modelling of a system of contacted filaments . 163
5.2.4.3 Modelling of the development of crystallinity . 165
5.2.5 Temperature-rate-crystallinity relation 168
5.3 Conclusions 174

5.1 Introduction

This chapter presents the methodology used in and results obtained from the crystallisation and thermal modelling of Nylon-12 filament. The main focus of this chapter is to whether the crystallisation behaviour of Nylon-12 fits the model laid out by Avrami and modified by Nakamura, as described in Section 1.2.5.

The Avrami and modified Nakamura-Avrami models represent a benchmark for modelling the crystallisation behaviour of semi-crystalline polymers, and are used frequently in literature both to analyse DSC data [65, 94, 113, 114, 123] and to predict crystallisation behaviour [16, 50]. Given the unique thermal history experienced in FFF, as well as the crystal morphology seen in Chapter 3 that is unique to the filament production and FFF process, it is important to assess whether these models can also be applied to modelling the crystallisation behaviour of FFF samples.

The Hoffman growth model is then used to predict the crystallisation behaviour of Nylon-12 when crystallised under conditions closer resembling those of FFF. Hoffman's seminal work on polymer crystallisation [15, 137] remains widely used in literature today; other authors [49, 69, 125] have found success using the Hoffman growth model to describe FFF, and analysis of DSC data from this study in Section 4.3 did not find any deviations from Hoffman-Lauritzen theory to suggest that the theory might not be applicable to FFF samples.

The utility of the isothermal and non-isothermal crystallisation paradigms in describing the FFF process has been discussed in Chapter 4. Thermal history data indicates that the process corresponds approximately to a highly non-isothermal cooling followed by a quasi-isothermal period, the temperature of which converges to the ambient temperature T_{amb} of the print chamber. Based on this, the generation of accurate models that can predict the crystallisation behaviour of Nylon-12 filament is necessary for the development of a more precise process-structure-property relation.

MATLAB is used to build a series of models: firstly, isothermal and non-isothermal crystallisation models based on the calculated material parameters; subsequently an arctangent-based model which fits the experimental data more

closely, and finally a heat flow model predicting the thermal history of an individual filament during FFF, into which the crystallisation model is fed.

5.2 Results and discussion

The results are split into three sections, as follows:

1. **Section 5.2.1: Isothermal and non-isothermal crystallisation models**
2. **Section 5.2.2: Refinement of experimental data fitting**
3. **Section 5.2.3: Thermal history model incorporating prediction of crystallinity**

5.2.1 Isothermal crystallisation model

5.2.1.1 Methodology

The isothermal model was built according to the unmodified Avrami equation:

$$X(t) = 1 - e^{-K(T)t^n}$$

where n represents the nucleation mode and dimensionality of crystal growth, and the isothermal crystallisation rate parameter $K(T)$ is temperature dependent, but constant for a given T_c. The crystallisation rate parameter is related to the crystallisation halftime $t_{1/2}$ by:

$$t_{1/2} = \left(\frac{\ln 2}{K(T)}\right)^{\frac{1}{n}}$$

The values of n and $K(T)$ used in the model are extracted directly from the isothermal data obtained in Chapter 4, with values of $K(T)$ calculated from measured values of $t_{1/2}$. Values of n were obtained from the double logarithmic plot of $\ln(-\ln(1 - X(t))) = \ln K(T) + n \ln t$. These values are shown in Table 5.1.

Deviation analysis of the $X(t)$ vs time and temperature was undertaken and is calculated at each temperature by:

$$\frac{t_{model} - t_{exp}}{t_{exp}} \cdot 100 \tag{5.1}$$

5.2.1.2 Results and analysis

Figure 5.1 shows the overlay of the calculated curves and the experimental data. It can be observed that the curves fit closely together in the initial phase of crystallisation, up until $X(t)$ 50%. The extracted crystallisation half-time $t_{1/2}$ from the calculated curve is shown alongside the used $t_{1/2}$ in Table 5.1.

T_c (°C)	176	174	172	170	168
$t_{1/2}$ (II) (s)	537.10	380.70	325.50	224.30	177.60
Model $t_{1/2}$ (s)	494.42	355.88	310.55	229.58	184.06

Table 5.1: Crystallisation halftimes for the experimental data and the Avrami model.

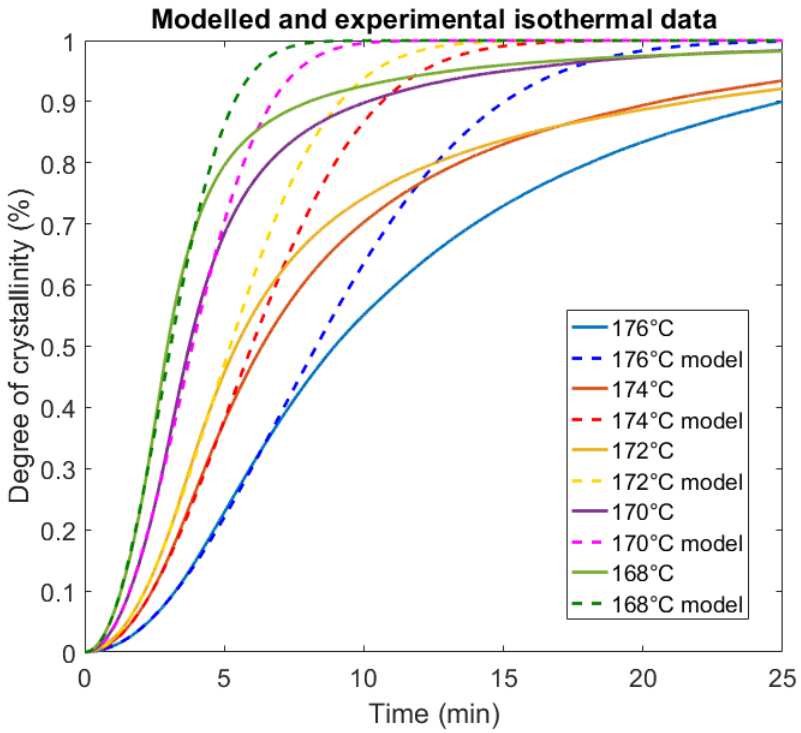


Figure 5.1: An overlay of the modelled data and the experimental data, showing the deviations between model and data.

Figure 5.2 shows the relative deviation of the experimental data from the Avrami model. When $X(t) > 60\%$, significant deviation from the calculated curves is observed, up to 58% at its highest value.

The deviation is more strongly pronounced with a lower isothermal crystallisation temperature T_c. This was hypothesised by Zhao [16] to be due to the continued

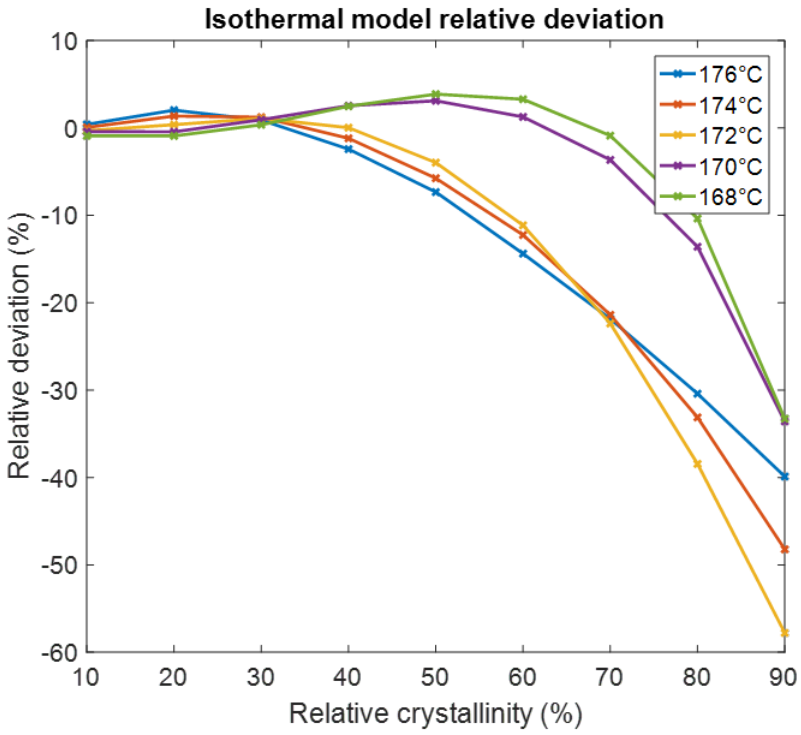


Figure 5.2: The relative deviation in percent between the modelled and experimental data.

growth of the spherulite boundaries and the transformation of the internal structure in each spherulite. The Avrami equation takes into account the fact that new crystal growth cannot take place on already crystallised material; however it operates on the following assumptions:

1. Nucleation occurs randomly and homogeneously over the entire untransformed portion of the material

2. The growth rate does not depend on the extent of transformation

3. Growth occurs in the same rate in all directions

Zhao's experimental analysis was done on Nylon-12 powder within the context of SLS, rather than on extruded filament as was performed here. However, the filament case differs from the powder case substantially, as demonstrated in the obtained XRD data in Chapter 3. The microstructure of filament and FFF-manufactured Nylon-12 is proposed to be highly oriented, due to Nylon-12 chain backbone

alignment that takes place during the extrusion process. Furthermore, optical microscopy data from [78] indicated that spherulite distribution in FFF-processed PLA filament was highly inhomogeneous, with the majority of crystalline structures being concentrated near the filament boundary.

As a result, assumption 1 is unlikely to hold for the filament case, as growth will not be homogeneous across the entire cross-section of the filament. Furthermore, the emergence of the 200 diffraction ring on melting and recrystallisation of Nylon-12 filament indicates a high degree of orientation of crystal structures in a preferred direction, indicating that assumption 3 holds only weakly for the filament case. The Avrami model suggests that transformation begins to slow as the ratio of transformed to untransformed material increased; the concentration of transformable material into a smaller region as in the filament case would cause a more significant slowing of crystallisation compared to the model. The consequences of this deviation from the Avrami model and the proposal of an alternative fit are described in Section 5.2.3.

5.2.2 Non-isothermal crystallisation model

5.2.2.1 Methodology

The non-isothermal model was constructed according to the Nakamura-Avrami model, as described in Section 1.2.5. The non-isothermal rate parameter $Z(T)$ is given from Equation 1.14 as follows:

$$Z(T) = (\ln 2)^{\frac{1}{n}} K_0 e^{-\frac{U^*}{R(T-T_\infty)}} e^{-\frac{K_g(T+T_m^0)}{2T^2\Delta T}} \tag{5.2}$$

This is substituted into the exponent of the Nakamura-Avrami equation (from Equation 1.12) and integrated:

$$X(t) = 1 - e^{-\left(\int_0^\tau Z(T)dt\right)^n}$$

The values of K_0 and K_g are determined from the isothermal crystallisation experiments via the plot of $\ln(1/t_{1/2})+U^*/R(T-T_\infty)$ vs $(T+T_0)/(2T^2\Delta T)$, as shown in Figure 4.23. The obtained values were $K_0 = 30{,}981\ s^{-1}$ and $K_g = 83283\ K^2$.

Deviation analysis of the $X(t)$ vs time and temperature was undertaken and is calculated at each temperature by:

$$\frac{t_{model} - t_{exp}}{t_{exp}} \cdot 100 \tag{5.3}$$

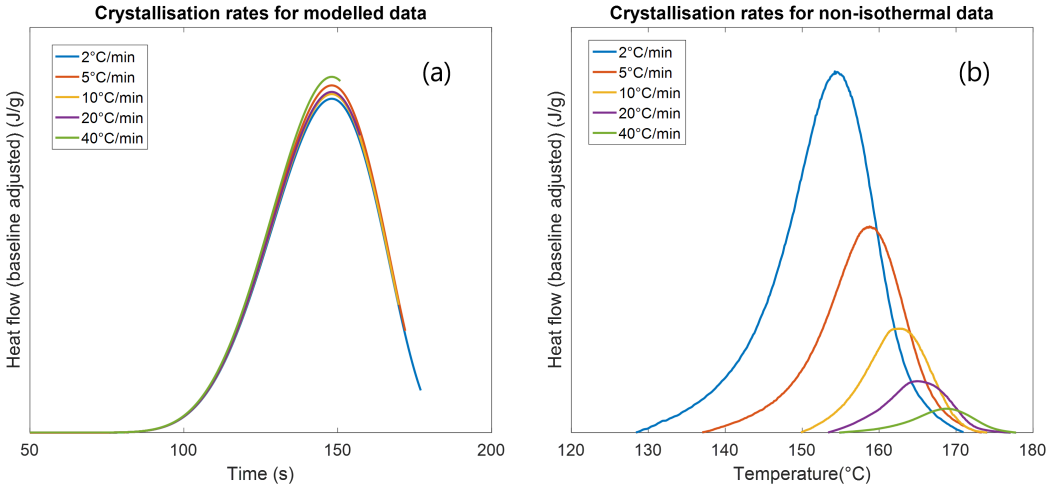


Figure 5.3: (a) shows the modelled crystal growth rate curves, and (b) shows the experimental crystal growth rate data for the non-isothermal crystallisation.

5.2.2.2 Results and analysis

In the non-isothermal crystallisation model, the temperature-dependent crystallisation rate parameter curve has a characteristic shape that is material dependent, as all other variables except T and n in Equation 5.7 are material dependent. Each material thus has its own unique crystallisation rate curve. In principle, plotting the crystallisation rate parameter as a function of time for different cooling rates yields the same shaped set of curves as in Figure 4.13. Figure 5.3 shows this plot and its comparison to the obtained experimental data for the crystallisation rate.

It is clear from Figure 5.3 that the modified non-isothermal crystallisation model does not precisely describe reality. This shows that the modelled material-dependent crystallisation rate parameter also depends on cooling rate in practice. The reasons for the breakdown of the model are hypothesised to be closely related to those put forward in Section 5.2.1.2.

Figure 5.4 shows the non-isothermal experimental data and model superposed on each other. At high cooling rates, the curves are well-matched however there is considerable deviation at slower cooling rates. The relative deviation as a function of X_c is plotted in Figure 5.5. Alteration of the cooling rate results in changes to the non-isothermal crystallisation temperature T^*, which is given by the maximum of the crystallisation exotherm. The data shown in Figure 4.15 shows that the onset of crystallisation occurs at different temperatures for different cooling rates; this onset temperature T_{on} must be corrected for. The slower cooling rates result in a higher level of instability of measurement signal, as the magnitude of the crystallisation exotherm is smaller relative to measurement error, however the issues highlighted in Figure 5.3 also contribute heavily to the deviation between the model and the experimental data.

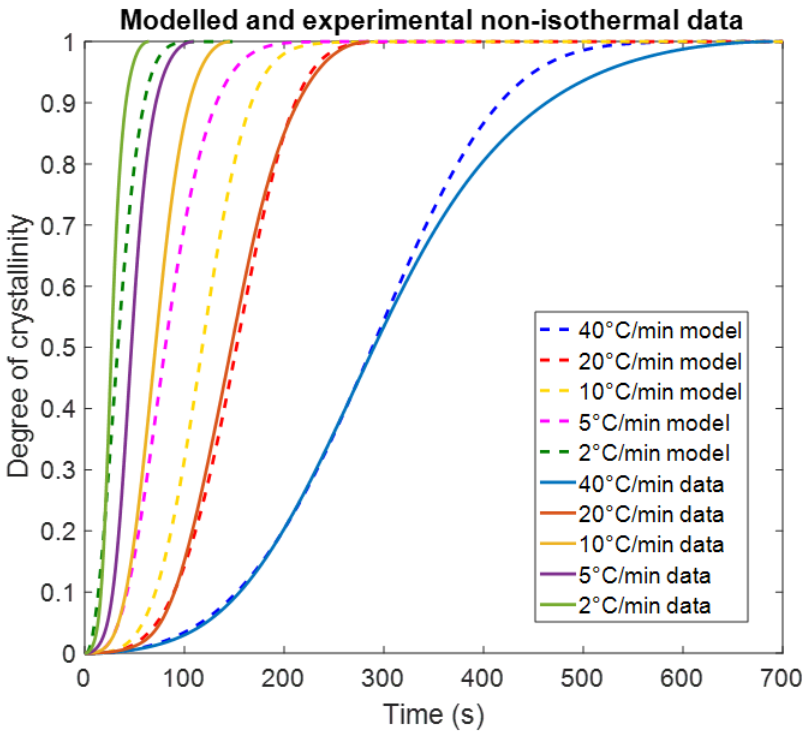


Figure 5.4: An overlay of the modelled data and the experimental data, showing the deviations between model and data.

However, both the isothermal and non-isothermal models reveal that there are clear limitations in using the Avrami and modified Nakamura-Avrami models to

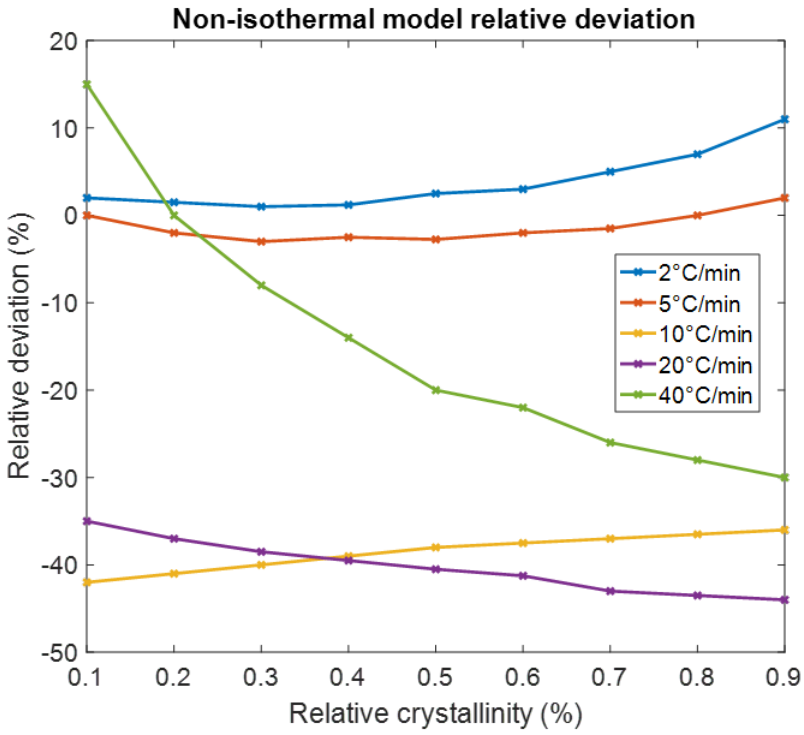


Figure 5.5: The relative deviation in percent between the modelled and experimental data.

describe the crystallisation behaviour of Nylon-12 filament. The limitations of the Avrami model to describe crystallisation in FFF have been previously described. An additional limitation of the Nakamura-Avrami model is that crystallisation rate $Z(t)$ is assumed to depend on T for a given material, but is independent of current degree of crystallinity X_c. These limitations may be the cause of the deviation between the models and the data. The consequences of this deviation from the Nakamura-Avrami model and the proposal of an alternative fit are described in Section 5.2.3.

5.2.3 Refinement of experimental data fitting

5.2.3.1 Methodology

In order to create a function that fitted the experimental data more closely, an arctangent-based function was employed. This function was chosen due to its considerably closer fit to the obtained data, as will be discussed in Section 5.2.3.2. Its use can be additionally justified on the following grounds: (i) its resemblance to the Avrami function both graphically and in Taylor expansion form, and (ii)

its differentiation to a neat function, as shown:

$$\frac{d}{dx}\arctan x = \frac{1}{x^2+1} \tag{5.4}$$

A comparison between an Avrami curve and a plot of $\arctan x$, as well as between a crystallisation rate curve and $1/(x^2+1)$ is shown in Figure 5.6.

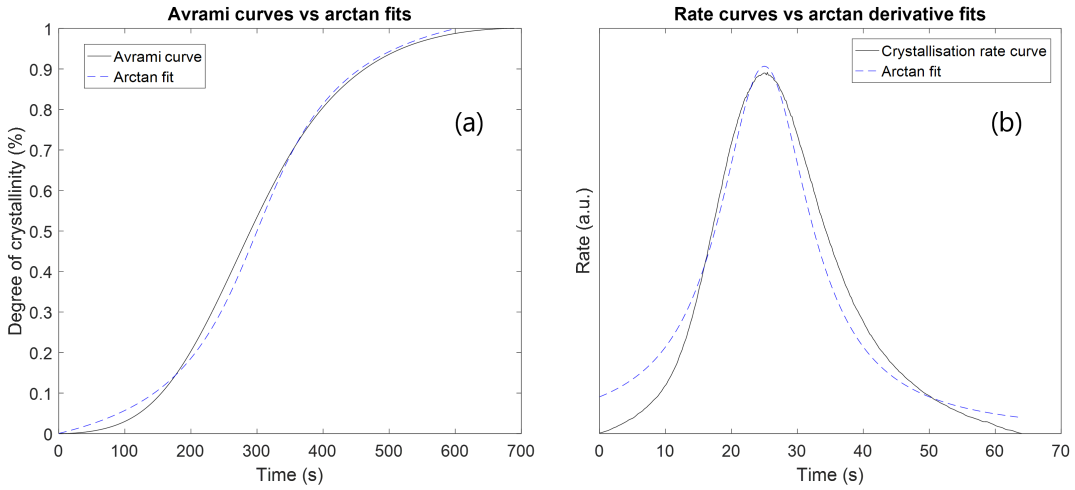


Figure 5.6: (a) shows an Avrami curve superposed on an arctan curve, while (b) shows an the same for a crystallisation rate curve and an arctangent derivative curve. The qualitative similarities are notable.

The function $\arctan x$ passes through the origin, with horizontal asymptotes at $\pm\pi/2$, analogous to the Avrami curve's limits at $X(t) = 0, 100\%$. The $\arctan x$-based function must therefore be shifted in the horizontal and vertical axes, according to the following general form:

$$f(x) = A \cdot \arctan\left(B \cdot x + C\right) + D \tag{5.5}$$

where $A - D$ are constants.

The Taylor expansion of e^{-Ax^B} is given by:

$$e^{Ax^B} \longrightarrow \sum_{k=0}^{\infty} \frac{(Ax^B)^k}{k!} = 1 + Ax^B + \frac{A^2x^{2B}}{2} + \frac{A^3x^{3B}}{6} + \ldots \tag{5.6}$$

which gives the Taylor expansion of an Avrami-based equation as:

$$1 - e^{-Kt^n} \longrightarrow Kt^n - \frac{K^2t^{2n}}{2} + \frac{K^3t^{3n}}{6} - \ldots \tag{5.7}$$

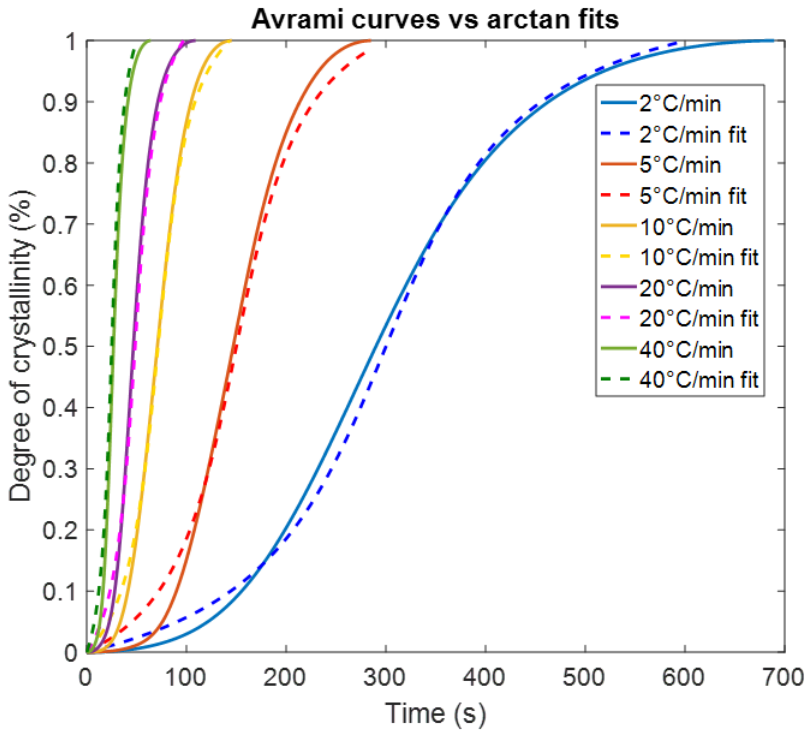


Figure 5.7: The non-isothermal data overlaid with arctangent fits. It is notable that the quality of fit is considerably better than with the Nakamura-Avrami model.

The Taylor expansion of $\arctan x$ is given by:

$$\arctan x \longrightarrow \sum_{k=0}^{\infty} \frac{(-1)^k x^{1+2k}}{1+2k} = x - \frac{x^3}{3} + \frac{x^5}{5} - \dots \tag{5.8}$$

When shifted in accordance with Equation 5.10, however, the Taylor expansion of $\arctan(A \cdot x + B)$ is given by:

$$\arctan(A \cdot x + B) \longrightarrow \frac{Ax}{B^2+1} - \frac{A^2Bx^2}{(B^2+1)^2} + \frac{A^3(3B^2-1)x^3}{3(B^2+1)^3} - \dots \tag{5.9}$$

which can be simplified to a form more resembling the expansion of the Avrami equation in Equation 5.12 such that:

$$\arctan(A \cdot x + B) \longrightarrow C\left(D_1 x - D_2\frac{x^2}{2} + D_3\frac{x^3}{6} - \dots\right) \tag{5.10}$$

Unlike the Avrami equation, which is derived from material transport as described in Section 1.2.5, the arctangent function lacks a physical justification for its use in describing polymer crystallisation kinetics. However, on the basis of its utility for fitting of the obtained data and the fact that to first order approximation it has the same terms as the Avrami equation, it is proposed as an alternative fit.

5.2.3.2 Results and analysis

Figure 5.7 shows the results of the fitting of the non-isothermal crystallisation data to the arctangent function $A \cdot \arctan(B \cdot x + C) + D$, with Figure 5.8 showing the relative deviation of the curves as a function of time, according to the methodology in Section 5.2.1. A close fit can be observed between the curves, with the results at high $X(t)$ ($> 70\%$) being considerably closer than the Nakamura-Avrami model utilised in Section 5.2.2.

Although there is relatively high percentage deviation (up to 25%) at low relative crystallinities ($< 5\%$), the actual deviation is low. This is primarily due to the shape of the arctangent function, which can output negative y-values. In this model, the arctan function is constrained to pass through the origin such that at $t = 0$ the degree of crystallinity is 0%, and output positive values when t is positive. This constraint leads to a more imperfect fit at low relative crystallinities, but ensures that the model does not output non-zero crystallinity at $t = 0$ or negative crystallinity.

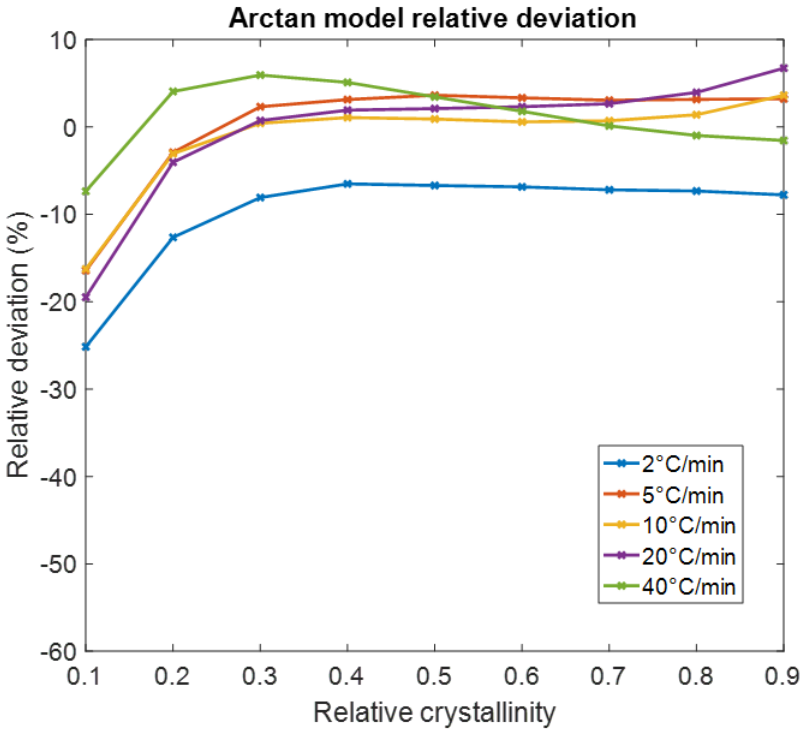


Figure 5.8: The relative deviation in percent between the modelled and experimental data.

The fitted function was found to take the form:

$$f(x) = 0.4 \arctan\left(A(\Phi) \cdot x - 3\right) + 0.5 \tag{5.11}$$

where $A(\Phi)$ is a constant that varies depending on cooling rate Φ. The obtained values of $A(\Phi)$ are shown in Table 5.2, with the relation between $A(\Phi)$ and Φ plotted in Figure 5.9. A linear relation can be fitted to this plot, according to:

$$A(\Phi) = 0.0028\Phi + 0.0072 \tag{5.12}$$

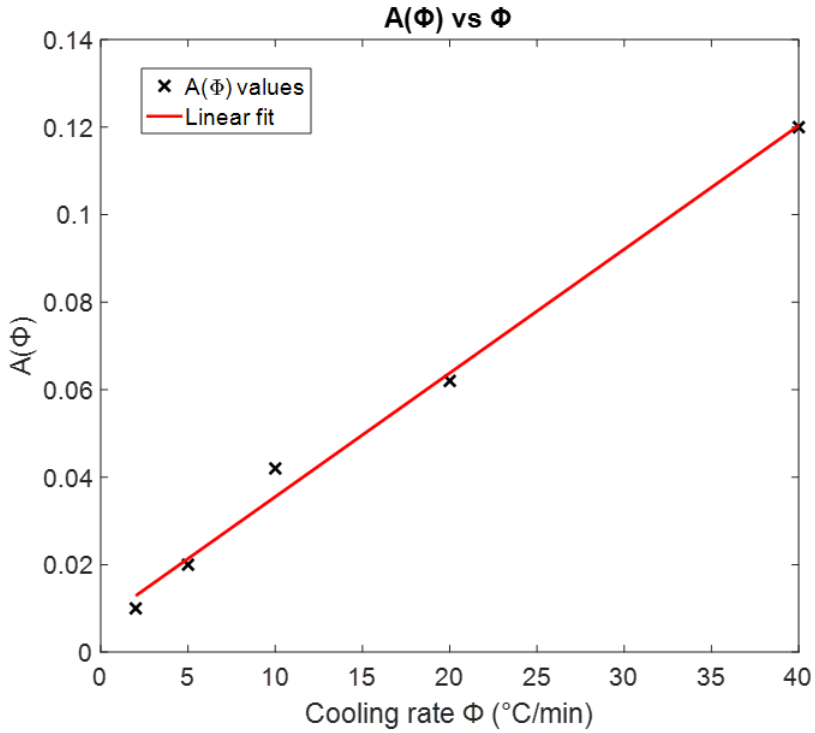


Figure 5.9: Fitting of the data of $A(\Phi)$ vs Φ for the arctangent function

Φ (°C/min)	2	5	10	20	40
$A(\Phi)$	0.011	0.020	0.042	0.062	0.120

Table 5.2: Melting temperatures for peak II (T_m (II)) and actual crystallisation temperatures (T_c^{actual}) for the low-temperature isothermal crystallisation experiments

Figure 5.10 shows the results of the fitting of the non-isothermal crystal growth rate data to the derivative of the arctangent function in Equation 5.16. Although there is some deviation during the first half of the crystallisation process (prior to

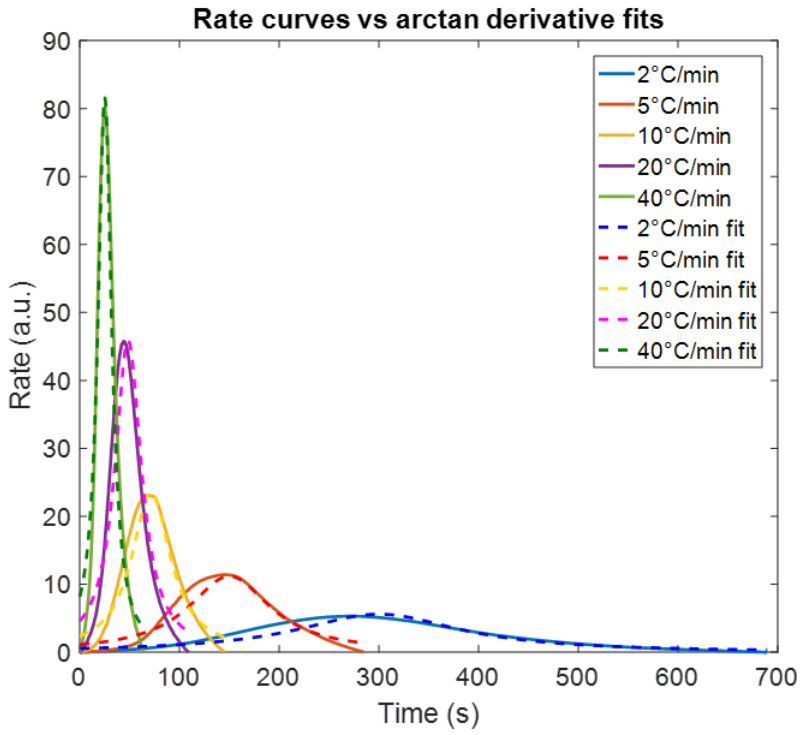


Figure 5.10: The non-isothermal data crystal growth rate data overlaid with arctangent fits. It is notable that the quality of fit is considerably better than with the Nakamura-Avrami model.

non-isothermal crystallisation temperature T^*), there is a close relation between the experimental data and the fitted curve.

The general form of the derivative of $A \cdot \arctan(B \cdot x + C) + D$ is given by:

$$\frac{d}{dx} A \cdot \arctan(B \cdot x + C) + D = \frac{AB}{(Bx + C)^2 + 1} \tag{5.13}$$

such that the fitted curve was given by:

$$f'(x) = \frac{0.4A(\Phi)}{(3 - A(\Phi)x)^2 + 1} \tag{5.14}$$

where $A(\Phi)$ is as given in Table 5.2.

Based on the above fitted data, the arctangent function and its derivative fit the data from the non-isothermal crystallisation behaviour of Nylon-12 filament with less deviation compared to the ideal Nakamura-Avrami model. It should be noted that the arctangent function represents an *a posteriori* description of the non-isothermal crystallisation behaviour and is not, *per se*, an *a priori* model of

polyamide crystallisation. However, the closeness of fit across a wide range of cooling rates allows the arctangent function to act as a powerful predictive tool for the crystallisation behaviour of Nylon-12 filament.

5.2.3.3 Extension to the isothermal case

The arctangent function was further tested by using it to model isothermal crystallisation of Nylon-12. The results and therefore fitting efficacy were compared to the Avrami model. Data from the high-temperature isothermal crystallisation was fitted with the arctangent function.

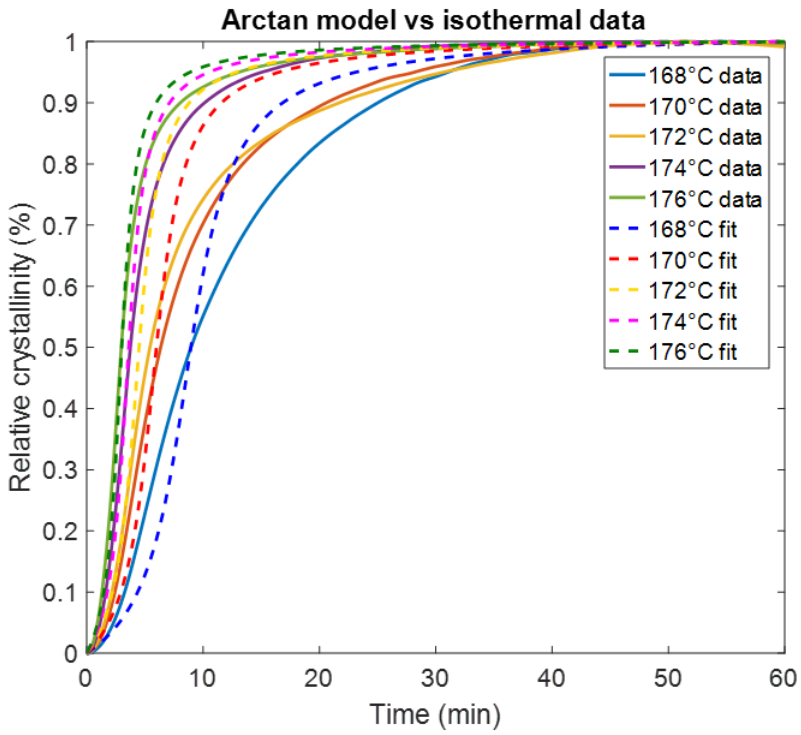


Figure 5.11: The isothermal data overlaid with arctangent fits. While the fit is imperfect, it represents a closer fit to the data than the Nakamura-Avrami fit did to the non-isothermal data.

The function required a degree of modification to make it suitable for isothermal crystallisation fitting. Equation 5.16 shows that the function takes as its primary variable $A(\Phi)$, which from Equation 5.17 is dependent on cooling rate Φ. Taking $\Phi = 0$, as is the case for all isothermal crystallisation, yields the same curve for all isothermal crystallisation temperatures. However, isothermal crystallisation

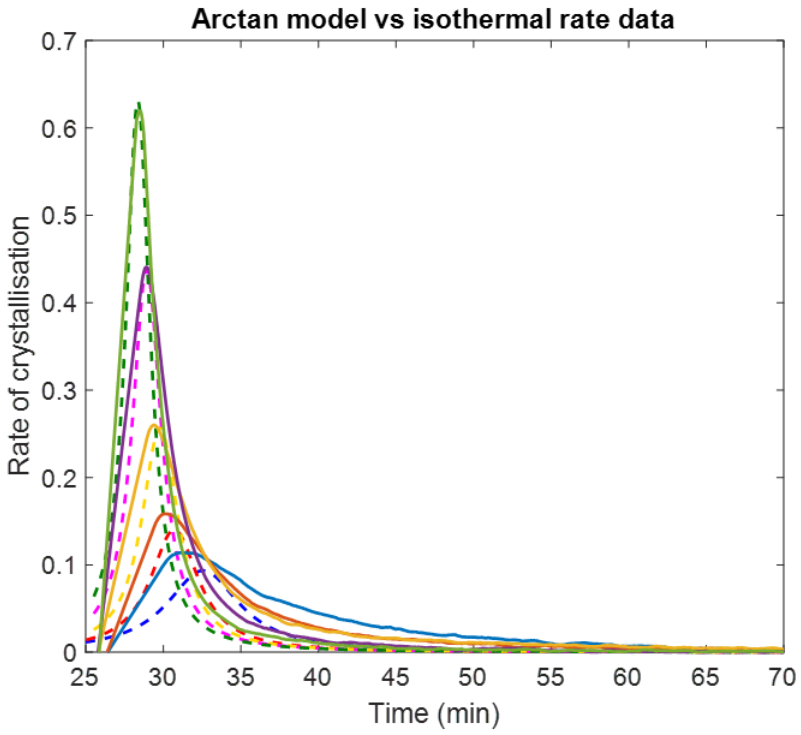


Figure 5.12: The isothermal data crystal growth rate data overlaid with arctangent fits. The quality of fit for the lower isothermal temperatures, but deviates at higher isothermal temperatures.

experiments cool at a constant rate to T_c before the isothermal period; we can therefore express for constant cooling rate:

$$T(t) = T_0 - \Phi t$$

such that

$$\Phi t = T_0 - T(t)$$

Then, since Equation 5.16 is driven by the term $A(\Phi)t$, we can express at time of isothermal crystallisation onset t_c^0 and isothermal crystallisation temperature T_c:

$$At_c^0 = 0.0028(T_0 - T_c) + 0.0072t_c^0$$

which can be extended to the duration of the isothermal crystallisation as follows:

$$At = (0.0028(T_0 - T_c) + 0.0072t_c^0) \cdot \frac{t}{t_c^0} \tag{5.15}$$

The results of the arctangent fitting of the isothermal crystallisation data is shown in Figure 5.11, with Figure 5.12 showing the fitting of the crystallisation rate data according to the same modification. A close relationship can be observed for the early phase of crystallisation onset ($X(t) < 0.7$) which diverges as crystallisation nears completion. For the highest isothermal crystallisation temperature ($T_c = 176$°C) there is considerable divergence throughout.

In particular, the isothermal crystallisation data displays a slower completion of crystallisation ($X_c > 0.7$) than the non-isothermal data; the reasons for this are discussed in Section 5.2.1.2. This slower completion appears more pronounced at higher T_c, which is proposed to be due to the shape of the crystal growth rate curve displayed in Section 1.2.5. Additional modifications to the arctangent function may be necessary to more accurately fit this; for instance by introducing a temperature dependence to other constants A, C, D in Equation 5.5.

The quality of the experimental data for the isothermal crystallisation experiments is lower than for the non-isothermal experiments due to experimental inertia, which will necessarily result in a less close fit for isothermal data than non-isothermal data. However, the modified arctangent function was shown to be able to well-fit isothermal crystallisation data below 174 °C, and likewise was able to well fit the crystal growth rate curves.

5.2.4 Thermal modelling of Nylon-12 in FFF

Isothermal and non-isothermal crystallisation modelling are powerful tools to predict the rate of crystallisation and relative crystallinity of a semi-crystalline polymer. However, they do not suffice to fully model the processing or structure components of the processing-structure property relationship.

The crystal structure of Nylon-12 is more dependent on absolute crystallinity compared to relative crystallinity. The absolute crystallinity can be computed from the relative crystallinity using the Hoffman growth model, using the nucleation and rate constants determined from isothermal and non-isothermal crystallisation

experiments and modelling. The development of this absolute crystallinity is likewise dependent on the thermal history of the sample.

The FFF process has been described as a convolution of an isothermal and non-isothermal component, with rapid cooling from the melt (and subsequent reheatings) leading into a long period of quasi-isothermal cooling at the ambient temperature of the print chamber. In order to simulate more closely the development of the crystallinity during these phases, a model was built in MATLAB to model the thermal history of a series of extruded filaments in thermal contact. On the basis of the thermal history generated by this model and the relative crystallinity data obtained in previous sections, a prediction of absolute crystallinity as a function of thermal history was made.

5.2.4.1 Modelling of an individual filament

Modelling of an individual filament was undertaken as described in Section 2.4.1. The results from the model are shown in Figure 5.13. Cooling proceeds rapidly, with filament temperature reaching T_∞ within 6s.

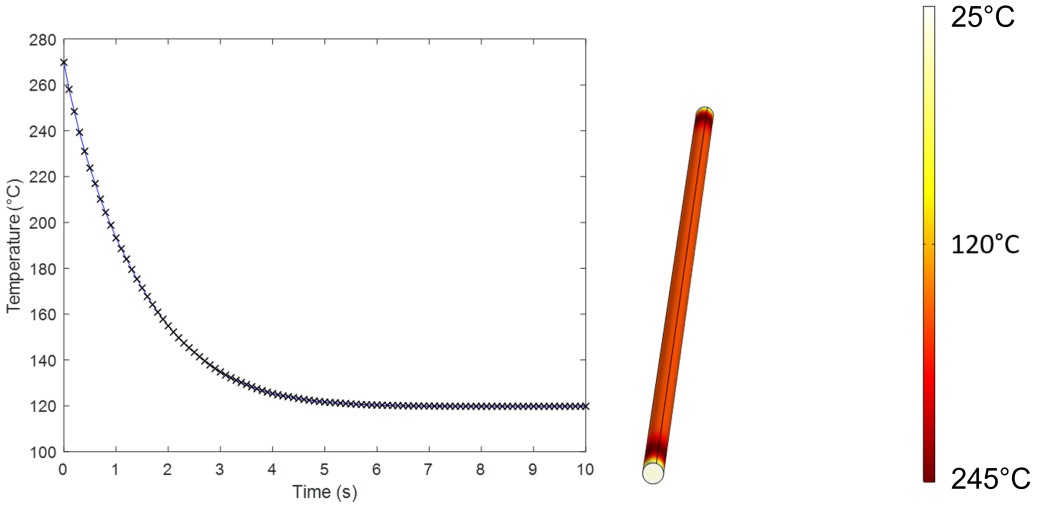


Figure 5.13: The modelled cooling rate of a single filament in a simulated printing environment.

The small cross-section of the filament means that the Biot number can be computed in order to assess whether or not there is significant variation in

thermal history within the cross-section of each filament during cooling. The Biot number is defined as:

$$Bi = \frac{h}{k}L \tag{5.16}$$

where k is the thermal conductivity of the body ($W/m \cdot K$), h is the convective heat transfer coefficient ($W/m^2 \cdot K$) and L is the characteristic length of the geometry, given by:

$$L = \frac{V}{A_Q} \tag{5.17}$$

where V is the volume of the sample and A_Q is the cooling surface of the sample. The Biot number of the sample was calculated to be 1.73×10^{-7}. This value signifies that the heat conduction inside the filament's body is much faster than heat convection away from the filament's surface, and therefore temperature gradients inside the sample are negligible.

In addition, it was notable that there was negligible difference in thermal history across the cross-section of the filament; this is in line with the calculated Biot number of the system. It was concluded from this that a basic model for a system of contacted filaments could be built in 2D, where each filament is reduced to a cross-section in thermal contact with neighbouring cross-sections, and that intra-filament heat transfer can be neglected in favour of heat transfer to and from neighbouring filaments.

5.2.4.2 Modelling of a system of contacted filaments

Modelling of a series of contacted filaments was performed according to the methodology described in Section 2.4.2.

Figure 5.14 shows the results of the model of the thermal history of the deposited filament A for different values of T_∞ between 100 and 150 °C for an inter-layer time period of one second. It can be seen that there is a clear response from the filament when subsequent layers are deposited on top of it, however this response gets gradually smaller until it can no longer be observed after the third layer

is deposited. It is notable that while the shape of the curve mirrors literature experimental data (demonstrated in Figure 1.14) for filaments in an FFF sample, the spike in temperature caused by subsequent reheatings is considerably smaller, and fewer spikes are observed as subsequent layers are deposited. However, the filament temperature never exceeds T_m on subsequent reheatings, which is in line with literature experimental data.

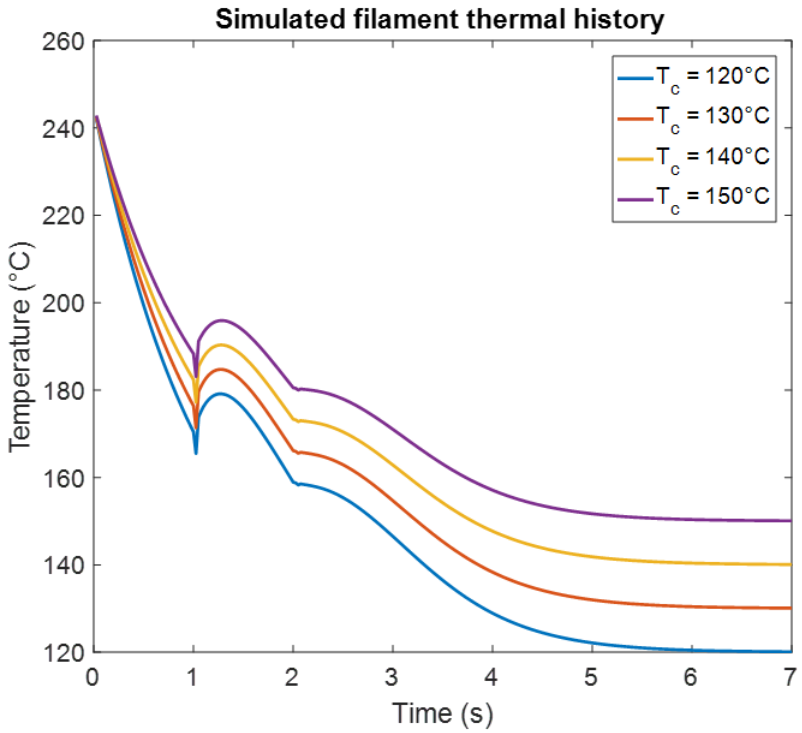


Figure 5.14: The simulated thermal history for a given cross-section in a contacted system of filaments, with T_{inf} ranging from 120 °C to 150 °C.

Cooling to T_∞ taking place within 10 seconds for all values of T_∞; the model suggests that T_∞ has a comparatively small effect on the thermal history. However, the low-temperature isothermal crystallisation data presented in Chapter 4 suggested that crystallisation takes place rapidly, often being nearly complete during the period of cooling from melt to isothermal crystallisation temperature T_c. The effect of this thermal history on the modelled crystallisation behaviour is explored in the following section.

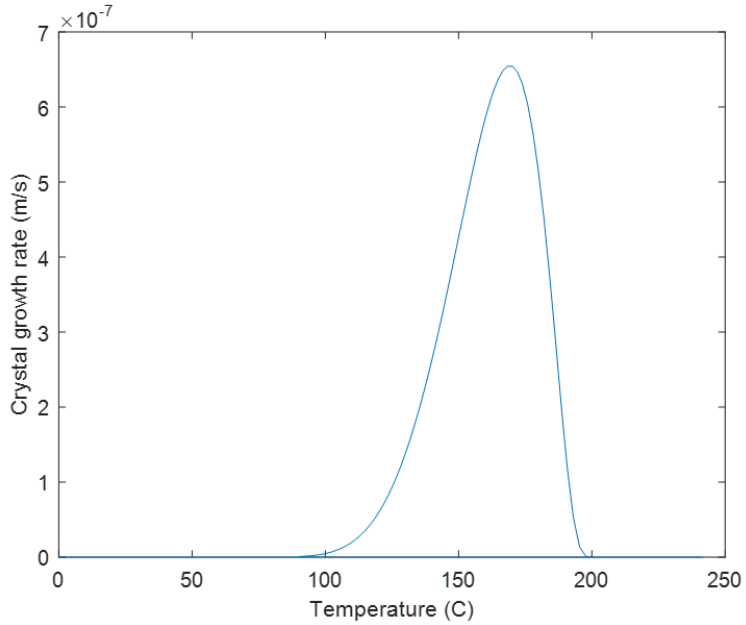


Figure 5.15: The simulated crystal growth rate as a function of temperature.

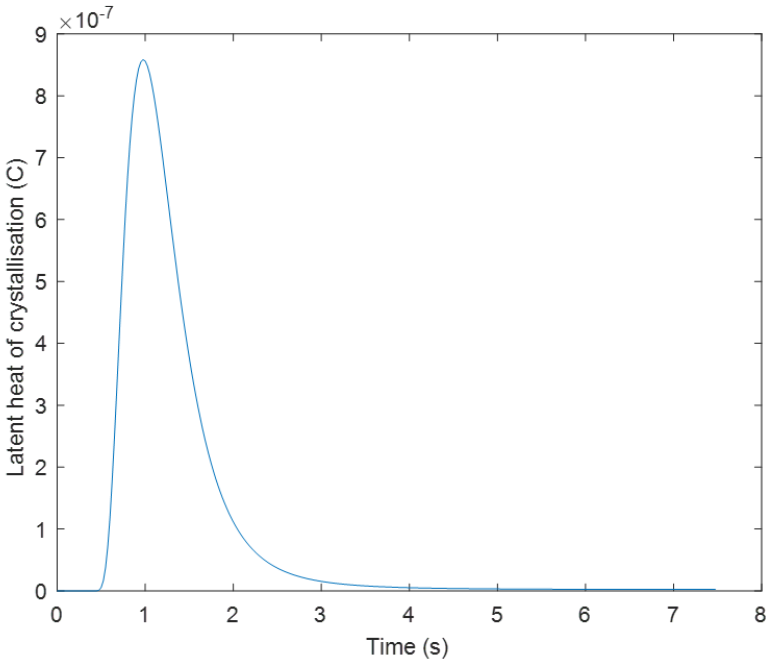


Figure 5.16: The simulated latent heat of crystallisation.

5.2.4.3 Modelling of the development of crystallinity

Figure 5.15 shows the crystal growth rate as a function of temperature, as given by Hoffman-Lauritzen theory in Equation 2.8. It can be noted that this curve resembles

the theoretical temperature-crystallisation rate curve shown in Figure 5.3(a); both are derived from Equation 1.23. According to this model, crystal growth begins just below T_m and continues until just above T_g, reaching a peak at 166 °C.

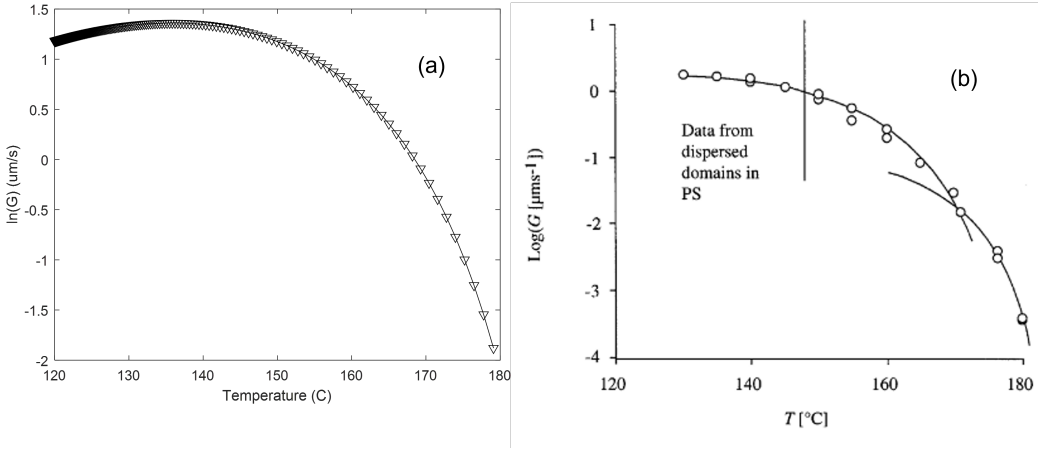


Figure 5.17: (a) shows the obtained data for $\ln G$. (b) shows data from the study of Plummer *et al* [125] on Nylon-12, as a qualitative comparison of curve shape.

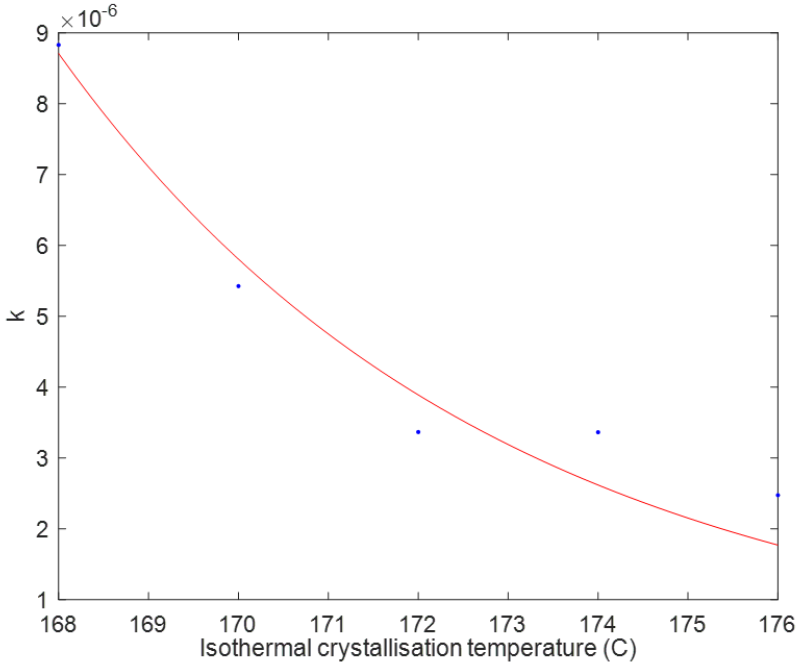


Figure 5.18: The simulated isothermal crystallisation rate parameter K as a function of temperature.

Figure 5.16 shows the latent heat of crystallisation, calculated by multiplying the ratio of transformed material to total material by L/c_p. It can be seen that

the total volume of transformed material in each filament is sufficiently small that the effect on the cooling rate is negligible, with the thermal contribution at peak crystallisation rate being 8.7×10^{-7} °C.

Crystal growth rate G is computed according to Equation 1.23, and $\ln G$ is plotted against temperature in Figure 5.17(b). Figure 5.17(a) shows a comparison of curve shape to data from [125] in (b) to demonstrate the consistency of the data with the literature. The nucleation density N_0 is calculated from this data for G and from the isothermal crystallisation rate parameter obtained for Nylon-12 in Section 4.3.1, using the following equations:

$$X(t) = 1 - e^{-\frac{4\pi G^3}{3} N_0 t^3} \tag{5.18}$$

$$K = \frac{4\pi N_0 G^3}{3} \tag{5.19}$$

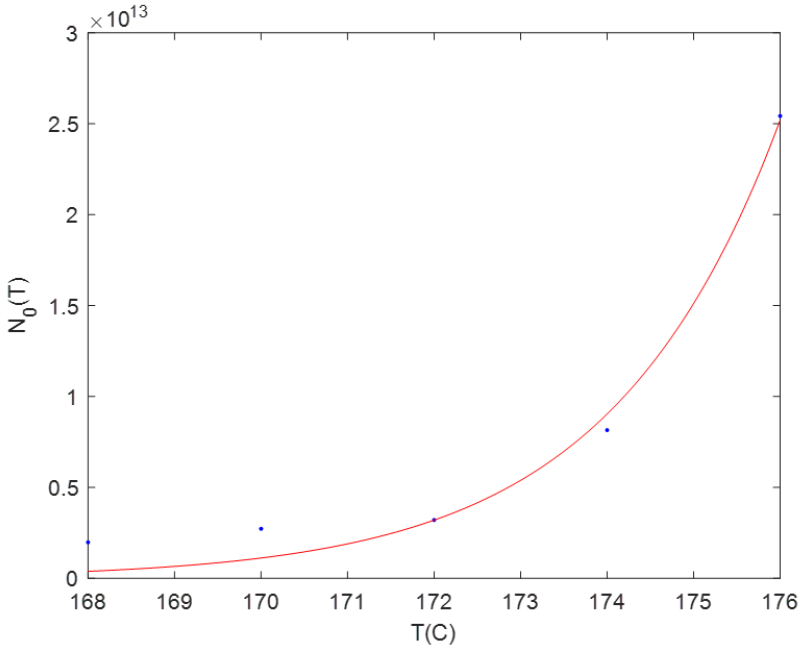


Figure 5.19: The simulated nucleation density as a function of temperature.

The isothermal crystallisation rate parameter K is plotted and fitted as a function of isothermal crystallisation temperature T_c in Figure 5.18. The nucleation density N_0 is plotted in Figure 5.19 as a function of temperature.

Finally, the radius of a single crystal is calculated using Equation 5.30 and the data for G and is plotted for the cooling model with 120 °C as T_∞ as a function

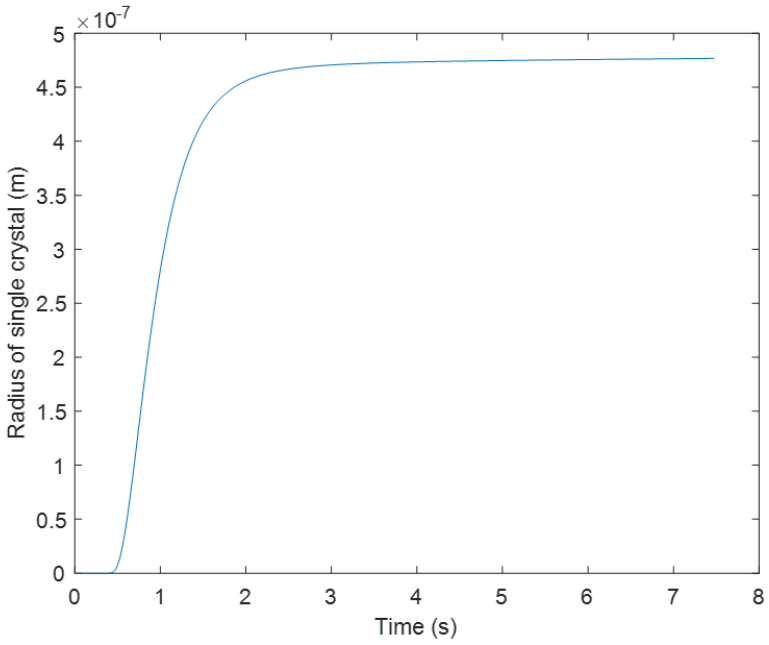


Figure 5.20: The simulated radius of a single crystal as a function of time derived from the contacted filament model.

of time in Figure 5.20. It can be seen that there is rapid crystal growth as the temperature falls through the peak crystallisation range, before levelling off as the temperature decays to T_∞.

5.2.5 Temperature-rate-crystallinity relation

The modification to the crystallisation rate parameter $K(T)$ to produce the non-isothermal parameter $Z(T)$ implies the existence of a material-specific crystallisation rate parameter, which gives a specific crystallisation rate for a given temperature at all cooling rates. This parameter can be integrated in the Nakamura-Avrami model to give a specific degree of relative crystallinity $X(t)$ for a given temperature at all cooling rates. The specific crystallisation properties of Nylon-12 are therefore expressible in a plot of T vs $Z(T)$ vs $X(T)$, whereby a projection onto the $x-y$ plane shows the Avrami curves, while a projection onto the $x-z$ plane shows the rate curves.

The $T-Z(T)-X(T)$ unnormalised plot for the experimental data for the non-isothermal crystallisation is shown in Figure 5.21.

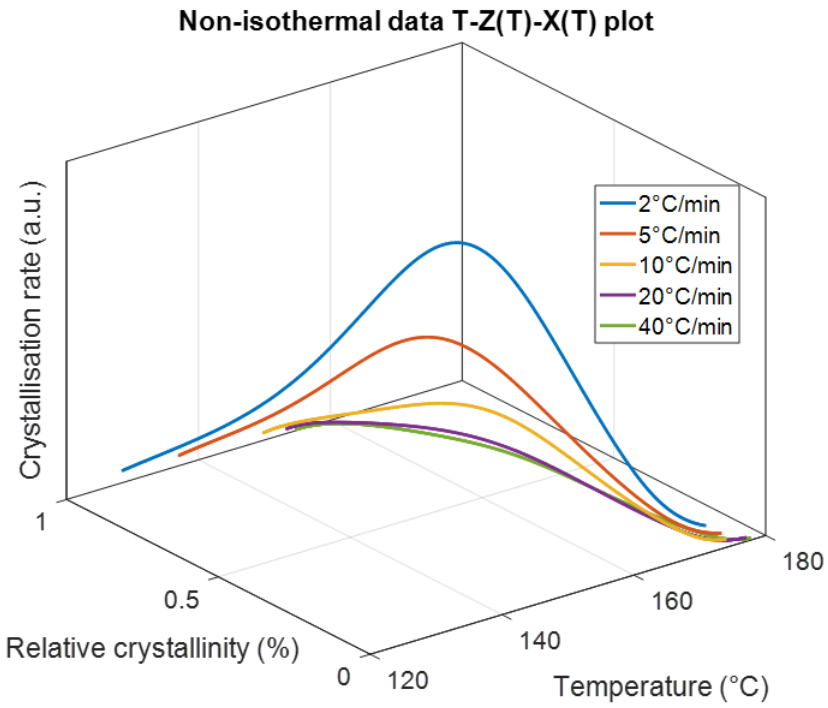


Figure 5.21: The $T - Z(T) - X(T)$ plot for the experimental non-isothermal crystallisation data from Section 4.2.2.

As seen in Section 5.2.3, an arctangent-based fitting function provides a closer fit for the experimental data than the Nakamura-Avrami model. Based on the fitted function given in Equation 5.16, the 3-dimensional $T - Z(T) - X(T)$ surface is derived using the following governing equations:

$$T = T_{onset} - \frac{\Phi \cdot t}{60}$$

$$X(t) = 0.4 \arctan\left(A(\Phi) \cdot t - 3\right) + 0.5$$

$$Z(t) = \frac{0.4A(\Phi)}{(3 - A(\Phi)t)^2 + 1}$$

$$A(\Phi) = 0.0028\Phi + 0.0072$$

T_{onset} is a Φ-dependent constant.

Figure 5.22 shows the arctangent model data plotted discretely for a range of cooling rates between 0.5 and 100 °C/min in intervals of 0.1 °C/min.

Based on Figure 5.22, it can be seen that crystallisation rate, degree of crystallinity and thermal history are related by the surface of the $T - Z(T) - X(T)$

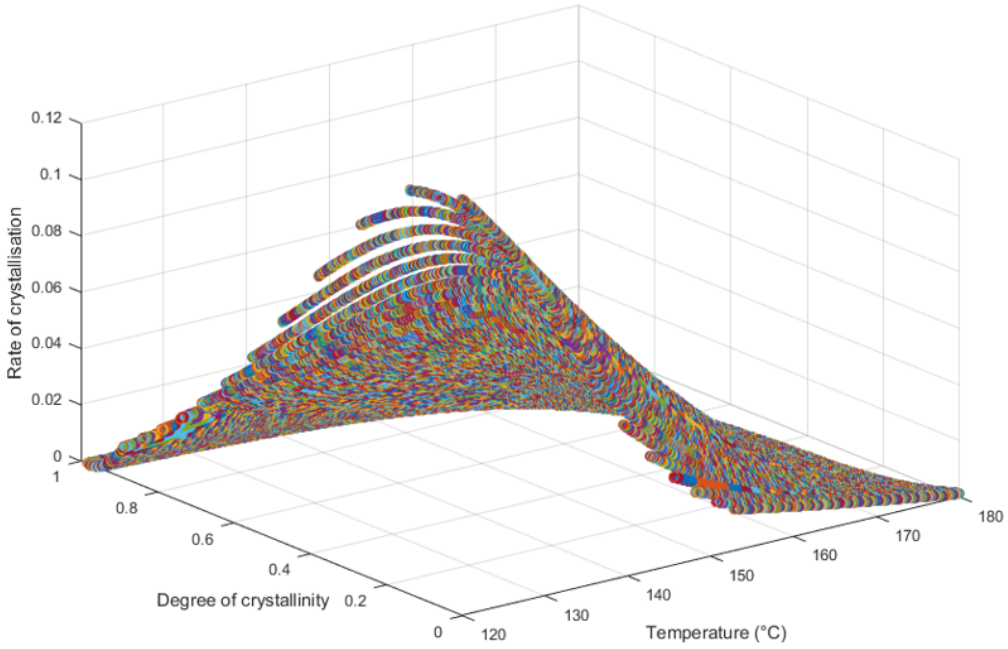


Figure 5.22: The $T - Z(T) - X(T)$ plot for the arctangent function, plotted for 0.5°C/min$< \Phi <$ 100°C/min to form a discrete three-dimensional surface.

curve. From this, for any non-isothermal crystallisation of Nylon-12 the degree of crystallinity and crystallisation rate can be predicted simply from the thermal history by tracing the phase contour lines on the curve. The projection of degree of crystallinity and crystallisation rate from a specific Φ phase contour line is shown in Figure 5.23.

It is possible to extend this function to describe any non-isothermal thermal history, regardless of whether or not the cooling rate is constant. This can be done by modifying the governing equations to make A and Φ time-dependent variables. By letting $\Phi(t)$ at instantaneous time τ be equal to dT/dt at τ, we obtain the following for a general time-dependent thermal history:

$$T(t) = f(t)$$

$$\Phi(\tau) = \left(\frac{dT}{dt}\right)_{\tau}$$

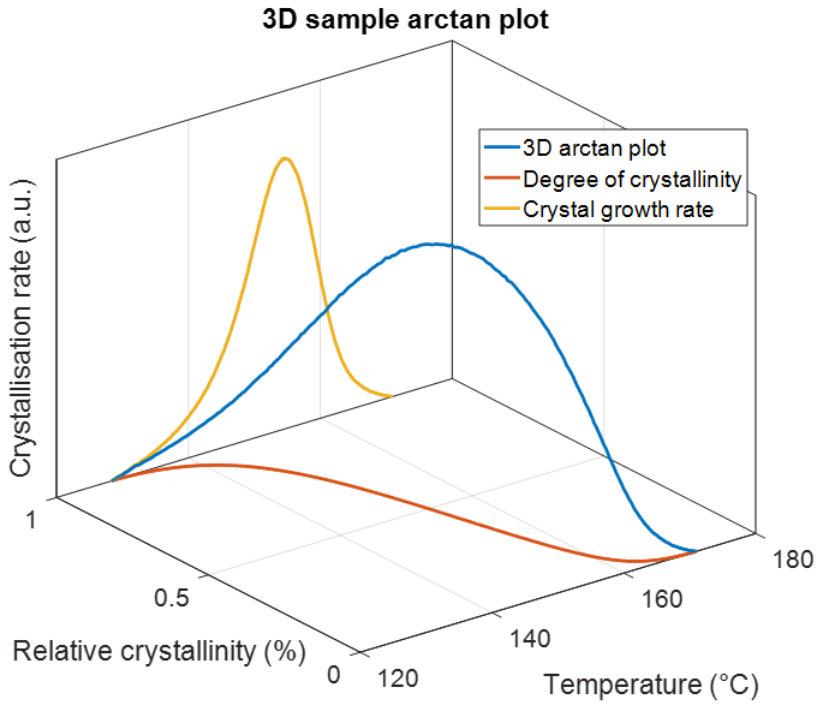


Figure 5.23: A phase contour line for the $T - Z(T) - X(T)$ arctangent plot, projected onto the $x - y$ and $x - z$ axes to show the degree of crystallinity and crystal growth rate.

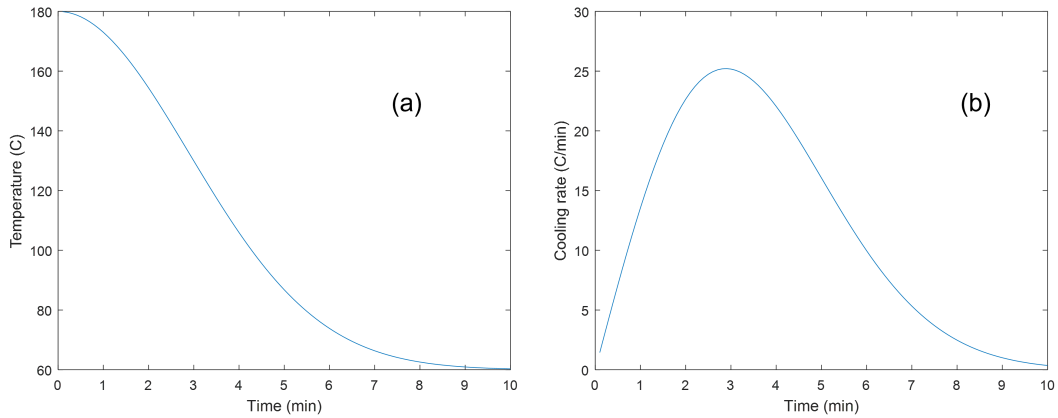


Figure 5.24: (a) shows the temperature profile of the simulated non-constant cooling rate function, while (b) shows the associated cooling rate.

Then $A(\Phi)$ becomes $A(t)$ such that:

$$A(\tau) = 0.0028 \left(\frac{dT}{dt} \right)_{\tau} + 0.0072$$

Similarly to the Nakamura modification of the Avrami model, which introduces a time-dependent rate constant $Z(t)$ (in Equation 1.12), we can therefore write

the general form of the governing equations as:

$$X(\tau) = 0.4 \arctan\left(\int_0^\tau A(t)dt - 3\right) + 0.5 \tag{5.20}$$

$$Z(\tau) = \frac{0.4A(\tau)}{\left(3 - \int_0^\tau A(t)dt\right)^2 + 1} \tag{5.21}$$

To give an example of this, consider a non-isothermal thermal history in which the cooling rate is not constant, but cools from 180 °C to 60 °C over the course of 10 minutes with the cooling rate increasing through the middle of the cooling duration before reducing to zero at 60 °C. This cooling rate loosely resembles the cooling profile from a reheating caused by a subsequent layer, as seen in Figure 5.14. Let this function $f(t)$ be given by:

$$T(t) = 120e^{-0.06t^2} + 60 \tag{5.22}$$

whose plot is shown in Figure 5.24(a). Then $\Phi(t)$ is given by dT/dt:

$$\Phi(t) = -14.4te^{-0.06t^2} \tag{5.23}$$

whose plot is shown in Figure 5.24(b). This therefore yields for $A(t)$ at instantaneous time τ:

$$A(\tau) = 0.0028\left(-14.4\tau e^{-0.06\tau^2}\right) + 0.0072 \tag{5.24}$$

The 3-dimensional $T - Z(T) - X(T)$ curve is shown in Figure 5.25. Figure 5.26 shows this curve imposed on the constant cooling rate $T - Z(T) - X(T)$ surface plotted in Figure 5.22. It can be observed that the curve follows the surface, however not along any contour phase line of constant Φ. As a result, it can be seen that the general governing equations 5.42 and 5.43 represent a general algorithm for the prediction of degree of relative crystallinity and rate of crystallisation from any given thermal history.

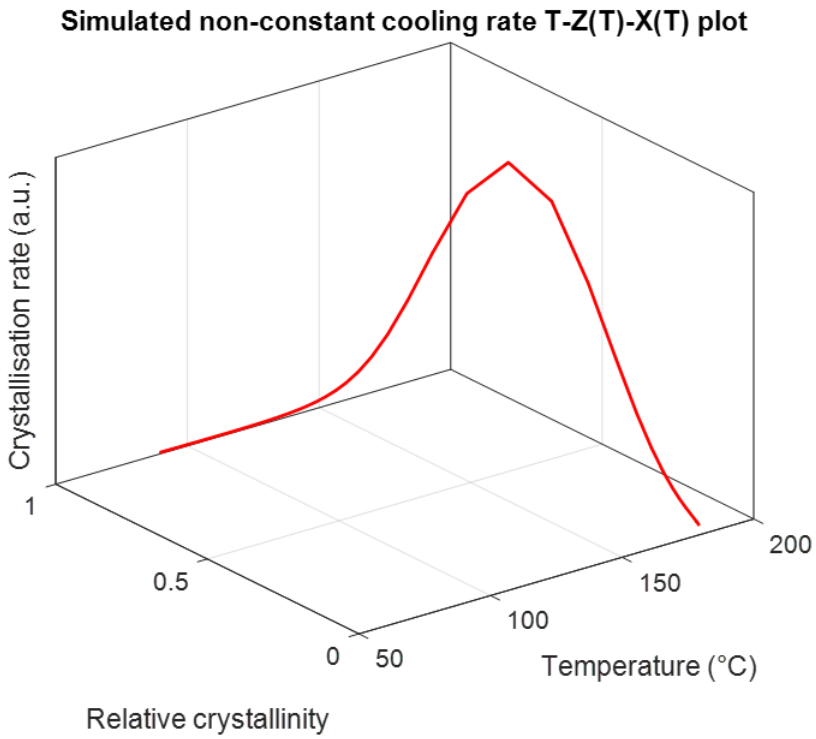


Figure 5.25: The $T - Z(T) - X(T)$ plot of the simulated non-constant cooling rate crystallisation.

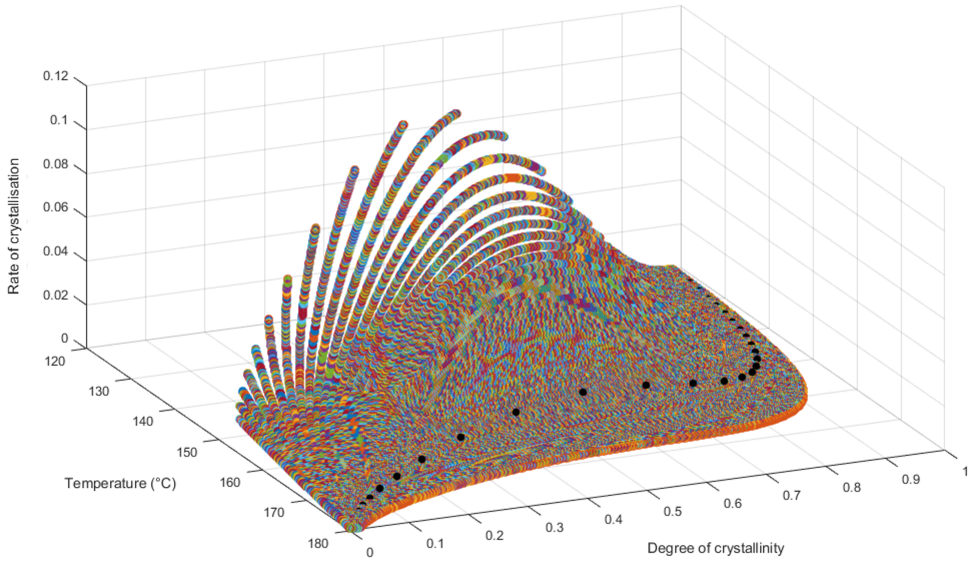


Figure 5.26: The $T - Z(T) - X(T)$ plot of the simulated non-constant cooling rate crystallisation, superimposed onto the $T - Z(T) - X(T)$ arctangent three-dimensional surface.

5.3 Conclusions

It is clear from the modelling of crystallisation behaviour using the Nakamura-Avrami model that due to the highly inhomogeneous and directional nature of extruded Nylon-12 filament, the ideal Avrami behaviour does not represent the actual crystallisation behaviour of the filament. Similarly, the limitations of Hoffman-Lauritzen theory and the Hoffman growth model in modelling the non-isothermal crystallisation behaviour of the Nylon-12 filament is clearly visible. This is perhaps to be expected; Zhao's [16] study on Nylon-12 powder, which has a much higher degree of directional homogeneity, also revealed some significant deviation from Avrami theory in both the isothermal and non-isothermal cases.

Nevertheless, it is notable that application of the Hoffman growth model can be useful in modelling the behaviour of Nylon-12 filament. The model produced data for predicted crystal growth rate and radius of single crystal are consistent with the behaviour that would be expected based on the experimental data. However, the shape of the crystal growth rate curve in Figure 5.15 closely resembles that generated by the non-isothermal crystallisation model in Figure 5.3, suggesting that the same limitations apply when describing in detail the crystallisation behaviour of Nylon-12 filament.

The MATLAB model to describe the thermal history is a useful tool for roughly describing the thermal history for modelling purposes, but likewise is severely limited. Although the model takes thermal contacts into account, it fails to fully replicate the sharpness of the subsequent reheatings as seen in literature experimental data, and fails to produce a similar number of reheatings. It is hypothesised that thermal contact with neighbouring filaments alone is insufficient to describe the thermal history of an individual filament. This may be due to underestimating the magnitude of the effect of the thermal field of the nozzle, which may permeate multiple layers due to the size and proximity of the nozzle. This thermal field would result in reheating of layers below more than the thermal contact of a newly-deposited filament at 245 °C would.

Regarding the arctangent fitting of the experimental non-isothermal data, it must be stressed that despite the suitability of the function for fitting, and the close resemblance of its Taylor expansion to that of the Avrami function, it does not constitute a model *per se*, as it does not resemble an *a priori* mathematical description of the physical processes and is simply an *a posteriori* description of the shape of the experimental data.

Nevertheless it is a highly useful tool for plotting and predicting the shape of crystallisation and crystallisation rate curves for non-isothermal crystallisation, and is capable of being adapted for non-constant cooling rates. Most crucially, its neatness as a function allows it to be used to plot the $T - Z(T) - X(T)$ surface that allows for the degree of crystallinity and crystal growth rate to be predicted from any thermal history. This represents a powerful tool for the prediction of material properties from thermal history, and serves as a key link in establishing the processing-structure-property link in FFF Nylon-12.

6

Mechanical testing of FFF Nylon-12 samples

Contents

6.1 Introduction 178
6.1.1 Samples tested 179
6.2 Results and discussion 179
6.3 Analysis 182
6.3.1 Young's Modulus 182
6.3.2 Ultimate tensile strength 184
6.3.3 Yield point 186
6.3.4 Elongation at break 187
6.4 Conclusions 188

6.1 Introduction

This section presents the results obtained from the tensile testing of FFF Nylon-12 samples. Samples were produced contemporaneously with the samples in Section 4.2.3.2; that is, samples were printed in the Apium P220 at a bed and chamber temperature of 120 °C before being annealed for 60 minutes at temperatures between 130 and 190 °C. A list of samples produced and tested is given in Table 6.1.

Samples were tested using a 1kN Deben Microtest MT1000 tensile stage, with jaw movement speed of 0.2 mm/s. Samples were stretched to the maximum possible jaw width of 20 mm, a maximum strain ϵ of 1.17. The load cell on the Deben MT1000 measures force and extension at intervals of 500 ms, outputting a force-extension curve. From this data, the stress-strain curve was calculated using the measured cross-section of the samples as 8.75×10^{-6} m^2. The Young's modulus, yield point and ultimate tensile strength were calculated from this data according to the schematic in Figure 6.1.

120°C	Apium P220 at 120°C
130°C	Apium P220 at 120°C plus anneal at 130°C
140°C	Apium P220 at 120°C plus anneal at 140°C
150°C	Apium P220 at 120°C plus anneal at 150°C
160°C	Apium P220 at 120°C plus anneal at 160°C
170°C	Apium P220 at 120°C plus anneal at 170°C
180°C	Apium P220 at 120°C plus anneal at 180°C
190°C	Apium P220 at 120°C plus anneal at 190°C

Table 6.1: Sample preparation details for all FFF samples mechanically tested.

The aim of this section was to examine the effect of annealing on the tensile properties of the samples. Since these samples were produced contemporaneously with the samples in Section 4.2.3.2, a quantitative link could subsequently be made between degree of crystallinity and mechanical properties. All samples were printed with the same geometry and scan strategy to minimise the effect of mesostructural variation on tensile properties.

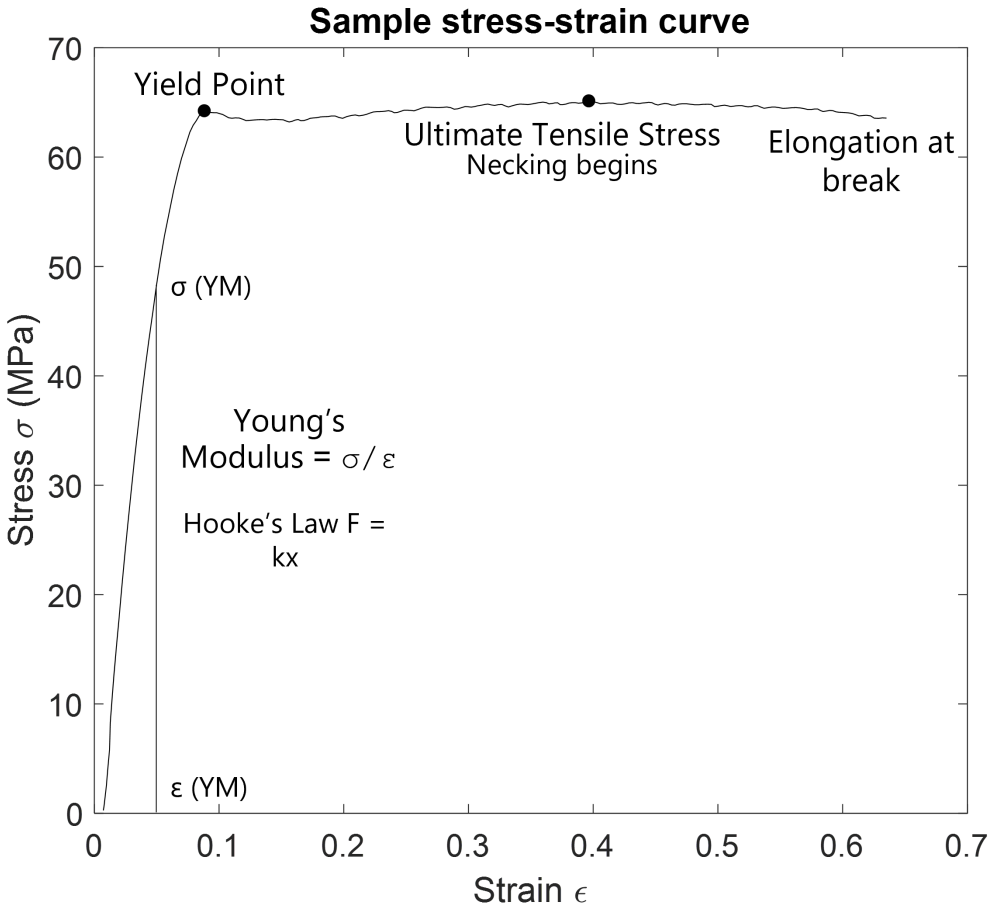


Figure 6.1: A sample stress-strain curve with annotations indicating the relevant metrics for mechanical analysis.

6.1.1 Samples tested

Table 6.1 shows a list of all samples produced, and their thermal history.

6.2 Results and discussion

The results for the tensile testing of the FFF samples are shown below in Table 6.2.

T_c (°C)	120	130	140	150	160	170	180	190
Young's Modulus E (GPa)	0.77	0.77	0.88	0.89	0.91	1.03	1.08	1.26
Yield point (MPa)	49.8	53.0	55.8	58.6	60.5	64.2	68.1	71.9
Ultimate Tensile Strength (MPa)	51.3	55.2	56.9	59.9	61.2	65.1	69.6	72.8
Necking strain	0.31	0.31	0.30	0.39	0.39	0.39	0.40	0.40
Elongation at Break	0.80	1.17	0.55	1.17	0.57	0.63	1.06	0.67

Table 6.2: Mechanical testing data for the FFF samples.

The stress-strain curves for the samples is shown in Figure 6.2. All samples display the same stress-strain curve shape: an initial elastic region up to the yield point, where the stress then subsequently decreases before increasing again to the UTS, its maximum value. It is notable that the stress declines after the UTS until fracture. This is in line with stress-strain curves seen in literature for ductile materials [143] and for FFF-produced thermoplastic samples [91, 144, 145], however stands in contrast to the stress-strain curve most often seen for semi-crystalline thermoplastics [2], in which the stress rises to a maximum just before breaking.

It is also notable that after the yield point, strain hardening occurs for all samples, resulting in a rise in measured stress up to the UTS. This is caused by a large scale orientation of chain molecules and lamellar crystals; the results from the *in situ* mechanical testing in Chapter 3 bear this out. The appearance of the 040 reflection in the meridional (tensile testing) direction in Figure 3.12 show the orientation of FFF Nylon-12 samples in the direction of tensile stress.

It can be observed that the annealing temperature has a clear effect on the tensile properties of the samples. Annealing at 190 °C increases the Young's Modulus from 0.77 GPa at 120 °C to 1.26 GPa, an increase of 64%. A similar relationship between UTS and yield point is recorded. The UTS increases by 37% from 51.3 MPa to 72.8 MPa as the annealing temperature rises from 120 to 190 °C, while the yield point increases by 46% from 49.3 MPa to 71.9 MPa.

The values in Table 6.2 compare favourably to literature. A range of values for the UTS of Nylon-12 have been reported. Kam *et al* [146] reported a value of 29.1 MPa for FFF Nylon-12 printed at room temperature. Other studies [147–151] have reported values between 37 and 50 MPa, with the highest values being for SLS Nylon in the studies of Majewski *et al* [94] and Puttonen *et al* [148]. This is around the same as the lowest value for UTS obtained in this study (51.3 MPa); it is proposed that the build conditions of the Apium P220 at 120 °C is comparable to those experienced during SLS, resulting in these comparable figures.

Reported values of Young's Modulus for Nylon-12 range from 1.08 [151] to 1.83 GPa [148], with the highest value being recorded for SLS Nylon-12. Nylon-12

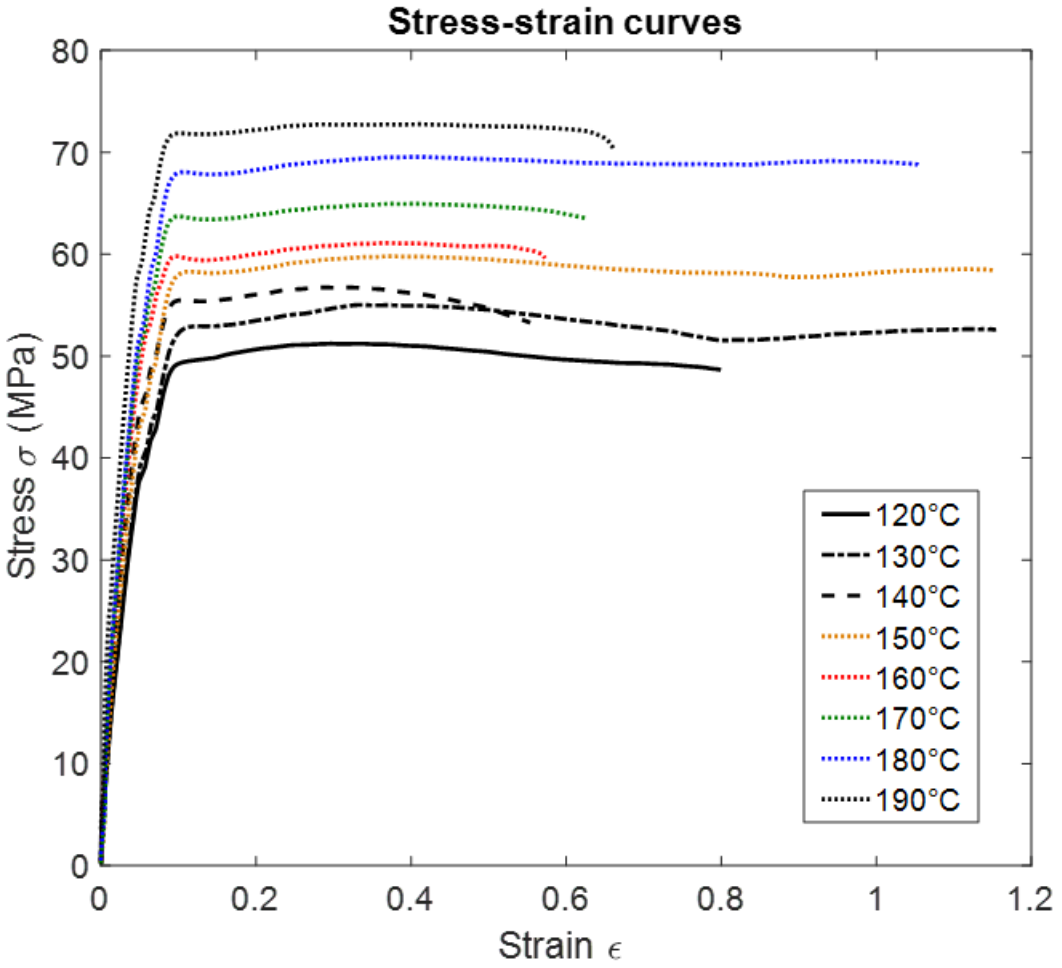


Figure 6.2: The stress-strain curves for the tested FFF samples.

samples manufactured through injection moulding record Young's Moduli around 1.33 GPa [150]. Values for FFF-produced Nylon-12 samples tend to be around 1.05 GPa, with the highest value recorded in the study of Knoop *et al* [64] as 1.55 GPa. The highest value recorded in this study is 1.26 GPa, which is comparable with these literature figures.

It can also be observed that necking commences at approximately the same strain for all samples. Table 6.2 shows that samples annealed between 120 to 140 °C have similar necking strains, while samples annealed between 150 to 190 °C have similar but 25% higher necking strains. This is in line with the isothermal crystallisation data, which shows that samples isothermally crystallised above 150°C have different thermal properties to those below. It is also correlated with the DSC

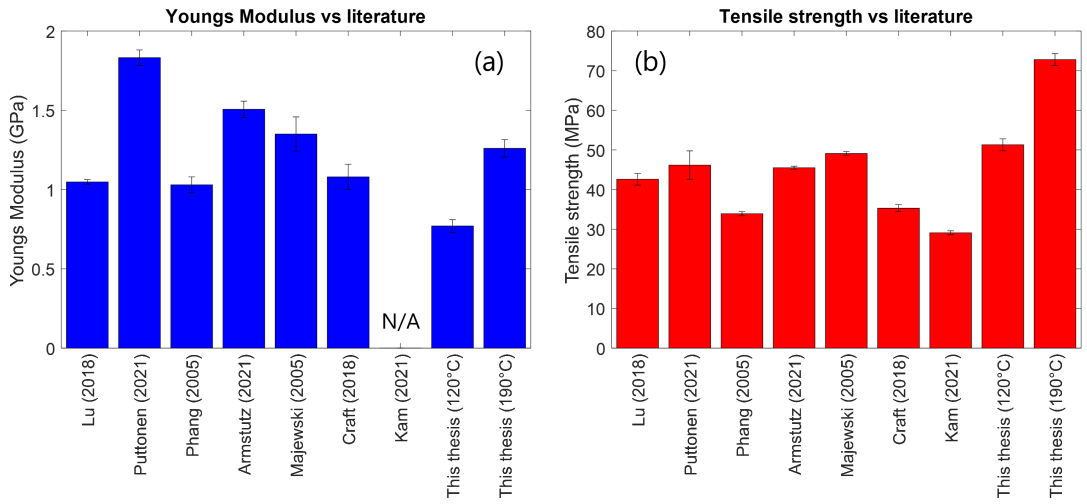


Figure 6.3: A comparison of obtained values for (a) Young's Modulus and (b) UTS with data from the literature for Nylon-12.

data in Section 4.2.1.2, which shows a more prominent Peak II appearing at 150 °C.

Literature data for EAB varies considerably depending on how samples are manufactured, with SLS Nylon-12 samples recording EAB of between 0.05 and 0.15 [94, 148]. In studies on FFF Nylon-12, Kam *et al* [146] recorded EAB of 0.22. Rahim *et al* [144] recorded EAB >0.25, where 0.25 was the maximum value recordable in the study. The values recorded in this study are all in excess of 0.55, in excess of many of these recorded values. Notably, EAB data in this study does not appear to be correlated to the annealing temperature, as considerable variation is seen. Two samples reached the end of the Deben MT1000 tensile stage's limit of travel without fracture.

A comparison of the obtained values for tensile properties with those obtained in literature is plotted in Figure 6.3.

6.3 Analysis

6.3.1 Young's Modulus

Figure 6.4 shows the Young's Modulus E plotted against annealing temperature. The data shows a non-linear fit, which has been fitted in Figure 6.4 with the

following function:

$$E = A + Be^{\frac{C}{T_m^0 - T}} \tag{6.1}$$

with coefficients $A = 1.7, B = -1.05, C = -12.59$.

The rationale for this fit is as follows. The Hookean behaviour of semi-crystalline thermoplastics is driven by the strain on the crystal structure, and thus E might be expected to be directly proportional to the degree of crystallinity X_c. This relationship of direct proportionality between E and X_c is consistent with data observed in literature and described in Section 1.4.3.1 for semi-crystalline polymers [86, 87, 99], in which a linear relationship has been observed.

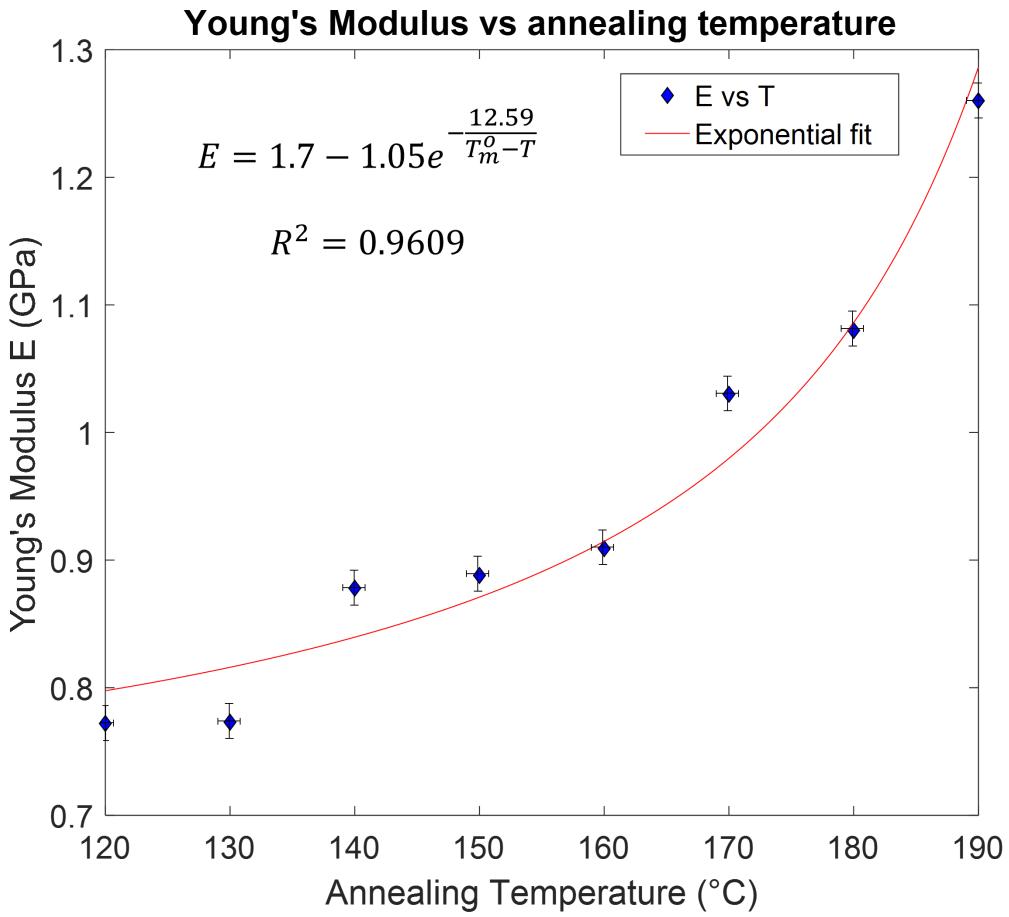


Figure 6.4: The Young's Modulus E plotted against sample preparation temperature.

Based on this known relationship between E and X_c, it was proposed to fit the E vs T data with the same function that was used to fit X_c and T in Section 4.2.1. This function was found to be a good fit, with $R^2 = 0.9609$.

Many literature studies on the effect of annealing temperature on tensile properties have not attempted to fit the data; however, the data from this study is broadly consistent with the findings of Malekmotiei *et al* [152], who noted a similar fit for data on polymethyl methacrylate (PMMA).

6.3.2 Ultimate tensile strength

Figure 6.5 shows the ultimate tensile strength (UTS) plotted against annealing temperature. It can be observed that the data is well-fitted by a linear relationship, with the following equation:

$$\sigma_{UTS} = AT + B \tag{6.2}$$

with $A = 2.96 \times 10^5$ and $B = 1.566 \times 10^7$. R^2 for this fit is 0.9830.

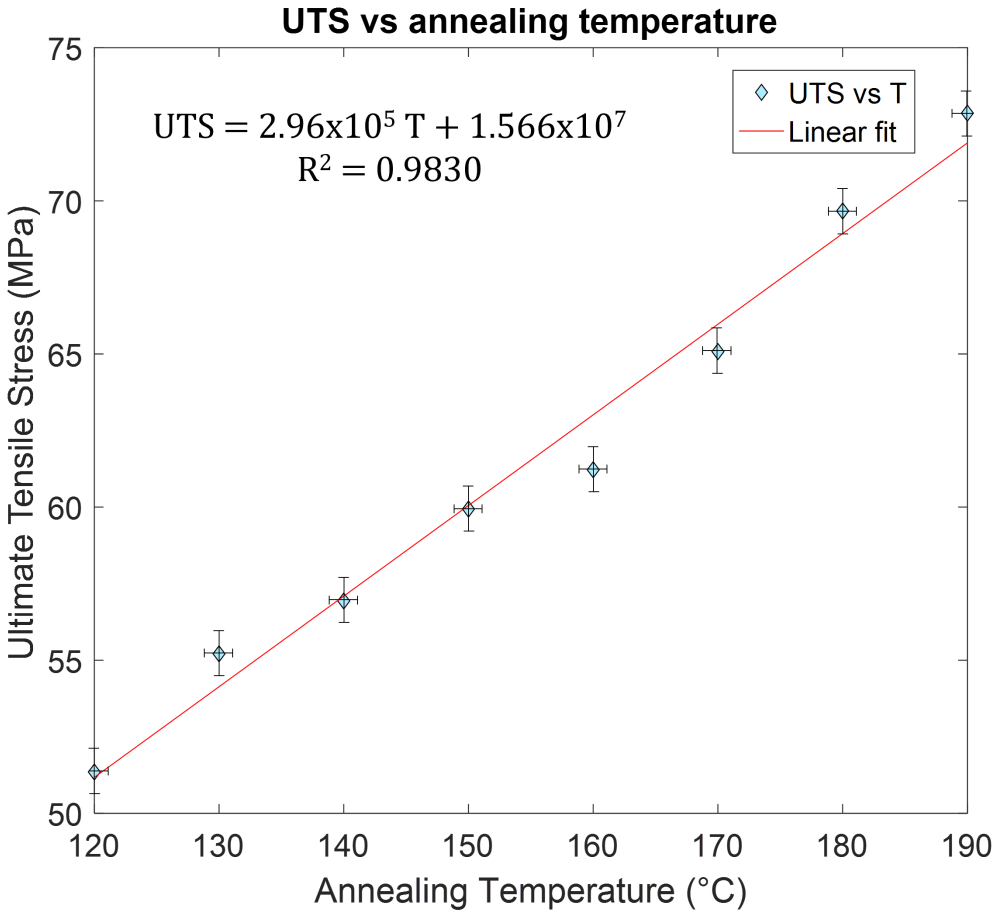


Figure 6.5: The ultimate tensile strength plotted against sample preparation temperature.

The increase in UTS with increased annealing temperature is well-aligned with results from the literature [44, 88–92]; however comparatively little literature has focused on attempting to establish a quantitative relationship. Dencheva *et al* [153] found a broadly linear relationship between annealing temperature and UTS for Nylon-6, albeit with only 3 data points, whereas Suder *et al*'s study on PLA found no strong correlation at all [154].

Previous studies on relationship between degree of crystallinity and UTS have found that they have a broadly linear relationship [89, 96, 152]. Given the non-linear relationship between annealing temperature and degree of crystallinity in this study, the linear relationship obtained here between annealing temperature and UTS stands in direct contrast to some literature works.

The reason for this differing relationship compared to the literature is not fully known. However, different literature studies have reported widely different relationships between crystallinity and UTS depending on the material and method of production. While Starkweather *et al* [86] report higher UTS at higher degree of crystallinity for injection moulded Nylon-66, Valerga *et al* [99] report the opposite phenomenon for FFF-produced PLA. Furthermore, in the study of Majewski *et al* [94] on SLS Nylon-12, increased crystallinity led to increased UTS up until 25% crystallinity, after which a decrease was seen.

It is proposed that the data for UTS here can be clarified from a physical standpoint. The UTS is most affected by the entanglement density of the amorphous phase [155–158], which is affected by the thermal history. In particular, as described in Equation 1.2 (Section 1.2.3.2), the mean squared displacement of a polymer chain due to reptation is given by:

$$s(t)^2 = 2k_B T \mu_{tube} t$$

where k_B is Boltzmann's constant and μ_{tube} is the coefficient of friction in a tube. At a given time t, this equation shows a linear dependence of $s(t)^2$ on T. Treating chain entanglement as a proxy for entanglement density, this results in the linear relationship observed in this study's data.

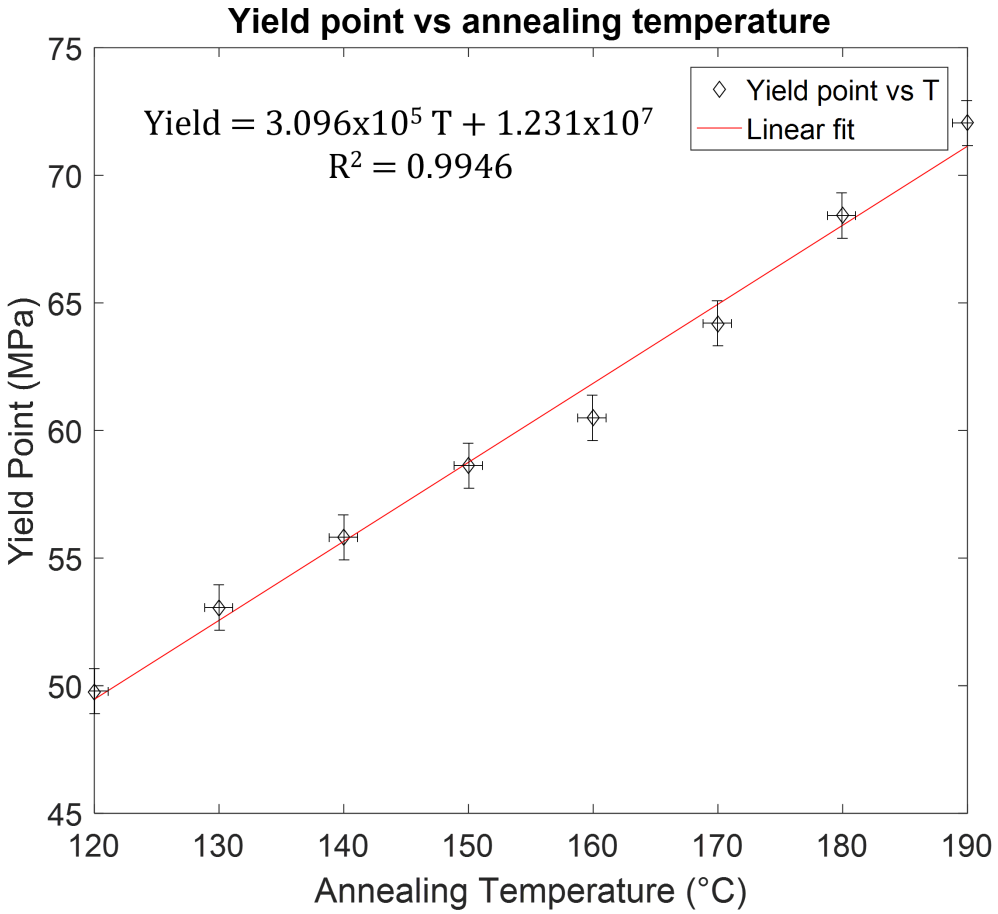


Figure 6.6: The yield point plotted against sample preparation temperature.

6.3.3 Yield point

Figure 6.6 shows the yield point plotted against annealing temperature. It can be observed that the data is well-fitted by a linear relationship, with the following equation:

$$\sigma_{UTS} = AT + B \tag{6.3}$$

with $A = 3.096 \times 10^5$ and $B = 1.231 \times 10^7$. R^2 for this fit is 0.9946.

Like UTS, yield point has been reported in literature studies [86, 87] to have a linear relationship on degree of crystallinity. The yield point is the maximum stress above which permanent deformation occurs. In semi-crystalline polymers, this is the point at which the crystal lamellae begin to unravel; prior to the yield point, the lattice stress and strain is being recorded, while thereafter the measured stress is on the oriented polymer chains in the direction of the load. Yield point

and by extension Young's Modulus is most directly influenced by stiffness-inducing components to the crystal structure, and therefore degree of crystallinity; this stands in direct contrast to the data obtained in this study.

The yield point of a semi-crystalline polymer has been reported to be directly proportional to the lamellar thickness by [159, 160]. This is given by Equation 1.24 in Section 1.2.5.4 to be inversely proportional to $T_m^0 - T_c$. This would result in a hyperbolic curve rather than the linear relationship seen in this data.

However, studies have also found a linear dependence on annealing temperature, in agreement with the results in this study. Dencheva *et al* [153] and Malekmotiei *et al* [152] both reported a linear dependence on annealing temperature.

6.3.4 Elongation at break

The fracture behaviour and elongation at break (EAB) of FFF Nylon-12 prepared at different temperatures remain unclear. Table 6.2 shows that the necking strain appears to be correlated to temperature, however the behaviour after necking varies from sample to sample, with two samples displaying ductile rather than brittle failure. It is theorised that crack formation in FFF samples is affected by the inter-layer bond formation in addition to structural properties.

Due to the sample geometry, the z-orientation of FFF printed samples was perpendicular to the tensile direction. This results in a set of weak boundaries perpendicular to tensile direction and therefore to crack formation. It was shown by Hills, Korsunsky et al [161] that a weak interface perpendicular to crack growth inhibits the crack growth in its original direction. In fact, it was previously observed that FFF samples tend suffer from layer delamination during the tensile process, which damages the samples but simultaneously inhibits crack growth. This is proposed as a mechanism for the varied EAB results observed in these tests.

Literature data on EAB as a function of annealing temperature also yields a variety of results. Li *et al* [162], Vielle *et al* [163] and Benwood *et al* [164] also report EAB results with no clear correlation to annealing temperature.

6.4 Conclusions

Based on the data presented, it is clear that the degree of crystallinity has a significant impact on the mechanical properties of the sample. The relations between degree of crystallinity X_c, E, UTS and yield point are plotted in Figure 6.7. UTS and yield point are fitted with a function derived from the X_c vs T relation, such that:

$$\sigma = C + \frac{D}{\ln(A - X_c) - \ln(-B)} \tag{6.4}$$

where A and B are from the X_c vs T relation with values 35.2 and -21.35 respectively. C and D are calculated to be 7.53×10^7 and 5.05×10^6 respectively for the yield point, and 7.59×10^7 and 4.83×10^6 respectively for the UTS.

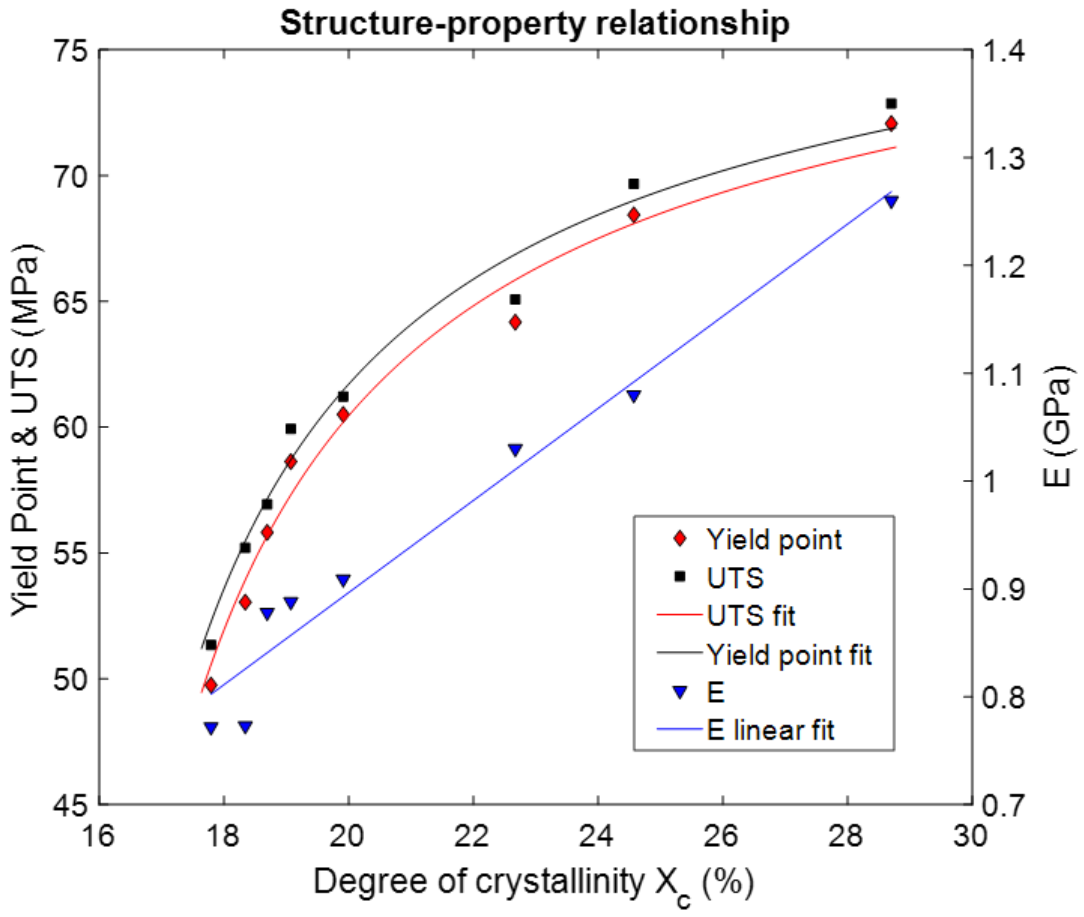


Figure 6.7: Young's Modulus, UTS and yield point plotted against crystallinity.

The shape of these curves is to be expected given the relationships between X_c and T and E and T. The appropriateness of the linear fit for E vs X_c affirms the

choice to fit E and X_c using the same function type. This relationship is also in line with the physics; E is driven by the crystal properties of the sample, while UTS is dependent on chain entanglement; an increase in degree of crystallinity will therefore have a progressively smaller effect on UTS.

The mechanical testing shows the clear effect of annealing temperature post-printing on the tensile properties of FFF Nylon-12 samples. Young's Modulus, ultimate tensile strength and yield all have a close linear relationship to printing temperature. This allows the establishment of the processing-property link, between printing temperature and mechanical properties, but also of the structure-property link, between degree of crystallinity and mechanical properties.

It is proposed that this data, to an extent, fits the results from Chapters 3 and 4. It was demonstrated in Section 4.2.1 that isothermal crystallisation at a high temperature resulted in the same DSC trace as non-isothermal crystallisation at a slow rate; namely, a single principal peak. In Section 4.2.3.2, it was further noted that annealing at a higher temperature such as 190 °C also resulted a DSC trace which resembled this, albeit with the peak position at a higher temperature. It is therefore proposed that the samples annealed at a high temperature tested in this chapter and in Section 4.2.3.2 will demonstrate similar crystal morphology, with larger and more perfectly formed crystalline structures. The more dense and better formed lamellae that were observed in the slowest-cooled samples in Section 3.2.2 are likewise proposed to be a key component of the improved tensile properties observed in this chapter.

In addition, the data also shows that the tensile properties can be tailored through control of the thermal history. In this case, annealing temperature has been examined rather than cooling rate during printing, however this parameter alone is capable of a 64% increase in Young's Modulus over a 58% increase in printing temperature.

7

Processing-Structure-Property Relationship

Contents

7.1 Processing-structure relationship 192
7.2 Structure-property relationship 197
7.3 Processing-structure-property relationship in FFF Nylon-12 198
7.3.1 Governing equations 200
7.3.2 Conclusions 201

7.1 Processing-structure relationship

The processing-structure relationship discussed in this chapter concerns specifically the correlation between the conditions of FFF sample preparation and subsequent heat treatment, on the one hand, and the material structure in terms of the degree of crystallinity. Clearly, the term "processing-structure relationship" allows a much broader interpretation, depending on the aspect of semi-crystalline polymer structure chosen as the subject of study. Semi-crystalline polymers possess complex hierarchical structure that consists of crystal lamellae sandwiched between amorphous regions, which grow to form crystallites or spherulites on the scale of microns [165]. This structural hierarchy leads to a large number of structural parameters that can be analysed; on the microscale the lamellar thickness and long period for instance, and on the mesoscale the spherulite radius or direction of growth. However, for the purposes of the present study, and as will become apparent further in this chapter, the degree of crystallinity X_c can be chosen as the principal structural parameter of interest in view of its determining significance for material's mechanical properties.

The relationship between 3D printing temperature (and/or cooling rate) and the degree of crystallinity is, in theory, expressed by the Avrami model which relates the thermal history of a sample to its rate of crystallisation and degree of relative crystallinity. The Hoffman growth model predicts values of the average crystal radius, nucleation rate and crystal growth rate as a function of thermal history. However the application of the Avrami model to the isothermal crystallisation data and the Nakamura-modified Avrami model to the non-isothermal crystallisation data reveals significant disagreement between the experimentally obtained data and the model.

The arctangent function used to describe crystallisation kinetics in Chapter 5 was found to be an improved fit for the range of non-isothermal data collected in this project, and was found to describe the isothermal data with comprable accuracy to the Avrami model. Furthermore, the arctangent function's primary variable was found to have a linear dependence on cooling rate. This allowed for the construction of a surface plot created from the arctangent functions circumscribing a large range of cooling rates, which link temperature (and therefore thermal history)

to relative crystallinity and crystal growth rate. Any thermal history phase contour line on this surface plot can be projected onto the $x - y$ and $x - z$ axis planes to show the resultant relative crystallinity and crystal growth rate curves. This allows for considerable predictive power, as any thermal history can be drawn out on the surface plot. For any temperature arising from a given thermal history, the instantaneous relative degree of crystallinity and crystal growth rate can thus be computed. Therefore, for any given temperature profile that might occur during cooling, the crystallisation behaviour can be predicted from this model.

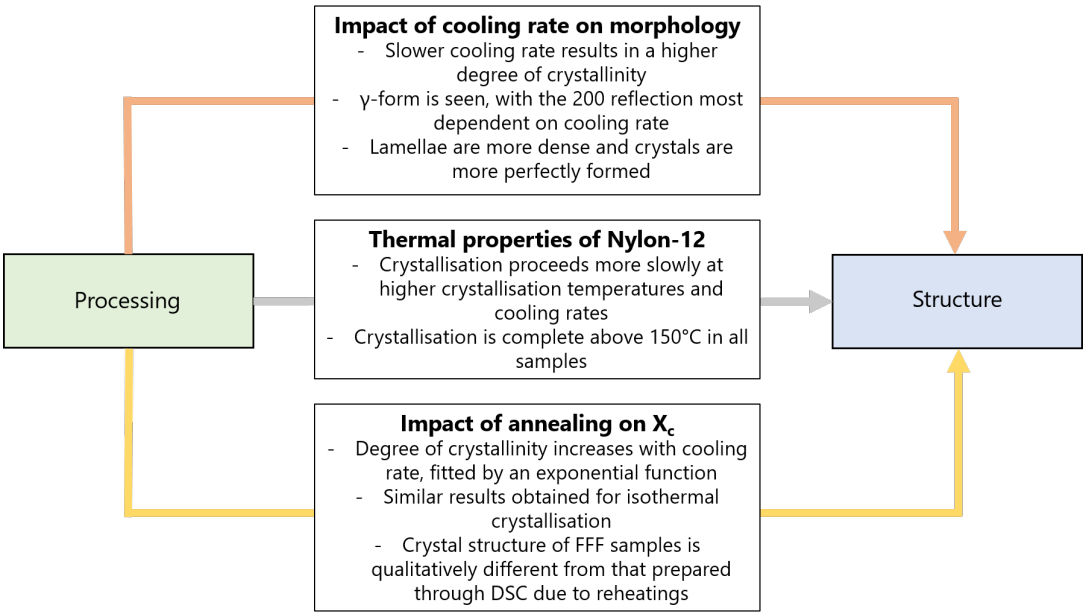


Figure 7.1: A summary of the findings relating to the processing-structure relationship.

The thermal history for a given FFF print can be described using the adapted model from Costa *et al.* This model, which uses a series of contacted filaments to model thermal history, assumes that heat flow into a deposited layer derives from the subsequent deposition of molten filament above it. This model, however, did not incorporate the effect of latent heat of crystallisation, and did not use its modelled thermal history to make quantitative predictions about crystallisation behaviour. The model's contacted filament methodology was adapted to add a crystallisation term into the governing equations, and extended their output to predict number of nucleations, crystal growth rate and crystal radius in order to

examine the effect of FFF's unique thermal history on Nylon-12's crystallisation behaviour. However, comparing of the modelled thermal history results to the literature data shows that some key elements of the thermal history are not captured by the model, including multiple reheatings from proximity to the nozzle, and the long period of time taken for a sample to cool to T_∞ seen in actual prints. Thermal history is therefore at this stage better generated from real world data. The thermal contact model fails to describe fully the thermal history of FFF, as it does not incorporate the effect of the nozzle as a source that remains present and significant even when separated by multiple deposited layers.

The isothermal crystallisation data bears quantitative similarity to the DSC data from samples printed at different chamber temperatures, which sheds light on the link between thermal history and structure in FFF. FFF, as a thermal AM method, relies on temperature change to effect phase transition from molten to solid. To make this process practicable for large volumes, temperature change must occur rapidly, both in terms of melting of the filament and cooling of extruded volumes to obtain solid shapes, which is the key factor in predicting the final material structure. The initial rapid cooling from melt, and subsequent reheatings and recoolings make up a highly non-isothermal period of the FFF process. The subsequent period, which is driven by the ambient chamber temperature, can be considered to be long isothermal hold. The similarities between the isothermal crystallisation data and the DSC data from samples printed at different chamber temperatures show firstly that isothermal crystallisation can be used as an limited but useful approximation for FFF. This data also provides the opportunity to plot degree of crystallinity in FFF samples against chamber temperature. The X_c vs T data from samples printed at different chamber temperatures is well fitted by an exponential relationship in accordance with Hoffman-Lauritzen theory, from which predictions of absolute crystallinity can be made from the thermal history in FFF. In addition, the plot of absolute crystallinity in isothermally crystallised samples versus isothermal crystallisation temperature shows the same relation between T_c and X_c.

The link between thermal history and crystal structure is shown well by the results from the XRD analysis, which clearly show the effect of the FFF process on the crystal structure. The FFF process is proposed to result in a high degree of chain alignment in the direction of the filament due to the extrusion through the nozzle; simultaneously, the melting of the filament that takes place in the nozzle also allows for a more energetically favourable realignment of the lamellar sheets. This process causes the appearance of the second diffraction peak, attributable to the 200 reflection.

The results obtained from the XRD analysis detailing the formation and splitting of the two diffraction peaks are in good agreement with the DSC data, as the 200 reflection coalesces with the $001(+20\bar{1})$ reflection as $T > T_g$. The position and intensity of the 200 reflection corresponds to the lamellar density and crystal perfection respectively. The slower the cooling rate, the more perfect the crystal structure that is formed.

Furthermore, the proposed model of crystallisation and chain alignment from the XRD data is given weight by the results from the *in situ* mechanical testing, in which the patterns in the equatorial and meridional direction directions diverge as strain increases. Additional chain alignment is seen by the appearance of the 040 reflection, corresponding to the *b*-axis of the Nylon-12 unit cell.

The XRD, DSC and thermal modelling data combine to give clear insights into the processing-structure relationship in FFF Nylon-12. The effect of the extrusion through the nozzle and remelting on the crystal structure is visible from the XRD data, which shows the effect on the unit cell and lamellar structures in Nylon-12. The thermal history is related to the structure via the *in situ* non-isothermal crystallisation experiments, in which a slower cooling rate was clearly seen to result in a more perfectly formed crystal structure. This is in line with the DSC data, which has a more pronounced single melting endotherm at the slowest cooling rate, indicating larger crystallites.

Changing the cooling rate effects comparable results in both the DSC and the XRD data. As the cooling rate increases, the crystallisation time decreases and thus

the crystals are less well formed. This is displayed as the lower temperature shoulder in the DSC data, corresponding to smaller and less perfect crystal structures that melt at lower temperatures. In the XRD data, this is displayed as a 200 reflection with a broader width and a larger d-spacing, indicating less dense lamellae. Based on the correlation between non-isothermal and isothermal DSC data, whereby high-temperature isothermal crystallisation was proposed to result in similar crystal morphology to slow non-isothermal crystallisation and vice-versa, high-temperature isothermal crystallisation or high-temperature annealing are proposed to result in the same well-formed crystals and would be expected to see a clearly defined 200 reflection with a smaller d-spacing.

It is proposed that, in the case of FFF, the effect of annealing on crystal structure and degree of crystallinity can be extended to some extent to bed and chamber temperature. Should a printer be constructed capable of reliably building at 180 or 190 °C, the data from Chapters 3 and 4 suggest that this would result in optimal crystal structure.

From the experimental data, the arctangent model can be used as an alternative to Avrami or Nakamura-Avrami theory to predict the crystallisation behaviour of Nylon-12 which is applicable to FFF. As a function of any combination of cooling rates, the relative degree of crystallinity and crystal growth rate can be predicted. Predictions about the thermal and structural properties can be made, since $X(t)$ and $Z(t)$ are calculated experimentally from the DSC curves; by knowing the properties of the crystallisation exotherms, predictions about the melting endotherms can be made on the basis of the data gathered. The isothermal crystallisation data and FFF DSC data allows for predictions of the absolute crystallinity of FFF samples with a given chamber temperature via the established relationship between X_c and T.

This data allows for a strong processing-structure link to be formed. The link between the thermal properties of isothermally (crystallisation temperature) and non-isothermally crystallised (cooling rate) samples has been established through DSC. The link between crystal structure and cooling rate has been established through *in situ* XRD. The link between annealing temperature and degree of

crystallinity has been established through DSC, and has been shown to have the same relation as for isothermal crystallisation. From this, a given thermal history of an FFF sample can now be used to predict the absolute degree of crystallinity, crystal structure, relative degree of crystallinity and crystal growth rate at time t during and after sample preparation.

7.2 Structure-property relationship

The tensile test data sheds considerable light on the nature of the structure property relationship. Firstly, the processing-property relationship is reliably established via the relationship between print chamber temperature and the mechanical properties of Young's Modulus E, ultimate tensile strength and yield point. All three of these properties show a clear linear relationship with chamber temperature for the temperature range at which the data was taken. The nature of the theoretical dependence of the yield strength on the lamellar thickness may mean that the data is a linear excerpt from a wider hyperbolic relationship, however no signs of deviation from the linear fit were seen within the temperature range analysed.

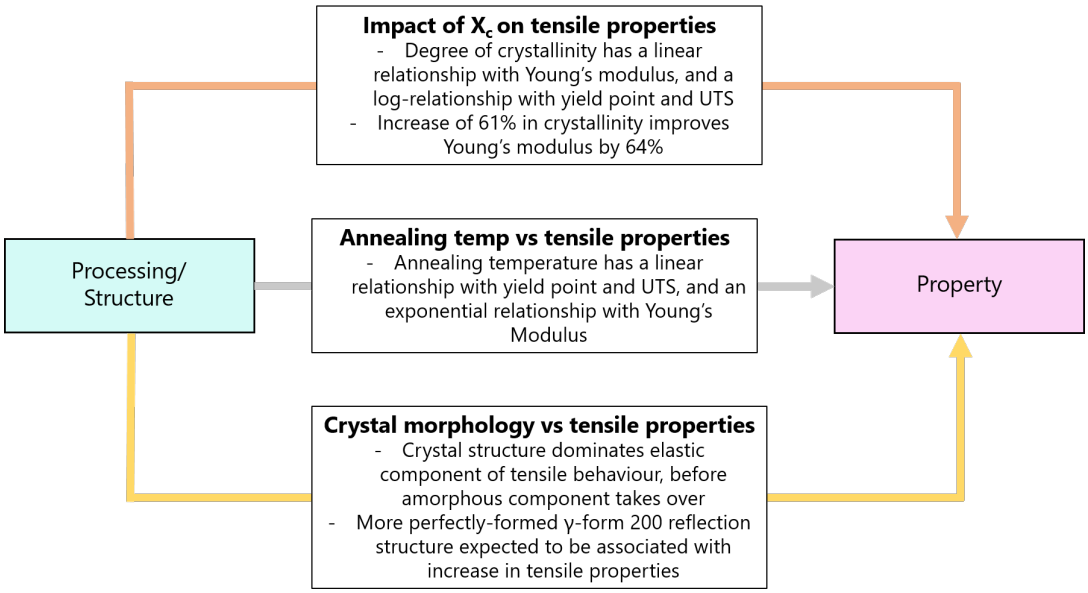


Figure 7.2: A summary of the findings relating to the structure-property relationship.

The increase in tensile performance is proposed to be correlated to the higher lamellar density and more perfect crystal structures that are associated with a

better defined 200 peak seen in the XRD in Chapter 3. These more perfectly formed crystal structures are in turn associated with the higher degree of crystallinity that is due to a higher annealing temperature. The lamellar thickening process that is described in Section 1.2.5 is proposed to be responsible for the alteration in crystal structure during the annealing process.

From this data and the processing-structure relationship, the structure-property link for FFF Nylon-12 can be established. The mechanical properties are plotted against degree of crystallinity, and a consistent trend emerges whereby a power law can be used to link the properties to the structure. As the degree of crystallinity increases, so too do the yield strength, Young's Modulus and UTS. Since the mechanical properties of a fully crystalline and fully amorphous sample can be predicted from the properties of a pure Nylon-12 crystal and the Nylon-12 backbone chain, these can be plotted on the structure-property relationship curve to extrapolate this relationship outside the bounds of the range of temperatures used for analysis.

7.3 Processing-structure-property relationship in FFF Nylon-12

Figure 7.3 shows the three plots from this study that show the components of the processing-structure-property relationship. Plot (a) shows the link between the thermal history and degree of crystallinity. Plot (b) shows the link between the degree of crystallinity and the mechanical properties. Plot (c) shows the link between the thermal history and the mechanical properties. Together these three make up an unbroken relation between the thermal history and the mechanical properties of the sample, and thus the processing-structure-property relationship for fused filament fabrication of Nylon-12 is established.

Although this represents a small fraction of the extent of the processing-structure-property link (for instance, it does not take into account the nature of the crystal structure as established via XRD on mechanical properties) it nevertheless serves as an extremely powerful tool for assessing and improving the performance of FFF. The data collected in this study establishes the link and has shown that it fits the

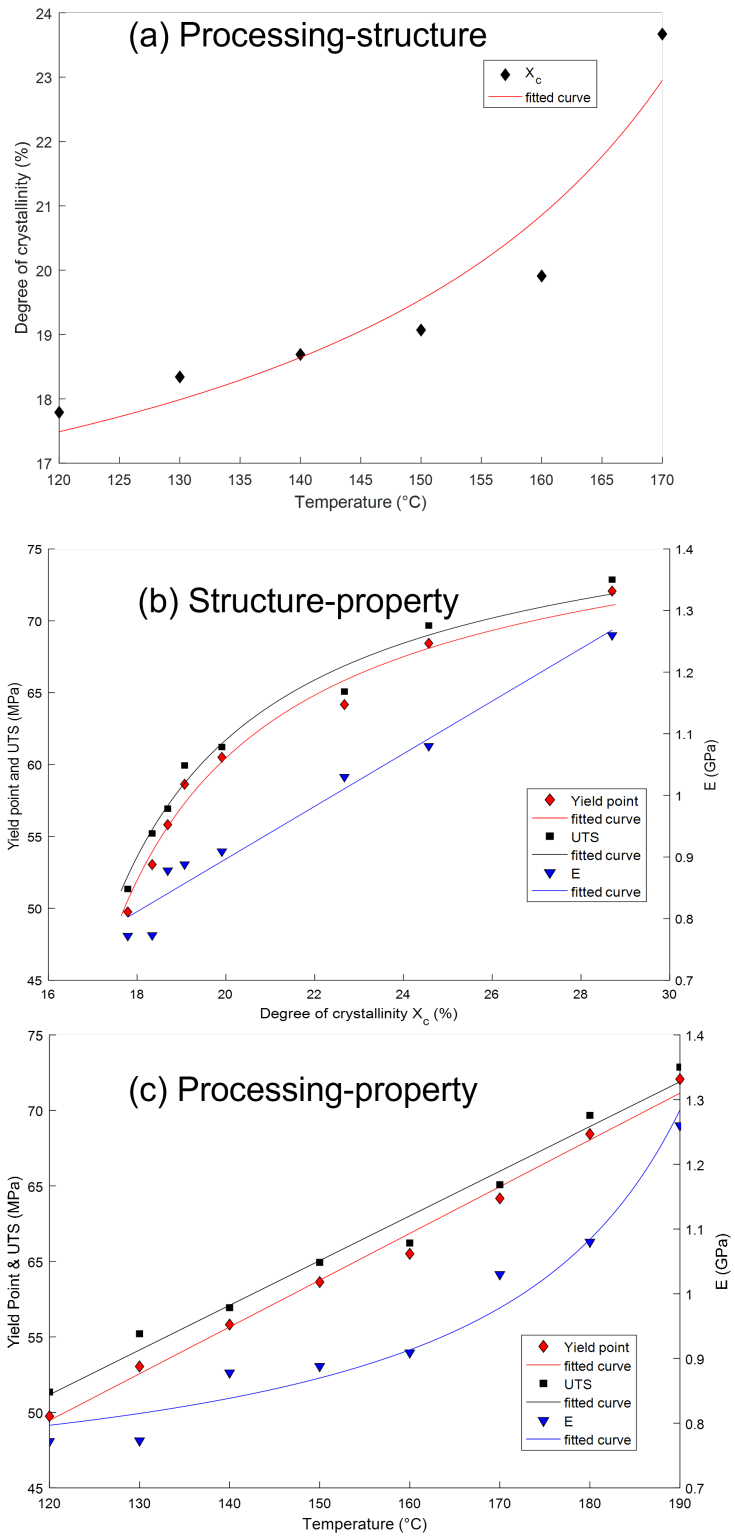


Figure 7.3: Three graphs indicating the three components of the processing-structure-property relationship for fused filament fabrication of Nylon-12.

governing equations of each stage. The processing-structure link between print chamber temperature and degree of crystallinity has been shown to be consistent with Hoffman-Lauritzen theory, namely the equations for lamellar thickness:

$$l_c \propto \frac{1}{(T_m^0 - T)}$$

and for total volume of crystallisation:

$$G = G_0 e^{-\frac{U^*}{R(T-T_\infty)}} e^{-\frac{K_g}{T_c \Delta T f}}$$

The processing-structure-property link between print chamber temperature and tensile properties has been shown to have a linear relationship; this is consistent with the relationship between ultimate tensile stress and polymer chain entanglement, given by:

$$s(t)^2 = 2k_B T \mu_{tube} t$$

where $s(t)^2$ is the mean squared displacement of a polymer chain, T is the temperature and t is the unit time at which $s(t)^2$ is measured. For the same time τ:

$$s(t)^2 \propto T$$

7.3.1 Governing equations

On the basis of the data presented in this thesis, the key governing equations for the processing-structure-property relationship of FFF Nylon-12 are proposed as follows.

Processing-structure relationship between thermal history and degree of crystallinity:

$$X_c(\%) = 35.2 - 21.35e^{-\frac{16.33}{T_m^0 - T}} \tag{7.1}$$

Processing-property relationship between thermal history and tensile properties:

$$\begin{cases} E(\text{GPa}) = 1.7 - 1.05e^{-\frac{12.59}{T_m^0 - T}} & (7.2) \\ \sigma_{yield}(\text{Pa}) = 3.096 \times 10^5 T + 1.231 \times 10^7 & (7.3) \\ \sigma_{UTS}(\text{Pa}) = 2.96 \times 10^5 T + 1.566 \times 10^7 & (7.4) \end{cases}$$

Structure-property relationship between degree of crystallinity and tensile properties:

$$\begin{cases} E(\text{GPa}) = 0.04271X_c + 0.04254 & (7.5) \\ \sigma_{yield}(\text{Pa}) = 7.534 \times 10^7 + \dfrac{5.05 \times 10^6}{\ln(35.2 - X_c) - \ln 21.35} & (7.6) \\ \sigma_{UTS}(\text{Pa}) = 7.593 \times 10^7 + \dfrac{4.83 \times 10^6}{\ln(35.2 - X_c) - \ln 21.35} & (7.7) \end{cases}$$

7.3.2 Conclusions

The establishment of the processing-structure-property relationship and governing equations provide evidence that variation in the thermal history results in significant variation in the structural and thermal properties of the FFF Nylon-12 samples. The FFF process is shown to result in a reorganisation of the crystalline morphology in Nylon-12 filament, creating alignment in the direction of the bonded lamellar sheets. A slowing of cooling rate or increase in annealing temperature is proposed to result in a lamellar densification, the formation of more perfect crystals and an increase in degree of crystallinity. A 58% variation in annealing temperature results in a 61% increase in degree of crystallinity and a 64% increase in Young's Modulus. The data that has been gathered can be cautiously extrapolated using the fits to these governing equations to provide significant predictive power for a larger range of temperatures. For instance, an attempt can be made to extrapolate the processing-structure link up to T_m^0. Although this is above the operating temperature of Nylon-12, a theoretical maximum crystallinity attainable is predicted. The governing equations can therefore be used to give a broad prediction of the processing-structure link, which is shown in Figure 7.4.

Moreover, the establishment of this link means that the processing conditions can be tailored to create a particular thermal history desired to achieve certain combination of structure and properties. From this link, the FFF process can be tailored to create a set of desired local properties; whether this is ultimate tensile stress, degree of crystallinity or otherwise. The detailed study into the effect of cooling rate and crystallisation temperature on the degree of crystallinity and

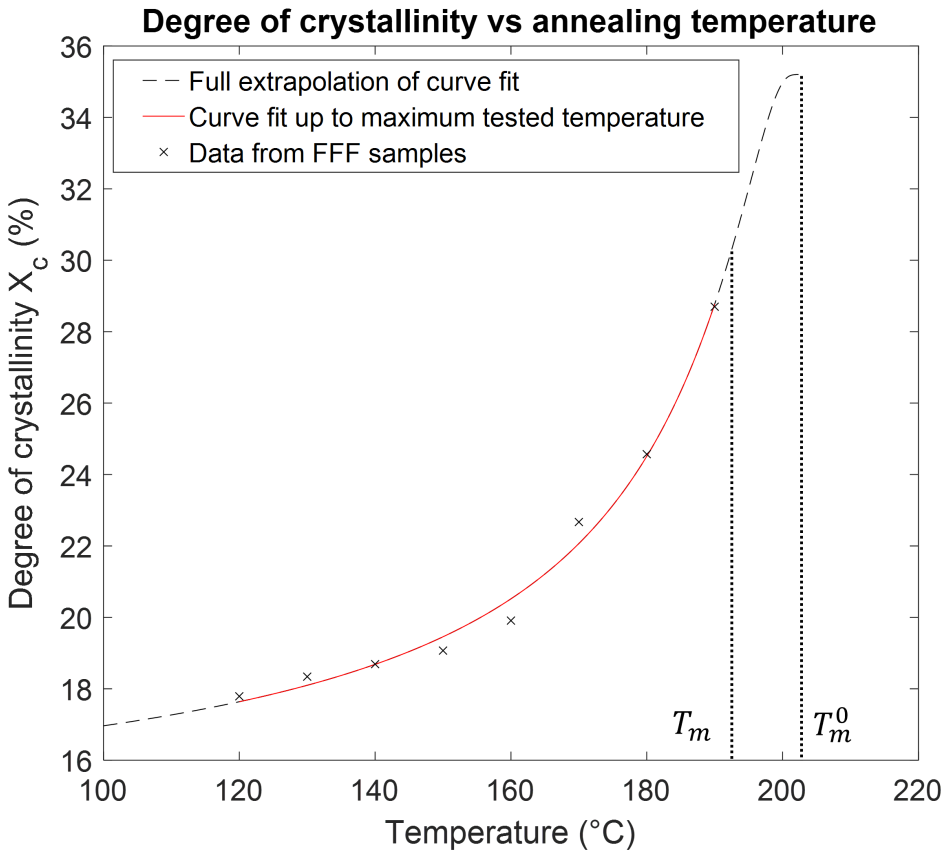


Figure 7.4: An extrapolation of the curve fit from the DSC data, allowing for predictions of degree of crystallinity across a broader range of FFF processing temperatures.

therefore mechanical properties offers considerable scope for prediction of mechanical properties from thermal history. More importantly, it allows for prediction of thermal history from mechanical properties. For a set of desired sample properties, therefore, a set of processing parameters for FFF can be output.

8

Conclusions and future work

Contents

8.1 Conclusions 204
8.1.1 Thermal properties of Nylon-12 204
8.1.2 On the viability of isothermal and non-isothermal crystallisation models for FFF 206
8.1.3 Impact on the structure of Nylon-12 207
8.2 Outlook 209

8.1 Conclusions

8.1.1 Thermal properties of Nylon-12

The isothermal and non-isothermal crystallisation of Nylon-12 filament result in several interesting conclusions. The non-isothermal crystallisation tests largely mirror the results previously seen in the literature, with a higher cooling rate resulting in a lower temperature of crystallisation onset, and a higher time of crystallisation. In particular, the thermal properties that result from cooling at higher temperatures are interesting to observe, which are revealed by subsequent reheating.

The double melting endotherm which is observed for Nylon-12 filament when cooled at temperatures exceeding 10 °C/min indicates a change in the crystalline structure of the material due to the more rapid cooling from melt. It is clear, therefore, that an alteration to the cooling rate has a much more significant role than simply changing the temperature of crystallisation onset or crystallisation half-time; it also affects the type of crystal structure that is formed, which in turn affects the thermal and likely the mechanical properties of the sample.

By contrast, the isothermal crystallisation results deviate considerably more from the literature results. There was agreement across multiple tests that the thermal properties of the Nylon-12 filament used in this thesis differ from bulk Nylon-12; it is unknown whether this is caused by the highly oriented nature of extruded filament, or whether there is adulterant added to the Nylon-12 filament during the filament manufacturing process. The equilibrium melting temperature T_m^0 was found to be several degrees higher than other values previously observed. Furthermore, the high temperature isothermal crystallisation experiments were required to be performed at a higher range of temperatures than in literature in order to get usable crystallisation exotherm data that was not significantly altered by instrumental inertia. Typically isothermal crystallisation experiments for Nylon-12 are performed between 162 and 170 °C; tests on Nylon-12 filament were performed between 168 and 176 °C.

Regarding the deviation of calculated thermal properties of Nylon-12 filament from literature values, various things may be said. The majority of previous tests

on Nylon-12 were performed on Nylon-12 crystals or films (by Ishikawa, Inoue *et al*) or on bulk Nylon-12 or Nylon-12 powder. Specific tests on filament are uncommon. It is hypothesised to be unlikely that an additive into the Nylon-12 filament could result in this deviation, as the filament is uncoloured and therefore undyed; furthermore tests done on powderised Nylon-12 for SLS have not yielded similar results despite being equally likely to contain additives. The deviation of the experimental crystallisation data from the Avrami and Nakamura-Avrami models, which will be discussed further in subsequent sections, suggests that there is a significant difference in thermal and structural properties in filament Nylon-12 which would result in this observed deviation. It is considered most likely to be due to the highly non-homogeneous and oriented nature of Nylon-12 filament.

The results from the high-temperature crystallisation correspond to previous results for Nylon-12 in terms of a lower isothermal crystallisation temperature resulting in a smaller crystallisation halftime and a higher magnitude of crystal growth rate. The results from the low-temperature crystallisation reveal several points: firstly, that isothermal crystallisation below 150 °C results in non-isothermal crystallisation, as the sample is fully crystallised during the non-isothermal cooling process to isothermal crystallisation temperature. It was found that samples nominally crystallised at T_c below 150 °C nevertheless crystallised at $\sim$ 152 °C.

Secondly, the reheating of the isothermally crystallised samples similarly revealed alterations to the thermal properties and crystal structure due to isothermal crystallisation temperature. The fact that samples crystallised below 150 °C show the same melting endotherm provides further evidence for the assertion that in fact a non-isothermal crystallisation at 60 °C/min took place for all of these samples. The gradual emergence of a second melting endotherm as T_c decreases is striking and shows the clear effect of a lower crystallisation temperature on the crystal structure.

Most importantly, the following conclusion can be made about FFF, which can be described as a non-isothermal cooling, followed by a saw-tooth temperature profile, followed by a quasi-isothermal crystallisation at T_∞. If T_∞ is lower than 150 °C, then the bulk of crystallisation takes place in the non-isothermal cooling

from melt, with additional crystallisation taking place during the reheatings due to deposition of subsequent layers. Time spent above 150 °C is hypothesised to be key to additional significant crystal growth. These results show the importance of a high T_∞, which is often overlooked during design of FFF machines due to its potential impact on resolution of detailed features. Nevertheless, for optimisation of material properties, there is a necessity to raise it above 150 °C.

8.1.2 On the viability of isothermal and non-isothermal crystallisation models for FFF

As discussed in Chapter 4, there is significant variation between the melting endotherms of samples crystallised at low temperatures and the FFF RS sample, where T_∞ is equal to 25 °C. In fact, despite the significant difference in WAXS pattern and mechanical properties compared to the FFF Apium sample, the DSC melting endotherms are broadly similar, with both displaying a small shoulder that broadly resembles the onset of the second melting endotherm seen in the lower-temperature isothermally crystallised samples.

In fact, the low-temperature isothermal crystallisation results show that this result is to be expected. Since all isothermal crystallisation temperatures below 150 °C result in the same melting endotherm DSC trace, a similar DSC trace is to be expected for these two samples despite the significant difference in T_∞. Any differences are hypothesised to be due to the time spent above 150 °C, which is expected to differ for the two samples due to the effect of the zone heater in the Apium P220. However, the position of the melting endotherm at 197 °C for the FFF Apium and FFF RS samples most closely resembles the position of the principal of the two melting endotherms in the samples isothermally crystallised below 150 °C and non-isothermally crystallised at 40 °C/min.

This is borne out by the DSC results of the samples printed by FFF at different chamber temperatures. The principal peak at 197 °C that ensues from FFF samples is close to the peak designated as Peak II in the low-temperature isothermal crystallisation experiments at 195 °C; why the double peak seen in the

isothermal crystallisation becomes a single peak during FFF remains a subject to be further researched. The presence of the low-temperature shoulder in DSC trace of the Apium FFF samples may be an indication that Peak I from the isothermal crystallisation experiments is present, albeit in a reduced state. The reduction of Peak I to a shoulder is hypothesised to be due to the effect of the reheatings during the FFF process.

Furthermore, the FFF samples prepared at higher chamber temperature also show the presence of an additional peak in addition to the FFF peak at 97 °C. Analysis of this peak indicates that it is a reduced form of Peak I from the isothermal crystallisation experiments, with its position increasing in temperature as the chamber temperature rises. The isothermal crystallisation experiments can thus be considered to be an integral component of the FFF process. This indicates that the isothermal and non-isothermal crystallisation tests represent a strong approximation for the effects of the thermal history of the FFF process. Deviation from the isothermal and non-isothermal crystallisation process is hypothesised to be due to the effects of the reheatings caused by deposition of subsequent layers, which is not accounted for by the DSC process.

The WAXS analysis sheds further light on the utility of isothermal and non-isothermal crystallisation as a basis for FFF analysis. The single melting endotherm observed during reheating after cooling at 20 °C/min is indicative of more perfect crystals formed, corresponding to the sharp and well defined 200 reflection peak in the WAXS data from Sample IV. By contrast, the sample cooled at 40 °C/min which has a double melting endotherm is due to the melting and recrystallisation of imperfectly formed crystals from rapid cooling; this corresponds to the poorly defined 200 peak in the WAXS data from Sample I. Thereby, the better defined the secondary 200 peak is in the WAXS data, the DSC data tends towards a single melting endotherm.

8.1.3 Impact on the structure of Nylon-12

The differences in structure that the FFF process imparts to Nylon-12 are most easily visible in the DSC traces and the degree of crystallinity. The degree of crystallinity

produced via isothermal crystallisation at a given temperature in Section 4.2.1.1 is lower than that in samples produced via FFF and then annealed at the same temperature in Section 4.2.3. The DSC traces for FFF-produced samples always show a characteristic "FFF endotherm" even after annealing.

It is difficult to precisely identify the effect of the FFF process on the crystal structure based on the available data. The WAXS data for cooling rate showed that the FFF RS sample, with fast cooling rates during the print, had the same WAXS pattern as a filament sample non-isothermally crystallised at 35 °C/min. Meanwhile, the FFF Apium sample, with lower cooling rates during the build and a higher "isothermal crystallisation temperature" had the same WAXS pattern as a filament sample non-isothermally crystallised at 2 °C/min.

It has been proposed by other authors [55, 57], as mentioned in Section 1.4.2.1, that the higher degree of crystallinity associated with FFF samples versus raw filament is due to the repeated heating and cooling that a filament undergoes during FFF;, this thermodynamic driving force induces more nucleation, leading to more and smaller crystals. This heating and cooling during FFF is proposed to be the cause of the "FFF endotherm" on the DSC trace; however, the precise crystal structure corresponding to this characteristic "FFF endotherm" remains unidentified in this study.

The following conclusion can be made based on the data, however: slower cooling rates and higher temperatures result in thicker lamellae and more perfectly formed crystals that contribute significantly to the tensile performance of Nylon-12 samples. The higher lamellar density associated with slower cooling rates was established in Chapter 3, while in Section 4.2.3.2 the increase in melting temperature of the sample annealed at 190 °C indicates a similar lamellar thickening process according to Equation 1.25. The FFF process is therefore proposed to produce $\gamma-$form Nylon-12 with two characteristic reflections ($001(+20\bar{1})$ and 200) corresponding to the inter-chain spacing in a single lamella and the spacing between bonded lamellar sheets respectively. Alteration of the thermal history, either via changing the cooling rate or annealing, will result in the same crystal structure but with different lamellar

thickness, and is proposed also to result in changes to the crystal size and perfection. In turn, these changes affect the tensile performance as described in Chapter 6.

8.2 Outlook

There remains scope for further investigation on the process-structure property relationship in fused filament fabrication of Nylon-12. Although the current study provides a strong basis for constructing a quantitative link between the thermal history and the mechanical properties of FFF Nylon-12, additional precision would be required for an optimal model.

Firstly, the current study provides only a very rough basis for simulating thermal history of Nylon-12 during FFF. Two possible studies are proposed: firstly, construction of a broader-scope physics-based finite element model to more accurately model the thermal history during the FFF process. Secondly, the acquisition of thermocouple or infrared camera data to precisely measure the temperature of individual filaments during the FFF process. Although the second approach would not allow for precise prediction of thermal history, it would provide a valuable dataset detailing the link between T_∞ and thermal history. This would allow for a more precise evaluation of the isothermal and non-isothermal components of the FFF process, and a precise evaluation of the time that a Nylon-12 sample spends cooling to T_∞ and subsequently crystallising isothermally at that temperature. This would additionally provide a dataset with which the output of an FEA model could be compared.

The FEA model could be produced via considering both the evolution of thermal history using a multiphysics model, and by considering the development of crystal growth using the block-by-block addition model proposed by Hoffman and Lauritzen [15], a method used by Trigg *et al* [166]. This would simulate the actual crystal growth given the thermal gradients output by the multiphysics model, and would provide estimates of crystal size and thickness which could be correlated to the WAXS data. It would also allow for a better estimate of the actual cooling rates

experienced by a Nylon-12 filament and therefore provide a basis for comparison to the crystallisation predictions made by the arctangent model.

Secondly, a more detailed model of the crystallisation behaviour is necessary. Although the present study has extensively analysed the thermal properties and crystallisation behaviour under isothermal and non-isothermal circumstances, a definitive quantitative model relating the $T - X(T) - Z(T)$ surface plot to the absolute rather than relative crystallinity is desired. This is attempted during the model of thermal history in Chapter 5, where absolute crystallinity parameters such as crystal radius and number of nucleations are output, and the total volume of transformed material is computed to find the latent heat of crystallisation. The crystallisation rate parameter K and the growth rate G in the Hoffman growth model are both governed by a qualitatively similar set of equations, although with different pre-exponential constants. It is therefore plausible that in a future study, the arctangent model for crystal growth rate could be adapted to output the time- and temperature-dependent crystal radius and nucleation rate, and therefore the absolute crystallinity could be output from the $T - X(T) - Z(T)$ plot. Since the tensile strength of the Nylon-12 samples is shown to be dependent on degree of crystallinity in Chapter 6, this would allow for a fully analytic prediction of mechanical properties from any given thermal history. The predictive power of the processing-structure-property model for FFF Nylon-12 could therefore be greatly enhanced.

Finally, further study into the dependence of the other mechanical properties described in Section 1.3.2.3 is necessary. The variation in tensile properties as a function of annealing temperature and therefore crystallinity provide a useful insight into the potential control over the mechanical properties of FFF Nylon-12 samples. However, compression testing, impact testing, fatigue testing and flexural testing among others would be necessary to give a more complete understanding of how mechanical properties depend on annealing temperature, and therefore how FFF Nylon-12 samples can be best optimised for their desired use.

In this thesis, the processing-structure and structure-property relationships in the fused filament fabrication of Nylon-12 have been studied in detail using

bulk thermal, mechanical and structural characterisation methods, and the data has been incorporated into the framework of a quantitative model to relate the three links in the chain to one another. Detailed study of the thermal properties of filament-based Nylon-12 has been undertaken. A hypothesis as to the nature of the changes to the crystal structure caused by the FFF process has been put forwards, and a predictive model relating the thermal history to the degree of crystallinity and crystal growth rate has been built and tested against experimental data. Finally, a quantitative link between the degree of crystallinity, influenced by thermal history and print chamber T_∞ has been constructed from the experimental data. It is hoped that this thesis can be a good instrument to better understand the nature of the FFF process, and to further develop the processing-structure property link in FFF Nylon-12 and other materials.

References

[1] Robert J. Young and Peter A. Lovell. *Introduction to Polymers*. 3rd ed. CRC Press, 2011.

[2] Gauthier Jarrousse. "Self adhesion of semi-crystalline polymers between their glass transition temperature and their melting temperature". In: December 2004 (2017).

[3] P. G. de Gennes. "Reptation of a Polymer Chain in the Presence of Fixed Obstacles". In: *The Journal of Chemical Physics* 55.2 (July 1971), pp. 572–579. URL: http://aip.scitation.org/doi/10.1063/1.1675789.

[4] S F Edwards. "The statistical mechanics of polymerized material". In: *Proceedings of the Physical Society* 92.1 (Sept. 1967), pp. 9–16. URL: https://iopscience.iop.org/article/10.1088/0370-1328/92/1/303.

[5] Gert Strobl. *The Physics of Polymers: Concepts for Understanding Their Structures and Behavior*. Ed. by Springer. Third. 2007.

[6] J.E. Spruiell. *A REVIEW OF THE MEASUREMENT AND DEVELOPMENT OF CRYSTALLINITY AND ITS RELATION TO PROPERTIES IN NEAT POLY(PHENYLENE SULFIDE) AND ITS FIBER REINFORCED COMPOSITES*. Tech. rep. Oak Ridge, TN: Oak Ridge National Laboratory (ORNL), Jan. 2005. URL: http://www.osti.gov/servlets/purl/885940-0p7nRC/.

[7] A. Keller. "A note on single crystals in polymers: Evidence for a folded chain configuration". In: *Philosophical Magazine* 2.21 (Sept. 1957), pp. 1171–1175. URL: http://www.tandfonline.com/doi/abs/10.1080/14786435708242746.

[8] Paul J. Flory and Do Yeung Yoon. "Molecular morphology in semicrystalline polymers". In: *Nature* 272.5650 (Mar. 1978), pp. 226–229. URL: http://www.nature.com/articles/272226a0.

[9] Ru Zhang et al. "Crystallization of poly(lactic acid) accelerated by cyclodextrin complex as nucleating agent". In: *Polymer Bulletin* 70.1 (Jan. 2013), pp. 195–206. URL: http://link.springer.com/10.1007/s00289-012-0814-y.

[10] Melvin Avrami. "Kinetics of Phase Change. I General Theory". In: *The Journal of Chemical Physics* 7.12 (Dec. 1939), pp. 1103–1112. URL: http://aip.scitation.org/doi/10.1063/1.1750380.

[11] T. Ozawa. "Kinetics of non-isothermal crystallization". In: *Polymer* 12.3 (Mar. 1971), pp. 150–158. URL: https://linkinghub.elsevier.com/retrieve/pii/0032386171900413.

[12] K. Nakamura et al. “Some aspects of nonisothermal crystallization of polymers. I. Relationship between crystallization temperature, crystallinity, and cooling conditions”. In: *Journal of Applied Polymer Science* 16.5 (May 1972), pp. 1077–1091. URL: https://onlinelibrary.wiley.com/doi/10.1002/app.1972.070160503.

[13] A Ziabicki. *Fundamentals of fibre formation: The science of fibre spinning and drawing*. Wiley, 1976.

[14] C. C. Lin. “The rate of crystallization of poly(ethylene terephthalate) by differential scanning calorimetry”. In: *Polymer Engineering and Science* 23.3 (Feb. 1983), pp. 113–116. URL: https://onlinelibrary.wiley.com/doi/10.1002/pen.760230302.

[15] John D. Hoffman, G. Thomas Davis, and John I. Lauritzen. “The Rate of Crystallization of Linear Polymers with Chain Folding”. In: *Treatise on Solid State Chemistry*. Boston, MA: Springer US, 1976, pp. 497–614. URL: http://link.springer.com/10.1007/978-1-4684-2664-9%7B%5C_%7D7.

[16] M Zhao, K Wudy, and D Drummer. “Crystallization Kinetics of Polyamide 12 during Selective Laser Sintering”. In: *Polymers* 10.2 (Feb. 2018), p. 168. URL: http://www.mdpi.com/2073-4360/10/2/168.

[17] John I. Lauritzen and John D. Hoffman. “Theory of formation of polymer crystals with folded chains in dilute solution”. In: *Journal of Research of the National Bureau of Standards Section A: Physics and Chemistry* 64A.1 (Jan. 1960), p. 73. URL: https://nvlpubs.nist.gov/nistpubs/jres/64A/jresv64An1p73%7B%5C_%7DA1b.pdf.

[18] Chad R. Snyder and Hervé Marand. “Effect of Chain Transport in the Secondary Surface Nucleation Based Flux Theory and in the Lauritzen-Hoffman Crystal Growth Rate Formalism”. In: *Macromolecules* 30.9 (May 1997), pp. 2759–2766. URL: https://pubs.acs.org/doi/10.1021/ma961633u.

[19] Chao Fu et al. “The correlation between crystallization kinetics and polymorphism behavior in the nanocomposite of poly(vinylidene fluoride) and quaternary phosphonium salts”. In: *physica status solidi (a)* 214.5 (May 2017), p. 1600869. URL: https://onlinelibrary.wiley.com/doi/10.1002/pssa.201600869.

[20] E H Andrews. “Spherulite morphology in thin films of natural rubber”. In: *Proceedings of the Royal Society of London. Series A. Mathematical and Physical Sciences* 270.1341 (Nov. 1962), pp. 232–241. URL: https://royalsocietypublishing.org/doi/10.1098/rspa.1962.0214.

[21] A. J. Pennings and A. M. Kiel. “Fractionation of polymers by crystallization from solution, III. On the morphology of fibrillar polyethylene crystals grown in solution”. In: *Kolloid-Zeitschrift & Zeitschrift für Polymere* 205.2 (Oct. 1965), pp. 160–162. URL: http://link.springer.com/10.1007/BF01507982.

[22] J Rieger. “Use of scattering methods in chemical industry - SAXS and SANS from fibers and films”. In: *Neutrons, X-rays and Light: Scattering Methods Applied to Soft Condensed Matter*. Ed. by P Lindner and Th Zemb. North-Holl. 2002. Chap. 21.

[23] A. Reuss. “Berechnung der Fließgrenze von Mischkristallen auf Grund der Plastizitätsbedingung für Einkristalle .” In: *ZAMM - Journal of Applied Mathematics and Mechanics / Zeitschrift für Angewandte Mathematik und Mechanik* 9.1 (1929), pp. 49–58.

[24] W. Voigt. “Ueber die Beziehung zwischen den beiden Elasticitätsconstanten isotroper Körper”. In: *Annalen der Physik* 274.12 (1889), pp. 573–587. URL: http://doi.wiley.com/10.1002/andp.18892741206.

[25] Gideon N. Levy, Ralf Schindel, and J.P. Kruth. “RAPID MANUFACTURING AND RAPID TOOLING WITH LAYER MANUFACTURING (LM) TECHNOLOGIES, STATE OF THE ART AND FUTURE PERSPECTIVES”. In: *CIRP Annals* 52.2 (2003), pp. 589–609. URL: https://linkinghub.elsevier.com/retrieve/pii/S0007850607602066.

[26] J.-P. Kruth, M.C. Leu, and T. Nakagawa. “Progress in Additive Manufacturing and Rapid Prototyping”. In: *CIRP Annals* 47.2 (1998), pp. 525–540. URL: https://linkinghub.elsevier.com/retrieve/pii/S0007850607632405.

[27] T. Reiher and R. Koch. “Product Optimisation With and For Additive Manufacturing”. In: *Proceedings of the 27th Annual International Solid Freeform Fabrication Symposium*. 2016, pp. 2236–2249.

[28] Chen Chu, Greg Graf, and David W. Rosen. “Design for Additive Manufacturing of Cellular Structures”. In: *Computer-Aided Design and Applications* 5.5 (Jan. 2008), pp. 686–696. URL: http://www.cad-journal.net/files/vol%7B%5C_%7D5/Vol5No5.html.

[29] Michael Stöcker. “From rapid prototyping to rapid manufacturing”. In: *AutoTechnology* 2.2 (2002), pp. 38–40. URL: https://doi.org/10.1007/BF03246677.

[30] Neil Hopkinson and Phill Dickens. “Rapid prototyping for direct manufacture”. In: *Rapid Prototyping Journal* 7.4 (Oct. 2001), pp. 197–202. URL: https://www.emerald.com/insight/content/doi/10.1108/EUM0000000005753/full/html.

[31] Syed A.M. Tofail et al. “Additive manufacturing: scientific and technological challenges, market uptake and opportunities”. In: *Materials Today* 21.1 (Jan. 2018), pp. 22–37. URL: https://linkinghub.elsevier.com/retrieve/pii/S1369702117301773.

[32] A. Molazemhosseini et al. “Nanoindentation and nanoscratching responses of PEEK based hybrid composites reinforced with short carbon fibers and nano-silica”. In: *Polymer Testing* 32.3 (May 2013), pp. 525–534. URL: https://linkinghub.elsevier.com/retrieve/pii/S0142941813000287.

[33] Osama Abdulhameed et al. “Additive manufacturing: Challenges, trends, and applications”. In: *Advances in Mechanical Engineering* 11 (2 Feb. 2019), p. 168781401882288.

[34] I. John Solomon, P. Sevvel, and J. Gunasekaran. “A review on the various processing parameters in FDM”. In: *Materials Today: Proceedings* 37 (2021), pp. 509–514.

[35] Alba Cano-Vicent et al. “Fused deposition modelling: Current status, methodology, applications and future prospects”. In: *Additive Manufacturing* 47 (Nov. 2021), p. 102378.

[36] Haiguang Zhang et al. “Recent progress of 3D printed continuous fiber reinforced polymer composites based on fused deposition modeling: a review”. In: *Journal of Materials Science* 56 (23 Aug. 2021), pp. 12999–13022.

[37] Dries Vaes and Peter Van Puyvelde. “Semi-crystalline feedstock for filament-based 3D printing of polymers”. In: *Progress in Polymer Science* 118 (July 2021), p. 101411.

[38] Ali Alperen Bakır, Resul Atik, and Sezer Özerinç. “Mechanical properties of thermoplastic parts produced by fused deposition modeling:a review”. In: *Rapid Prototyping Journal* 27 (3 Apr. 2021), pp. 537–561.

[39] O.S. Carneiro, A.F. Silva, and R. Gomes. “Fused deposition modeling with polypropylene”. In: *Materials Design* 83 (Oct. 2015), pp. 768–776.

[40] Tuan Noraihan Azila Tuan Rahim, Abdul Manaf Abdullah, and Hazizan Md Akil. “Recent Developments in Fused Deposition Modeling-Based 3D Printing of Polymers and Their Composites”. In: *Polymer Reviews* 59 (4 Oct. 2019), pp. 589–624.

[41] Steven Easter et al. “Using advanced manufacturing to produce unmanned aerial vehicles: a feasibility study”. In: ed. by Tien Pham, Michael A. Kolodny, and Kevin L. Priddy. May 2013, p. 874204.

[42] Manav Doshi et al. “Printing parameters and materials affecting mechanical properties of FDM-3D printed Parts: Perspective and prospects”. In: *Materials Today: Proceedings* 50 (2022), pp. 2269–2275.

[43] Alberto Cattenone, Ferdinando Auricchio, and Simone Morganti. “Analysis and Simulation of Additive manufacturing processes”. In: (2018).

[44] Yuhan Liao et al. “Effect of Porosity and Crystallinity on 3D Printed PLA Properties”. In: *Polymers* 11.9 (Sept. 2019), p. 1487. URL: https://www.mdpi.com/2073-4360/11/9/1487.

[45] Bastian Brenken et al. “Fused filament fabrication of fiber-reinforced polymers: A review”. In: *Additive Manufacturing* 21 (May 2018), pp. 1–16. URL: https://linkinghub.elsevier.com/retrieve/pii/S2214860417304475.

[46] Céline Bellehumeur et al. “Modeling of Bond Formation Between Polymer Filaments in the Fused Deposition Modeling Process”. In: *Journal of Manufacturing Processes* 6.2 (Jan. 2004), pp. 170–178. URL: https://linkinghub.elsevier.com/retrieve/pii/S1526612504700717.

[47] Charoula Kousiatza and Dimitris Karalekas. “Experimental study of fabrication-induced residual strains and distortions in polymeric square plates built using fused deposition modeling process”. In: *Material Design & Processing Communications* (Feb. 2020). URL: https://onlinelibrary.wiley.com/doi/abs/10.1002/mdp2.149.

[48] Varun Srinivas, Catharina S.J. van Hooy-Corstjens, and Jules A.W. Harings. “Correlating molecular and crystallization dynamics to macroscopic fusion and thermodynamic stability in fused deposition modeling; a model study on polylactides”. In: *Polymer* 142 (Apr. 2018), pp. 348–355. URL: https://linkinghub.elsevier.com/retrieve/pii/S0032386118302799.

[49] Jonathan E. Seppala et al. "Weld formation during material extrusion additive manufacturing". In: *Soft Matter* 13.38 (2017), pp. 6761–6769. URL: http://xlink.rsc.org/?DOI=C7SM00950J.

[50] Dries Vaes et al. "Assessment of Crystallinity Development during Fused Filament Fabrication through Fast Scanning Chip Calorimetry". In: *Applied Sciences* 9.13 (June 2019), p. 2676. URL: https://www.mdpi.com/2076-3417/9/13/2676.

[51] Masoumeh Pourali and Amy M. Peterson. "A tale of two polyamides: Comparing the crystallization kinetics of a hot-melt adhesive and a PA 6/66 copolymer". In: *Thermochimica Acta* 710 (Apr. 2022), p. 179176.

[52] M. Doumeng et al. "A comparative study of the crystallinity of polyetheretherketone by using density, DSC, XRD, and Raman spectroscopy techniques". In: *Polymer Testing* 93 (Jan. 2021), p. 106878.

[53] Babs Van de Voorde et al. "Effect of extrusion and fused filament fabrication processing parameters of recycled poly(ethylene terephthalate) on the crystallinity and mechanical properties". In: *Additive Manufacturing* 50 (Feb. 2022), p. 102518.

[54] Wangwang Yu et al. "Melt crystallization of PLA/Talc in fused filament fabrication". In: *Materials Design* 182 (Nov. 2019), p. 108013.

[55] Dietmar Drummer, Sandra Cifuentes-Cuéllar, and Dominik Rietzel. "Suitability of PLA/TCP for fused deposition modeling". In: *Rapid Prototyping Journal* 18 (6 Sept. 2012), pp. 500–507.

[56] Y. Song et al. "Measurements of the mechanical response of unidirectional 3D-printed PLA". In: *Materials Design* 123 (June 2017), pp. 154–164.

[57] Makara Lay et al. "Comparison of physical and mechanical properties of PLA, ABS and nylon 6 fabricated using fused deposition modeling and injection molding". In: *Composites Part B: Engineering* 176 (Nov. 2019), p. 107341.

[58] How Wei Benjamin Teo et al. "Non-isothermal crystallization behaviour of polyamide 12 analogous to multi-jet fusion additive manufacturing process". In: *Polymer* 235 (Nov. 2021), p. 124256.

[59] A. Gradys et al. "Kinetics of isothermal and non-isothermal crystallization of poly(vinylidene fluoride) by fast scanning calorimetry". In: *Polymer* 82 (Jan. 2016), pp. 40–48.

[60] Hamidreza Vanaei et al. "Influence of process parameters on thermal and mechanical properties of <scp>polylactic acid</scp> fabricated by fused filament fabrication". In: *Polymer Engineering Science* 60 (8 Aug. 2020), pp. 1822–1831.

[61] Wilco M.H. Verbeeten, Miriam Lorenzo-Bañuelos, and Pablo J. Arribas-Subiñas. "Anisotropic rate-dependent mechanical behavior of Poly(Lactic Acid) processed by Material Extrusion Additive Manufacturing". In: *Additive Manufacturing* 31 (Jan. 2020), p. 100968.

[62] Muhammad Harris et al. "In-process thermal treatment of polylactic acid in fused deposition modelling". In: *Materials and Manufacturing Processes* 34 (6 Apr. 2019), pp. 701–713.

[63] Jennifer Gonzalez Ausejo et al. "A comparative study of three-dimensional printing directions: The degradation and toxicological profile of a PLA/PHA blend". In: *Polymer Degradation and Stability* 152 (June 2018), pp. 191–207.

[64] F Knoop and V Schoeppner. *MECHANICAL AND THERMAL PROPERTIES OF FDM PARTS MANUFACTURED WITH POLYAMIDE 12*. 2015.

[65] Prakhyat Hejmady et al. "Laser sintering of PA12 particles studied by in-situ optical, thermal and X-ray characterization". In: *Additive Manufacturing* 52 (Apr. 2022), p. 102624.

[66] S. Felder et al. "Modeling the effect of temperature and degree of crystallinity on the mechanical response of Polyamide 6". In: *Mechanics of Materials* 148 (Sept. 2020), p. 103476.

[67] Iago Augusto Reis et al. "Annealing and crystallization kinetics of poly(lactic acid) pieces obtained by additive manufacturing". In: *Polymer Engineering Science* 61 (7 July 2021), pp. 2097–2104.

[68] Jie Leng, Junjie Wu, and Jie Zhang. "Preparation of Thermoplastic Polyurethane Parts Reinforced with in Situ Polylactic Acid Microfibers during Fused Deposition Modeling: The Influences of Deposition-Induced Effects". In: *Industrial & Engineering Chemistry Research* 58.47 (Nov. 2019), pp. 21476–21484. URL: https://pubs.acs.org/doi/10.1021/acs.iecr.9b04285.

[69] Ying-Guo Zhou et al. "Balance between bonding and deposition during fused deposition modeling of polycarbonate and acrylonitrile-butadiene-styrene composites". In: *Polymer Composites* 41.1 (Jan. 2020), pp. 60–72. URL: https://onlinelibrary.wiley.com/doi/abs/10.1002/pc.25345.

[70] Aurora Nogales et al. "Structure Development in Polymers during Fused Filament Fabrication (FFF): An in Situ Small- and Wide-Angle X-ray Scattering Study Using Synchrotron Radiation". In: *Macromolecules* 52 (24 Dec. 2019), pp. 9715–9723.

[71] Neiko P. Levenhagen and Mark D. Dadmun. "Bimodal molecular weight samples improve the isotropy of 3D printed polymeric samples". In: *Polymer* 122 (July 2017), pp. 232–241.

[72] Yuval Shmueli et al. "In Situ Time-Resolved X-ray Scattering Study of Isotactic Polypropylene in Additive Manufacturing". In: *ACS Applied Materials Interfaces* 11 (40 Oct. 2019), pp. 37112–37120.

[73] Jennifer Gonzalez Ausejo et al. "Three-dimensional printing of PLA and PLA/PHA dumbbell-shaped specimens of crisscross and transverse patterns as promising materials in emerging application areas: Prediction study". In: *Polymer Degradation and Stability* 156 (Oct. 2018), pp. 100–110.

[74] Yixin Jiang et al. "Reinforced and toughened PP/PS composites prepared by Fused Filament Fabrication (FFF) with in-situ microfibril and shish-kebab structure". In: *Polymer* 186 (Jan. 2020), p. 121971.

[75] Jian-Wei Tseng et al. "Screw extrusion-based additive manufacturing of PEEK". In: *Materials Design* 140 (Feb. 2018), pp. 209–221.

[76] Fengyuan Liu et al. "Structural Evolution of PCL during Melt Extrusion 3D Printing". In: *Macromolecular Materials and Engineering* 303 (2 Feb. 2018), p. 1700494.

[77] Geoffrey R. Mitchell et al. "Controlling and Evaluating the Structure and Morphology of Polymers on Multiple Scales". In: *Journal of Materials Science and Chemical Engineering* 03.12 (2015), pp. 48–60. URL: http://www.scirp.org/journal/doi.aspx?DOI=10.4236/msce.2015.312009.

[78] Lu Wang, William M. Gramlich, and Douglas J. Gardner. "Improving the impact strength of Poly(lactic acid) (PLA) in fused layer modeling (FLM)". In: *Polymer* 114 (Apr. 2017), pp. 242–248. URL: https://linkinghub.elsevier.com/retrieve/pii/S0032386117302586.

[79] Gregory D. Smith et al. "Non-isothermal fusion bonding of polypropylene". In: *Polymer* 42.14 (June 2001), pp. 6247–6257. URL: https://linkinghub.elsevier.com/retrieve/pii/S003238610100060X.

[80] Y.-Q. Xue et al. "Welding Behavior of Semicrystalline Polymers. 2. Effect of Cocrystallization on Autoadhesion". In: *Macromolecules* 33.19 (Sept. 2000), pp. 7084–7087. URL: https://pubs.acs.org/doi/10.1021/ma000754y.

[81] A. N. Gent, E.-G. Kim, and P. Ye. "Autohesion of crosslinked polyethylene". In: *Journal of Polymer Science Part B: Polymer Physics* 35.4 (Mar. 1997), pp. 615–622. URL: http://doi.wiley.com/10.1002/%7B%5C%%7D28SICI%7B%5C%%7D291099-0488%7B%5C%%7D28199703%7B%5C%%7D2935%7B%5C%%7D3A4%7B%5C%%7D3C615%7B%5C%%7D3A%7B%5C%%7D3AAID-POLB9%7B%5C%%7D3E3.0.CO%7B%5C%%7D3B2-O.

[82] Seth Collins Partain and Douglas Cairns. "Fused Deposition Modeling with Localized Pre-deposition Heating Using Forced Air". In: *Mechanical and Industrial Engineering* Master of.January (2007), p. 99.

[83] Abinesh. Ravi. "A Study on an In-Process Laser Localized Pre-Deposition Heating Approach to Reducing FDM". In: *Paper Knowledge . Toward a Media History of Documents* August (2014).

[84] Cemile Basgul et al. "Does annealing improve the interlayer adhesion and structural integrity of FFF 3D printed PEEK lumbar spinal cages?" In: *Journal of the Mechanical Behavior of Biomedical Materials* 102 (Feb. 2020), p. 103455. URL: https://linkinghub.elsevier.com/retrieve/pii/S1751616119306824.

[85] Meng Luo et al. "Controllable interlayer shear strength and crystallinity of PEEK components by laser-assisted material extrusion". In: *Journal of Materials Research* 33.11 (June 2018), pp. 1632–1641. URL: http://link.springer.com/10.1557/jmr.2018.131.

[86] Howard W. Starkweather et al. "Effect of crystallinity on the properties of nylons". In: *Journal of Polymer Science* 21.98 (Aug. 1956), pp. 189–204. URL: https://onlinelibrary.wiley.com/doi/10.1002/pol.1956.120219803.

[87] D.G.M. Wright et al. "The effect of crystallinity on the properties of injection moulded polypropylene and polyacetal". In: *Polymer* 29.5 (May 1988), pp. 793–796. URL: https://linkinghub.elsevier.com/retrieve/pii/0032386188901346.

[88] Sunil Bhandari, Roberto A. Lopez-Anido, and Douglas J. Gardner. "Enhancing the interlayer tensile strength of 3D printed short carbon fiber reinforced PETG and PLA composites via annealing". In: *Additive Manufacturing* 30 (Dec. 2019), p. 100922.

[89] Kevin R. Hart et al. “Increased fracture toughness of additively manufactured amorphous thermoplastics via thermal annealing”. In: *Polymer* 144 (May 2018), pp. 192–204. URL: https://linkinghub.elsevier.com/retrieve/pii/S0032386118303185.

[90] Jonathan Torres et al. “Mechanical Property Optimization of FDM PLA in Shear with Multiple Objectives”. In: *JOM* 67 (5 May 2015), pp. 1183–1193.

[91] Sridher Rangisetty and Larry D. Peel. “The Effect of Infill Patterns and Annealing on Mechanical Properties of Additively Manufactured Thermoplastic Composites”. In: American Society of Mechanical Engineers, Sept. 2017.

[92] K. Sathish Kumar et al. “Augmenting effect of infill density and annealing on mechanical properties of PETG and CFPETG composites fabricated by FDM”. In: *Materials Today: Proceedings* 45 (2021), pp. 2186–2191.

[93] S. Valvez et al. “Annealing effect on mechanical properties of 3D printed composites”. In: *Procedia Structural Integrity* 37 (2022), pp. 738–745.

[94] C. E. Majewski, H. Zarringhalam, and N. Hopkinson. “Effects of degree of particle melt and crystallinity in SLS Nylon-12 parts”. In: *19th Annual International Solid Freeform Fabrication Symposium, SFF 2008* (2008), pp. 45–54.

[95] Siddharth Ram Athreya, Kyriaki Kalaitzidou, and Suman Das. “Mechanical and microstructural properties of Nylon-12/carbon black composites: Selective laser sintering versus melt compounding and injection molding”. In: *Composites Science and Technology* 71.4 (Feb. 2011), pp. 506–510. URL: https://linkinghub.elsevier.com/retrieve/pii/S0266353810005154.

[96] Radoslaw A. Wach, Piotr Wolszczak, and Agnieszka Adamus-Wlodarczyk. “Enhancement of Mechanical Properties of FDM-PLA Parts via Thermal Annealing”. In: *Macromolecular Materials and Engineering* 303.9 (Sept. 2018), p. 1800169. URL: http://doi.wiley.com/10.1002/mame.201800169.

[97] Vukašin Slavković et al. “Influence of Annealing and Printing Directions on Mechanical Properties of PLA Shape Memory Polymer Produced by Fused Deposition Modeling”. In: *International Congress of Serbian Society of Mechanics* June (2017), pp. 1–8. URL: https://www.researchgate.net/publication/317617713%7B%5C_%7DInfluence%7B%5C_%7Dof%7B%5C_%7DAnnealing%7B%5C_%7Dand%7B%5C_%7DPrinting%7B%5C_%7DDirections%7B%5C_%7Don%7B%5C_%7DMechanical%7B%5C_%7DProperties%7B%5C_%7Dof%7B%5C_%7DPLA%7B%5C_%7DShape%7B%5C_%7DMemory%7B%5C_%7DPolymer%7B%5C_%7DProduced%7B%5C_%7Dby%7B%5C_%7DFused%7B%5C_%7DDeposition%7B%5C_%7DModeling.

[98] Dong Yang et al. “Effects of crystallinity control on mechanical properties of 3D-printed short-carbon-fiber-reinforced polyether ether ketone composites”. In: *Polymer Testing* 97 (May 2021), p. 107149. URL: https://linkinghub.elsevier.com/retrieve/pii/S0142941821000994.

[99] A.P. Valerga et al. “On the Relationship between Mechanical Properties and Crystallisation of Chemically Post-Processed Additive Manufactured Polylactic Acid Pieces”. In: *Polymers* 12.4 (Apr. 2020), p. 941. URL: https://www.mdpi.com/2073-4360/12/4/941.

[100] P. Arjun et al. "Effects of process parameters and annealing on the tensile strength of 3D printed carbon fiber reinforced polylactic acid". In: *Materials Today: Proceedings* (Feb. 2022).

[101] Qing Chen et al. "Improved bond strength, reduced porosity and enhanced mechanical properties of 3D-printed polyetherimide composites by carbon nanotubes". In: *Composites Communications* 30 (Feb. 2022), p. 101083.

[102] J.M. Chacón et al. "Additive manufacturing of PLA structures using fused deposition modelling: Effect of process parameters on mechanical properties and their optimal selection". In: *Materials Design* 124 (June 2017), pp. 143–157.

[103] Gurmaheshinder Singh Sandhu, Kamaljit Singh Boparai, and Kawaljit Singh Sandhu. "Influence of slicing parameters on selected mechanical properties of fused deposition modeling prints". In: *Materials Today: Proceedings* 48 (2022), pp. 1378–1382.

[104] Ranjith Gopi Mohan et al. "Comparitive analysis of mechanical properties of FDM printed parts based on raster angles". In: *Materials Today: Proceedings* 47 (2021), pp. 4730–4734.

[105] Majid R. Ayatollahi et al. "The influence of in-plane raster angle on tensile and fracture strengths of 3D-printed PLA specimens". In: *Engineering Fracture Mechanics* 237 (Oct. 2020), p. 107225.

[106] Strahinja Milenkovic et al. "Effect of the raster orientation on strength of the continuous fiber reinforced PVDF/PLA composites, fabricated by hand-layup and fused deposition modeling". In: *Composite Structures* 270 (Aug. 2021), p. 114063.

[107] Hao Liu et al. "Three-dimensional printing of poly(lactic acid) bio-based composites with sugarcane bagasse fiber: Effect of printing orientation on tensile performance". In: *Polymers for Advanced Technologies* 30 (4 Apr. 2019), pp. 910–922.

[108] S.F. Khan et al. "Effect of infill on tensile and flexural strength of 3D printed PLA parts". In: *IOP Conference Series: Materials Science and Engineering* 429 (Nov. 2018), p. 012101.

[109] Brian W. Kaplun et al. "Influence of orientation on mechanical properties for high-performance fused filament fabricated ultem 9085 and electro-statically dissipative polyetherketoneketone". In: *Additive Manufacturing* 36 (Dec. 2020), p. 101527.

[110] B. Caulfield, P.E. McHugh, and S. Lohfeld. "Dependence of mechanical properties of polyamide components on build parameters in the SLS process". In: *Journal of Materials Processing Technology* 182.1-3 (Feb. 2007), pp. 477–488. URL: https://linkinghub.elsevier.com/retrieve/pii/S0924013606007886.

[111] O. S. Es-Said et al. "Effect of Layer Orientation on Mechanical Properties of Rapid Prototyped Samples". In: *Materials and Manufacturing Processes* 15.1 (Jan. 2000), pp. 107–122. URL: http://www.tandfonline.com/doi/abs/10.1080/10426910008912976.

[112] Sung-Hoon Ahn et al. "Anisotropic material properties of fused deposition modeling ABS". In: *Rapid Prototyping Journal* 8.4 (Oct. 2002), pp. 248–257. URL: https://www.emerald.com/insight/content/doi/10.1108/13552540210441166/full/html.

[113] Li, Michel H. J. Koch, and Wim H. de Jeu. “Crystalline Structure and Morphology in Nylon-12: A Small- and Wide-Angle X-ray Scattering Study”. In: *Macromolecules* 36.5 (Mar. 2003), pp. 1626–1632. URL: https://pubs.acs.org/doi/10.1021/ma025732l.

[114] Minying Liu et al. “Melting behaviors, isothermal and non-isothermal crystallization kinetics of nylon 1212”. In: *Polymer* 44.8 (Apr. 2003), pp. 2537–2545. URL: https://linkinghub.elsevier.com/retrieve/pii/S0032386103001010.

[115] Tom O’Haver. *peakfit*. 2018.

[116] Sidonie Costa, Fernando Duarte, and Jose A. “Using MATLAB to Compute Heat Transfer in Free Form Extrusion”. In: *MATLAB - A Ubiquitous Tool for the Practical Engineer*. InTech, Oct. 2011. URL: http://www.intechopen.com/books/matlab-a-ubiquitous-tool-for-the-practical-engineer/using-matlab-to-compute-heat-transfer-in-free-form-extrusion.

[117] Y. Yuan et al. “Prediction of temperature and crystal growth evolution during 3D printing of polymeric materials via extrusion”. In: *Materials & Design* 196 (Nov. 2020), p. 109121. URL: https://linkinghub.elsevier.com/retrieve/pii/S0264127520306560.

[118] Sasan Dadbakhsh et al. “Effect of PA12 powder reuse on coalescence behaviour and microstructure of SLS parts”. In: *European Polymer Journal* 92 (July 2017), pp. 250–262. URL: https://linkinghub.elsevier.com/retrieve/pii/S0014305716316615.

[119] Nobuyasu Hiramatsu, Kazunao Haraguchi, and Susumu Hirakawa. “Study of Transformations among α, γ and γ’ Forms in Nylon 12 by X-Ray and DSC”. In: *Japanese Journal of Applied Physics* 22.Part 1, No. 2 (Feb. 1983), pp. 335–339. URL: https://iopscience.iop.org/article/10.1143/JJAP.22.335.

[120] Kazuo Inoue and Sadao Hoshino. “Crystal structure of nylon 12”. In: *Journal of Polymer Science Part A-2: Polymer Physics* 11.6 (June 1973), pp. 1077–1089. URL: http://doi.wiley.com/10.1002/pol.1973.180110604.

[121] Toshihiko Ishikawa et al. “Change of Fine Texture of Nylon 12 by Drawing”. In: *NIPPON KAGAKU KAISHI* 9 (1973), pp. 1744–1751. URL: http://joi.jlc.jst.go.jp/JST.Journalarchive/nikkashi1972/1973.1744?from=CrossRef.

[122] T. Ishikawa, S. Nagai, and N. Kasai. “Gamma-to-alpha partial transformation in nylon 12 by drawing”. In: 988 (1981), pp. 977–988.

[123] Ning Ma et al. “Crystal transition and thermal behavior of Nylon 12”. In: *e-Polymers* 20.1 (June 2020), pp. 346–352. URL: https://www.degruyter.com/document/doi/10.1515/epoly-2020-0039/html.

[124] F. Paolucci et al. “Quantification of isothermal crystallization of polyamide 12: Modelling of crystallization kinetics and phase composition”. In: *Polymer* 155 (Oct. 2018), pp. 187–198. URL: https://linkinghub.elsevier.com/retrieve/pii/S0032386118308735.

[125] C. J. G. Plummer et al. “The crystallization kinetics of polyamide-12”. In: *Colloid & Polymer Science* 279.4 (Apr. 2001), pp. 312–322. URL: http://link.springer.com/10.1007/s003960000425.

[126] S Aharoni. *n-Nylons: Their Synthesis, Structure and Properties*. Wiley-IEEE Press, 1997, p. 622.

[127] S. Gogolewski. "Effect of annealing on thermal properties and crystalline structure of polyamides. Nylon 11 (polyundecaneamide)". In: *Colloid and Polymer Science* 257.8 (Aug. 1979), pp. 811–819. URL: http://link.springer.com/10.1007/BF01383352.

[128] Neil L. A. McFerran, Cecil G. Armstrong, and Tony McNally. "Nonisothermal and isothermal crystallization kinetics of nylon-12". In: *Journal of Applied Polymer Science* 110.2 (Oct. 2008), pp. 1043–1058. URL: http://doi.wiley.com/10.1002/app.28696.

[129] Benjamin de Jager et al. "Synchrotron X-ray Scattering Analysis of Nylon-12 Crystallisation Variation Depending on 3D Printing Conditions". In: *Polymers* 12.5 (May 2020), p. 1169. URL: https://www.mdpi.com/2073-4360/12/5/1169.

[130] Andrea Monami et al. "Fracture Mechanics Properties of Polymorphic Polypropylene". In: *Procedia Materials Science* 3 (2014), pp. 276–281.

[131] John Kauffman and Waller George. "Load Induced X-Ray Line Broadening in Nylon Filaments". In: *Journal of Applied Physics* 21.5 (May 1950), pp. 431–434. URL: http://aip.scitation.org/doi/10.1063/1.1699679.

[132] N.A.J.M. van Aerle. "A real-time drawing study of melt-crystallized ultra-high molecular weight polyethylene. Comparison with conventional X-ray results". In: *Die Makromolekulare Chemie* 189.7 (1988), pp. 1569–1577.

[133] T. Choupin et al. "Isothermal crystallization kinetic modeling of poly(etherketoneketone) (PEKK) copolymer". In: *Polymer* 111 (Feb. 2017), pp. 73–82. URL: https://linkinghub.elsevier.com/retrieve/pii/S0032386117300514.

[134] Tanguy Choupin et al. "A more reliable DSC-based methodology to study crystallization kinetics: Application to poly(ether ketone ketone) (PEKK) copolymers". In: *Polymer* 155 (Oct. 2018), pp. 109–115. URL: https://linkinghub.elsevier.com/retrieve/pii/S0032386118308061.

[135] Peggy Cebe and Su-Don Hong. "Crystallization behaviour of poly(ether-ether-ketone)". In: *Polymer* 27.8 (Aug. 1986), pp. 1183–1192. URL: https://linkinghub.elsevier.com/retrieve/pii/0032386186900066.

[136] D. Turnbull and J. C. Fisher. "Rate of Nucleation in Condensed Systems". In: *The Journal of Chemical Physics* 17.1 (Jan. 1949), pp. 71–73. URL: http://aip.scitation.org/doi/10.1063/1.1747055.

[137] John D. Hoffman. "Thermodynamic Driving Force in Nucleation and Growth Processes". In: *The Journal of Chemical Physics* 29.5 (Nov. 1958), pp. 1192–1193. URL: http://aip.scitation.org/doi/10.1063/1.1744688.

[138] F. Van Antwerpen and D. W. Van Krevelen. "Influence of crystallization temperature, molecular weight, and additives on the crystallization kinetics of poly(ethylene terephthalate)". In: *Journal of Polymer Science Part A-2: Polymer Physics* 10.12 (Dec. 1972), pp. 2423–2435. URL: https://onlinelibrary.wiley.com/doi/10.1002/pol.1972.180101211.

[139] Bruce B. Burnett and W. F. McDevit. “Kinetics of Spherulite Growth in High Polymers”. In: *Journal of Applied Physics* 28.10 (Oct. 1957), pp. 1101–1105. URL: http://aip.scitation.org/doi/10.1063/1.1722586.

[140] Jonas Nitzler et al. “A novel physics-based and data-supported microstructure model for part-scale simulation of laser powder bed fusion of Ti-6Al-4V”. In: *Advanced Modeling and Simulation in Engineering Sciences* 8.1 (Dec. 2021), p. 16. URL: https://amses-journal.springeropen.com/articles/10.1186/s40323-021-00201-9.

[141] Homer E. Kissinger. “Variation of peak temperature with heating rate in differential thermal analysis”. In: *Journal of Research of the National Bureau of Standards* 57.4 (Oct. 1956), p. 217. URL: https://nvlpubs.nist.gov/nistpubs/jres/057/jresv57n4p217%7B%5C_%7DA1b.pdf.

[142] Qing-xin Zhang and Z. Mo. “MELTING CRYSTALLIZATION BEHAVIOR OF NYLON 66”. In: *Chinese Journal of Polymer Science* 19 (), p. 237.

[143] Shengwen Tu et al. “Stress–strain curves of metallic materials and post-necking strain hardening characterization: A review”. In: *Fatigue & Fracture of Engineering Materials & Structures* 43.1 (Jan. 2020), pp. 3–19. URL: https://onlinelibrary.wiley.com/doi/10.1111/ffe.13134.

[144] Tuan Noraihan Azila Tuan Rahim et al. “Comparison of mechanical properties for polyamide 12 composite-based biomaterials fabricated by fused filament fabrication and injection molding”. In: 2016, p. 020007. URL: http://aip.scitation.org/doi/abs/10.1063/1.4968862.

[145] Javaid Butt and Raghunath Bhaskar. “Investigating the Effects of Annealing on the Mechanical Properties of FFF-Printed Thermoplastics”. In: *Journal of Manufacturing and Materials Processing* 4.2 (Apr. 2020), p. 38. URL: https://www.mdpi.com/2504-4494/4/2/38.

[146] Menderes Kam, Ahmet İpekçi, and Ömer Şengül. “Investigation of the effect of FDM process parameters on mechanical properties of 3D printed PA12 samples using Taguchi method”. In: *Journal of Thermoplastic Composite Materials* (Apr. 2021), p. 089270572110064. URL: http://journals.sagepub.com/doi/10.1177/08927057211006459.

[147] Xuan Lu and Yunxue Jin. “Mechanical properties and morphology of nylon 12 composites reinforced with graphene flake”. In: *Materials Research Express* 5.6 (June 2018), p. 065301. URL: https://iopscience.iop.org/article/10.1088/2053-1591/aac5bd.

[148] Tuomas Puttonen, Mika Salmi, and Jouni Partanen. “Mechanical properties and fracture characterization of additive manufacturing polyamide 12 after accelerated weathering”. In: *Polymer Testing* 104 (Dec. 2021), p. 107376. URL: https://linkinghub.elsevier.com/retrieve/pii/S0142941821003214.

[149] In Yee Phang et al. “Morphology, thermal and mechanical properties of nylon 12/organoclay nanocomposites prepared by melt compounding”. In: *Polymer International* 54.2 (Feb. 2005), pp. 456–464. URL: https://onlinelibrary.wiley.com/doi/10.1002/pi.1721.

[150] C. Armstutz, B. Weisse, and A. Zurbuchen. "Temperature-dependent tensile properties of polyamide 12 for the use in percutaneous transluminal coronary angioplasty balloon catheters". In: *Biomedical Engineering* 20.110 (2021).

[151] Garrett Craft et al. "Impact of extended sintering times on mechanical properties in PA-12 parts produced by powderbed fusion processes". In: *Additive Manufacturing* 22 (Aug. 2018), pp. 800–806. URL: https://linkinghub.elsevier.com/retrieve/pii/S2214860418302124.

[152] Leila Malekmotiei et al. "Effect of annealing temperature on interrelation between the microstructural evolution and plastic deformation in polymers". In: *Journal of Polymer Science Part B: Polymer Physics* 55.17 (Sept. 2017), pp. 1286–1297. URL: https://onlinelibrary.wiley.com/doi/10.1002/polb.24379.

[153] Nadya Dencheva et al. "Relationship between crystalline structure and mechanical behavior in isotropic and oriented polyamide 6". In: *Journal of Applied Polymer Science* 103.4 (Feb. 2007), pp. 2242–2252. URL: https://onlinelibrary.wiley.com/doi/10.1002/app.25250.

[154] Jiri Suder et al. "THE INFLUENCE OF ANNEALING TEMPERATURE ON TENSILE STRENGTH OF POLYLACTIC ACID". In: *MM Science Journal* 2020.4 (Nov. 2020), pp. 4132–4137. URL: http://www.mmscience.eu/2020048.

[155] Kantesh Balani et al. "Physical, Thermal, and Mechanical Properties of Polymers". In: *Biosurfaces* (2015), pp. 329–344.

[156] Joy J. Cheng et al. "Chain Entanglements and Mechanical Behavior of High Density Polyethylene". In: *Journal of Engineering Materials and Technology* 132.1 (Jan. 2010). URL: https://asmedigitalcollection.asme.org/materialstechnology/article/doi/10.1115/1.4000220/403653/Chain-Entanglements-and-Mechanical-Behavior-of.

[157] J. T. Yeh and J. Runt. "Fatigue crack-propagation in annealed poly(butylene terephthalate)". In: *Journal of Materials Science* 24.7 (July 1989), pp. 2637–2642. URL: http://link.springer.com/10.1007/BF01174538.

[158] Feng Zuo et al. "The role of interlamellar chain entanglement in deformation-induced structure changes during uniaxial stretching of isotactic polypropylene". In: *Polymer* 48.23 (Nov. 2007), pp. 6867–6880. URL: https://linkinghub.elsevier.com/retrieve/pii/S0032386107008774.

[159] Bernard A. G. Schrauwen et al. "Intrinsic Deformation Behavior of Semicrystalline Polymers". In: *Macromolecules* 37.16 (Aug. 2004), pp. 6069–6078. URL: https://pubs.acs.org/doi/10.1021/ma035279t.

[160] Koh-hei Nitta and Naoto Yamaguchi. "Influence of Morphological Factors on Tensile Properties in the Pre-yield Region of Isotactic Polypropylenes". In: *Polymer Journal* 38.2 (Feb. 2006), pp. 122–131. URL: http://www.nature.com/doifinder/10.1295/polymj.38.122.

[161] D. A. Hills et al. *Solution of Crack Problems*. Vol. 44. Solid Mechanics and Its Applications. Dordrecht: Springer Netherlands, 1996. URL: http://link.springer.com/10.1007/978-94-015-8648-1.

[162] Jie Li et al. "Effect of annealing temperature on the mechanical properties, thermal behavior and morphology of β-iPP/PA6 blends". In: *Materials & Design* 40 (Sept. 2012), pp. 392–399. URL: https://linkinghub.elsevier.com/retrieve/pii/S0261306912002567.

[163] B. Vieille et al. "On the improvement of thermo-mechanical behavior of carbon/polyphenylene sulfide laminated composites upon annealing at high temperature". In: *Composites Part B: Engineering* 216 (July 2021), p. 108858. URL: https://linkinghub.elsevier.com/retrieve/pii/S1359836821002493.

[164] Claire Benwood et al. "Improving the Impact Strength and Heat Resistance of 3D Printed Models: Structure, Property, and Processing Correlationships during Fused Deposition Modeling (FDM) of Poly(Lactic Acid)". In: *ACS Omega* 3 (4 Apr. 2018), pp. 4400–4411.

[165] Gregory Beaucage. *Hierarchical Nanostructed Materials*. 2019.

[166] Edward B. Trigg, Mark J. Stevens, and Karen I. Winey. "Chain Folding Produces a Multilayered Morphology in a Precise Polymer: Simulations and Experiments". In: *Journal of the American Chemical Society* 139.10 (Mar. 2017), pp. 3747–3755. URL: https://pubs.acs.org/doi/10.1021/jacs.6b12817.